Université de Paris

Université de Paris

École doctorale BIO SPC 562

Laboratoire Institut Cochin, UMR_S1016 UMR8104, Immunology of Diabetes

Role of ICOS and ICOSL in the Physiology and the Physiopathology of the Peripheral Nervous System

Rôle d'ICOS/ICOSL dans la physiologie et la pathophysiologie du système nerveux périphérique

Par Rasha BARAKAT

Thèse de doctorat de Neurobiologie

Dirigée par Pr Christian BOITARD
Et par Pr Assaad EID

Présentée et soutenue publiquement le 30 Novembre 2020

Devant un jury composé de:

Michael SCHUMACHER, DR, Université Paris Saclay, Rapporteur
Benoit SALOMON, DR, Sorbonne Université, Rapporteur
Claire BRIET, MCU-PH, CHU Angers, Examinatrice
Rima NABBOUT-TARANTINO, PU-PH, Université de Paris, Examinateur
Ruth STASSART, MD, University Hospital Leipzig, Membre Invité
Charbel MASSAAD, PU, Université de Paris, Membre Invité

Except where otherwise noted, this is work licensed under
https://creativecommons.org/licenses/by-nc-nd/3.0/fr/

“If I told you a flower bloomed in a dark room, would you trust it?”

- Kendrick D. Lamar

ACKNOWLEDGMENTS

I would like to start by thanking my thesis director Pr Assaad Eid who has been mentoring me since my Master's degree. Thank you for providing me with the opportunity to pursue a PhD degree as well as for your support throughout the years.

I express my deepest thanks to my director Pr Christian Boitard. Thank you for introducing me to the immunology field that was completely foreign to me. The knowledge I have acquired through your didactic teaching methods and scientific discussions helped in broadening my way of thinking and taught me how to merge different approaches. Your rigor and high standards for scientific work made me step out of my comfort zone and push my boundaries to make me the budding scientist that I am today.

I would like to convey a special thanks to Pr Charbel Massaad who even though was not listed as director on paper has welcomed me in his lab and treated me as his own student. You have been a true mentor throughout my PhD and without your support all of this would not have been possible. Thank you for your constant motivation and for always pushing me forward.

Thank you for the jury members for their time and efforts in reviewing my work.

I would like to thank all the teams that I have been a part of; the Eid team, the Leuhen team, and the Massaad team. Each one of you helped get through this journey. I would like to specially thank Dr Julien Grenier and Dr Delphine Meffre for the scientific and emotional support throughout my PhD. Thank you Dr Sandrine Luce for your constant help that started even before the beginning of my thesis. You were a motherly figure in the lab constantly handing out a helping hand.

A huge thank you for the PhD students and their endless support, without you this journey would have been unbearable. Aida Padilla-Ferrer, Venkatkrishnan Sundaram, Tatiana El Jalkh, Julia Fath, Dr Alex Carrete, Dr Nirmal Kumar Sampathkumar, Mirella El Khoury, Cynthia Bezier I wish you all the best. I would like to thank the members of the team who helped me in my work through experiments and scientific discussions: Chantal Becourt, Dr Ute Rogner, Pamela Al Houeiss, Alexis Gadault, Pr Mehrnaz Jafarian-Tehrani, Dr Christel Becker, Pr Sophie Bernard, Fatima El Ouazzani, Celine Becker, Julia Montanaro, Dr Damien Le menuet, Dr Anne Simon. I am also thankful for the help that my interns, Akram Remlawi and Ali Ferhi, have provided.

I would like to also thank Pr Frederic Charbonnier and his team for always being there for scientific and non-scientific discussion (special thanks to Dr Laure Weill and Dr Olivier Biondi). Thank you Pr Agnes Leuhen and her team for welcoming me into the lab and for their immunology contributions to my work.

Last but not least I would like to thank my family who has been my support system since I embarked on this journey. To my parents, Aline and Khalil, my sisters, Lama and Rim, and my grandmother Olivia, none of this would have been possible without you. To my best friend and partner Halim, you have been my rock since 2011. Thank you for your unconditional support.

ABSTRACT

The knockout of ICOS/ICOSL in a NOD background resulted in the deviation of the autoimmune system from the pancreas towards the PNS. The NOD KO mice are prevented from developing diabetes, but develop a severe autoimmune neuropathy characterized by behavioral, electrophysiological, and histological deficits. The NOD ICOS-/- and NOD ICOSL-/- mice have motor and sensory deficits characterized by poor motor coordination, reduced grip strength, altered perception of heat, and pathological CMAP response. The ultrastructure of the nerve was also affected; demyelinated areas, defected myelinated axons, and defected Remak bundles were observed in the NOD KO mice. The phenotype appears earlier in the NOD ICOS-/- (26 weeks) compared to the NOD ICOSL-/- (35 weeks) with lesions occurring in advance in the brachial nerve compared to the sciatic nerve. Interestingly, the knockout of ICOS in C57BL/6J or ICOSL in NOD SCID mice did not show any alteration in the phenotype (one-year-old mice). The characterization of the nerve infiltrate in NOD ICOS-/- and NOD ICOSL-/- mice revealed the presence of CD4+ and CD8+ T-cells as well as macrophages. Our data shows that ICOS is not expressed by the PNS however ICOSL mRNA is detected in the nerve and in particularly in Schwann cells. Our model shows the necessity of having a reactive autoimmune background for the development of the pathology as well as the importance of the ICOS-ICOSL interaction in the maintenance of self-tolerance in the nerves of NOD animals. Taken together, our results provide a robust animal model for immune-mediated neuropathies and in particular Chronic Inflammatory Demyelinating Polyneuropathy (CIDP).

RESUME DE THESE EN FRANCAIS

Le modèle murin NOD est utilisé pour l'étude du diabète auto-immun de type 1. La souris souffre d'une insulite (présence d'un infiltrat lymphocytaire dans les îlots de Langerhans du pancréas) après le sevrage avec un taux d'incidence de 60-80% chez les femelles et de 20-30% chez les males. Ce modèle a une prédisposition génétique au développement du diabète de type 1 et exprime I-Ag7 qui est une molécule de classe II du complexe majeur d'histocompatibilité (CMH). L'invalidation de la voie ICOS / ICOSL (Inducible T-Cell Co-Stimulator / Inducible T-Cell Co-Stimulator Ligand) sur le fond génétique de la souris Non-Obese Diabetic (NOD) contribue à la déviation du système immunitaire du pancréas vers le système nerveux périphérique. Les molécules ICOS/ICOSL font partie de la famille CD28/B7.2 de molécules de co-activation du système immunitaire. L'interaction entre ICOS et ICOSL est nécessaire pour l'activation des lymphocytes T lors d'une réponse immunitaire.

Les souris invalidées pour les gènes *icos* et *icosl* sont protégées du diabète mais développent une neuropathie auto-immune sévère caractérisée par des troubles comportementaux (des difficultés de locomotion, une diminution des sensations, et de la douleur), une étude électrodiagnostique anormale (électromyogramme et vitesse de conduction nerveuse pathologiques) et une histologie montrant des anomalies du nerf avec la présence de macrophages et de lymphocytes. Le nerf est composé d'axones moteurs qui sont enveloppés par une gaine de myéline produite par une cellule de Schwann myélinisante assurant une conduction nerveuse rapide. Afin de relayer les informations sensorielles, il existe une structure appelée « Remak bundle » formée d'un groupe d'axones de petit calibre qui sont enveloppés par une

cellule de Schwann non-myélinisante. Les souris NOD ICOS -/- et NOD ICOSL -/- souffrent de troubles moteurs et sensoriels se manifestant lors de tests comportementaux et électrophysiologiques. Parmi les tests comportementaux effectués, nous avons utilisé le « locotronic » pour évaluer la coordination motrice fine où la vitesse de locomotion était observée ainsi que le nombre d'erreurs chez les animaux testés ; le « grip strength test » pour mesurer la force de traction maximale de l'animal au niveau de ses pattes antérieures et postérieures, et le « hot plate test » pour voir si les animaux souffrent d'une hyperalgésie en plaçant la souris sur une plaque chaude et en mesurant la durée nécessaire pour que la souris ressente la douleur. Le test electrophysiologique effectué est le « compound muscle action potential » (CMAP) afin de mesurer la réponse musculaire au niveau du *tibialis* après une stimulation électrique du nerf sciatique. Le CMAP permet aussi de mesurer la période de latence avant la réponse musculaire. La structure du nerf est également affectée comme le montre la présence d'axones et de fibres nerveuses non myélinisées défectueuses chez les souris NOD ICOS -/- et NOD-ICOSL -/-. Le phénotype apparaît plus prématurément chez la souris NOD ICOS -/- (26 semaines) comparé à la souris NOD ICOSL -/- (35 semaines), avec des lésions plus précoces dans le nerf brachial que dans le nerf sciatique. Nous avons également voulu étudier l'invalidation de *icos* et *icosl* chez des souris ayant un fond génétique diffèrent de la souris NOD qui a un terrain auto-immun réactif. Nous avons généré deux modèles : la souris C57BL/6J ICOS -/- sur un fond C57BL/6J qui n'a pas de terrain auto-immun réactif et la souris NOD.*scid* ICOSL -/- qui n'a pas de lymphocyte T et B. L'invalidation du gène *icos* chez la souris C57BL/6J ou du gène *icosl* chez la souris NOD.*scid* n'a pas généré de phénotype après une observation sur 12 mois. Ces animaux ne souffrent pas de troubles comportementaux ni d'anormalités électrophysiologiques. De plus, l'histologie du nerf chez ces souris est normale sans défaut au

niveau de la gaine de myéline ou des fibres nerveuses myélinisées / non-myélinisées. La caractérisation de l'infiltrat chez les animaux NOD ICOS -/- et NOD ICOSL -/- montre la présence de lymphocytes T CD4+ et CD8+ ainsi que de macrophages. De plus, les ARNm codant pour *icos* ne sont pas détectés dans le système nerveux périphérique, alors que *icosl* est détecté dans le nerf et en particulier dans la cellule de Schwann. En effet, le gène *icosl* est exprimé dans les cultures de cellules de Schwann primaires aux stades de différentiation et de prolifération ainsi que dans les co-cultures de cellules de Schwann et de ganglions rachidiens. Cependant, d'autres types cellulaires présents dans le nerf pourraient exprimer *icosl*, en particulier les cellules endoneuriales, tels que les fibroblastes et les macrophages.

Notre modèle montre la nécessité d'avoir un système immunitaire réactif auto-immun pour le développement de la pathologie ainsi que l'importance de l'interaction entre ICOS et ICOSL dans le maintien de la tolérance du soi dans les nerfs de la souris NOD. En conclusion, nos résultats présentent un modèle robuste pour l'étude des neuropathies auto-immunes, en particulier celle de la Polyneuropathie Inflammatoire Démyélinisante Chronique (PIDC).

LIST OF IMPORTANT ABBREVIATIONS:

APC: Antigen Presenting Cell

β2M: β-2-Microglobulin

BNB: Blood Nerve Barrier

CIITA: Class II Major Histocompatibility Complex Transactivator

CIDP: Chronic Inflammatory Demyelination Polyradiculopathy

CMAP: Compound Muscle Action Potential

CNS: Central Nervous System

DRG: Dorsal Root Ganglia

EAN: Experimental Autoimmune Neuritis

GBS: Guillain-Barre Syndrome

ICOS: Inducible T-cell Co-Stimulato

ICOSL: Inducible T-cell Co-Stimulator Ligand

IVIg: Intravenous Immunoglobulin

MHC: Major Histocompatibility Complex

MPZ: Myelin Protein Zero

PMP22: Peripheral Myelin Protein 22

PNS: Peripheral Nervous System

T1D: Type 1 Diabetes

Treg: Regulator T-cell

WD: Wallerian Degeneration

This list contains the most important abbreviations in the manuscript, other abbreviations are defined in the text.

Table of Contents

CHAPTER I: INTRODUCTION 1
1. The Peripheral Nervous System (PNS) 1
1.1. General Overview 1
1.1.1. Anatomy and Function of the PNS 1
1.1.2. Structure and Cellular Composition of the Sciatic Nerve 9
1.2. PNS development and Myelination 12
1.2.1. Overview of PNS and Schwann Cell Development 12
1.2.2. Myelin Proteins 17
1.3. The Immune System and The PNS 21
1.3.1. Wallerian Degeneration 21
1.3.2. Nerve Injury in Immune Mediated Neuropathies 25
2. Autoimmune Peripheral Neuropathies 27
2.1. Guillain–Barre Syndrome (GBS) 27
2.1.1. Acute Inflammatory Demyelinating Polyradiculoneuropathy (AIDP) 29
2.1.2. Acute Motor Axonal Neuropathy (AMAN) and Acute Motor and Sensory Axonal Neuropathy (AMSAN) 31
2.1.3. Miller Fisher syndrome (MFS) 34
2.2. Chronic inflammatory neuropathies 35
2.2.1. Chronic Inflammatory Demyelinating Polyradiculoneuropathy (CIDP) and its variants. 35
2.2.2. Chronic inflammatory neuropathies distinct from CIDP 40
3. Experimental Models of Autoimmune Neuropathies 42
3.1. Experimental Autoimmune Neuritis 42
3.2. Transgenic Animal Models 44
4. Co-stimulatory Molecules and T-cell Activation 50
5. Aim of the Project 57
CHAPTER II: METHODS OPTIMIZATION FOR THE PNS 59
1. Retracing Schwann cell developmental transitions in embryonic dissociated DRG cocultures 59
2. Triz'Old is gold: A reliable and efficient method to extract total RNA from mouse sciatic nerve across all ages 80
CHAPTER III: RESULTS 106
CHAPTER IV: DISCUSSION 141

1. Phenotype differences between NOD ICOS-/- and NOD ICOSL-/- 141
2. Histological differences between NOD ICOS-/- and NOD ICOSL-/- 142
3. Absence of neuropathy in the C57 and NOD SCID backgrounds 144
4. Infiltration of the nerve 145
5. Variation of ICOS and ICOSL expression in the nerve throughout different timepoints 146
6. Similarities between the animal model and the human disease 146
CHAPTER V: PERSPERCTIVES AND CONCLUSION 149
1. Could a “leaky” BNB trigger the neuropathy? 149
2. What role does ICOS-ICOSL play in remyelination? 149
3. What other animal models could be generated to study autoimmune neuropathy? 150
4. Conclusion 151
REFERENCES 152

CHAPTER I: INTRODUCTION

1. The Peripheral Nervous System (PNS)

1.1. General Overview

The nervous system can be divided into two entities; the central nervous system (CNS) and the peripheral nervous system (PNS). The former is composed of the brain and the spinal cord whereas the latter is constituted of the nerves arising from the spinal cord (Hudspeth, Jessell, Kandel, Schwartz, & Siegelbaum, 2013). These nerves can be classified into sensory afferent and motor efferent fibers. They innervate different organs such as the muscles, skin, and the gastro-intestinal tract (Rasband, 2016). The sensory afferent division receives somatic sensory and visceral sensory information. The motor efferent division is further segregated into the autonomous nervous system responsible for involuntary responses and the somatic nervous system that controls voluntary movements. Moreover, the myelinating cells are one key difference between the CNS and PNS with the oligodrendrocytes present in the former and the Schwann cells in the latter (Hudspeth et al., 2013).

1.1.1. Anatomy and Function of the PNS

The human body has 12 pairs of cranial nerves (CN); they are all part of the PNS with the exception of CN I and CN II that are attached to the CNS division (Fig 1). The CNs from III to XII are myelinated by Schwann cells whereas CN I and II are myelinated by oligodendrocytes.

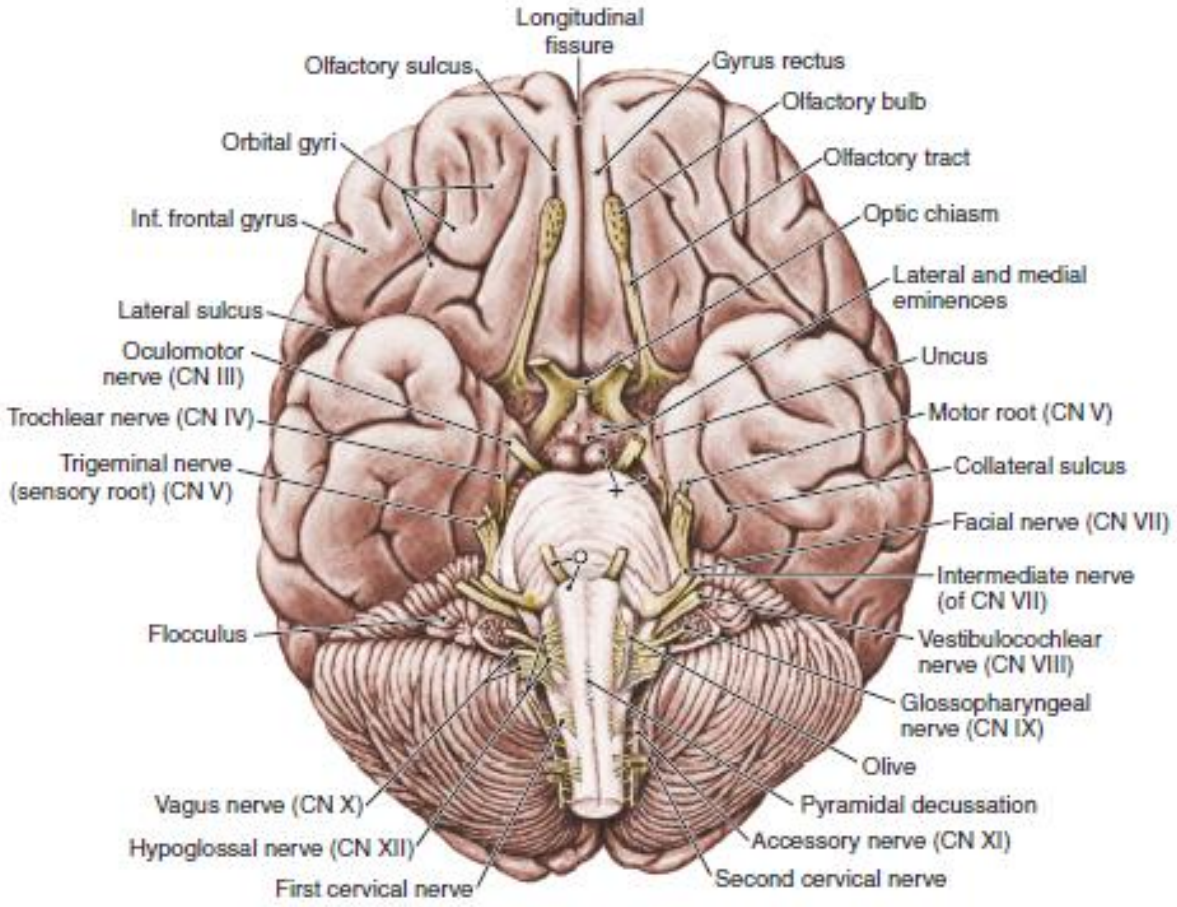


Figure 1: Anatomy of the base of the brain. This picture shows the exit points of the cranial nerves. (Modified from Truex RC, Kellner CE. Detailed Atlas of the Head and Neck. New York, NY: Oxford University Press; 1958:34.) (Gould, 2019)

The following table will provide a detailed description of the CNs (Table 1).

Cranial Nerve	**Type**	**Function**
I - Olfactory	SVA (Sensory)	Smell (olfaction)
II - Optic	SSA (Sensory)	Vision
III - Oculomotor	GVE (Parasympathetic)	Sphincter pupillae, ciliaris
	GSE (Motor)	Superior, inferior, and medial recti; inferior oblique; levator palpebrae superioris
IV - Trochlear	GSE (Motor)	Superior oblique
V - Trigeminal	SVE (Motor)	Muscles of mastication, tensor tympani, anterior belly of the digastric, nylohyoid and tensor palati
	GSA (Sensory)	Tactile, pain, and thermal sensation from the face; the oral and nasal cavities and the supratentorial dura
VI - Abducens	GSE (Motor)	Lateral rectus
VII - Facial	GVE (Parasympathetic)	Lacrimal gland (via pterygopalatine ganglion); submandibular and sublingual glands (via submandibular ganglion)
	SVE (Motor)	Muscles of facial expression; stapedius
	GSA (Sensory)	Tactile sensation to skin of ear
	SVA (Sensory)	Taste sensation from the anterior two-thirds of tongue (via chorda tympani)
VIII - Vestibulocochlear	SSA (sensory) Vestibular nerve	Equilibrium (innervates hair cells of semicircular ducts, saccule, and utricle)
	SSA (sensory) Cochlear nerve	Hearing (innervates hair cells of the organ of Corti)
IX - Glossopharyngeal	GVE (Parasympathetic)	Parotid gland (via the otic ganglion)
	SVE (Motor)	Stylopharyngeus
	GSA (Sensory)	Tactile sensation to middle ear cavity
	GVA (Sensory)	Tactile sensation to posterior third of tongue, pharynx, middle ear, and auditory tube; input from carotid sinus and carotid body
	SVA (Sensory)	Taste from posterior third of the tongue
X - Vagus	GVE (Parasympathetic)	Viscera of the thoracic and abdominal cavities to the midtransverse colon [via

		terminal (mural) ganglia]
	SVE (Motor)	Muscles of the larynx and pharynx
	GSA (Sensory)	Tactile sensation to the external ear
	GVA (Sensory)	Mucous membranes of the pharynx, larynx, esophagus, trachea, and thoracic and abdominal viscera to the mid-transverse colon
	SVA (Sensory)	Taste from the epiglottis
XI - Accessory	SVE (Motor)	Sternocleidomastoid and trapezius
XII - Hypoglossal	GSE (Motor)	Intrinsic and extrinsic muscles of the tongue (except the palatoglossus)

Table 1: Table of Cranial Nerves. The 12 cranial nerves are listed with their type and function along with the innervated structure (Gould, 2019).

Abbreviations: SVA: special visceral afferent; SSA: special somatic afferent; GVE: general visceral efferent; GSE: general somatic efferent; SVE: special visceral efferent; GSA: general somatic afferent; GVA: general visceral afferent.

Humans have 31 pairs of spinal nerves that exit the vertebral canal through vertebral or sacral foramina with the exception of first spinal nerve C1. The spinal nerves are segregated into 5 groups; cervical, thoracic, lumbar, sacral, and coccygeal nerves (Fig 2). They carry motor, sensory, and autonomous signals between the spinal cord and various locations of the body.

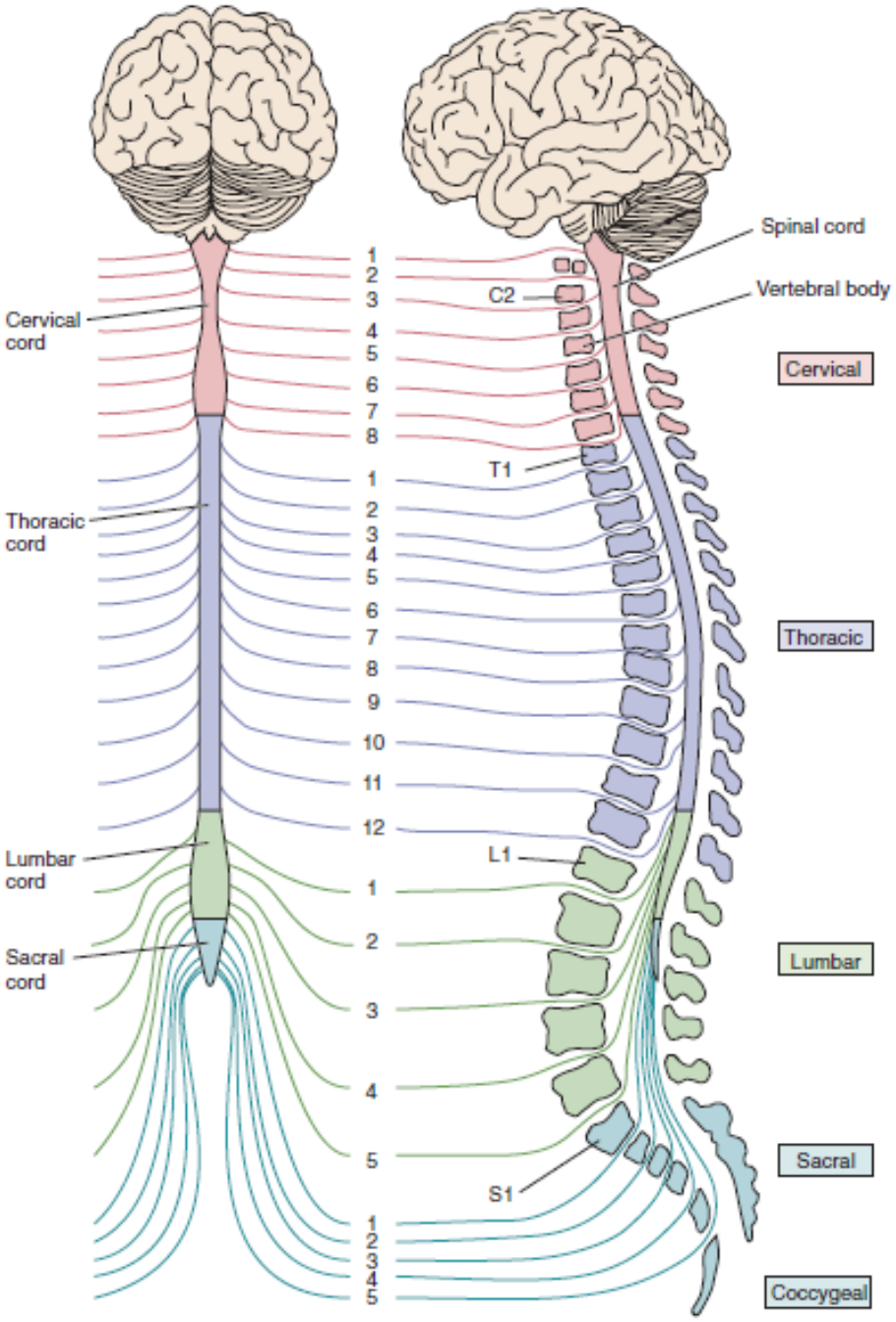


Figure 2: Diagram of the spinal nerves' positions. The five groups of spinal nerves are shown along with the foramen though which they exit, except for the first cranial nerve. Adapted with permission from Bear MF, Connors BW, Paradiso MA. Neuroscience: Exploring the Brain. 2nd ed. Philadelphia, PA: Lippincott Williams & Wilkins; 2001, Fig. 12-10.) (Gould, 2019)

The spinal nerves can be separated into two categories based on their function; somatic or autonomous. Somatic fibers are either sensory with functions carried out by sensory neurons (soma in the dorsal root ganglia) or motor with functions carried out by motor neurons (soma in the ventral horn) (Fig 3). These fibers innervate organs such as the skin and the skeletal muscles. Autonomous neurons arise at the lateral horns of the spinal cord and they innervate the ganglia located outside the spinal cord. Autonomous ganglia can be divided into 2 categories; the sympathetic ganglia situated next to the spinal cord, and the parasympathetic ganglia found to the organs innervated by the nerve fibers. This arrangement gives rise to pre-ganglionic and post-ganglionic connections that are specific to the autonomous nervous system, which in turn innervates diverse organs (Fig 4).

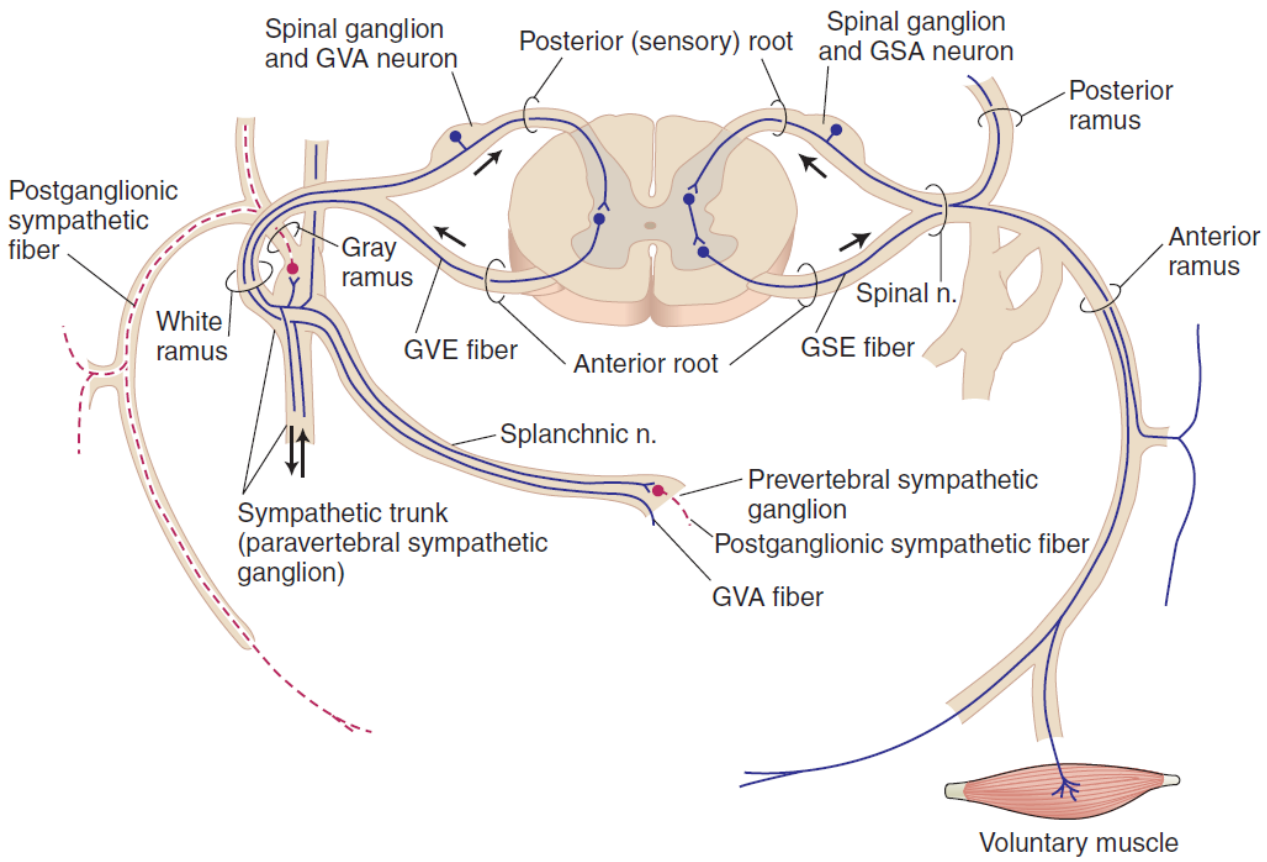


Figure 3: A section of the spinal cord and its branches and reflex connections. This figure depicts how motor and sensory informations are relayed through the ventral and dorsal root ganglia respectively. The afferent signal can originate from visceral organs (GVA) or bone, skin, joints, and skeletal muscles (GSA). Efferent signal reaches glands and smooth muscles (GVE) and skeletal muscle (GSE).

Abbreviations: GVA: general visceral afferent; GSA: general somatic afferent; GSE: general somatic efferent; and GVE: general visceral efferent (Gould, 2019).

A. B.

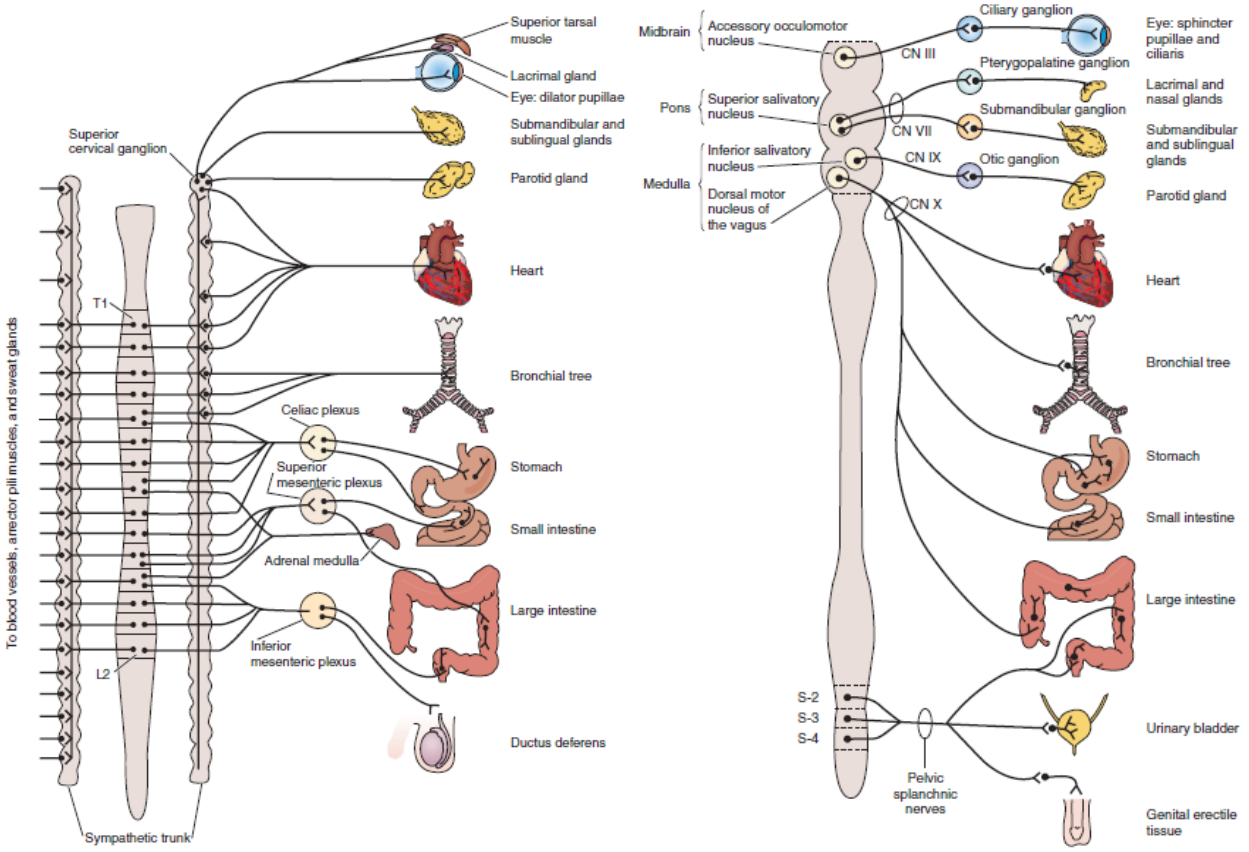


Figure 4: Schematic diagram of the sympathetic (A) and parasympathetic (B) divisions of the autonomous nervous system. This figure depicts the different organs under the control of the autonomous nervous system. (Gould, 2019) Modified from Fix JD. High-Yield Neuroanatomy. 3rd ed. Philadelphia, PA: Lippincott Williams & Wilkins; 2005:128.).

1.1.2. Structure and Cellular Composition of the Sciatic Nerve

The sciatic nerve is the most commonly studied nerve in PNS-centered research. It is used in developmental, neuromuscular junctions, nerve regeneration, and myelination studies (Jessen & Mirsky, 2005; G. Liu, Jiang, & Jin, 2014). In humans, the sciatic nerve originates from the vertebral foramina between L4 and S3 whereas in mice it exits between L3-L4 (Fig 5).

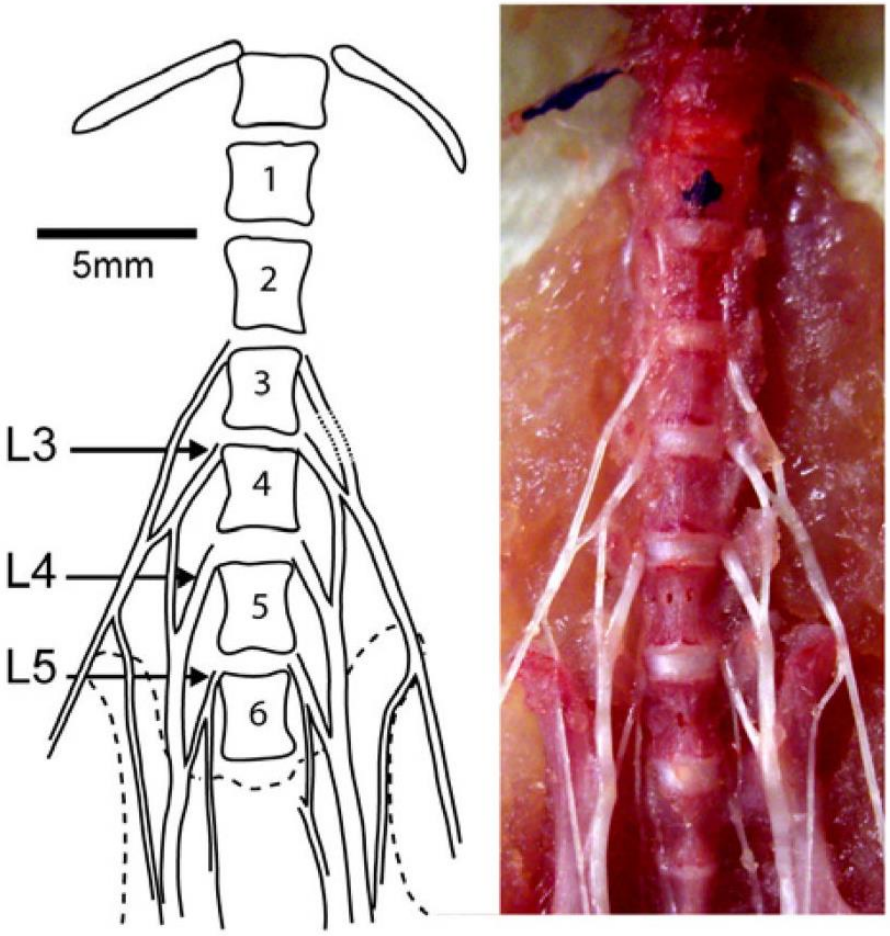


Figure 5: A ventral view of the lumbar vertebral column of a C57BL/6J mouse with the origin of the sciatic nerve. This image of a dissected mouse shows the foramina where the sciatic nerve emanates from. (Rigaud et al., 2008).

In order to study the PNS, a thorough understanding of the structure, ultra-structure, and cellular composition of the nerves is mandatory. The sciatic nerve is composed of sensory and motor fibers as well as specialized cells. The bulk of these fibers are surrounded by connective tissue which is organized in 3 components – the endoneurium which encapsulates single fibers, the perineurium surrounds nerve fasicules, and the epineurium encapsulating the peripheral nerve (Ross, Kaye, & Pawlina, 2003) (Fig 6).

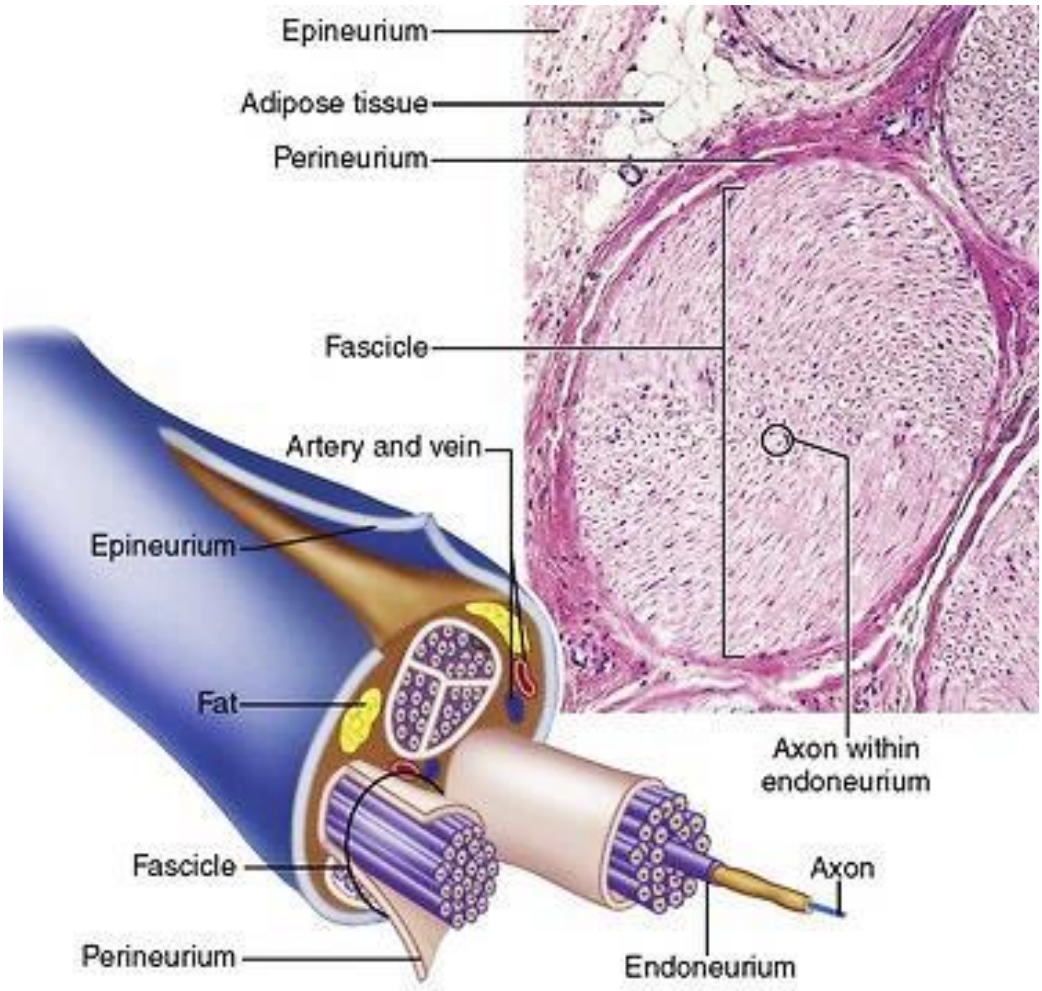


Figure 6: Cross section of the sciatic nerve. The organization of the nerve is depicted with its 3-layer organization at macro- and microscopic levels; the endoneurium, the perineurium, and the epineurium. (Patton & Thibodeau, 2018).

Different cell types make up the composition of the sciatic nerve. Schwann cells ensheath the axons and they can be separeted into 2 categories; the myelinating Schwann cells wrapping the motor axons, and the non-myelinating Schwann cells encapsulting several axons of small diameter forming Remak bundles. The latter structure is responsible for carrying sensory information. Fasicules are delineated by perineurial cells providing structural and mechnical integrity. Endoneurial cells contribute to the formation of the extracellular matrix, perform immune-surveillance, and are implicated in remyelination. Blood vessels are also present in the nerve and are surrounded by pericytes forming the blood nerve barrier (BNB).

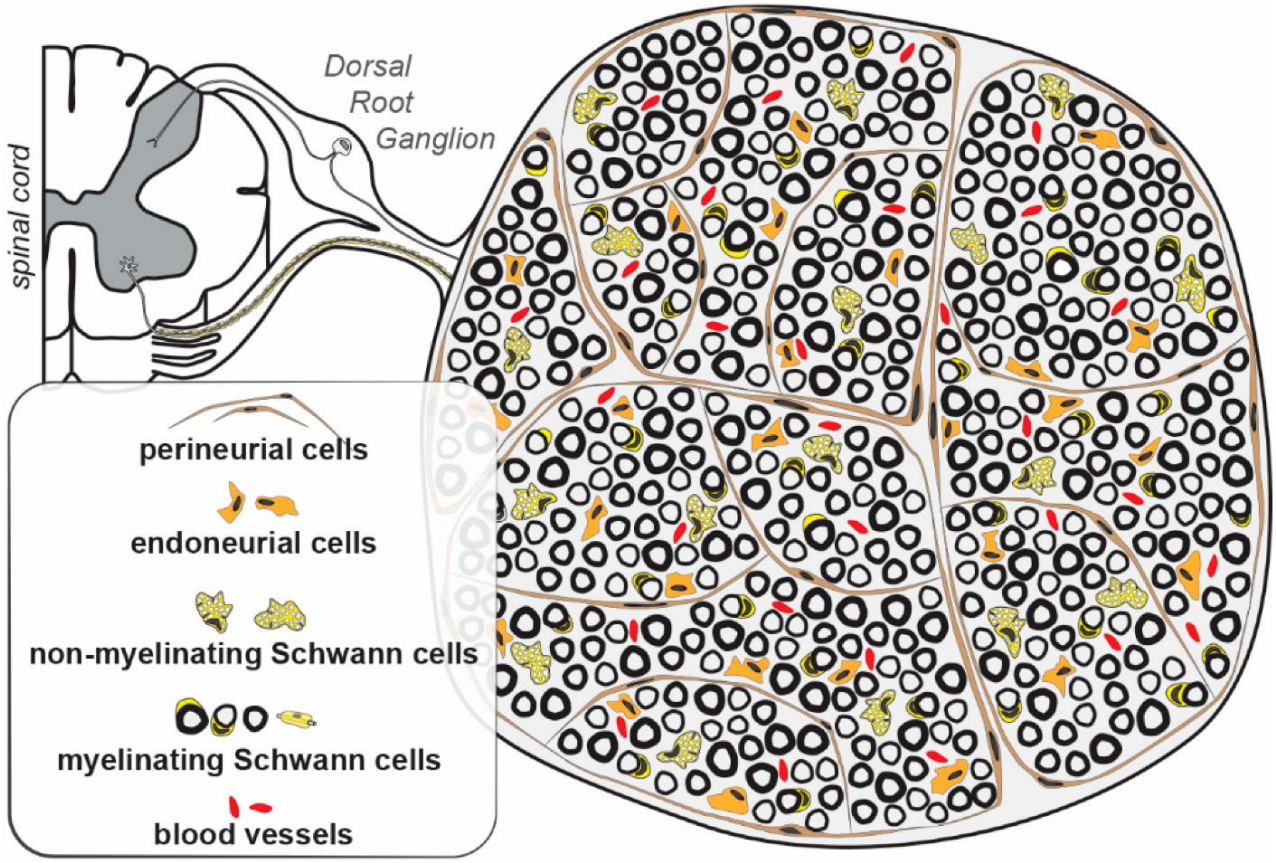


Figure 7: A detailed cross-sectional view of the mouse sciatic nerve. Different cells that constitute the nerve are highlighted in the in the legend to the left of the figure (V. K. Sundaram, Massaad, & Grenier, 2019).

1.2. PNS development and Myelination

1.2.1. Overview of PNS and Schwann Cell Development

Nervous system development is a topic that has been widely studied in developmental biology. The nervous system forms after the embryo has developed its 3 principal germ layers; the endoderm, the mesoderm, and the ectoderm (Le Douarin & Dupin, 2014). The endoderm, which is the innermost cell layer, gives rise to the liver, lungs, pancreas, and the gut tube. The mesoderm, the middle germ layer, generates the vasculature, connective tissue, and muscles. The ectoderm, the outermost layer, produces the skin and the columnar epithelium of the neural plate. This structure is the precursor of the CNS and PNS. After the neural plate is formed, neurulation begins. This process is characterized by the folding of the neural plate into a tubular structure known as the neural tube (Fig 8). The rostral area of the neural tube gives rise to the brain whereas the caudal region becomes the spinal cord (Hudspeth et al., 2013).

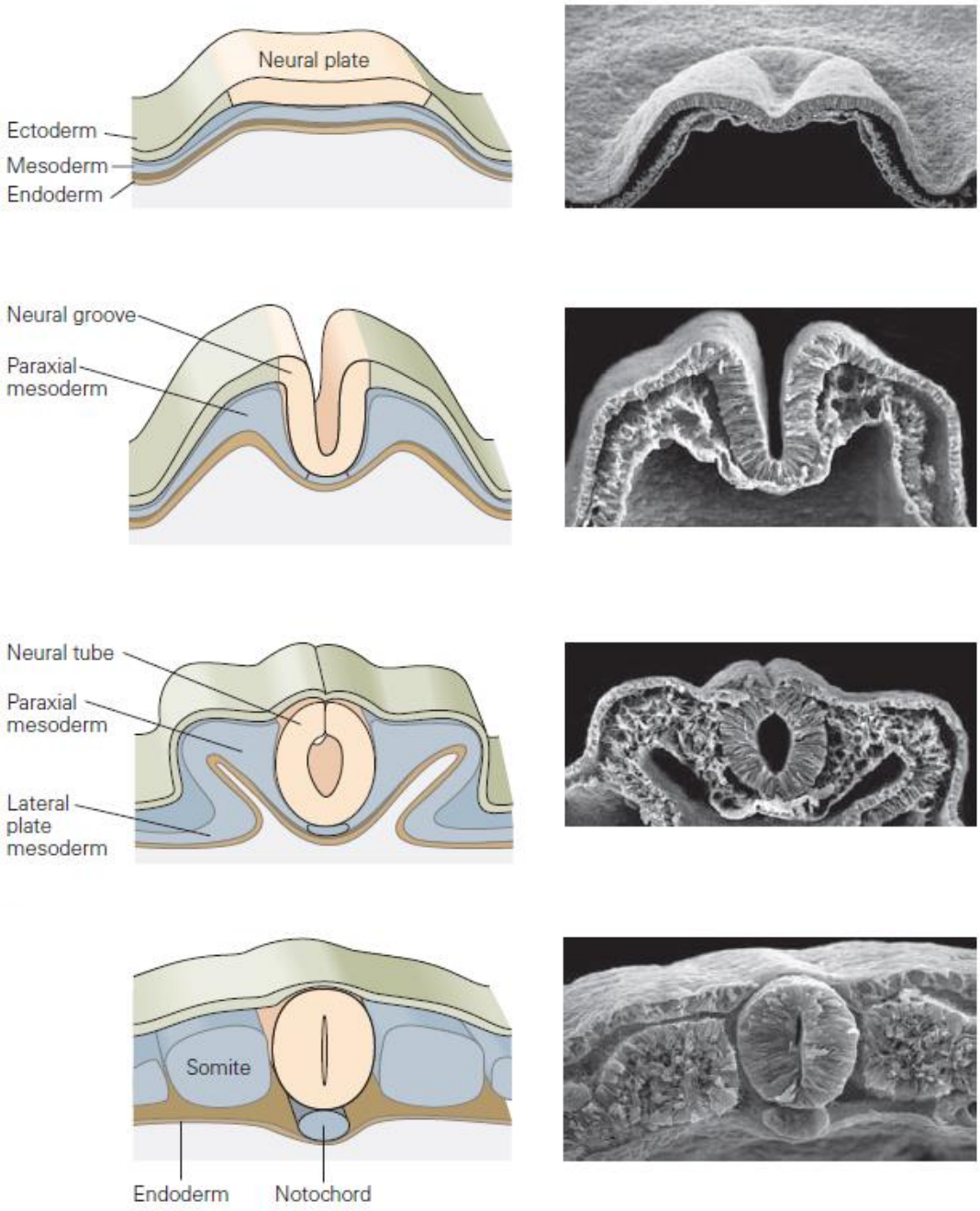


Figure 8: Formation of the neural tube. The electron microscopy images provide a high-definition visualization of the neural tube formation in a vertebrate embryo. ((Hudspeth et al., 2013) Electron micrographs of chick neural tube reproduced, with permission, from G. Schoenwolf.)

The PNS arises from the neural crest stem cells; they are a group of neuro-epithelial cells located between the epidermal ectoderm and the neural tube. These neural crest cells undergo an epithelial to mesenchymal transition (EMT), delaminate from the neural tube, and migrate to different sites (Fig 9). This migration does not rely on scaffolding; it is a free migration since there are no pre-existing axon tracts. The induction of neural crest cells is tightly controlled by molecular cues. Bone morphogenic protein (BMP) signaling is critical in the EMT of the neural epithelial cells. BMPs trigger the expression of different transcription factors such the zinc finger proteins slug, snail, and twist. These transcription factors are crucial in promoting the EMT; they direct the expression of enzymes that break down extracellular matrix proteins and the expression of proteins involved in the regulation of cytoskeletal properties. These catabolic enzymes are necessary for the migration process. Furthermore, changes in the expression of cell adhesion molecules occur. One of the main alterations in the expression of adhesive proteins is that of cadherins. This alteration allows the neural crest cells to loosen their contact with the cells of the neural tube thus beginning the delamination process. Neural crest cells also start expressing laminins, collagens, and intergrins (C.-J. Bae & Saint-Jeannet, 2014; Gilbert, 2008; Hudspeth et al., 2013).

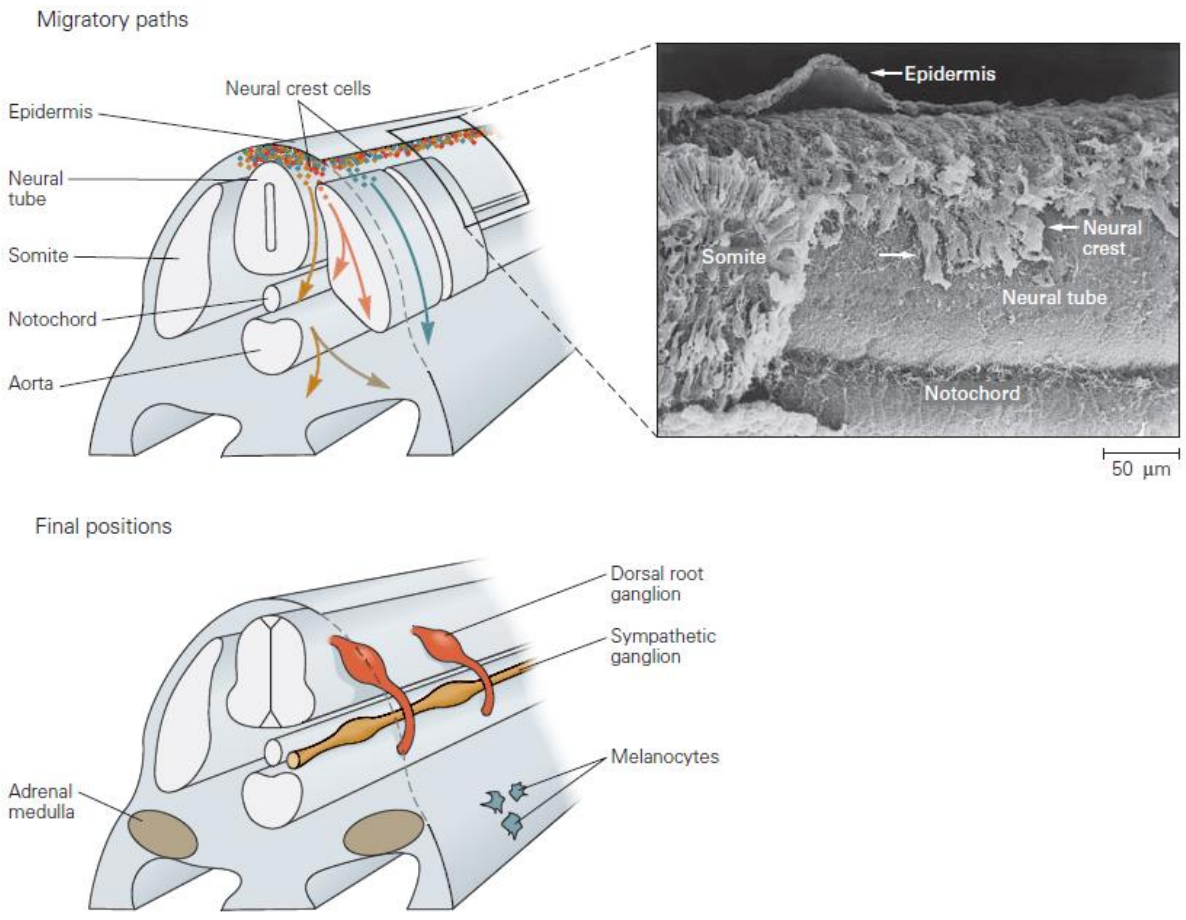


Figure 9: Neural crest cell migration in the PNS. The EMT of the neural crest cells is mandatory for the formation of the PNS. (Hudspeth et al., 2013) (Micrograph, used with permission, courtesy of K. Tosney.)

Neural crest cells give rise to 3 types of glial cells; satellite cells, boundary cap cells, and Schwann cell precursors (SCP). The neural crest cells that will generate the SCPs migrate and accumulate into the future dorsal root ganglia (DRG). The SCPs then migrate along the growing peripheral nerves via 2 routes; they can migrate through the DRG or they can migrate around the DRG (Jacob, 2015).

Prior to differentiating into myelinating and non-myelinating Schwann cells, the SCPs go through an intermediate stage of immature Schwann cells (iSC) (Fig 10) (Jessen & Mirsky,

2005; Monk, Feltri, & Taveggia, 2015). This transition is regulated by 2 signaling molecules – neuregulin 1 (NRG1) and Notch. Radial sorting is the principle role of iSC in Schwann cell development. The purpose of this event is to segregate small caliber axons that will form Remak bundles from large caliber axons destined to be myelinated. Schwann cells will myelinate a single axon segment once they reach a 1:1 relationship with it. However, a non-myelinating Schwann cell will engulf several small caliber axons, forming a Remak bundle without producing any myelin. iSCs require radial sorting to be able to form proper connections with axons which are crucial for further differentiation (Monk et al., 2015).

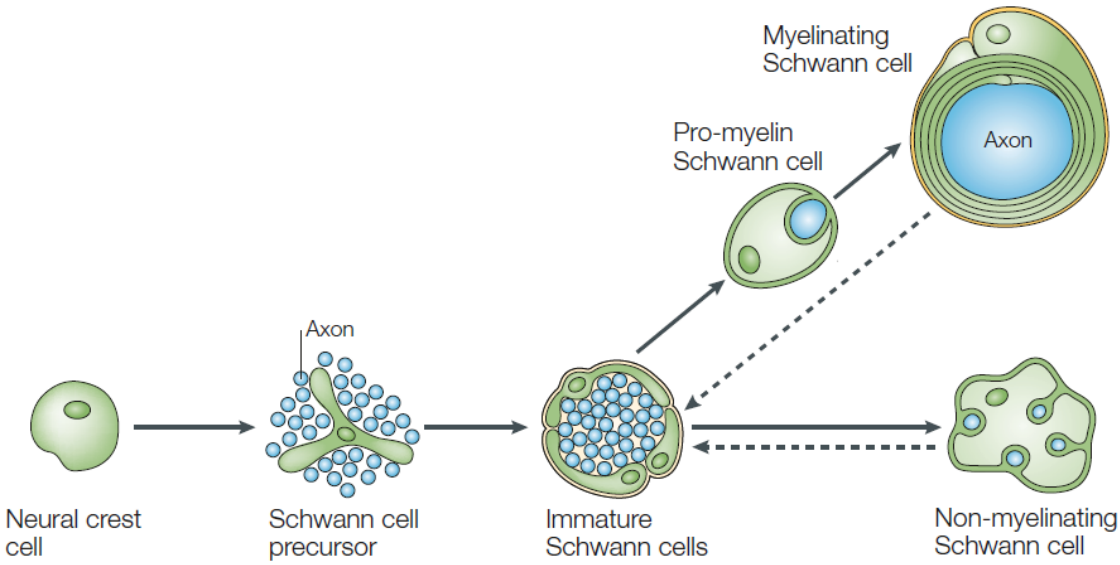


Figure 10: Schwann cell lineage. This diagram shows the different stages that a neural crest cell goes through to become a myelinating or non-myelinating Schwann cell. The neural crest cell differentiates to a Schwann cell precursor then an immature Schwann cell before reaching the mature state. (Jessen & Mirsky, 2005).

Three important signaling axes in the Schwann cells are required for the initiation of the myelination process; intracellular signaling cascades, extracellular signals, and expression of Schwann cell specific transcription factors and epigenetic regulations. The pro-myelin pathways include transcription factors such as octamer-binding transcription factor (OCT6), early growth

response protein 2 (KROX20), brain 2 class III POU domain protein (BRN2), and NGFI-A-binding proteins 1and 2 (NAB1/2) (Jessen & Mirsky, 2005). The intracellular signaling cascades driving and sustaining myelination are receptor tyrosine kinase (RTK) pathways downstream of the the NRG1/ErbB pathway (Monk et al., 2015; Salzer, 2015). The RTK pathways include the MAPK, PI3K/Akt/mTORC, cAMP, and PLCγ/Calcineurin/NFAT signaling. Extracellular signaling also promotes myelination through axonal regulation via NRG1. Other signals include secretases (ADAM17, BACE, ADAM10), neurotrophins (BDNF, NGF, NT3, GDNF), Notch1 signaling, and cell adhesion molecules (Cadm) or nectin like proteins (Necl) are also involved. For the sake of pertinence to my PhD project I have provided a summarized listing of critical signaling axes, however exhaustive reviews by Jessen & Mirsky, Monk et al, and Salzer et al describe all the signaling pathways mentioned (Jessen & Mirsky, 2005; Monk et al., 2015; Salzer, 2015).

1.2.2. Myelin Proteins

The coordinated symphonies of the different aforementioned signaling cascades converge to the production of myelin lipids and proteins, and ultimately the wrapping of the axons. Myelin specific proteins in Schwann cells include signaling and structural protein in non-compact myelin – connexin-32 (Cx32) and myelin associated glycoprotein (MAG), and in compact myelin – myelin basic protein (MBP), myelin protein zero (MPZ), and peripheral myelin protein 22 (PMP22) (Fig 11) (Monk et al., 2015). These proteins undergo a tight regulation and are essential to the proper maintenance of the myelin sheath. The compact and insulating myelin layer is crucial for the propagation of nerve conduction. Any dysregulation in myelin proteins has drastic consequences of the sensory and motor functions (Garbay, Heape, Sargueil, &

Cassagne, 2000). Diseases affecting myelin have been extensively studied throughout the years and results have shown a genetic basis for their emergence (Hudspeth et al., 2013).

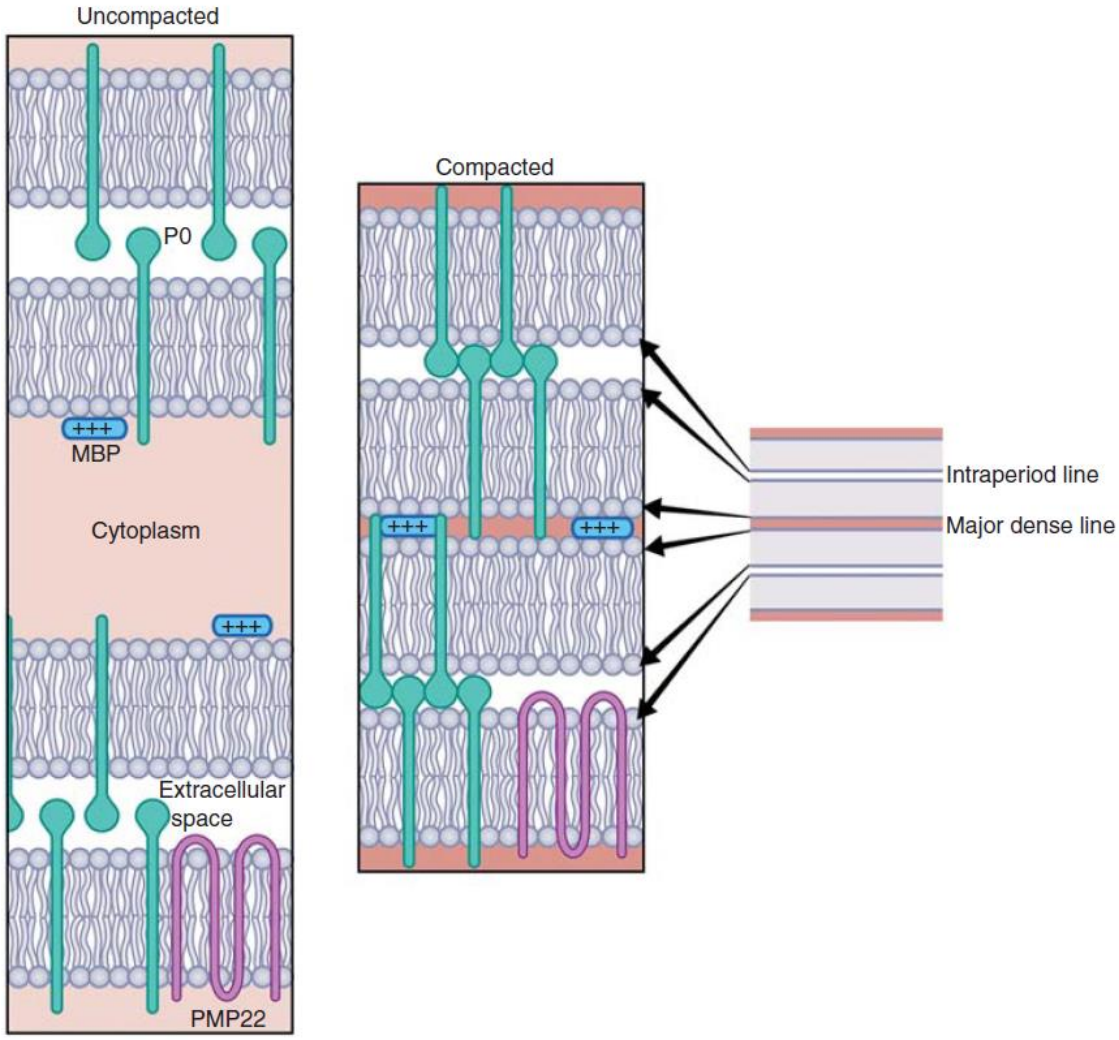


Figure 11: Compaction of the myelin layer requires an interaction between different myelin proteins. The different myelin proteins of the PNS have a specific location within the myelin layer to ensure a proper compaction of the myelin sheath guaranteeing an optimal nerve conduction (Salzer, 2015).

Myelin Associated Glycoprotein

MAG is protein found in the CNS and the PNS. It belongs to the immunoglobulin superfamily containing cell surface proteins speculated to be involved in cell to cell recognition such as T-cell surface antigens, major histocompatibility complex of antigens, and neural cell adhesion molecule. MAG is expressed by Schwann cells during the myelination process rendering this protein an essential component of mature myelin. Its subcellular location, structural similarity to surface recognition proteins, and early expression imply that MAG is an adhesion molecule crucial for the initiation of myelin (Hudspeth et al., 2013; Quarles, 2007). One of the animal models for autoimmune neuropathy can be generated by injection of MAG debris in complete Freund's adjuvant; this model is known as experimental autoimmune encephalopathy (EAE) in the CNS or as experimental autoimmune neuritis (EAN) in the PNS (Hays, Latov, Takatsu, & Sherman, 1987; Weerth, Berger, Lassmann, & Linington, 1999). The EAN model will be further discussed in the last section of the introduction.

Myelin Basic Protein

MBP is abundantly present in both the CNS and PNS. It exerts most of its functions by regulating MAG and Cx-32 (Smith-Slatas & Barbarese, 2000). The *shiverer* mutant mice have a deletion of five of the six exons for the MBP gene on chromosome 18 resulting in the mutant mice developing frequent convulsions, tremors, and an early death. This is an autosomal recessive disease where 10% of the normal amount of MBP is produced in the mutants. In these animals, CNS axons are poorly myelinated however in the PNS severe demyelination is not

observed due to the presence of compensatory mechanisms (Chernoff, 1981; Readhead et al., 1987).

Myelin Protein Zero

MPZ is the major myelin protein in the PNS. It spans the plasmalemma of Schwann cell with a basic intracellular domain. Similarly to MAG, it is a member of the immunoglobulin superfamily. The immunoglobulin domain, which is the glycosylated extracellular portion of the protein, acts as a hemophilic adhesion protein during the formation of the myelin sheath. MPZ interacts with identical domains located on the apposed membrane to guarantee proper myelin compaction (Spiryda, 1998). Mice deficient for MPZ suffer from occasional convulsions, tremors, and poor motor coordination. MPZ knock out animals also have thinner myelin sheaths (Giese, Martini, Lemke, Soriano, & Schachner, 1992; R. Martini, Zielasek, Toyka, Giese, & Schachner, 1995).

PMP22

PMP22 is a transmembrane Schwann cell protein that spans the membrane four times. It is usually present in compact myelin (Salzer, 2015). The PMP22 gene is located on chromosome 17 in humans, and mutations of this gene can produce multiple hereditary peripheral neuropathies. A duplication of PMP22 causes one of the forms of Charcot Marie Tooth disease (CMT) known as CMT1A. Patients suffering from CMT develop progressive muscle weakness accompanied by a decrease in nerve conduction velocity as well as cycles of demyelination/re-myelination (Lupski & Garcia, 1992).

1.3. The Immune System and The PNS

Resident macrophages make up 5-10% of the endoneurial cells present in the PNS nerves. The embryonic origin of these macrophages is still unknown, however they are thought to come from the yolk sac like their CNS equivalent – the microglia (Ginhoux & Jung, 2014). The nerve-resident macrophages have a ramified elongated appearance and are located between myelinated axons. Nerve-resident macrophage express major histocompatibility complex (MHC) class I molecules and can express MHC class II as well (John W. Griffin, George, & Ho, 1993; Klein & Martini, 2016). In addition to their role of immune surveillance, the PNS macrophages play a key role during nerve injury induced by trauma or a disease. Resident macrophage involvement has been widely described in Wallerian degeneration however their participation remains obscure in immune mediated neuropathies. This section will briefly describe Wallerian degeneration mechanism and will shed some light on the immune system implication in the two aforementioned nerve injuries.

1.3.1. Wallerian Degeneration

When an injury is inflicted upon a nerve, such as a nerve crush or an axotomy, the insult elicits a response from non-neuronal cells present in the nerve. The section of the nerve disconnected from the cell body, known as the distal stump, undergoes a process known as Wallerian degeneration (WD) named after Augustus Waller (G. Stoll & Muller, 1999). WD sets in motion a plethora of molecular changes in the different cell types present in the nerves. A synergy between the nervous and immune systems fosters the implementation of a specific sequence of events to guarantee proper recovery.

Firstly, axon degeneration does not occur immediately after nerve injury; a lag of 1-2 days is observed in mice (Beirowski et al., 2005) and young rats (Miledi & Slater, 1970), and this lag can last several days in humans (Chaudhry & Cornblath, 1992) and other primates (Gilliatt & Hjorth, 1972). During the lag period, the detached nerve segment is still capable of transmitting action potentials upon stimulation. When the axon detaches, a calcium influx from intra- and extra- cellular stores enters the axoplasm leading to axonal degeneration (Stirling & Stys, 2010). The calcium influx activates calpain which is a protease implicated in axonal degeneration and cytoskeletal degradation (Touma, Kato, Fukui, & Koike, 2007). Moreover, the ubiquitin-proteasome system is activated and it seems to be involved in degenerative processes (Zhai et al., 2003). Additionally, the blood nerve barrier (BNB) is compromised immediately after injury and its permeability increases 4-7 days post injury. This breach allows the entry of cells and soluble factors to injury site promoting tissue repair (Mizisin & Weerasuriya, 2011; Weerasuriya & Mizisin, 2011).

The first responders after a nerve injury are the Schwann cells. These cells start by de-differentiating in the distal stump. Within 48 hours post injury, they stop producing myelin protein such as MPZ, PMP22, MAG, MBP (LeBlanc & Poduslo, 1990). The Schwann cells increase the synthesis of proteins associated to regeneration, such as NCAM, L1, GFAP, and 75NTR, and they begin proliferating (Jessen & Mirsky, 2008). The proliferating Schwann cells line up with the basal lamina to create bands of Büngner (Arthur-Farraj et al., 2012) providing a supportive substrate for regenerating nerve fibers.

Furthermore, the Schwann cells develop a phagocytic activity during the first 5 days after injury. The “macrophage-like” Schwann cells express MHC class II molecules (Rudolf Martini, Fischer, López-Vales, & David, 2008; Meyer zu Horste, Hu, Hartung, Lehmann, & Kieseier,

2008; zu Hörste et al., 2010). The phagocytic Schwann cells along with the endoneurial macrophages clean up myelin debris that hinder axonal growth (Gomez-Sanchez et al., 2015). Additionally, Schwann cells secrete extracellular matrix molecules such as laminins, and trophic factors (NGF, NRG-1) promoting axonal growth (Z. L. Chen, Yu, & Strickland, 2007; Markus, Patel, & Snider, 2002). Chemokines and cytokines (TNF-α, interleukins IL-1/IL-6/IL-10) are also produced to attract hematogenous macrophages (Bourde, Kiefer, Toyka, & Hartung, 1996; G Stoll, Griffin, Li, & Trapp, 1989; G. Stoll & Muller, 1999). These macrophages will take over the task of myelin debris clearance. T-cells are the last cells to arrive at the site of injury and reach their maximum number between 14 to 28 days post injury in rats. T-cells can secrete pro- or anti-inflammatory cytokines shaping the later phases of the immune response (Fig 12) (Gaudet, Popovich, & Ramer, 2011).

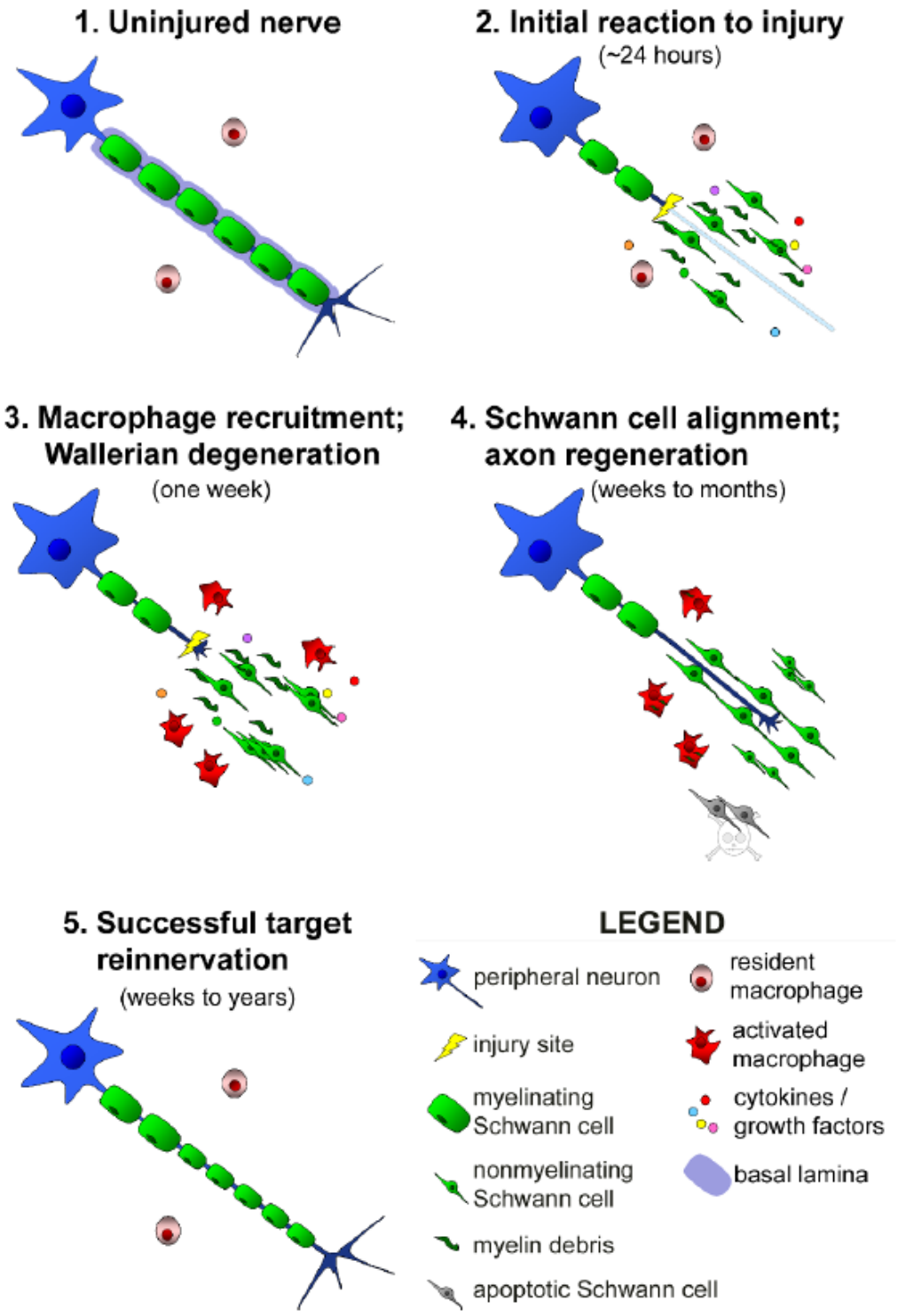


Figure 12: Wallerian degeneration and axon regeneration in the PNS after nerve injury. This schematic representation of the Wallerian degeneration and regeneration shows a step by step depiction of this biological process. (Gaudet et al., 2011)

1.3.2. Nerve Injury in Immune Mediated Neuropathies

In autoimmune peripheral neuropathies, nerve injury is immune mediated (for further details kindly refer to II. Autoimmune peripheral neuropathies). Although common pathogenic mechanisms in immune mediated neuropathies have been described, no precise pathogenesis of autoimmune neuropathies has been elucidated yet. Certain viral or bacterial infections can lead to the activation of autoreactive T cells. The process known as molecular mimicry is due to the cross reactivity between peripheral nerves antigens and bacterial epitopes. The autoreactive T cells secrete different cytokines stimulating antibody production by plasma cells. The antibodies then cross the damaged BNB and enter the peripheral nerves. Adhesion molecules on activated T cells interact with the vascular endothelium of the endoneurial blood vessel thus allowing the activated T cells to cross the BNB through intracellular or transcellular diapedesis (Archelos, Previtali, & Hartung, 1999). Next, the activated T cells secrete metalloproteinases that damage the basement membrane and consequently permeabilizing the BNB allowing the entry of immune cells and large molecules (B. Kieseier et al., 1998). The T cells that have infiltrated the peripheral nerves secrete various inflammatory cytokines such as interleukin-2 (IL-2) and tumor necrosis factor (TNF) (Hartung, Reiners, Schmidt, Stoll, & Toyka, 1991; Misawa et al., 2001). These cytokines amplify and maintain inflammation inside the nerve by in situ clonal expansion and by the recruitment of immune cells present in the circulation. Autoantibodies and complement can now cross the permeable BNB. Proinflammatory cytokines, proteases, and reactive oxygen species are released by activated macrophages. These molecules contribute to the propagation of the inflammatory response and inflict damage upon axons and Schwann cells. The autoantibodies that have crossed the BNB can bind to proteins at the nodal and paranodal regions or to myelin glycoproteins. Such proteins are crucial for the maintenance of the myelin

sheath integrity as well as the maintenance of insulation, node organization, and sodium channel clustering. Once the autoantibodies bind to these proteins, complement activation follows. Demyelination and axonal degeneration occur through macrophage-mediated mechanisms along with the disruption of nodal architecture. A long-term disability is positively correlated with the extent of axonal degeneration. Finally, the immune response is halted by apoptosis. The underlying mechanisms in the programmed cell death remain unknown (Fig 13) (B. C. Kieseier et al., 2004; B. C. Kieseier, Mathey, Sommer, & Hartung, 2018).

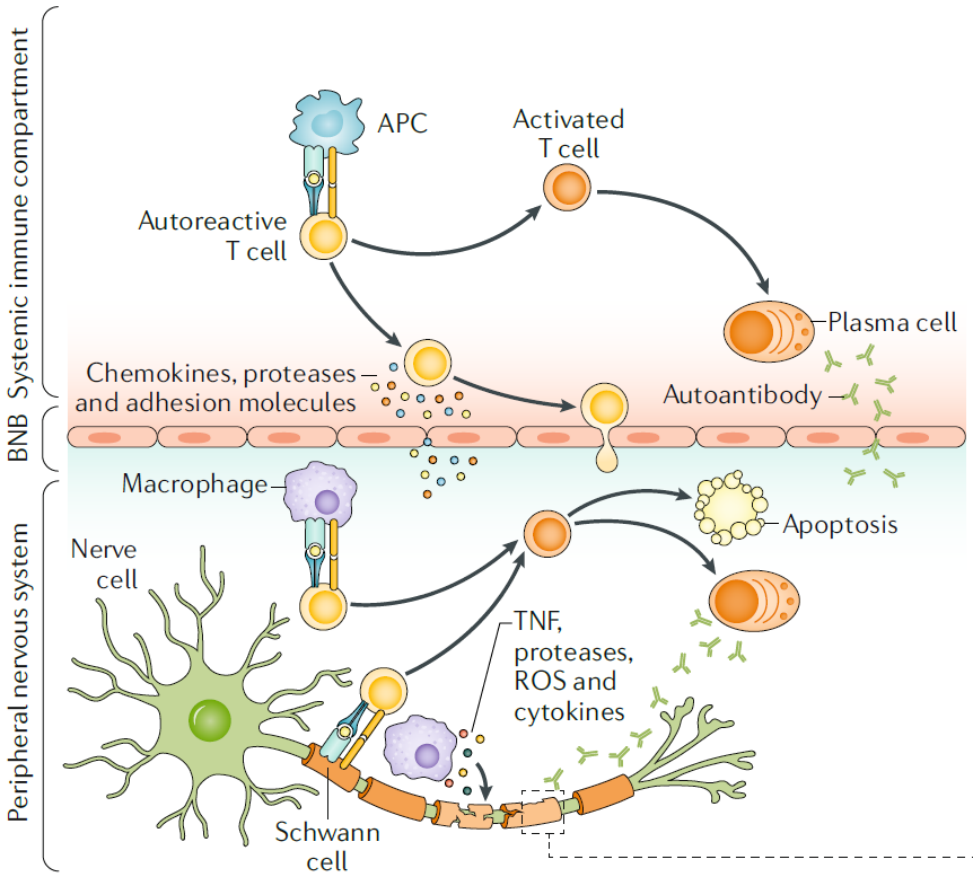


Figure 13: Mechanism of nerve injury in immune mediated neuropathies. This figure summarizes the immune response in autoimmune neuritis after T-cell activation. (B. C. Kieseier et al., 2018)

The following section will go more in depth in the description of immune mediated neuropathies.

2. Autoimmune Peripheral Neuropathies

2.1. Guillain–Barre Syndrome (GBS)

GBS is an acute autoimmune neuropathy characterized by a flaccid paralysis in patients. The disease is present worldwide with an incidence of 0.81 to 1.89 per 100 000 individuals, and it is more common in males than in females with a ratio of 3:2 (Hauck et al., 2008; Sejvar, Baughman, Wise, & Morgan, 2011) .

The principal clinical features of GBS are progressive symmetric muscle weakness accompanied by depressed or absent deep tendon reflexes. The weakness can affect all extremities, respiratory muscles, facial muscles, and bulbar muscles. Symptoms progress during the first two weeks and by the fourth week 97% of the patients reach their clinical nadir (Fokke C et al, 2014). Cerebrospinal fluid (CSF) analysis may also be useful in GBS diagnosis. Most cases present with an albuminocytologic dissociation which is a high albumin and protein content with a normal cell count (B. C. Kieseier et al., 2018). Electrodiagnostic studies, electromyography (EMG) and nerve conduction studies (NCS), are also used to confirm the diagnosis. These tools help in determining the type of neuropathy present; axonal (AMAN, AMSAN, MFS), demyelinating (AIDP), or mixed (Azhary, Farooq, Bhanushali, Majid, & Kassab, 2010). Nerve biopsies are not recommended for the diagnosis of GBS. Occasionally sural nerve biopsies can be taken and analyzed.

The underlying pathophysiology and etiology of GBS are not fully elucidated yet. One of the proposed mechanisms by which GBS develops is the triggering of the immune system by an antecedent infection. As a matter of fact, the majority of GBS cases (60-70%) present symptoms that appear 1 to 3 weeks after an acute respiratory or gastrointestinal infection. Campylobacter

Jejuni is one of the most commonly associated pathogens (Jacobs et al., 1998). The infection with these bacteria could lead to an aberrant antibody cross reactivity, a process known as molecular mimicry, between the gangliosides present on the axons and the lipo-oligosaccarides on the bacteria. Infections with Mycoplasma pneumonia, cytomegalovirus (CMV), Epstein–Barr virus, and Zika virus have also been linked with the onset of GBS (Cao-Lormeau et al., 2016; B. Van Den Berg et al., 2014) but these relationships are not as well established as those with C. *jejuni* and GBS (B. C. Kieseier et al., 2004) . A possible association between the onset of GBS and vaccines has also been reported. Vaccines for rabbies and influenza were speculated to provide a sufficient antigenic stimulus for the triggering of GBS. However, this causative link is not supported, several studies have shown that there is no increased risk in increased GBS incidence and vaccines in pediatric and adult cohorts (Chang et al., 2019; Y. Chen, Zhang, Chu, Xu, & Ma, 2019). Other triggering events such as trauma, treatment with immunomodulatory drugs (TNF α), and surgery, were reported in a small percentage of patients with GBS (Rudant et al., 2018; Shin, Baer, Kwon, Papadopoulos, & Siegel, 2006; Steiner, Argov, Cahan, & Abramsky, 1985).

GBS is a disorder with characterized forms or variants. The major variants include Acute Inflammatory Demyelinating Polyradiculoneuropathy (AIDP), Acute Motor Axonal Neuropathy (AMAN), Acute Motor and Sensory Axonal Neuropathy (AMSAN), and Miller Fisher syndrome (MFS). Each variant has distinct pathologic, pathophysiologic, and clinical features, which will be further detailed.

2.1.1. Acute Inflammatory Demyelinating Polyradiculoneuropathy (AIDP)

AIDP is one of the main subtypes of GBS that is predominantly found in Europe, Australia, Canada, and in the United States of America. It accounts for 60-80% of GBS cases in these countries (Blum, Reddel, Spies, & McCombe, 2013; B. C. Kieseier et al., 2018).

AIDP manifests through a demyelinating neuropathy where segmental myelin degeneration occurs in the patients' nerves. Motor, sensory, cranial, and sympathetic nerves can all be affected in this GBS variant. The diagnosis is confirmed via NCS within the first week of the onset of the disease, or after two weeks if the first results were not conclusive (a delay of more than two weeks would allow the potential peak of abnormalities). At least three sensory nerves, and four motor nerves (including F-waves) should be investigated (B. Van Den Berg et al., 2014). The patients show a decreased conduction velocity accompanied by an increase in distal motor latency.

The mechanism by which injury occurs in AIDP is mediated by an immune reaction directed against Schwann cell or axolemmal epitopes (B. C. Kieseier et al., 2018) leading to an infiltration of T-cells and macrophage via epineural and endoneural small vessels. Inflammation can also be seen at the nodes of Ranvier in early stages of the disease (B. C. Kieseier et al., 2004). Axonal degeneration then follows leading to a conduction block in the nerve. Moreover, mechanisms of molecular mimicry have not yet been identified in AIDP despite the high incidence of patients suffering from an antecedent infection. No specific myelin antigens, such as P2, PMP22 and MPZ (Kwa, Van Schaik, Brand, Baas, & Vermeulen, 2001; Makowska et al., 2008), or gangliosides antigens have been clearly identified despite the inconsistent data of the

extensive searches (de Seze et al., 2016; Rinaldi et al., 2013; Shahrizaila et al., 2014). Moesin, a protein present on the Schwann cell microvilli, has been proposed as a potential autoantibody in Cytomegalovirus induced AIDP by Sawai et al. (Sawai et al., 2014) but Miyaji et al. (Miyaji et al., 2014) could not confirm it. Another target was identified in the sera of patients, contactin-associated protein 1 (CASPR1), which is expressed in the paranodal region (Doppler et al., 2016).

The equally efficient treatments for GBS are intravenous immunoglobulins (IVIg) and plasma exchange as shown throughout different clinical studies (Hughes & Cornblath, 2005; Hughes, Swan, & van Doorn, 2011; B. C. Kieseier et al., 2004; Willison, Jacobs, & Van Doorn, 2016). These therapies helped in improving motor and sensory deficits in patients. IVIg come from purified donor immunoglobulins that are injected intravenously into the patients. Plasmapheresis is the replacement of the patients' plasma by a plasma substitute or by donor plasma. Rare side effects of IVIg such as hemolytic anemia, thromboembolism, hypersensitivity reactions, and aseptic meningitis may occur in some cases. As for plasmapheresis, four plasma exchanges every other day yielded the best outcome for patients with mild GBS in terms of muscle strength recovery and time to walk with assistance (Syndrome, 1997). Some uncommon side effects may appear such as haemodynamic changes, and hypocalceamia and metabolic alkalosis (related to the use of citrate). Treatments with corticosteroids, regardless of whether they are used alone or in combination with another drug, are not recommended since no effectiveness has been reported in patients with GBS.

2.1.2. Acute Motor Axonal Neuropathy (AMAN) and Acute Motor and Sensory Axonal Neuropathy (AMSAN)

AMAN is a GBS variant that is predominantly found in Central and South America and in Asia (Kuwabara & Yuki, 2013; Mitsui et al., 2015; Nachamkin et al., 2007; Shang et al., 2020). The underlying cause of these regional differences remains unknown but could be linked to genetic factors, temperature, or antecedent infections (J. S. Bae et al., 2014). AMSAN is the motor and sensory variant.

Patients with AMAN or AMSAN differ from those with AIDP regarding the type of neuropathy. AMAN and AMSAN patients suffer from a motor neuropathy with less frequent cranial nerve involvement as opposed to patients with AIDP who have a demyelinating neuropathy. Throughout the disease course, 10% of AMAN patients demonstrate normal or exaggerated tendon reflexes. NCS show transient motor nerve conduction block, motor neuropathy features (reduced CMAP amplitude) without sensory action potential alternation and demyelinating features (increased latency). Pain and autonomic involvement have been rarely described in AMAN cases. In the sensory-motor variant, the sensory nerves are additionally affected with a reduced or absent sensory action potential.

AMAN and AMSAN are classified as axonal neuropathies where the immune process is directed towards the nodal and paranodal regions (J. W. Griffin et al., 1996; Hafer-Macko et al., 1996). This leads to functional axonal involvement, myelin sheath detachment, node lengthening, Na+ channel dysfunction, as well as altered water and ion homeostasis (Uncini & Kuwabara, 2015). These injuries are reversible but in some cases they may progress to axonal degeneration and loss of function. Lesions are also present at the level of the ventral roots. Between 30 to 66% of AMAN patients had an antecedent infection with C. *jejuni* (Ho et al.,

1995; Zautner et al., 2014). However, less than 0.1% of patients with a C. *jejuni* infection are likely to develop AMAN (Hughes & Cornblath, 2005). The process of molecular mimicry is speculated to be the mechanism by which the autoimmune neuropathy develops. Several ganglioside antibodies were detected in AMAN and AMSAN patients. In the pure motor neuropathy, the gangliosides GM1, GM1B, GD1a, and GalNAC-GD1a are the antigens found whereas in the motor and sensory variant GM1 and GD1a are usually detected. GalNAC-GD1a and GM1 are expressed on the axolemma of the motor nerves. The anti-GalNAC-GD1a and anti-GM1 antibodies bind to the axolemma causing complement activation. This is followed by membrane attack complex formation and destruction of Na+ channels. Consequently, the paranodal myelin is detached and nerve conduction failure occurs (Fig 14).

Treatment strategies for AMAN or AMSAN do not differ from AIDP, the use of IVIG and plasma exchange remain the gold standard.

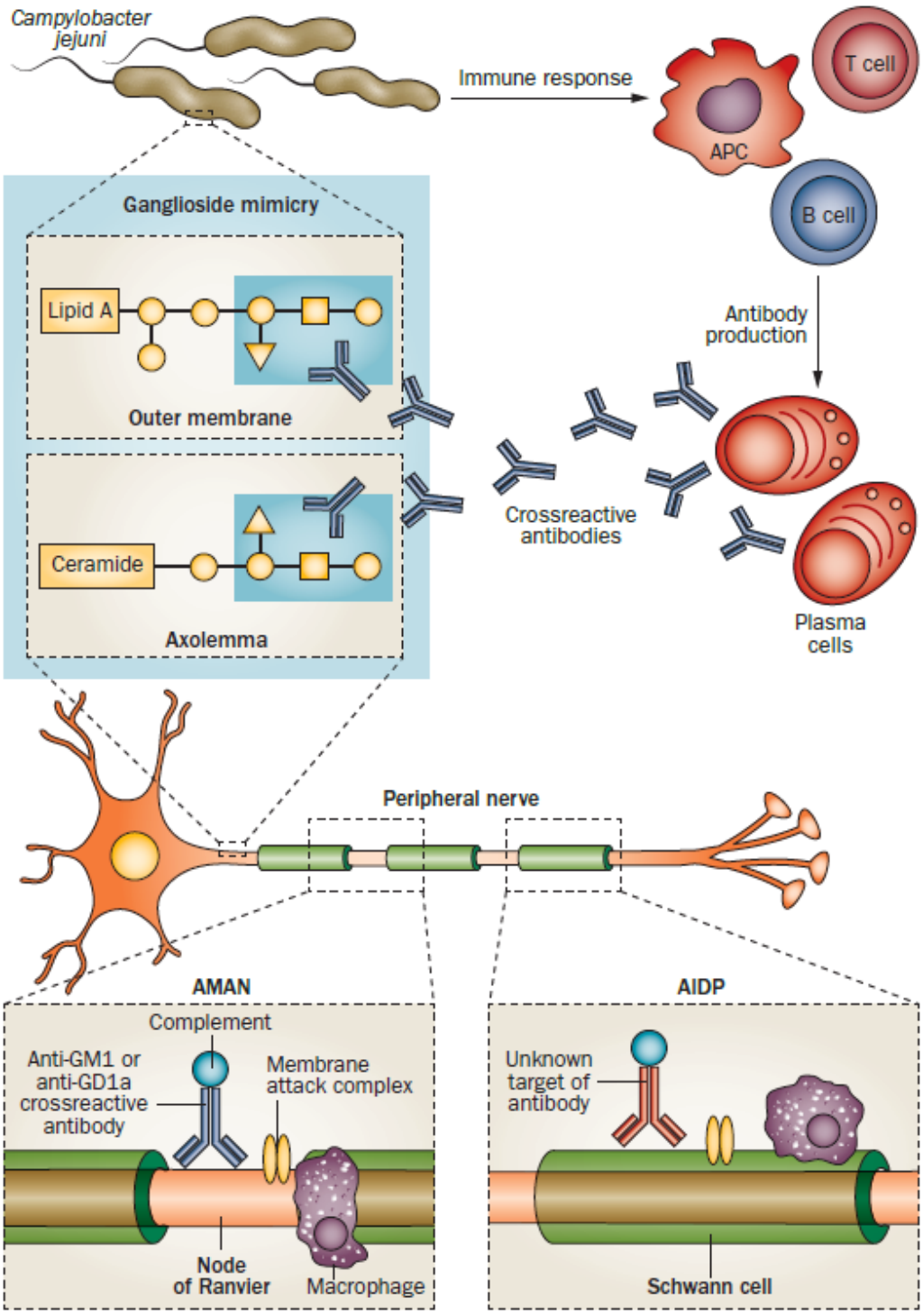


Figure 14: Pathogenesis of AMAN and AIDP. Schematic representation of the immune response in two variants of GBS; AMAN and AIDP. In the first variant, the axon is attacked by the immune system resulting in the development of an axonal neuropathy whereas in the second variant the immune response is targeted towards the myelin sheath leading to a demyelinating neuropathy. (B. Van Den Berg et al., 2014)

2.1.3. Miller Fisher syndrome (MFS)

MFS is a fourth GBS variant that accounts for 5% of GBS cases in the Western hemisphere and with a 26% incidence in Japan (Mitsui et al., 2015).

Patients suffering from MFS present with a triad of symptoms; ataxia, areflexia, and ophtalmoplegia (Wakerley, Uncini, & Yuki, 2014). Although patients do not suffer from limb weakness, Compound Muscle Action Potential (CMAP) results shown a subclinical motor dysfunction in some MFS patients (Drenthen et al., 2013). If the patient presents with hypersomnolence in addition to the previously mentioned symptoms, he or she is diagnosed with Bickerstaff brainstem encephalitis (BBE), which is the CNS subtype of MFS. MFS-GBS overlap syndrome is given to patients who developed MFS with cranial nerve involvement and limb weakness. Incomplete forms of MFS exist such as acute opthalmoparesis (absence of ataxia) and acute ataxic neuropathy (absence of opthalmoplegia) (Yuki, Odaka, & Hirata, 2001). A very incomplete MFS would manifest in isolated mydriasis (unusual dilation or widening of the pupil) or ptosis (drooping or falling of the upper eyelid) (Jindal, Parmar, & Gupta, 2009; Yuki, Koga, & Hirata, 1998).

Antecedent infections with *C. jejuni* are known to be associated with the development of not only GBS but also with that of MFS. More specifically, the Asn51 variant of the bacteria is linked to the occurrence of MFS (Godschalk et al., 2007). Clinical serology with antiganglioside antibody testing is useful in MFS diagnosis as 90% of patients have anti-GQ1b antibodies (Kusunoki, Kaida, & Ueda, 2008; Mori & Kuwabara, 2011; Wakerley et al., 2014). GQ1b is mainly expressed in the trochlear, oculomotor, abducens nerves, and muscle spindles. Therefore, anti-GQ1b antibodies are speculated to be the culprit in the development of cerebellar like ataxia

and ophtalmoplegia (Chiba, Kusunoki, Obata, Machinami, & Kanazawa, 1993; J. X. Liu, Willison, & Pedrosa-Domellof, 2009).

Almost all patients with MFS fully recover regardless of receiving IVIg treatment/plasma exchange or not. A retrospective study showed that patients' improvement starts slightly earlier upon IVIg treatment compared to absence of treatment or plasma exchange. Taking these studies into consideration, some clinicians justify the withholding of treatment in MFS patients since they show a full recovery with no medication. Nonetheless, individuals with MFS-GBS overlap syndrome or with BBE can require plasma exchange or IVIg treatment since they are more severely affected (Mori, Kuwabara, Fukutake, & Hattori, 2007; Overell, Hsieh, Odaka, Yuki, & Willison, 2007).

2.2. Chronic inflammatory neuropathies

Chronic inflammatory neuropathies are a cluster of immune neuromuscular disorders affecting myelin. They can be subdivided into Chronic Inflammatory Demyelinating Polyradiculoneuropathy (CIDP) and its variants, and into chronic demyelinating neuropathies distinct from CIDP (Dimachkie, Barohn, & Katz, 2013).

2.2.1. Chronic Inflammatory Demyelinating Polyradiculoneuropathy (CIDP) and its variants

CIDP is the most common chronic inflammatory neuropathy affecting 1 – 9 cases per 100000 individuals. The incidence is higher in men with a 2:1 ratio. CIDP prevalence rates vary across different countries with no explanation for the difference in incidence (Lehmann, Burke, & Kuwabara, 2019). Previous studies have reported an incidence of 8.9 per 100000 in Olmsted

County USA (Laughlin et al., 2009), 5.9 per 100000 in Ireland (Lefter, Hardiman, & Ryan, 2017), 2.84 per 100000 in England (Mahdi-Rogers & Hughes, 2014), and 0.8 per 100000 in Tottori Japan (KUSUMI, NAKASHIMA, NAKAYAMA, & TAKAHASHI, 1995). CIDP can be clinically classified into typical and atypical cases. According to Italian CIDP Database study group patients diagnosed with typical CIDP make up 82% of CIDP cases, 7% suffer from Distal Acquired Demyelinating Symmetric neuropathy (DADS), and 4% have Multifocal acquired demyelinating sensory and motor neuropathy (MADSAM) or Lewis-Sumner syndrome. The remaining 7% of CIDP patients suffer from atypical forms that are less common such as pure motor and pure sensory CIDP (Doneddu et al., 2019).

2.2.1.1.General Overview of CIDP/Typical CIDP

This demyelinating neuropathy affects the nerve roots and the peripheral nerves, and has a progressive or relapsing-remitting course. Symptoms develop over the course of two months and last for more than eight weeks. The classical form manifests as a symmetric and motor-predominant form, leading to distal and proximal myasthenia. Up to 90% of CIDP patients suffer from sensory deficits. NCS show the presence of a segmental demyelination with a decreased latency, temporal dispersion and/or conduction block. Nerve biopsies, although not performed routinely, corroborate these findings. The sections show onion bulb formations, features of demyelination/re-myelination, T-cell infiltration (mainly CD8+ t-cells), as well as nerve edema. Nerve root enlargement is highlighted by MRI results. Albuminocytologic dissociation is also observed in CIDP patients (EFNS & PNS, 2010; B. C. Kieseier et al., 2018; Lehmann et al., 2019; Mathey et al., 2015).

The cause of CIDP remains unknown. Unlike GBS, there is no strong correlation between an antecedent infection and the onset of the disease. Recent studies have taken an interest in the implication of autoantibodies in CIDP. Several autoantibodies have been associated a particular disease phenotype; Contactin-1 (CNTN1) with aggressive onset or axonal involvement at onset of the disease, Neurofascin splice variant 155 (NF-155) with distal motor involvement, ataxia, and prominent tremor, Contactin-associated protein 1 (CASPR1) with pain, Sialosylneolactotetraosylceramide (LM1) ganglioside with ataxia and subacute onset, Neurofascin splice variant 140 (NF-140) and Neurofascin splice variant 186 (NF-186) with sensory ataxia and conduction block. CNTN1, CASPR1, NF-140, and NF-186 are neuronal proteins located at the paranodal and nodal levels, NF-155 is a paranodal protein expressed by glial cells, and LM1 is the predominant ganglioside in nerve myelin (Fig 15). The interaction between neuronal and glial proteins is crucial for the maintenance of structural integrity of the myelinated fibers. Loss of this attachment exposes the potassium channels in the juxtaparanodal region therefore limiting saltatory conduction and causing a conduction delay or block (Delmont et al., 2017; Querol, Devaux, Rojas-Garcia, & Illa, 2017; Schafflick, Kieseier, Wiendl, & Meyer Zu Horste, 2017). Furthermore, neuropathies where antibodies against CNTN1, NF-155, and CASPR1 are present in the sera of patients have been given the label of “paranodopathies” as they affected individuals seem to respond better to PE than IVIg (Uncini & Vallat, 2018). Even though autoantibodies are detected in a small subset of CIDP patients, their relevance should not be undermined as they provide insight on the underlying mechanisms of the pathology and they can guide therapeutic decision making.

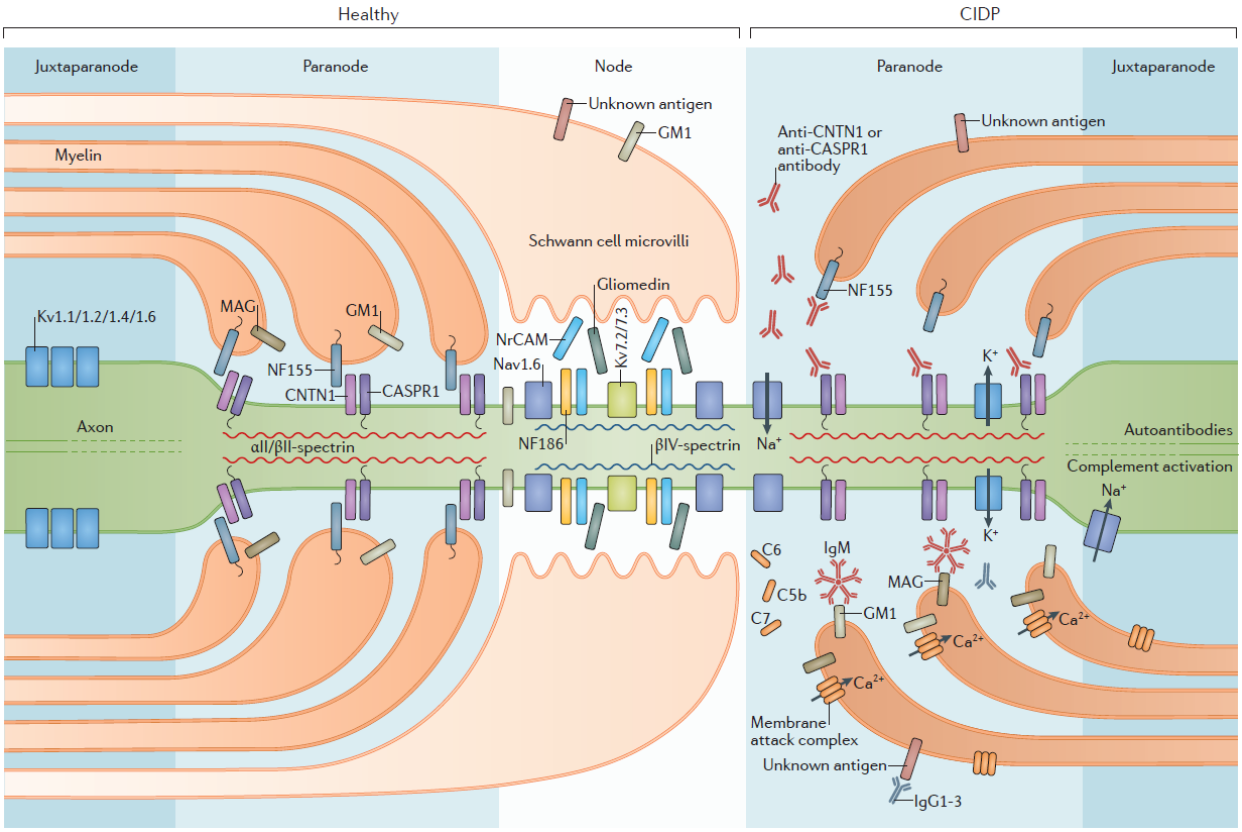


Figure 15: Autoantibodies presence at the node of Ranvier. The schematic representation shows a healthy vs. a CIDP state. In the healthy state, CNTN1, CASPR1, and NF-140 are located at the paranode, and NF-186 is at the nodal levels. The Schwann cell at the paranode expresses NF-155. In the case of CIDP, autoantibodies targeting the aforementioned protein can be seen. Additionally, there are other autoantibodies targeting GM1 and MAG. (Querol et al., 2017)

Typical treatment for CIDP patients is the administration of IVIGs or plasma exchange. These patients also respond well to corticosteroid treatment as opposed to GBS patients. However, not all CIDP patients respond to these classical treatments. Patients with autoantibodies for CNTN1 and NF-155 do not respond to IVIg treatment whereas patients with antibodies against NF-140 and NF-186 show improvement upon IVIg/corticosterone administration (B. C. Kieseier et al., 2018; Querol et al., 2017).

2.2.1.2. Multifocal Acquired Demyelinating Sensory and Motor Neuropathy (MADSAM) (also known as Lewis-Sumner syndrome)

Lewis-Sumner syndrome (LSS) or multifocal acquired demyelinating sensory and motor neuropathy (MADSAM) is characterized by an asymmetrical multifocal neuropathy in mainly the upper limbs. Patients with MADSAM show abnormal sensory and motor nerve conduction where the presence of conduction block is the hallmark of the disease (Dimachkie et al., 2013; Lewis, Sumner, Brown, & Asbury, 1982). NCS also show prolonged distal latencies, slow conduction velocities, temporal dispersion, and delayed/absent F-waves in at least one motor nerve (Lewis et al., 1982). 50% of the patients' neuropathy eventually progresses to the legs and their disease evolves into a typical CIDP. Pain and paresthesias have also been reported. Laboratory findings also include an elevated CSF protein in up to 82% of patients (D. S. Saperstein et al., 1999). Nerve biopsies taken from MADSAM patients resemble findings in CIDP where onion bulbs and demyelinating features are observed. Treatment for MADSAM patients includes IVIg, PE, and corticosteroid administration.

2.2.1.3. Distal Acquired Demyelinating Symmetric neuropathy (DADS)

DADS neuropathy is a symmetrical length-dependent neuropathy with predominantly sensory symptoms. The profound sensory symptoms can lead to tremors and unsteady gait. Electrophysiological evidence can also show motor involvement with widespread symmetric slowing in distal motor and sensory nerves. CSF protein is also increased in these patients (Larue et al., 2011). Patients with DADS neuropathy respond well to corticosterone treatment, IVIg, and PE (Dimachkie et al., 2013; David S. Saperstein, Katz, Amato, & Barohn, 2001). Interestingly 50-70% of DADS patients present an IgM paraprotein that has antimyelin-associated glycoprotein (anti-MAG) antibody activity (Katz, Saperstein, Gronseth, Amato, & Barohn,

2000). These patients are not considered to suffer from a CIDP variant according to the EFNS/PNS criteria since anti-MAG is excluded from the CIDP classification (EFNS & PNS, 2010). One major difference is that DADS patients with anti-MAG do not respond to the treatments effective in CIDP patients.

2.2.2. Chronic inflammatory neuropathies distinct from CIDP

Several chronic inflammatory neuropathies distinct from CIDP have been described in the literature such as the previously mentioned DADS with IgM presence (classified under demyelinating neuropathies associated with immunoglobulin M (IgM) monoclonal gammopathy of undetermined significance with and without anti- myelin-associated glycoprotein neuropathies). The most prevalent one is the Multifocal Motor Neuropathy (MMN) with an incidence rate ranging from 0.29 per 100000 individuals in Japan (Miyashiro et al., 2014), to 0.6 per 100000 in the Netherlands (Cats, van der Pol, et al., 2010). The median age for MMN onset is around 40 years with a higher incidence in males compared to females (2.7:1 ratio).

Clinical description of MMN consists of the presence of asymmetrical weakness and atrophy starting in the upper limbs with lesions in the ulnar, median, radial and tibial nerves. The affected limb shows a decreased or absent tendon reflexes. In MMN no sensory involvement has been reported (Dimachkie et al., 2013; Vlam et al., 2011). Electrophysiological studies show a conduction block in MMN patients, which is the electrodiagnostic hallmark, revealing axonal loss and degeneration (Bouche et al., 1995). In laboratory and pathology findings the CSF is normal and the biopsies show a mild degree of sensory fiber involvement as well as an increase in the number of thinly myelinated fibers (Kaji et al., 1993) . Imaging studies have also revealed a multifocal enlargement in the nerves. Anti-GM1 IgM antibodies have been detected in the sera

of 30-85% of the patients (Pestronk & Choksi, 1997; van Schaik, Bossuyt, Brand, & Vermeulen, 1995) however recent data with improved sensitivity report 40-50% of anti-GM1 IgM antibodies in MMN patients (Cats, Jacobs, et al., 2010; Nobile-Orazio, 2001). Even though the exact mechanism by which nerve injury occurs in MMN patients is yet to be elucidated, it is speculated to happen in a similar fashion as in AMAN; the autoantibodies would activate complement by previously binding at the nodes of Ranvier. This will disrupt the Na+ channel clustering resulting in conduction block (Susuki et al., 2007).

IVIg is the first line treatment for MMN patients as PE and corticosteroid administration are ineffective in these individuals (Léger, Guimarães-Costa, & Muntean, 2016; L. H. Van den Berg et al., 1995).

Although clinical studies have provided crucial information regarding the pathogenesis of immune-mediated neuropathies, animal models had to be created to answer the lingering questions regarding the mechanisms underlying these diseases. Scientists therefore took the arising problems from the bedside to the bench side.

3. Experimental Models of Autoimmune Neuropathies

The study of immune mediated neuropathies has proven to be challenging in terms of the creation of a suitable animal model. However, scientists have tackled this issue with the generation of two categories of animal model to study the different disorders; the Experimental Autoimmune Neuritis (EAN) models and the transgenic animal models.

3.1. Experimental Autoimmune Neuritis

The first animal model for EAN was created by Waksman and Adams in 1955 by inoculating rabbits with lysed nervous tissue homogenized in complete Freund's adjuvant (Waksman & Adams, 1955). EAN provided scientists with an animal model that resembles human GBS on the immunological and electrophysiological aspects; the animals' nerves where infiltrated by macrophages and lymphocytes and they developed a segmental demyelination. The EAN protocol was later extended to different species such as monkeys, guinea pigs, and rats. EAN was triggered in the Lewis rats, monkeys, and guinea pigs by injecting them with myelin proteins, myelin homogenates, or myelin protein-derived peptides such as MPZ, P2 and PMP22 (Deretzi et al., 1999; Eylar, Toro-Goyco, Kessler, & Szymanska, 1982; Snyder, Stone, & Raine, 1977). However, the induction in mice was problematic. Data has shown that the SJL strain was susceptible of developing mild neurological deficits upon EAN induction but the BALB/c and C57BL/6J mice were resistant (Mäurer & Gold, 2002; Taylor & Hughes, 1985). The scientific community had to solve this problem since EAN would be useful in mice, particularly in the C57BL/6J strain where most of the transgenic animal models are created. Zou et al tackled this

issue where they successfully induced EAN in C57BL/6J mice by adding pertussis toxin to P2 fragments (Zou et al., 2000). Blocking CTLA-4 in the aforementioned model resulted in an exacerbated phenotype (Zhu et al., 2001). Passive immunization of mice with antibodies against GD3, GT1a, and GQ1b resulted in animal model for the MFS (Halstead et al., 2004).

In addition to the active induction models, adoptive transfer EAN (AT-EAN) models were generated where host animals received injections with T-cells activated against different myelin antigens. In the Lewis rat, AT-EAN resulted in a rapid onset EAN with CIDP-like relapsing if transferred repeatedly. This experiment allowed the identification of MAG as a possible antigen in addition to MPZ and P2, showing the heterogeneity of potential antigens in the PNS (Lassmann, Fierz, Neuchrist, & Meyermann, 1991). AT-EAN was performed successfully in BALB/c mice with two MBP-specific T-cell clones; they specifically recognized the epitopes in the 21000 and 18500 but not in the 17000 and 14000 M_r MBP isoforms (Abromson-Leeman, Bronson, & Dorf, 1995). However, this model did not reach popularity, as no genetic mutants are available on the BALB/c background.

Even though these animal models contributed to the understanding of immune mediated neuropathies such as GBS, several limitations exist. The EAN model relies on an immunization using myelin peptides however a minimal proportion of patients suffering from GBS have auto-antibodies targeted at myelin in the sera. Furthermore, several treatments were successful in the EAN models but have failed upon application on patients (Meyer zu Hörste, Hartung, & Kieseier, 2007).

3.2. Transgenic Animal Models

With the scientific breakthrough of transgenesis, scientists were able to generate transgenic animal models to cater to their research needs. The first KO model for immune mediated neuropathies was created by Jeffrey Bluestone's group where B7.2 was abrogated on the Non Obese Diabetic (NOD) genetic background (Salomon et al., 2001). The NOD mouse is commonly used as a model for type 1 diabetes; it develops insulitis around 4-5 weeks resulting in the destruction of the B cells of the pancreas and the development of the disease (Box 1) (Makino et al., 1980). The NOD mouse expresses only one MHC II molecule; I-Ag7. The replacement of the I-Ag7 by a different molecule can lead to the deviation of the immune system; I-Ak causes a thyroid disease (Slattery et al., 1990), I-Aq leads to the development of systemic lupus erythematosus nephritis (Lindqvist et al., 2005), DQ8 gives rise to a cardiomyopathy (Elliott et al., 2003; Hayward et al., 2006). Salomon et al reported that the KO of B7.2, a molecule found on antigen presenting cells (APCs) that provides costimulatory signals upon binding to CD80 for T-cell activation, leads to the development of spontaneous autoimmune neuropathy. NOD B7.2 KO mice showed behavioral deficits with electrophysiological and histological evidence. The incidence of neuropathy was 100% in females and 30% in males. The disease was shown to be mediated by CD4+ cells; a transfer experiment of these cells in NOD.SCID mice induced neuritis. Since the NOD B7.2 KO is used as a mouse model for CIDP, a potential autoantigen was screened for as some CIDP patients have autoantibodies in their sera. MPZ was found to be a major autoantigen in this mouse model (Louvet et al., 2009). Moreover, no lesions in the CNS were observed.

Another KO model of a costimulatory molecule is the NOD ICOS KO and NOD ICOSL KO mice generated by our lab (Prevot et al., 2010). 80% female KO mice develop a spontaneous

autoimmune neuromyopathy where the incidence of neuropathy is 20% in males with no injury in the CNS. The neuromyopathy is mediated CD4+ cells in the KO mice. The following was demonstrated by creating NOD ICOSL KO mice deficient for CIITA or for β2microglobulin. The animals were either deprived for class II restricted CD4+ T-cells or for class I restricted CD8+ T-cells. NOD ICOSL -/- CIITA -/- mice did not develop neuropathy as opposed to NOD ICOSL -/- β2m -/- proving that the development of autoimmune neuropathy is mediated by CD4+ T-cells. As for the NOD ICOS KO and NOD ICOSL KO animals, a thorough description of these models will be provided in the results section of my thesis manuscript.

Similarly to Salomon et al's model, the NOD mouse deficient for ICAM-1 develops a peripheral autoimmune neuritis (Meyer zu Horste et al., 2014). ICAM-1 is a molecule expressed by APCs and the vascular endothelium. Its expression is important for costimulatory functions as well as leukocyte adhesion. The NOD ICAM-1 KO mice do not show an alteration in T-regulator cells (Tregs) but have an increase in Interlukin-17 production by T-cells. The $MPZ_{180-199}$ peptide caused a proliferation response in the NOD ICAM-1 KO mice showing an antigenic response. This result is similar to the NOD B7.2 mice where autoimmunity specifically targets the MPZ protein.

Other less frequently used NOD models exist for spontaneous autoimmune neuropathy such as NOD H-2b + PD-1 -/- (Yoshida, Jiang, Honjo, & Okazaki, 2008), NOD IL-2 mAb depleted (Setoguchi, Hori, Takahashi, & Sakaguchi, 2005), and NOD $Aire^{GW/+}$ (Zeng, Nagavalli, Smith, Howard, & Su, 2013). Animal models for CIDP have also been developed on a C57BL/6J background. The IL-10 over-expressing mice develop neuritis between 10 to 20 weeks (Dace et al., 2009). The suggested mechanism of action is with the downregulation of IL-10, ICAM-1 is upregulated triggering macrophage influx and resulting in the development of the pathology.

Another interesting model is the L31 mouse that constitutively expresses B7.2 on APCs (Zehntner, Brisebois, Tran, Owens, & Fournier, 2003). The animals develop sensory and motor deficits, which are exacerbated upon an additional KO of CD4+ T-cells (Brisebois, Zehntner, Estrada, Owens, & Fournier, 2006; Yang et al., 2015).

The different existing animal models for immune mediated neuropathies will be summarized in the following table (Table 2).

Species	**Strain**	**Type of Transfer**	**Possible Antigens**	**Description**	**Reference**
Guinea Pig		Active	PNS myelin	Heterogenous clinical picture in only 18% of inoculated animals	(Snyder et al., 1977)
Rhesus Monkey		Active	PNS myelin, P2	Mild-course EAN with inflammation and demyelination	(Eylar et al., 1982)
Rabbit	NZW	Active	PNS myelin, P2	First EAN Model	(Waksman & Adams, 1955)
	NZW	Active	Galactocerebroside	Chronic inflammation	(G. Stoll et al., 1986)
	JW	Active	GM1	AMAN-like	(Yuki, Yamada, et al., 2001)
	JW	Active	GD1b	Ataxic sensory neuronopathy	(Kusunoki et al., 1996)
Rat	Lewis	Active	PNS myelin, MPZ, MPZ 180-199, P2, P2 53-78, P2 57-81	Frequently used EAN models	(Mäurer & Gold, 2002) (Deretzi et al., 1999) (Miyamoto et al., 1999) (Abbas, Zou, Pelidou, Winblad, &

					Zhu, 2000)
		Active	PMP22	Mild-course EAN	(Gabriel, Hughes, Moore, Smith, & Walsh, 1998)
		Active	PNS myelin + Ciclosporin A	CIDP-like chronic relapsing, not robust	(McCombe, Harness, & Pender, 1999)
		Adoptive	MPZ, MPZ 180-199, P2, P2 61-70, MAG	Rapid onset EAN, CIDP-like relapsing if transferred repeatedly	(Mäurer & Gold, 2002) (Lassmann et al., 1991)
	BN, SD, BUF, Wistar	Active	PNS myelin	Less severe EAN course	(Hoffman, Powers, Weise, & Brostoff, 1980)
	Dark Agouti	Active	PNS myelin	CIDP-like relapsing	(Jung et al., 2004)
Mouse	SJL	Active	P2	Mild-course EAN	(Taylor & Hughes, 1985)
		Active	Myelin+PTX (+IL-12)	Severe-course EAN	(Calida et al., 2000)
	BALB/c	Adoptive	MBP (isoform 18500 and 21000M_r)	Peripheral and central demyelination	(Abromson-Leeman et al., 1995)
	C57BL/6J	Active	MPZ 180-199, MPZ 106-125 + PTX	Varying effectiveness reported	(Zou et al., 2000) (Miletic et al., 2005)
	C57BL/6J over expressing IL-10	Spontaneous	_	CIDP-like, demyelination, muscle weakness, paralysis, axonal loss	(Dace et al., 2009)
	C57BL/6J L31	Spontaneous	_	Autoimmune peripheral neuropathy	(Zehntner et al., 2003)
	Mouse axonal	Passive	Anti-GQ1b antibody	MFS-like	(Halstead et al., 2004)

	NOD	Active	Oral C. jejuni	Mild course AMAN	(St Charles et al., 2017)
	NOD IL-10 -/-	Active	Oral C. jejuni	AMAN	(St Charles et al., 2017)
	NOD B7.2 -/-	Spontaneous	_	Spontaneous autoimmune neuropathy CIDP-like	(Salomon et al., 2001)
		Active	Oral C. jejuni	AIDP	(St Charles et al., 2017)
	NOD ICAM -/-	Spontaneous	_	Spontaneous autoimmune neuritis	(Meyer zu Hörste et al., 2014)
	NOD H-2^b + PD-1 -/-	Spontaneous	_	Autoimmune peripheral neuropathy	(Yoshida et al., 2008)
	NOD IL-2 mAb depleted	Spontaneous	_	Autoimmune peripheral neuropathy	(Setoguchi et al., 2005)
	NOD $Aire^{GW/+}$	Spontaneous	_	Autoimmune peripheral neuropathy, CIDP-like	(Zeng et al., 2013)
	NOD ICOS -/- , NOD ICOSL -/-	Spontaneous	_	Autoimmune peripheral neuropathy	(Prevot et al., 2010)

Table 2: Animal models of immune mediated neuropathies. (Adapted from (Meyer zu Hörste et al., 2007; Schafflick et al., 2017))

Abbreviations: BN, Brown Norway rats; BUF, Buffalo rats; IL-12, interleukin 12; IL-10, interleukin 10; JW, Japanese White; NZW, New Zealand white rabbit; PTX, pertussis toxin; SD, Sprague-Dawley rats; PD-1, programmed cell death protein 1.

Box 1: The Non Obese Diabetic (NOD) Animal Model

The NOD mouse was created by Makino et al in Japan (Makino et al., 1980). A selection of a cataract-prone strain derived from the outbred Jcl/ICR mouse line was performed. After repetitive mating between siblings, a subline that spontaneously develops diabetes emerged. The NOD mouse line was thus created with a genetic background characterized by more than 40 genes implicated in the mapping of insulin-dependent diabetes (idd). The NOD animal develops insulitis after weaning with an incidence of 60-80% in females and 20-30% in males (Anderson & Bluestone, 2005). The pathology observed in affected animals shares similarities with the human form of the disease; the NOD mice suffer from insulitis, glycosuria, and hyperglycemia. Autoantibodies are also found in both species such as insulin, GAD, and IA-2. Peri-insulitis starts as early as 3-4 weeks in NOD mice and eventually progresses to insulitis by 10 weeks. The observed pancreatic infiltrate is composed of dendritic cells, natural killer cells, macrophages, as well as CD4+ and CD8+ T-cells (Kikutani & Makino, 1992). Adoptive transfer experiments in SCID recipients have shown that diabetes is mediated by the CD4+ and CD8+ T-cells (Wicker, Miller, & Mullen, 1986).

Similarly to humans, NOD mice have a genetic susceptibility that predisposes them to develop T1D. The most important genetic factor in both species is the MHC also known as idd1 (IDDM1 in humans). NOD mice express I-Ag7 as MHC-II (similar to HLA-DQ8 in humans) and $H\text{-}2K^{d}D^{b}$ as MHC-I molecules. However, they do not express I-E (equivalent to HLA-DR in humans) (Pearson, Wong, & Wen, 2016). I-Ag7 contributes significant susceptibility to developing diabetes and the expression of I-E in NOD mice hampers the development of T1D (Acha-Orbea & McDevitt, 1987; Hattori et al., 1986). The NOD mice are also prone to develop other autoimmune pathologies due to their reactive autoimmune background. Autoimmune sialitis (Hu, Nakagawa, Purushotham, & Humphreys-Beher, 1992), autoimmune peripheral neuropathy (Salomon et al., 2001), autoimmune thyroiditis (Many, Maniratunga, & Denef, 1996), and a systemic lupus erythematosus-like disease may arise in NOD animals (Silveira & Baxter, 2001).

4. Co-stimulatory Molecules and T-cell Activation

Immune regulation of adaptive immunity is central in the control of immune tolerance to self and its breakdown in autoimmune diseases. Costimulatory molecules have been endowed with a key role in this regulation. For the sake of pertinence to my PhD project, I have provided a summarized description of the different families of co-stimulatory molecules. The purpose of this brief summary is to shed some light on the different co-stimulatory molecules mentioned in this chapter and in particular the ICOS/ICOSL interaction.

The immune response is tightly regulated by co-stimulatory and co-inhibitory pathways. T-cell activation require several co-stimulatory signals provided by the APC. The first signal is the binding of the T-cell receptor (TCR) to the MHC molecule expressed by the APC (Bretscher & Cohn, 1970). However, this interaction alone is not sufficient for T-cell activation; a second co-stimulatory signal through CD28-B7 is mandatory (Jenkins & Schwartz, 1987). In the absence of the second co-stimulatory signal, the T-cell goes into a state of anergy. The CD28-B7 interaction allows Interleukin(IL)-2 production which is necessary for the survival of naïve T-cells. Once the immune response in no longer required, co-inhibitory signals function to attenuate and terminate the T-cell response (Schwartz, 1992). It is important to note that co-stimulation does not always activate the immune response. Co-stimulatory pathways may have an inhibitory effect, and the balance between the inhibitory signals and stimulatory signals is responsible for the modulation of the T-cell dependent immune response. The two most studied families of co-stimulatory molecules are the Tumor Necrosis Factor (TNF) related family and the CD28/B7 family (Azuma, 2019).

TNF related family

The interaction between TNF and its receptors (TNFR) has different effects on T-cell response. They impact lymphoid organization, activation of APCs, inflammation, innate immunity, and provide direct signals to T-cells. Members of the TNF/TNFR family include CD40/CD40L, CD27/CD70, CD137 (4-1BB)/4-1BBL, CD134 (OX40)/OX40L, GITR/GITRL, CD30/CD30L, and HVEM/LIGHT (Watts, 2005) (Fig). They play a role in cellular proliferation, inflammation, morphogenesis, and apoptosis (Aggarwal, Gupta, & Kim, 2012) (Fig).

TNFR can be categorized into 3 groups; decoy receptors, death domain (DD) containing receptor, and TNR receptor associated factor (TRAF) binding receptors. TNFRs with DDs such as DR3, TNFR1, and FAS can induce caspase cascades leading to apoptosis whereas TRAF binding receptors have a motif of 4-6 amino acids that helps in recruiting TRAF proteins (Locksley, Killeen, & Lenardo, 2001).

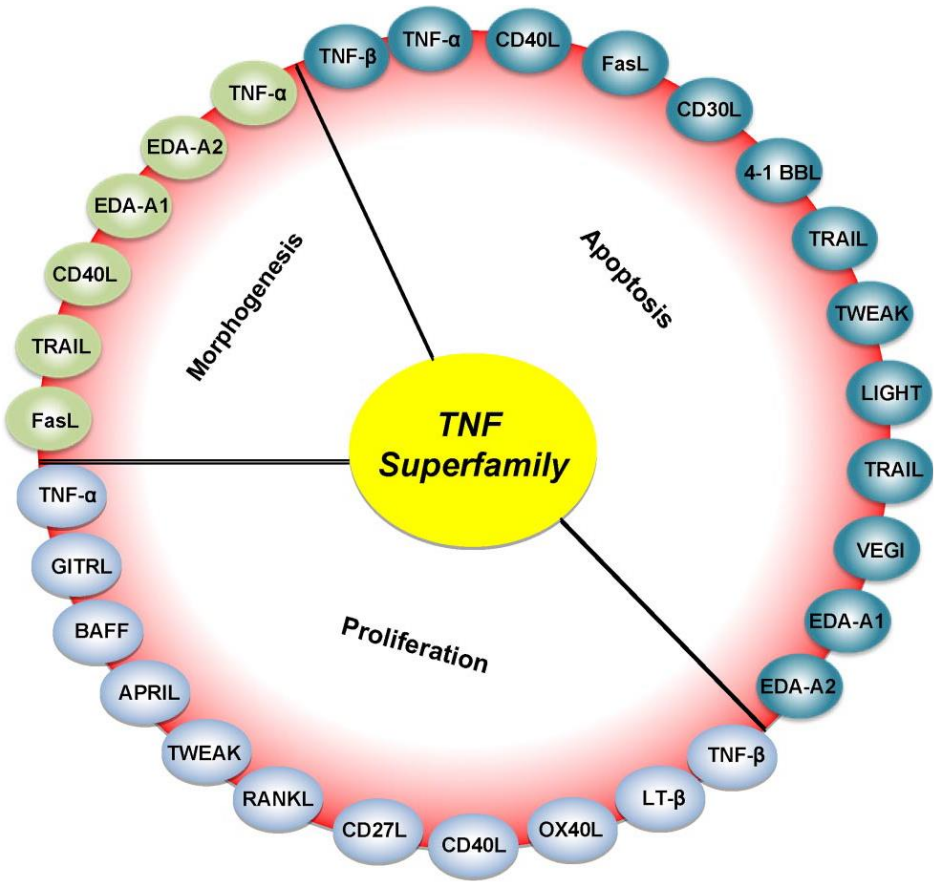


Figure 16: Roles of the TNF family members. TNF/TNFR family members play a role in cellular proliferation, inflammation, morphogenesis, and apoptosis (Aggarwal et al., 2012).

CD28/B7 Family

The CD28/B7 interaction has a pivotal role in the regulation of T-cell activity through its activation and inhibitory signals. CD28/CTLA-4/B7.1(CD80)/B7.2(CD86), ICOS/ICOSL, PD-1/PDL1/ PD-L2, BTLA/HVEM, B7-H3 and B7-H4 are members of the CD28/B7 family (Greenwald, Freeman, & Sharpe, 2005) (Fig).

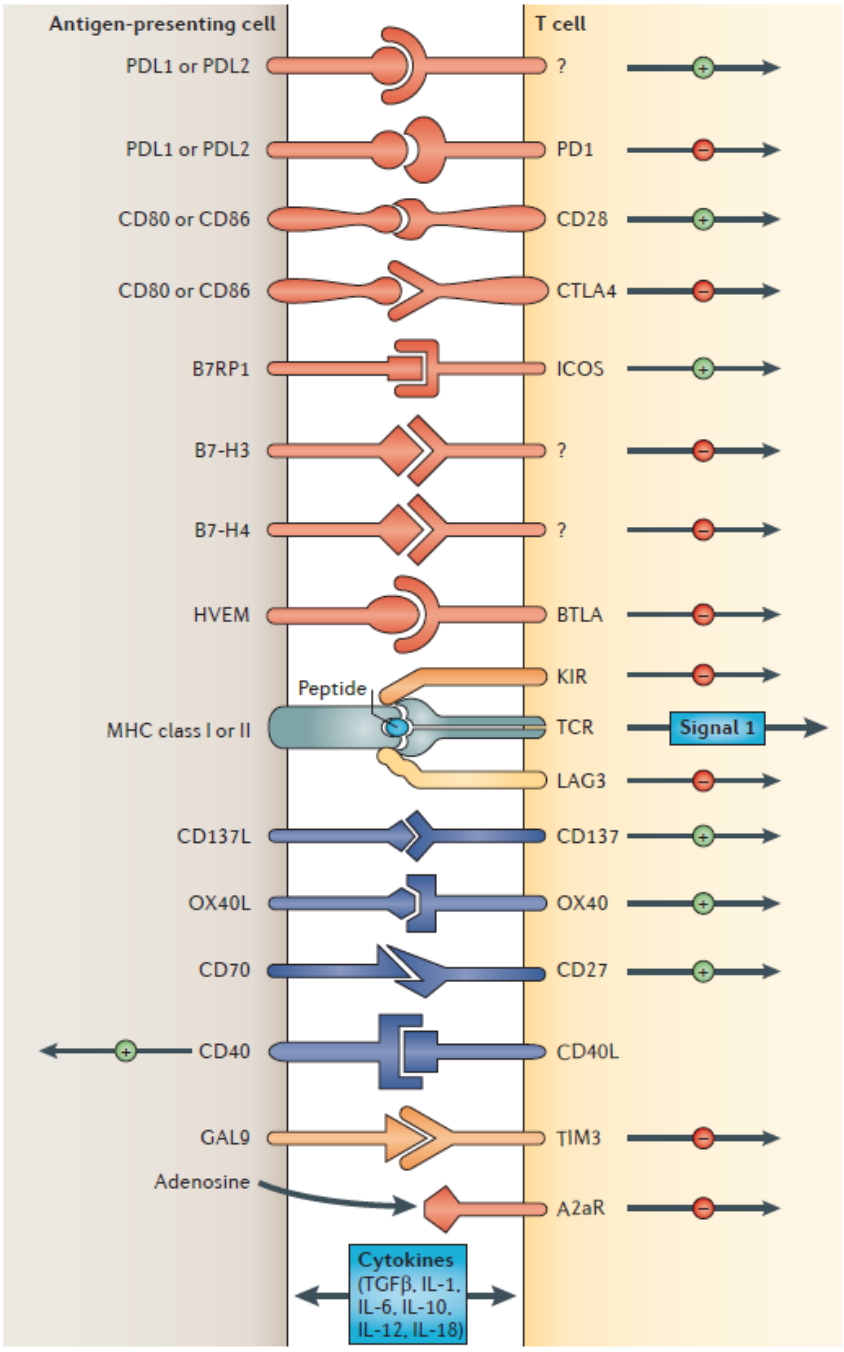


Figure 17: T-cell responses are mediated by co-stimulatory and co-inhibitory molecules. Receptors on T-cells bind to their ligands present on antigen-presenting cells (APCs) to regulate the T cell response to antigen. A2aR, adenosine A2a receptor; B7RP1, B7-related protein 1; BTLA, B and T lymphocyte attenuator; GAL9, galectin 9; HVEM, herpesvirus entry mediator; ICOS, inducible T cell co-stimulator; IL, interleukin; KIR, killer cell immunoglobulin like receptor; LAG3, lymphocyte activation gene 3; PD1, programmed cell death protein 1; PDL, PD1 ligand; TGFβ, transforming growth factor-β; TIM3, T cell membrane protein 3. (Pardoll, 2012)

The CD28/CTLA-4/B7.1(CD80)/B7.2(CD86) pathway is one of the most studied costimulatory pathways. CD28 is constitutively expressed on T-cells. Once CD28 binds to its receptors B7.1 and B7.2, naïve T-cells become activated. Following T-cell activation, CTLA-4 is upregulated. This molecule has a homologous structure to CD28 as well as a higher affinity for B7.1 and B7.2. CTLA-4 then exerts a negative regulation on T-cells by dissociating the CD28/B7.1/B7.2 interaction and causes an inhibitory effect by upregulating the immunosuppressive indoleamine 2,3-dioxygenase (IDO1) (Linsley et al., 1994; Mellor & Munn, 2004).

PD-1 is found on the surface of T-cells, monocytes, B-cells, and NK cells. Upon binding to its ligands PD-L1/PD-L2, the PD-1/PD-L1/PD-L2 interaction induces an inhibitory signal in the early stages of T-cell activation; cytokine production is reduced and the cell is arrested in the G0/G1 phase (Freeman et al., 2000).

B7-H3 and B7-H4 are molecules inducible in hematopoietic and immune cells. Their putative receptors in humans are still unidentified. These two molecules have a stimulatory and an inhibitory effect on cell growth, cytokine secretion, and differentiation. The BTLA-HVEM interaction has an inhibitory effect on B- and T-cells (Watanabe et al., 2003; Yi & Chen, 2009).

Inducible T-cell Co-stimulator (ICOS) (also known as AILIM, H4, and CD278) was firstly discovered in activated human T-cells over 20 years ago. It is part of the CD28/B7 superfamily of co-stimulatory molecules. The ICOS/ICOSL interaction provides a stimulatory signal for T-cell activation (Solinas, Gu-Trantien, & Willard-Gallo, 2020). Unlike CD28 which is constitutively expressed by T-cells, ICOS expression is induced in TCR/CD28-activated T-cells and persists in effector and memory T-cells. Even though ICOS shares a structural homology with CD28 and CTLA-4, ICOS lacks a homology domain required for the binding of

B7.1 and B7.2, namely the MYPPPY motif (Greenwald et al., 2005). Another difference with CD28 is the ICOS YMFM motif, which does not permit the adherence to Grb2. The absence of this interaction results in the lack of IL-2 production (Parry, Rumbley, Vandenberghe, June, & Riley, 2003). However, ICOS/ICOSL interaction contributes to the production of IL-10 which may play a role in T-cell tolerance, Treg regulation, and breakdown of immune tolerance to self. CTLA-4 engagement can also inhibit the ICOS/ICOSL signal in addition to inhibiting CD28/B7.1/B7.2 pathway (Riley et al., 2001).

Both ICOS and ICOSL (also known as B7h, B7RP-1, and CD275) are present in lymphoid tissues (Table). However, ICOSL is detected in non-lymphoid tissues where it is constitutively expressed by APCs such as macrophages, B-cells, and dendritic cells (Yoshinaga et al., 1999). Somatic cells in organs such as the liver, kidneys, lungs, peritoneum, and testes express ICOSL. It can also be induced in fibroblasts, lung epithelial cells, mesenchymal stem cells, endothelial cells, and tumor cells by TNF-α (Greenwald et al., 2005; Solinas et al., 2020; Swallow, Wallin, & Sha, 1999).

ICOS plays a major role in regulating self-tolerance in several animal model diseases. In experimental allergic encephalomyelitis (EAE) the mouse, blockade of ICOS expression during induction phase exacerbated the disease, whereas the blockade during the effector phase ameliorated the disease (Dong & Nurieva, 2003; Rottman et al., 2001). In the NOD mouse, ICOS plays a crucial role in the development of diabetes and its absence protects the animal from developing the pathology (Herman, Freeman, Mathis, & Benoist, 2004; Prevot et al., 2010). ICOS deficient animals are resistant to collagen induced arthritis and to a murine asthma model (Nurieva, 2005). The ICOS/ICOSL interaction plays a role in regulating the immune response during an infection. The blockade of ICOS upon an infection with *Listeria monocytogenes* or *S.*

mansoni results in an exacerbated disease whereas ICOS$^{-/-}$ mice infected with *L. major* or *N. brasiliensis* fared better than their infected WT littermates (Mittrücker et al., 2002; Miyahira et al., 2003; Rutitzky, Ozkaynak, Rottman, & Stadecker, 2003). ICOS also has an important role in transplantation and graft rejection. Delayed blocking of ICOS results in donor specific tolerance and long-term survival of a cardiac allograft (Ozkaynak et al., 2001). The combination of cyclosporine A and anti-ICOS mAb ensued in the permanent cardiac graft survival but not in islet allograft survival (Nanji et al., 2004). Taken together, these studies show the importance of timing/stage in the function of ICOS *in vivo*.

ICOS expression		
Naive T cells	no	
Activated T cells	yes, TH2 >TH1 cells, CD8+ T cells	
Memory T cells	yes	
Activated NK cells	yes	
Tissue location of ICOS	human fetal and new-born thymus; thymic medulla and cortico-medullary junction in mice; germinal centres in lymphoid tissues	
ICOS-L expression in lymphoid tissues	expressed on B cells, CD33+ cells in bone marrow, monocytes, DCs and T cells	
Regulation	induced by IFN-γ on B cells, monocytes and DCs; induced by GM-CSF/TNF-α or GM-CSF/IL-3 on CD34+ cells earlier than B7–1/B7–2; not induced by progenitor Ig or CD40 crosslinking on B cells or CD3+ T cells	
ICOS-L expression in nonlymphoid tissues	expressed on a variety of tissues including kidney, liver, peritoneum, lung, testes, embryonic fibroblasts, epithelial cells	
Regulation	induced by TNF-α, LPS and IFN-γ on fibroblasts, epithelial cells and other nonlymphoid tissues	
ICOS-L expression in leukemia and lymphoma		
Acute myeloid leukemia	CD13+/CD33+	0%
B cell lymphoblastic leukemia	CD19+	0%
Chronic lymphocytic leukemia	CD19+	20%
B cell prolymphocytic leukemia	CD19+	40%
Hairy cell leukemia	CD19+	66%
Folicular lymphoma	CD19+	0%

Table 3: ICOS and ICOSL expression. ICOS and ICOSL are both expressed in lymphoid tissues, however ICOSL can be found in in non-lymphoid tissues.(Richter & Burdach, 2004)

5. Aim of the Project

The NOD ICOS KO and NOD ICOSL KO mice were generated in our lab over 15 years ago in order to study the effect of the abrogation of these molecules on diabetes development. The discovery of the spontaneous autoimmune neuropathy that developed in these mice was a serendipitous event (Prevot et al., 2010). The immune aspect of the disease has been well characterized since then and data from our lab has shown that there is a dysregulation in the Regulatory T-cell (Treg) population compared to the Effector T-cells (Teff) and that the neuropathy is CD4+ and interferon-γ dependent. The blocking of class II major histocompatibility complex transactivator (CIITA) in NOD ICOSL KO mice hindered the development of autoimmune neuritis however neuropathy still ensued in NOD ICOSL KO β2-microglobulin KO mice. Transfer experiments were successful in NOD SCID recipients that have received CD4+ T-cell but not CD8+ T-cell from neuropathic NOD ICOSL KO donors (Briet et al., 2017). However, a thorough neurological assessment was still missing along with a histological characterization of nerve lesion. Different aims were therefore established:

- Perform behavioral, electrophysiological, and histological analyses of NOD WT, NOD ICOS-/-, NOD ICOSL-/- as well as in the control strains; C57BL/6J (WT and ICOS-/-) and NOD SCID (WT and ICOSL-/-).
- Study the expression of ICOS/ICOSL in the PNS at different timepoints and localize which cell types express these molecules
- Perform a RNA Seq analysis to look at the differences in gene expression in the nerves of pre-diabetic NOD WT and pre-neuropathic NOD ICOS-/- animals in order to have a better understanding of changes occurring in the nerves prior to the onset of neuropathy.

Moreover, we would to like to verify if the fold changes observed in certain genes are linked to a form of neuropathy seen in humans (ongoing experiment)

The obtained results will be shown in the form of an article in the following chapter.

CHAPTER II: METHODS OPTIMIZATION FOR THE PNS

In addition to the materials and methods mentioned in the article, methodological improvements have been made throughout my thesis to refine and optimize techniques previously used in the lab.

1. Retracing Schwann cell developmental transitions in embryonic dissociated DRG cocultures

The first methodological improvement was performed to obtain primary Schwann cells from embryonic dissociated DRG cultures and to understand the developmental transitions of Schwann cells in a coculture system. The primary Schwann cells were plated for one week, and RTqPCR experiments were performed to study the expression profiles of Schwann cell developmental genes. A comparison was then performed between our data and the expression profiles of developmental genes in developing spinal nerves studied in various high throughput and lineage tracing studies. We were able to pinpoint the transition from Schwann Cell Precursors to immature Schwann cells between the 5^{th} and 7^{th} day *in vitro* which has never been estimated in a culture system. The technique elaborated in this article will help in understanding, designing, and performing coculture experiments.

In the context of my thesis, the method described in this article was used to study the expression of ICOS and ICOSL across the different developmental stages of Schwann cells.

bioRxiv preprint doi: https://doi.org/10.1101/2020.07.31.231258. this version posted July 31, 2020. The copyright holder for this preprint (which was not certified by peer review) is the author/funder. It is made available under a CC-BY-NC-ND 4.0 International license.

Retracing Schwann cell developmental transitions in embryonic dissociated DRG cultures

Venkat Krishnan Sundaram[1*], Rasha Barakat[1,2], Charbel Massaad[1], Julien Grenier[1*]

1. Université de Paris, INSERM UMR 1124, Faculty of Basic and Biomedical Sciences, Paris, France.

2. Université de Paris, INSERM UMR 1016, Institut Cochin, Paris, France.

***Correspondance :**

Venkat Krishnan SUNDARAM
venkatkrishnan.sundaram@parisdescartes.fr
https://orcid.org/0000-0001-6024-6959

Julien GRENIER
julien.grenier@parisdescartes.fr
https://orcid.org/0000-0002-1897-1329

bioRxiv preprint doi: https://doi.org/10.1101/2020.07.31.231258. this version posted July 31, 2020. The copyright holder for this preprint (which was not certified by peer review) is the author/funder. It is made available under a CC-BY-NC-ND 4.0 International license.

Author Contributions:

CM, JG and VKS designed the study. VKS and RB performed the experiments. VKS analyzed the results and wrote the manuscript. CM validated the methodology. JG prepared the figures. All authors reviewed and edited the manuscript. JG and VKS prepared the final draft for submission.

Acknowledgements:

The authors thank Maja Adamsen and Claire Mader from the *Animal House Core Facility* of BioMedTech (INSERM US36/CNRS UMS2009) for the handling of mice used in the study. We also thank the *Cyto2BM Molecular Biology Platform* of BioMedTech Facilities for the research equipment and other services pertaining to the generation of qPCR data.

Funding:

No specific funding was sought for this study. VKS is funded by a PhD fellowship from the French Ministry of Research and Innovation and Université de Paris. RB is funded by a doctoral contract from INSERM U1016, Institut Cochin, Paris.

Conflict of interest:

The authors declare that there is no conflict of interest.

bioRxiv preprint doi: https://doi.org/10.1101/2020.07.31.231258. this version posted July 31, 2020. The copyright holder for this preprint (which was not certified by peer review) is the author/funder. It is made available under a CC-BY-NC-ND 4.0 International license.

Abstract:

Embryonic Dissociated Dorsal Root Ganglia cultures are often used to investigate the role of novel molecular pathways or drugs in Schwann cell development and myelination. These cultures largely recapitulate the order of cellular and molecular events that occur in Schwann cells of embryonic nerves. However, the timing of Schwann cell developmental transitions, notably the transition from Schwann Cell Precursors to immature Schwann cells, has not been estimated so far in this culture system. In this study, we use RTqPCR to determine the expression profiles of Schwann cell developmental genes during the first week of culture. We first identified stable reference genes that show minimal variation across different experimental time points. Consequently, we normalized the mRNA profiles of Schwann cell developmental genes using the best internal reference genes. We then compared our data to the expression profiles of these genes in developing spinal nerves elaborated in numerous high-throughput and lineage tracing studies. This comparison helped in identifying that Schwann Cell Precursors transition into immature Schwann Cells between the 5th and 7th day *in vitro*. In effect, our data allows for a better understanding and interpretation of DRG culture experiments especially in studies that aim to elucidate the role of a novel gene in Schwann Cell development and myelination.

Keywords: Dissociated DRG cultures, Schwann Cell Precursors, immature Schwann Cells, Development, RTqPCR

bioRxiv preprint doi: https://doi.org/10.1101/2020.07.31.231258. this version posted July 31, 2020. The copyright holder for this preprint (which was not certified by peer review) is the author/funder. It is made available under a CC-BY-NC-ND 4.0 International license.

Introduction:

Dissociated Dorsal Root Ganglia (DRG) cultures from mouse embryos have long been utilized as a resourceful model for exploring the nuances of Schwann cell development *in vitro* (Taveggia and Bolino, 2018). The co-culture system provides a solid experimental framework to study different aspects of Schwann cell development such as proliferation, migration, differentiation and myelination of neurites (Päiväläinen et al., 2008; Taveggia and Bolino, 2018). Furthermore, it holistically recapitulates the different aspects of Schwann cell development that is observed *in vivo*. Hence, dissociated DRG cultures form an indispensable part of studies that aim to understand the role of a novel gene in Schwann cell development and differentiation.

It is well known that temporal differences exist between Schwann cell development in Dissociated DRG cultures and in developing spinal nerves. In developing spinal nerves of mice, Neural Crest Cells (NCC), destined to a glial fate, differentiate into Schwann Cell Precursors (SCP) and appear in the DRGs at around E11 (Jacob, 2015). Then, SCPs start migrating on nascent axons between E12.5 and E13.5 to populate their peripheral targets. However, at around E15.5 in mice, SCP transition into immature Schwann cells (iSC) that further differentiate into myelinating and non-myelinating Schwann cells perinatally (Monk et al., 2015; Fledrich et al., 2019; Jessen and Mirsky, 2019).

Nevertheless, these observations cannot be used to extrapolate the timing of Schwann cell developmental transitions *in vitro* because of certain technical reasons. Firstly, the DRGs are dissected from mouse embryos towards the end of the 2nd week of gestation (E12.5 or E13.5). At this stage, SCP *in vivo* have started departing from the DRGs and begun migrating on developing axons (Jessen et al., 1994; Jessen and Mirsky, 2005). However, once dissected and dissociated, the DRG cells give rise to sensory neurons and Schwann cell precursors once again *in vitro* (Ratner et al., 2005; Kim and Maurel, 2009; Kim and Kim, 2018). This is rendered possible because of a reservoir of Neural Crest Cells located inside the DRGs that re-differentiate and populate the culture. Therefore, a significant portion of *in vivo* development is repeated in cell culture albeit with a phase difference. Our objective in this study was to better understand these temporal differences in cocultures in an effort to provide a better experimental and inferential framework.

In this research report, we have used RTqPCR to delineate the expression profiles of developmental genes that are expressed in SCP and iSC (*Dhh, Mpz, Cnp, Plp, Mbp, Krox20, Cad19 and Tfap2α*). Their expression pattern was determined in dissociated DRG cultures during the first 7 Days *in vitro* (DIV) at regular intervals of 48 hours. In order to produce robust and reproducible qPCR data, we first sought to identify stable reference genes from 10 candidates (*Actb*, *Gapdh*, *Tbp*, *Sdha*, *Pgk1*, *Ppia*, *Rpl13a*, *Hsp60*, *Mrpl10*, *Rps26*) using a data analysis workflow that we developed recently (Sundaram et al., 2019). This step is crucial as the cell culture environment is dynamic with different cell populations undergoing proliferation and differentiation simultaneously. Hence, arbitrary choice of reference genes without assessing their stability could possibly render biased expression profiles.

We next determined the expression profile of the developmental genes and compared them to their profiles *in vivo*. Previous high-though put studies in Neural Crest Cells and their derivatives in the Peripheral Nervous System have generated extensive data on the differential expression of genes during Schwann Cell development (Buchstaller et al., 2004; D'Antonio et al., 2006). Additionally, we also compared our data to numerous lineage tracing and gene expression studies performed in developing spinal nerves. This analysis helped us in determining the time window where SCP transition into iSC in Dissociated DRG cultures. Indeed, understanding the developmental transitions of Schwann cells in cocultures is crucial for designing rigorous cell culture experiments on Schwann cell development and *in vitro* myelination assays using different Schwann cell mutants.

bioRxiv preprint doi: https://doi.org/10.1101/2020.07.31.231258. this version posted July 31, 2020. The copyright holder for this preprint (which was not certified by peer review) is the author/funder. It is made available under a CC-BY-NC-ND 4.0 International license.

Materials and methods:

Animals and Tissue Harvesting

Timed pregnant C57Bl6/J mouse at E13.5 was purchased from Janvier Labs. The pregnant mouse was first anesthetized with isoflurane and sacrificed using cervical dislocation. A total of 5 embryos were surgically removed and placed in ice-cold L-15 media. DRGs were harvested from these embryos based on existing protocols (Kim and Kim, 2018; Taveggia and Bolino, 2018). All aspects of animal care and animal experimentation were performed in accordance with the relevant guidelines and regulations of INSERM and Université de Paris (authorization APAFIS#7405-2016092216181520).

Dissociated DRG cultures

A total of 40 DRGs were harvested from each embryo. DRGs were then trypsinized (0.25% Trypsin in HBSS1X) for 30min at 37°C. Trypsinization was stopped using L-15 media containing 10% Horse Serum (Gibco). DRGs were then spun down at 1500 rpm for 5min. The supernatant was removed, and the tissues were resuspended in DRG plating medium (refer to *Media Compositions*). The tissues were then triturated 10-20 times using flamed Pasteur pipettes until a homogenous cell suspension was obtained. Dissociated DRGs were then plated on 12 well plates for each time point –DIV1 (Days *In Vitro* 1*)*, DIV3, DIV5, DIV7. 40 DRGs from each embryo were plated into 8 wells at approximately 5 dissociated DRGs per well. 2 wells were assigned to each time point. The cells were first plated with DRG plating medium for 16h. The following day the medium was replaced by N2/NGF serum free medium to promote neurite growth and Schwann cell proliferation.

Media Compositions

DRG plating media: DMEM with 4.5g/L glucose (Gibco), 10% heat inactivated Horse Serum (Gibco), 1X Glutamax (Gibco), 1X Antibiotic/Antimycotic (Gibco) and 50ng/µL Nerve Growth Factor 2.5S (R&D Systems)

N2/NGF serum free media: DMEM:F12 (Gibco), 1X N2 supplement (Gibco), 1X Glutamax (Gibco), 1X Antibiotic/Antimycotic (Gibco) and 50ng/µL Nerve Growth Factor 2.5S (R&D Systems)

Total RNA isolation

Total RNA was extracted from each sample using 1mL of TRIzol reagent (Ambion Life Technologies 15596018) on ice as described in the manufacturer's instructions with slight modifications. Briefly, 100% Ethanol was substituted for Isopropanol to reduce the precipitation of salts. Also, RNA precipitation was carried out overnight at -20°C in the presence of glycogen. The following day, precipitated RNA was pelleted by centrifugation and washed at least 3 times with 70% Ethanol to eliminate any residual contamination. Tubes were then spin dried in vacuum for 5 minutes and RNA was resuspended in 20µL of RNase resuspension buffer containing 0.1mM EDTA, pH 8. RNA was then stored at -80°C till RTqPCR.

RNA quality, integrity and assay

RNA quantity was assayed using UV spectrophotometry on Nanodrop One (Thermo Scientific). Optical density absorption ratios A260/A280 & A260/A230 of the samples were above 1.8 and 1.5, respectively. The yield (mean ± SD) for each time point is as follows: DIV1 (26.74 ± 2.57 ng/µL), DIV3 (61.3 ± 8.01 ng/µL), DIV5 (51.86 ± 10.8 ng/µL), and DIV7 (77.34 ± 24.04 ng/µL). Furthermore, the extraction protocol used in the study was also validated using Agilent Bioanalyzer (RIN value 9.0 and above).

RTqPCR

bioRxiv preprint doi: https://doi.org/10.1101/2020.07.31.231258. this version posted July 31, 2020. The copyright holder for this preprint (which was not certified by peer review) is the author/funder. It is made available under a CC-BY-NC-ND 4.0 International license.

500ng of Total RNA was reverse transcribed with Random Primers (Promega C1181) and MMLV Reverse Transcriptase (Sigma M1302) according to prescribed protocols. Quantitative Real time PCR (qPCR) was performed using Absolute SYBR ROX 2X qPCR mix (Thermo AB1162B) as a fluorescent detection dye. All reactions were carried out in a final volume of 7µl in 384 well plates with 300 nM gene specific primers, around 3.5ng of cDNA (at 100% RT efficiency) and 1X SYBR Master Mix in each well. Each reaction was performed in triplicates. All qPCR experiments were performed on BioRad CFX384 with a No-Template-Control (NTC) to check for primer dimers and a No-RT-Control (NRT) to check for any genomic DNA contamination.

Primer design

All primers used in the study were designed using the Primer 3 plus software (https://primer3plus.com/cgi-bin/dev/primer3plus.cgi). Splice variants and the protein coding sequence of the genes were identified using the Ensembl database (www.ensembl.org). Constitutively expressed exons among all splice variants were then identified using the ExonMine database (https://imm.medicina.ulisboa.pt/group/exonmine/ack.html) (Mollet et al., 2010) Primer sequences that generated amplicons spanning two constitutively expressed exons were then designed using the Primer 3 plus software. For detailed information on Primer sequences used in the study, refer to the supplementary table S3.

Amplification efficiencies

The amplification efficiencies of primers were calculated using serial dilution of cDNA molecules. Briefly, cDNA preparations from all the time points were pooled and serially diluted three times by a factor of 10. qPCR was then performed using these dilutions and the results were plotted as a standard curve against the respective concentrations of cDNA. Amplification efficiency (E) was calculated by linear regression of standard curves using the following equation:

$$E=10^{(1/\text{slope of the standard curve})}$$

Primer pairs that exhibited a theoretical Amplification Efficiency (E) of 1.9 to 2.1 (95% - 105%) and an R^2 value (Determination Coefficient) of 0.98 and above were chosen for this study.

Statistical analysis and Data Visualization

qPCR readouts were analyzed in Precision Melt Analysis Software v1.2. The amplicons were subjected to Melt Curve analysis and were verified for a single dissociation peak at a Melting Temperature (T_m) > 75°C as expected from the primer constructs. The Cq data was exported to Microsoft Excel for further calculations. Each biological sample had 3 technical replicates thereby generating 3 individual Cq values. The arithmetic mean of the triplicates was taken to be the Cq representing the biological sample. The standard deviation (SD) of the triplicates was also calculated and samples that exhibited SD>0.20 were considered inconsistent. In such cases, one outlier Cq was removed to have at least duplicate Cq values for each biological sample and an SD<0.20.

Statistical analyses for reference gene validation were performed according to our qPCR data analysis workflow (Sundaram et al., 2019). Briefly, 10 conventional reference genes were chosen for the study. The Cq values of these genes were first linearized and the Coefficient of variation (CV) for each gene was calculated (Supplementary Table S1). As all the genes exhibited CV < 50%, they were subsequently screened through the NormFinder algorithm in R (https://moma.dk) (Andersen et al., 2004). The algorithm predicted *Tbp* and *Ppia* to be the most stable references. The normalization factor was then determined as the mean Cq value of *Tbp* and *Ppia* for each sample (Supplementary Table S2). Relative expression of target genes was quantified using the $2^{-\Delta\Delta Ct}$ method (Livak and Schmittgen,

bioRxiv preprint doi: https://doi.org/10.1101/2020.07.31.231258. this version posted July 31, 2020. The copyright holder for this preprint (which was not certified by peer review) is the author/funder. It is made available under a CC-BY-NC-ND 4.0 International license.

186 2001; Schmittgen and Livak, 2008). DIV1 group was used as the experimental calibrator and data was
187 visualized using Graph Pad Prism v7.0.

188 To assess statistical difference in relative RNA quantities between groups, One-way ANOVA was
189 performed in Graph Pad Prism v7.0. If statistical significance was observed between the means of the
190 groups, Tukey's post hoc was performed to compare all the 4 groups with each other. The alpha value
191 threshold was set at 5% and the P-values are represented as follows: $P<0.05$ - *, $P<0.01$ - **, $P<0.001$
192 - ***.

bioRxiv preprint doi: https://doi.org/10.1101/2020.07.31.231258. this version posted July 31, 2020. The copyright holder for this preprint (which was not certified by peer review) is the author/funder. It is made available under a CC-BY-NC-ND 4.0 International license.

Results:

Progression of dissociated DRG cultures:

We first documented the progression of the culture at Days *in Vitro* (DIV) 1, DIV3, DIV5 and DIV7 using phase-contrast microscopy. At DIV 1, we observed a very sparse population of dissociated cells that comprised of precursors to neurons, Schwann cells and fibroblasts (Figure 1A). At DIV3, however, we could see a neurite network gradually being formed with small bead-shaped cells located on top of neuronal extensions. These cells are presumably migratory Schwann cell precursors (Figure 1B). The neurites then grew out and established a well-connected network by DIV5 (Figure 1C). Schwann cells now densely populated neurites. Flattened Fibroblast like cells were also observed below the Neurite-Schwann cell network. Not much difference was observed between DIV5 and DIV7 except that more connections were established in the neurite-Schwann cell network (Figure 1D). From these observations, we could only deduce that Schwann cell precursors appear between DIV1 and DIV3. The transition of SCP to iSC could not be established, as we did not observe any significant morphological changes in the cells attached to the developing neurites as observed *in vivo* (Jessen and Mirsky, 2019).

Determination of stable reference genes for normalization:

As a prerequisite to determine the expression profiles of Schwann cell developmental genes using RTqPCR, we first identified suitable reference genes for our experimental setting. We chose 10 candidate reference genes and used our data analysis workflow (Sundaram et al., 2019) to determine the two most stable reference genes across all the time points under consideration.

Briefly, we first calculated the Co-efficient of Variation (CV) of the linearized Cq values of reference genes. All reference genes exhibited CV values lesser than 50% (Table 1 and Supplementary Table S1) indicating that they can all be screened by the NormFinder algorithm without compromising its robustness (Sundaram et al., 2019). Consequently, the Normfinder algorithm predicted *Tbp* and *Ppia* as the most stable reference genes with an S value of 0.16 followed by others with higher S values indicating lower stability (Table 1). The algorithm also determines the best combination of two genes for more accurate normalization. In this regard, the algorithm predicted the combination of *Tbp* and *Ppia* as the best with a grouped S value of 0.11 (Table 1).

Expression profiles of Schwann cell developmental genes:

We then determined the expression profiles our target genes using *Tbp* and *Ppia* as internal references (Figure 2). All target genes tested showed considerable variation across the time points when analyzed with one-way ANOVA (Figure 2A – 2H) To determine differences among groups, we performed Tukey's Post Hoc test.

Dhh showed a stark 14-fold increase between DIV1 and DIV3 (Figure 2A). Although the profile seemed to project a downward trajectory after DIV3, the levels of *Dhh* did not vary significantly between DIV3 and DIV7. *Mpz* displayed an initial spike between DIV 1 and DIV3 by about 12 folds, which was similar to *Dhh*. However, the quantity of *Mpz* gradually increased and reached about 17 folds at DIV7.

Cnp expression increased by about 7-folds between DIV1 and DIV3 and maintained a stable profile till DIV7 (Figure 2C). *Plp* showed an initial peak at DIV3 by about 7-folds, which was comparable to that of *Cnp*. However, *Plp* expressed momentarily dropped at DIV5 and reached a plateau by DIV7 (Figure 2D).

Mbp displayed a modest but statistically significant increase by 2-folds between DIV1 and DIV3 (Figure 2E). However, the expression did not increase significantly beyond DIV3. *Krox20* expression did not

bioRxiv preprint doi: https://doi.org/10.1101/2020.07.31.231258. this version posted July 31, 2020. The copyright holder for this preprint (which was not certified by peer review) is the author/funder. It is made available under a CC-BY-NC-ND 4.0 International license.

vary significantly between DIV1 to DIV5 (Figure 2F). However, at DIV7 we observed a sudden spike by about 4-folds.

Cad19 expression increased almost linearly between DIV1 and DIV5 (Figure 2G). However, between DIV5 and DIV7, we observe a drop in its expression level. *Tfap2α* maintains a flat profile from DIV1 and DIV3 (Figure 2H). It begins to decline after DIV3 and drops significantly to about 0.5 folds at DIV7.

Comparison of *in vitro* and *in vivo* expression profiles:

We then compared the *in vitro* expression profiles with the profiles of the genes assessed from previous gene profiling studies on the Schwann cell lineage (Buchstaller et al., 2004; D'Antonio et al., 2006). We also consulted seminal reviews on Schwann cell developmental markers (Jessen et al., 1994; Jessen and Mirsky, 2005; Woodhoo and Sommer, 2008; Monk et al., 2015) and other gene-specific expression profiling studies to gain a holistic understanding of the literature. A summary of the current consensus on the expression profiles of these genes *in vivo* along with the relevant literature is presented in Figure 3.

The expression of *Dhh, Mpz and Mbp* is upregulated in SCP at around E12.5 in mice (Jessen and Mirsky, 2005; Woodhoo and Sommer, 2008). In DRG cultures, *Dhh*, *Mpz* and *Mbp* expression is increased at DIV3, confirming our observation that SCP appears between DIV1 and DIV3 (Figure 2A and 2B). Interestingly, the profile of *Dhh* after DIV3 shows some minor differences with its expression *in vivo*. In developing nerves, *Dhh* expression is upregulated during the SCP/iSC transition where it reaches a plateau (Parmantier et al., 1999; Buchstaller et al., 2004; Sharghi-Namini et al., 2006). In culture, the expression seemed to decrease progressively as cells progress from DIV3 to DIV7, albeit the differences are not statistically significant (Figure 2A). On the contrary, *Mpz* expression between DIV3 and DIV7 complies perfectly with *in vivo* data (Blanchard et al., 1996; Lee et al., 1997; Buchstaller et al., 2004). *Mpz* expression increases gradually between DIV3 and DIV7 (Figure 2B).

The profile of *Mbp* concurs with its profile *in vivo* with minor differences. In embryonic nerves, *Mbp* expression is detected primarily in SCP at around E12.5 and keeps increasing till E18.5 (Paratore et al., 2002; Buchstaller et al., 2004). In DRG culture at DIV3, *Mbp* expression is increased and reached a plateau at DIV5 (Figure 2E).

Plp is expressed in migrating neural crest cells and Schwann cell Precursors (Timsit et al., 1992; Buchstaller et al., 2004). In developing nerves, *Plp* expression increases in schwann cells between E12.5 and E18.5. (Buchstaller et al., 2004). In DRG cultures, increase in *Plp* expression at DIV3 concurs with *in vivo* data. However, a momentary but significant drop of *Plp* expression is observed between DIV3 and DIV5 but it marginally increases again at DIV7 (Figure 2D).

Data on *Cnp* expression in SCP of embryonic nerves is inconclusive. We analyzed three separate studies that sought to trace *Cnp* expression in the PNS (Gravel et al., 1998; Yuan et al., 2002; Deng et al., 2014). One study demonstrated that *Cnp* is expressed in the satellite cells of DRGs at E14.5 and at the ventral roots at E17.5 but did not comment on its expression in SCPs (Deng et al., 2014). The other two studies dealt with post-natal time points. Nonetheless, our observations suggest that *Cnp* mRNA is expressed in SCP at DIV3 in culture. This observation, however, needs to be verified *in vivo*.

Krox20 is expressed at two different time points during the development of the PNS (Topilko et al., 1994; Voiculescu et al., 2000; Coulpier et al., 2010). At around E10.5, it is first expressed in the boundary cap cells that are located at the dorsal and ventral roots. This is followed by its expression as SCP transition into iSC at around E15.5. It is one of the genes used in the study that can categorically distinguish between SCP and iSC. In our study, Krox20 expression does not change significantly between DIV1 and DIV5. We then see a sudden spike in its expression between DIV5 and DIV7 suggesting that SCP transition to iSC in this time-period (Figure 2F).

bioRxiv preprint doi: https://doi.org/10.1101/2020.07.31.231258. this version posted July 31, 2020. The copyright holder for this preprint (which was not certified by peer review) is the author/funder. It is made available under a CC-BY-NC-ND 4.0 International license.

283 To test this hypothesis, we further looked at the expression profile of *Tfap2α*, which is expressed in
284 NCC and SCP but not in iSC (Stewart et al., 2001)(Figure 2H). The downregulation of this transcription
285 factor is indeed required for SCP to transition into iSC in developing nerves (Stewart et al., 2001;
286 Jacob, 2015). Consistent with this observation, *Tfap2α* levels drop by 50% between DIV5 and DIV7
287 thus providing further evidence of the SCP/iSC transition between DIV5 and DIV7. Moreover, we also
288 assayed the expression levels of *Cad19*, which is the only known gene that is uniquely expressed in
289 SCP but not in NCC or iSC (Jessen and Mirsky, 2005, 2019; Takahashi and Osumi, 2005). *Cad19*
290 expression *in vitro* was the highest around DIV3 and DIV5 but it reduced again at DIV7 reaching to
291 levels comparable to DIV3.

292 Taken together, these results give a clear picture of Schwann cell developmental transitions *in vitro*.
293 We thus conclude that SCP appear between DIV1 and DIV3. Between DIV3 and DIV5, SCP proliferate
294 and migrate on nascent neurites. At DIV5, SCP begin their transition into iSC and at DIV7 most of the
295 cells present on neurites are iSC.

bioRxiv preprint doi: https://doi.org/10.1101/2020.07.31.231258. this version posted July 31, 2020. The copyright holder for this preprint (which was not certified by peer review) is the author/funder. It is made available under a CC-BY-NC-ND 4.0 International license.

Discussion:

The objective of this study was to determine the SCP/iSC transition in DRG-SC cocultures using the mRNA expression profiles of Schwann cell developmental genes (*Dhh, Mpz, Cnp, Plp, Mbp, Krox20, Cad19, Tfap2α*). We first identified stable reference genes to normalize the expression of the target genes and determine their profiles. In this study, we have determined *Ppia* and *Tbp* to be the best combination of references genes to normalize qPCR data in dissociated DRG cultures before the induction of myelination. From the normalized profiles of developmental genes, we sought to estimate the time window where SCP transition to iSC in this culture system.

Our data seem to largely comply and concur with the order of molecular events observed in embryonic spinal nerves. However, we pinpoint certain differences in genes such as *Dhh* and *Plp*. We believe that such differences exist due to innate differences between DRG cultures and developing nerves. For instance, SCP which transition into iSC at around E15.5 further differentiate into promyelinating and Remak Schwann cells after radially sorting large caliber axons from smaller ones gradually between E18.5 and P10 (Jessen and Mirsky, 2005; Monk et al., 2015; Fledrich et al., 2019). This is accompanied by an intrinsic change in the expression of Schwann cell developmental genes. *Dhh*, for example, is not expressed in Remak Schwann cells but its expression is maintained in myelinating Schwann cells postnatally (Sharghi-Namini et al., 2006). Similarly, the expression of *Plp* and other myelin related genes such as *Mbp* and *Mpz* is further upregulated in myelinating Schwann cells but not in remak cells (Jessen and Mirsky, 2005; Woodhoo and Sommer, 2008; Salzer, 2015). This is primarily because *Krox20* drives the expression of myelin genes in myelinating cells and its expression in Remak cells in downregulated (Svaren and Meijer, 2008; Woodhoo et al., 2009). Hence, our data on DRG-SC cocultures can only be compared and contrasted to *in vivo* data up until the appearance of iSC in embryonic nerves between E15.5 to E17.5. Further comparison with *in vivo* data can be possible if we assess the expression of these genes using *in vitro* myelination assays. Myelination in coculture can be induced by the addition of Ascorbic Acid (Päiväläinen et al., 2008). Conventionally, ascorbic acid is added at DIV7, which concurs with the molecular profiles of iSC at DIV7 (highest RNA expression of *Krox20*, *Mpz*, *Mbp* and *Plp* coupled with the downregulation of *Tfap2α* and *Cad19*). Thus, deducing the profiles of these genes in myelination assays can further help in comparing *in vitro* and *in vivo* data beyond the SCP/iSC transition.

A notable limitation of our study is that we performed qPCR assays with total RNA extracted from all the cell types in the coculture system. Although most of our target genes are uniquely expressed in the Schwann cell lineage, certain genes such as *Tfap2α* and *Cad19* are not unique to Schwann cells. *Tfap2α* expression has also been documented in sensory neurons (Donaldson et al., 1995; Schmidt et al., 2011). However, in DRG-SC cocultures, the total number of sensory neurons pales in comparison to Schwann cells largely because neuronal cells do not actively proliferate in culture as opposed to SCP or iSC. Hence, it is safe to conclude that the difference we observed in *Tfap2α* expression at DIV7 is largely contributed by SCP transitioning into iSC. This is also supported by the concomitant increase in *Krox20* levels.

Similarly, *Cad19* mRNA is also detected in satellite glial cells (SGC) attached to the neuronal soma (Takahashi and Osumi, 2005). Interestingly, *Cad19* expression is retained in SGC postnatally but it is turned down in SCP as they transition to iSC in nerves (George et al., 2018). In culture, SGC are present attached to neuronal soma. However, their proportion is very minimal when compared to Schwann cells. This is mostly because their proliferation is intrinsically dependent on neuronal size and numbers (Hanani, 2005; George et al., 2018). Hence, although *Cad19* levels drop significantly between DIV5 and DIV7, it remains detectable in sufficient amounts even a DIV7 as its expression in retained in SGC.

bioRxiv preprint doi: https://doi.org/10.1101/2020.07.31.231258. this version posted July 31, 2020. The copyright holder for this preprint (which was not certified by peer review) is the author/funder. It is made available under a CC-BY-NC-ND 4.0 International license.

342 Nevertheless, despite these minor limitations, our data provides conclusive evidence that the SCP/iSC
343 transition occurs between DIV5 and DIV7. This information serves as a powerful frame of reference to
344 design, execute and comprehend coculture experiments using WT mice or other Schwann cell
345 mutants.

bioRxiv preprint doi: https://doi.org/10.1101/2020.07.31.231258. this version posted July 31, 2020. The copyright holder for this preprint (which was not certified by peer review) is the author/funder. It is made available under a CC-BY-NC-ND 4.0 International license.

Figures and Figure Legends

Figure 1

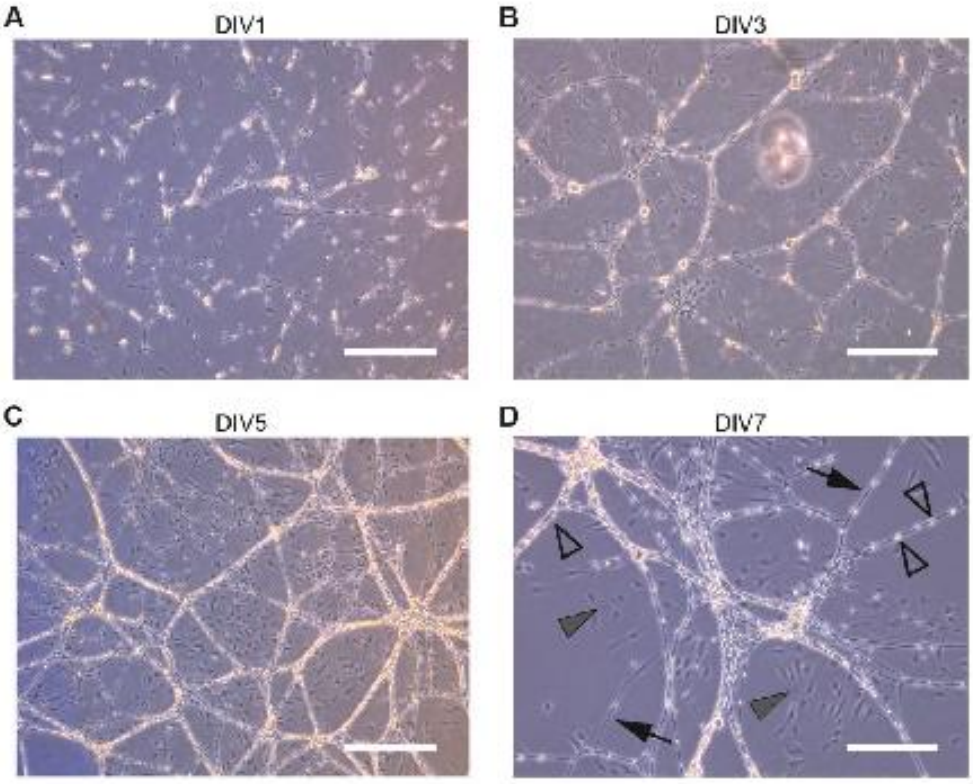


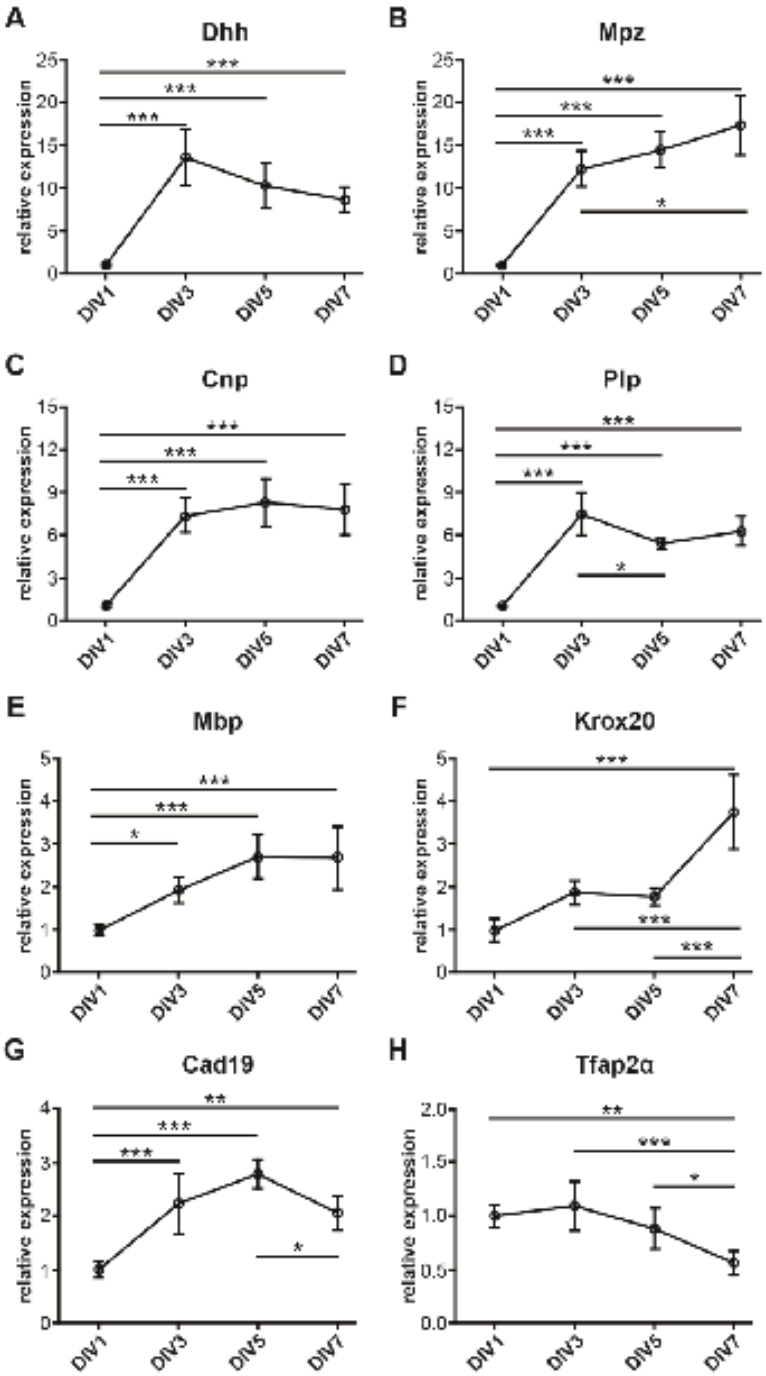
Figure 1: Progression of Dissociated DRG cultures between the first (DIV1) and the seventh (DIV7) day of culture.

Dissociated DRG cells form an extensive network comprised of neurites, Schwann Cells and fibroblasts.

(A) 1 day after plating - DIV1, spindle-shaped neuronal precursors start to form neurite outgrowths. (5X Magnification, Scale Bar = 500µm).
(B) 3 days after plating - DIV3, neurites extend and start to form a mesh like network. Refringent cells attached to the neurites are presumably SCP. Few fibroblasts grow on the bottom of the culture dish beneath the neurite network. (5X Magnification, Scale Bar = 500µm).
(C) 5 days after plating – DIV5, the neurite network is well established and connected. An increase in Schwann cells attached to the neurites is visible when compared to DIV3. Fibroblasts also proliferate in the same time. (5X Magnification, Scale Bar = 500µm).
(D) 7 days after plating – DIV7, the neurite-Schwann cell network now spans the entire dish and all neuronal extensions are covered with Schwann cells. Black arrows indicate neurite extensions. Hollow arrowheads indicate Schwann cells that appear bright under phase contrast. Grey arrowheads indicate flattened fibroblasts that proliferate beneath the network. (10X magnification, Scale Bar = 250µm).

bioRxiv preprint doi: https://doi.org/10.1101/2020.07.31.231258. this version posted July 31, 2020. The copyright holder for this preprint (which was not certified by peer review) is the author/funder. It is made available under a CC-BY-NC-ND 4.0 International license.

370 **Figure 2**



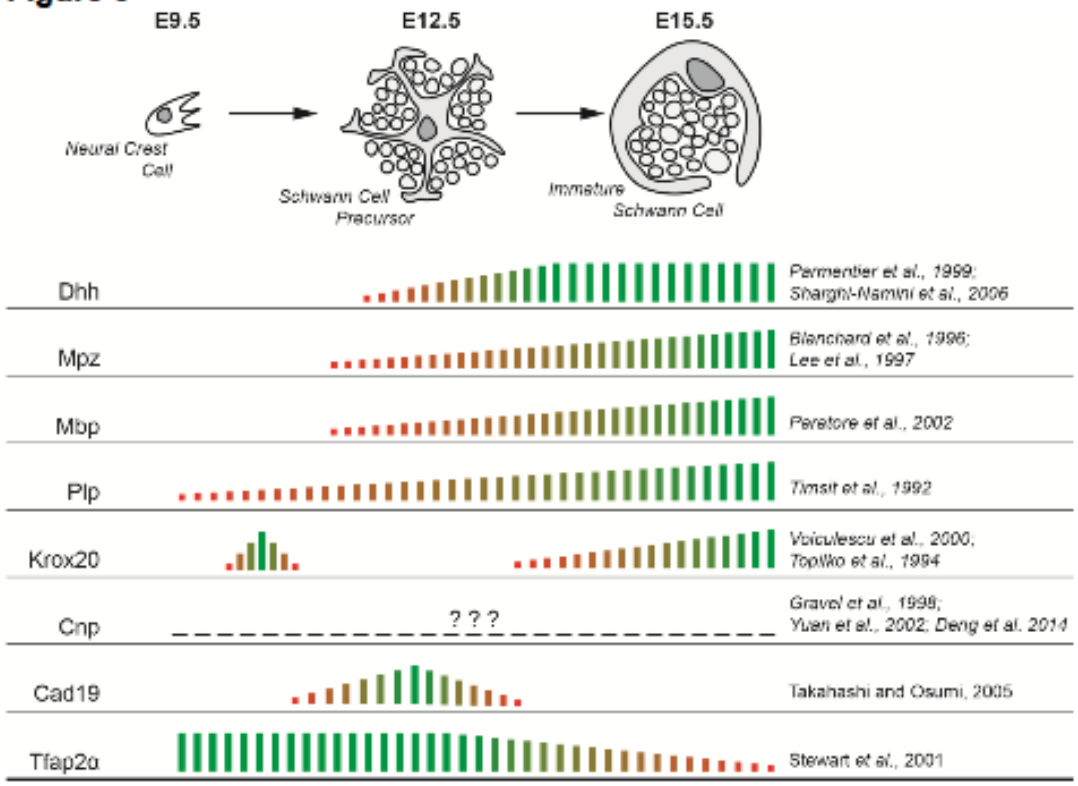
371
372 **Figure 2: Relative expression of Schwann cell developmental genes during the first**
373 **week of culture at regular intervals of 48 hours.**
374
375 Expression profiles of Dhh (A), Mpz (B), Cnp (C), Plp (D), Mbp (E), Krox20 (F), Cad19 (G) and
376 Tfap2α (H) are shown relative to DIV1, which was used as the experimental calibrator.
377 Ppia/Tbp were used as reference genes for normalization. To assess differences across

bioRxiv preprint doi: https://doi.org/10.1101/2020.07.31.231258. this version posted July 31, 2020. The copyright holder for this preprint (which was not certified by peer review) is the author/funder. It is made available under a CC-BY-NC-ND 4.0 International license.

timepoints, one-way ANOVA was performed followed by Tukey's Post Hoc analysis to compare all the 4 groups with each other. The alpha value threshold was set at 5% and the P-values are represented as follows: * for $P<0.05$, ** for $P<0.01$ and *** for $P<0.001$. Statistically significant comparisons are highlighted with horizontal lines spanning the groups under comparison. Group comparisons that are not highlighted with horizontal lines do not exhibit any statistically significant differences.

bioRxiv preprint doi: https://doi.org/10.1101/2020.07.31.231258. this version posted July 31, 2020. The copyright holder for this preprint (which was not certified by peer review) is the author/funder. It is made available under a CC-BY-NC-ND 4.0 International license.

384 **Figure 3**



385
386
387
388

389 **Figure 3: Expression levels of Schwann cell developmental genes in vivo as the**
390 **transition from SCP to iSC.**
391

392 The expression levels are expressed as horizontal bars with increasing height indicating
393 higher expression levels. This representation is based on microarray data (Buchstaller et al.,
394 2004) and other high-throughput data (D'Antonio et al., 2006). Additionally, relevant gene
395 profiling and lineage tracing studies are indicated for each gene. Dhh expression begins at the
396 SCP stage and reaches a plateau at the iSC stage. Mpz and Mbp expression is detected at
397 the SCP slightly before the expression of Dhh. Plp is expressed in migrating neural crest cells
398 that are destined towards a glial fate. Krox20 expression occurs in two distinct waves – the
399 first in Boundary Cap Cells that arise from NCC at around E10. The second wave occurs when
400 SCP transition into iSC at E15.5 in embryonic nerves of mice. Cnp expression in the glial
401 lineage is not well documented barring a couple of studies that have documented its
402 expression in satellite glial cells and ventral spinal roots. Cad19 is the only gene know so far
403 that is uniquely expressed in SCP but not in iSC or NCC. Tfap2α is a transcription factor that is
404 expressed from migrating NCC to SCP stages before being downregulated in iSC.

bioRxiv preprint doi: https://doi.org/10.1101/2020.07.31.231258. this version posted July 31, 2020. The copyright holder for this preprint (which was not certified by peer review) is the author/funder. It is made available under a CC-BY-NC-ND 4.0 International license.

Tables and Table Legends

Table 1

CV analysis	
Gene	CV%
SDHA	23.66
MRPL10	23.89
PPIA	25.53
TBP	25.73
GAPDH	29.12
RPL13A	30.94
PGK1	35.13
HSP60	36.29
RPS26	40.15
ACTB	47.27

NormFinder	
Gene	Stability Value (S)
PPIA	0.16
TBP	0.16
HSP60	0.22
GAPDH	0.24
RPL13A	0.24
MRPL10	0.34
ACTB	0.37
SDHA	0.38
RPS26	0.39
PGK1	0.44

NormFinder- Best pair of genes	
Gene	Stability Value (S)
TBP/PPIA	0.11
HSP60/PPIA	0.14
HSP60/GAPDH	0.15
HSP60/TBP	0.16
GAPDH/TBP	0.18
GAPDH/PPIA	0.18
TBP/RPL13A	0.18
RPL13A/PPIA	0.18
HSP60/RPL13A	0.19
GAPDH/RPL13A	0.22

Table 1: Determination of stable reference genes for qPCR assays on DRG-SC cocultures during the 1st week.

Coefficient of Variation analysis (CV analysis) calculates the overall variation of RNA expression across all samples and time points. It is used to identify genes with high overall variation (CV>50%). Such genes can decrease the performance of the Normfinder algorithm (Sundaram et al., 2019). Normfinder determines the stability of a reference as a weighted measure of its intergroup and intragroup variation (Andersen et al., 2004). The S value calculated by Normfinder ranks the genes from the most to the least stable with the former exhibiting the lowest S value. The method also predicts the best combination of two reference genes that can produce robust qPCR data. In our dataset, Tbp/Ppia combination is found to be the best.

bioRxiv preprint doi: https://doi.org/10.1101/2020.07.31.231258. this version posted July 31, 2020. The copyright holder for this preprint (which was not certified by peer review) is the author/funder. It is made available under a CC-BY-NC-ND 4.0 International license.

References:

Andersen, C., Jensen, J., and Orntoft, T. (2004). Normalization of Real Time Quantitative Reverse Transcription PCR Data : A Model Based Variance Estimation Approach to Identify Genes Suited for Normalization , Applied to Bladder and Colon Cancer Data Sets. *Cancer Res.* 64, 5245. doi:10.1158/0008.

Blanchard, A. D., Sinanan, A., Parmantier, E., Zwart, R., Broos, L., Meijer, D., et al. (1996). Oct-6 (SCIP/Tst-1) is expressed in Schwann cell precursors, embryonic Schwann cells, and postnatal myelinating Schwann cells: comparison with Oct-1, Krox-20, and Pax-3. *J. Neurosci. Res.* 46, 630–40. doi:10.1002/(SICI)1097-4547(19961201)46:5<630::AID-JNR11>3.0.CO;2-0.

Buchstaller, J., Sommer, L., Bodmer, M., Hoffmann, R., Suter, U., and Mantei, N. (2004). Efficient Isolation and Gene Expression Profiling of Small Numbers of Neural Crest Stem Cells and Developing Schwann Cells. *J. Neurosci.* 24, 2357–2365. doi:10.1523/JNEUROSCI.4083-03.2004.

Coulpier, F., Decker, L., Funalot, B., Vallat, J. M., Garcia-Bragado, F., Charnay, P., et al. (2010). CNS/PNS boundary transgression by central glia in the absence of schwann cells or Krox20/Egr2 function. *J. Neurosci.* 30, 5958–5967. doi:10.1523/JNEUROSCI.0017-10.2010.

D'Antonio, M., Michalovich, D., Paterson, M., Droggiti, A., Woodhoo, A., Mirsky, R., et al. (2006). Gene profiling and bioinformatic analysis of Schwann cell embryonic development and myelination. *Glia* 53, 501–515. doi:10.1002/glia.20309.

Donaldson, L. F., McQueen, D. S., and Seckl, J. R. (1995). Induction of transcription factor AP2 mRNA expression in rat primary afferent neurons during acute inflammation. *Neurosci. Lett.* 196, 181–184. doi:10.1016/0304-3940(95)11870-3.

Fledrich, R., Kungl, T., Nave, K. A., and Stassart, R. M. (2019). Axo-glial interdependence in peripheral nerve development. *Development* 146. doi:10.1242/dev.151704.

George, D., Ahrens, P., and Lambert, S. (2018). Satellite glial cells represent a population of developmentally arrested Schwann cells. *Glia* 66, 1496–1506. doi:10.1002/glia.23320.

Hanani, M. (2005). Satellite glial cells in sensory ganglia: From form to function. *Brain Res. Rev.* 48, 457–476. doi:10.1016/j.brainresrev.2004.09.001.

Jacob, C. (2015). Transcriptional control of neural crest specification into peripheral glia. *Glia* 63, 1883–1896. doi:10.1002/glia.22816.

Jessen, K. R., Brennan, A., Morgan, L., Mirsky, R., Kent, A., Hashimoto, Y., et al. (1994). The Schwann cell precursor and its fate: A study of cell death and differentiation during gliogenesis in rat embryonic nerves. *Neuron* 12, 509–527. doi:10.1016/0896-6273(94)90209-7.

Jessen, K. R., and Mirsky, R. (2005). The origin and development of glial cells in peripheral nerves. *Nat Rev Neurosci* 6, 671–682. doi:nrn1746 [pii]\n10.1038/nrn1746.

Jessen, K. R., and Mirsky, R. (2019). Schwann cell precursors; multipotent glial cells in embryonic nerves. *Front. Mol. Neurosci.* 12, 69. doi:10.3389/fnmol.2019.00069.

Kim, H. A., and Maurel, P. (2009). "Primary Schwann Cell Cultures," in (Humana Press), 253–268. doi:10.1007/978-1-60761-292-6_15.

Kim, J., and Kim, H. A. (2018). "Isolation and expansion of Schwann cells from transgenic mouse models," in *Methods in Molecular Biology* (Humana Press Inc.), 39–48. doi:10.1007/978-1-4939-7649-2_3.

Lee, M. J., Brennan, A., Blanchard, A., Zoidl, G., Dong, Z., Tabernero, A., et al. (1997). P0 is constitutively expressed in the rat neural crest and embryonic nerves and is negatively and positively regulated by axons to generate non- myelin-forming and myelin-forming Schwann cells, respectively. *Mol. Cell. Neurosci.* 8, 336–350. doi:10.1006/mcne.1996.0589.

bioRxiv preprint doi: https://doi.org/10.1101/2020.07.31.231258. this version posted July 31, 2020. The copyright holder for this preprint (which was not certified by peer review) is the author/funder. It is made available under a CC-BY-NC-ND 4.0 International license.

468 Livak, K. J., and Schmittgen, T. D. (2001). Analysis of relative gene expression data using real-time
469 quantitative PCR and the 2^-ΔΔCT Method. *Methods* 25, 402–408. doi:10.1006/meth.2001.1262.

470 Mollet, I. G., Ben-Dov, C., Felício-Silva, D., Grosso, A. R., Eleutério, P., Alves, R., et al. (2010).
471 Unconstrained mining of transcript data reveals increased alternative splicing complexity in the
472 human transcriptome. *Nucleic Acids Res.* 38, 4740–4754. doi:10.1093/nar/gkq197.

473 Monk, K. R., Feltri, M. L., and Taveggia, C. (2015). New insights on schwann cell development. *Glia*
474 63, 1376–1393. doi:10.1002/glia.22852.

475 Päiväläinen, S., Nissinen, M., Honkanen, H., Lahti, O., Kangas, S. M., Peltonen, J., et al. (2008).
476 Myelination in mouse dorsal root ganglion/Schwann cell cocultures. *Mol. Cell. Neurosci.* 37, 568–
477 578. doi:10.1016/j.mcn.2007.12.005.

478 Paratore, C., Hagedorn, L., Floris, J., Hari, L., Kléber, M., Suter, U., et al. (2002). Cell-intrinsic and cell-
479 extrinsic cues regulating lineage decisions in multipotent neural crest-derived progenitor cells. *Int.*
480 *J. Dev. Biol.* 46, 193–200. Available at: http://www.ncbi.nlm.nih.gov/pubmed/11902683 [Accessed
481 April 18, 2020].

482 Parmantier, E., Lynn, B., Lawson, D., Turmaine, M., Namini, S. S., Chakrabarti, L., et al. (1999).
483 Schwann cell-derived Desert hedgehog controls the development of peripheral nerve sheaths.
484 *Neuron* 23, 713–24. Available at: http://www.ncbi.nlm.nih.gov/pubmed/10482238 [Accessed July
485 18, 2019].

486 Ratner, N., Williams, J. P., Kordich, J. J., and Kim, H. A. (2005). Schwann Cell Preparation from Single
487 Mouse Embryos: Analyses of Neurofibromin Function in Schwann Cells. *Methods Enzymol.* 407,
488 22–33. doi:10.1016/S0076-6879(05)07003-5.

489 Salzer, J. L. (2015). Schwann cell myelination. *Cold Spring Harb. Perspect. Biol.* 7, 1–26.
490 doi:10.1101/cshperspect.a020529.

491 Schmidt, M., Huber, L., Majdazari, A., Schütz, G., Williams, T., and Rohrer, H. (2011). The transcription
492 factors AP-2β and AP-2α are required for survival of sympathetic progenitors and differentiated
493 sympathetic neurons. *Dev. Biol.* 355, 89–100. doi:10.1016/j.ydbio.2011.04.011.

494 Schmittgen, T. D., and Livak, K. J. (2008). Analyzing real-time PCR data by the comparative C(T)
495 method. *Nat. Protoc.* 3, 1101–8.

496 Sharghi-Namini, S., Turmaine, M., Meier, C., Sahni, V., Umehara, F., Jessen, K. R., et al. (2006). The
497 structural and functional integrity of peripheral nerves depends on the glial-derived signal desert
498 hedgehog. *J. Neurosci.* 26, 6364–76. doi:10.1523/JNEUROSCI.0157-06.2006.

499 Stewart, H. J. S., Brennan, A., Rahman, M., Zoidl, G., Mitchell, P. J., Jessen, K. R., et al. (2001).
500 Developmental regulation and overexpression of the transcription factor AP-2, a potential regulator
501 of the timing of Schwann cell generation. *Eur. J. Neurosci.* 14, 363–372. doi:10.1046/j.0953-
502 816X.2001.01650.x.

503 Sundaram, V. K., Sampathkumar, N. K., Massaad, C., and Grenier, J. (2019). Optimal use of statistical
504 methods to validate reference gene stability in longitudinal studies. *PLoS One* 14, e0219440.
505 doi:10.1371/journal.pone.0219440.

506 Svaren, J., and Meijer, D. (2008). The molecular machinery of myelin gene transcription in schwann
507 cells. *Glia* 56, 1541–1551. doi:10.1002/glia.20767.

508 Takahashi, M., and Osumi, N. (2005). Identification of a novel type II classical cadherin: Rat cadherin19
509 is expressed in the cranial ganglia and Schwann cell precursors during development. *Dev. Dyn.*
510 232, 200–208. doi:10.1002/dvdy.20209.

511 Taveggia, C., and Bolino, A. (2018). "DRG neuron/schwann cells myelinating cocultures," in *Methods in*
512 *Molecular Biology* (Humana Press Inc.), 115–129. doi:10.1007/978-1-4939-7862-5_9.

513 Timsit, S. G., Bally-Cuif, L., Colman, D. R., and Zalc, B. (1992). DM-20 mRNA Is Expressed During the

bioRxiv preprint doi: https://doi.org/10.1101/2020.07.31.231258. this version posted July 31, 2020. The copyright holder for this preprint (which was not certified by peer review) is the author/funder. It is made available under a CC-BY-NC-ND 4.0 International license.

514 Embryonic Development of the Nervous System of the Mouse. *J. Neurochem.* 58, 1172–1175.
515 doi:10.1111/j.1471-4159.1992.tb09378.x.

516 Topilko, P., Schneider-Maunoury, S., Levi, G., Baron-Van Evercooren, A., Chennoufi, A. B. Y.,
517 Seitanidou, T., et al. (1994). Krox-20 controls myelination in the peripheral nervous system. *Nature*
518 371, 796–799. doi:10.1038/371796a0.

519 Voiculescu, O., Charnay, P., and Schneider-Maunoury, S. (2000). Expression pattern of a Krox-20/Cre
520 knock-in allele in the developing hindbrain, bones, and peripheral nervous system. *genesis* 26,
521 123–126. doi:10.1002/(SICI)1526-968X(200002)26:2<123::AID-GENE7>3.0.CO;2-O.

522 Woodhoo, A., Alonso, M. B. D., Droggiti, A., Turmaine, M., D'Antonio, M., Parkinson, D. B., et al.
523 (2009). Notch controls embryonic Schwann cell differentiation, postnatal myelination and adult
524 plasticity. *Nat. Neurosci.* 12, 839–847. doi:10.1038/nn.2323.

525 Woodhoo, A., and Sommer, L. (2008). Development of the Schwann cell lineage: From the neural crest
526 to the myelinated nerve. *Glia* 56, 1481–1490. doi:10.1002/glia.20723.

2. Triz'Old is gold: A reliable and efficient method to extract total RNA from mouse sciatic nerve across all ages

A challenge that is commonly found in the field is the difficulty of extracting good quality RNA from the sciatic nerve of mice at different ages ranging from neonatal to adult. The amount of tissue in neonatal mice is very scarce therefore the researchers had to pool nerves from different animals in order to get a decent yield. Adult mice have more tissue than the neonates but other factors hinder the extraction of RNA. Sciatic nerves from adult mice contain large quantities of lipids from the myelin sheath and collagen from the extracellular matrix. The lipids hamper tissue homogenization and the collagen can entrap nucleic acid thus increasing the difficulty of extracting RNA. In this study we compared different RNA extraction methods; Trizol, Mirvana kit from Ambion, and Acid Phenol Chloroform. Our results showed that RNA extraction using Trizol is the most reliable technique regarding yield and RNA quality throughout different ages.

Triz'Old is gold : A reliable and efficient method to extract total RNA from mouse sciatic nerves across all ages

Venkat Krishnan Sundaram [1]*, Rasha Barakat [1,2], Nirmal Kumar Sampathkumar [1], Julien Grenier [1], Franck Letourneur [2], Laure Weill [1]*

1. INSERM U1124, Faculty of Basic and Biomedical Sciences, Campus Saint Germain Des Prés, Université de Paris, Paris, France
2. INSERM U1016, Institut Cochin, Paris, France

*Corresponding Authors:

Venkat Krishnan Sundaram
venkatkrishnan.sundaram@parisdescartes.fr

Laure Weill
laure.weill@parisdescartes.fr

Submitted for Review

Author Contributions:

VKS and RB designed the study. VKS, NKS, RB and FL performed the experiments. VKS analyzed the results and wrote the manuscript. LW validated the methodology and provided scientific inputs. JG prepared the figures. All authors reviewed and edited the manuscript. LW and VKS prepared the final draft for submission.

Acknowledgements:

We thank Maja Adamsen and Claire Mader from the *Animal House Core Facility* of BioMedTech (INSERM US36/CNRS UMS2009) for the handling of mice used in the study. We also thank the *Cyto2BM Molecular Biology Platform* of BioMedTech Facilities for the research equipment and other services pertaining to the generation of qPCR data. We also thank the Genomic Platform at Institut Cochin, Paris for the quality control of RNA samples. Finally, we thank Dr. Robert Fledrich for his valuable suggestions to standardize tissue harvesting and optimize tissue homogenization.

Funding:

No specific funding was sought for this study. VKS and NKS were funded by a PhD fellowship from the French Ministry of Research and Innovation and Université de Paris. RB was funded by CNRS Lebanon and a doctoral contract from INSERM U1016, Institut Cochin, Paris.

Conflict of interest:

The authors declare that there is no conflict of interest.

Submitted for Review

Abstract:

The sciatic nerve is extensively used in murine models that aim to study Schwann cell development, peripheral myelination, and associated pathologies. Quantifying differential gene expression through RTqPCR and RNA-seq forms an integral part of such studies. However, the extraction of total RNA from sciatic nerves for these applications proves to be difficult and results in inconsistent yields owing to the fact that the tissue in rich in lipids and collagens. Therefore, the primary objective of this study was to devise an RNA extraction protocol that renders sufficient and consistent yield of total RNA across all postnatal ages in mice. We have developed a modified version of the Trizol method that satisfies all the fundamental quality requirements for downstream applications such as RTqPCR and RNA-seq. Furthermore, we compared our protocol to two other methods that have been employed in previous studies. All the methods were subjected to stringent validation criteria such as RNA purity, integrity and yield consistency. The extracted RNA was also subjected to RTqPCR as an additional validation step. Using our data, we highlight the merits and drawbacks of each method along with the potential pitfalls in employing these protocols. Taking these insights into consideration, we exemplify the efficiency of the modified Trizol protocol and the advantages it offers on multiple fronts for downstream applications.

Keywords: RNA extraction, Trizol, Schwann cell, Sciatic Nerve, RTqPCR, RNA-seq

Submitted for Review

Introduction:

Peripheral nerve development and myelination are complex molecular processes that elicit a concerted effort of multiple molecular pathways implicating numerous genes (Woodhoo and Sommer, 2008; Monk et al., 2015). In peripheral neuropathies and demyelinating diseases, the molecular mechanisms and the regulation of associated genes are disrupted, thereby leading to disease progression. Therefore, identifying and quantifying such alterations in gene expression through RTqPCR and RNA-seq forms an integral part of a multitude of studies on peripheral nerves.

The most crucial outcome of RNA extraction is to obtain good quality RNA that is devoid of any chemical contaminants from the extraction process. Furthermore, it is also essential to obtain RNA with high integrity that can then be used for sequencing. The quality of the isolated RNA is quickly assessed by determining the spectrophotometric absorbance of the sample at 230nm, 260nm, 280nm and then calculating the A260/A230 & A260/A280 ratios. Highly pure RNA exhibits values around 1.8 – 2.0 for both these ratios. Lower values of A260/A230 and A260/A280 indicate contamination with guanidine salts and proteins, respectively. These contaminants hamper the quantification of RNA as well as downstream applications such as RTqPCR (Schrader et al., 2012).Therefore, the quality of the isolated RNA is of prime importance especially if amplification or sequencing is envisaged as a downstream application.

The extraction of total RNA from the sciatic nerve is rather unwieldy and it results in poor/inconsistent yields due to a couple of reasons. The cellular anatomy of the nerve reveals two major cell types: Schwann cells that produce the lipid-rich myelin sheath around axons and other fibroblast-like glial cells that produce collagen to maintain the structural integrity of the nerves (Shellswell et al., 1979; Morell and Quarles, 1999; Chen et al., 2015) **(Figure 1)**. Therefore, the tissue, by virtue of its molecular composition, is considered highly fibrous and lipid rich thus presenting with two major hurdles in the isolation of good quality RNA. Lipids hinder tissue disruption and facilitate coprecipitation of contaminants such as phenols and polysaccharides with RNA (Cirera, 2013; Lan et al., 2013). Collagen and proteoglycans, on the other hand, can entrap nucleic acids and thus result in poor yields if RNA is extracted using phase separation (Groppe and Morse, 1993; Wang and Stegemann, 2010). Moreover, in neonates between P0 (Postnatal day 0) and P3, the tissue mass is extremely small and hence it is common practice to pool different biological replicates to obtain copious amounts of RNA. This practice, however, proves to be disadvantageous if the study aims to quantify inherent biological variations of a given population. Therefore, the primary objective of this study was to devise an RNA extraction protocol that can render sufficient yields of RNA for RTqPCR and RNA-seq, irrespective of the age and tissue size.

To this end, we have modified the conventional Trizol method to render sufficient amounts of total RNA for RTqPCR and RNA-seq. We then compared our method to a modified version of the original Guanidium-Acid-Phenol-Chloroform method proposed by Dr. Chomczynski and Prof.

Submitted for Review

Sacchi (Chomczynski and Sacchi, 1987) and a commercially available column extraction kit (mirVana kit) that is gaining more popularity and is often used in peripheral nerve studies involving microRNAs (Yu et al., 2012; Wu and Murashov, 2013; Phay et al., 2015). Numerous parameters such as the yield consistency, RNA integrity (Agilent Bioanalyzer), A260/A280 ratio and A260/A230 ratio were taken into consideration to validate each method. The extracted RNA was also subjected to RTqPCR to check for the expression of two reference genes: β-Actin (*Actb)* and TATA-Box Binding Protein (*Tbp)* in order to assess how the quality of RNA extracted using these different methods played a role in this downstream application. Our results highlight the potential challenges that are involved in using these protocols and based on our data we find that our modified Trizol method renders sufficient and consistent yields across all ages and satisfies the fundamental RNA quality/integrity requirements for both RTqPCR and RNA-seq.

Submitted for Review

Materials and Methods:

Animals, Tissue Harvesting and Tissue homogenization:

C57Bl6/J mice at different timepoints were obtained from our animal breeding facility. Adult mice were first anesthetized with isoflurane and sacrificed using cervical dislocation. Neonatal mice were sacrificed using decapitation. Sciatic nerves from both the hind limbs were harvested and immediately subjected to tissue homogenization in Fisherbrand™ Bead Mill 24 Homogenizer (Fisher 15515799) using appropriate tubes (2mL Tubes with 2.8mm ceramic beads, Fisher 15565799). Homogenization was carried out using the following settings – Speed = 4.5, Cycles = 3, Time = 10sec, Duration = 1min30sec. Tissue lysis was carried out in different chaotropic lysis buffers as detailed in the following section. All aspects of animal care and animal experimentation were performed in accordance with the relevant guidelines and regulations of INSERM and Université de Paris (authorization APAFIS#7405-2016092216181520).

Total RNA isolation :

TRIzol Extraction :

Tissue homogenates were transferred to a new tube and placed on ice for 5 minutes. Next, RNA was extracted mostly in accordance with the manufacturer's instructions with slight modifications. A detailed schematic of the protocol along with the different modifications and suggestions are provided in Figure 4B. Briefly, 100% Ethanol was substituted for Isopropanol to reduce the precipitation of salts. Also, RNA precipitation was carried out overnight at -20°C in the presence of glycogen. The following day, precipitated RNA was pelleted by centrifugation and washed at least 3 times with 70% Ethanol to eliminate any residual contamination. Tubes were then spin dried in vacuum and RNA was resuspended in 20µL of RNA resuspension buffer (EDTA 0.1mM, pH 8.0). RNA was then stored at -80°C till RT-PCR.

Guanidine-Acid Phenol-Chloroform Extraction (APC method):

Nerves were placed in 500µL of lysis buffer (4M GuSCN, 0.1 M beta-mercaptoethanol, 0.5% N-lauryl sarcosine, 25 mM Na-citrate, pH 7) on ice (Chomczynski and Sacchi, 1987). This lysis buffer can be prepared in-house or purchased commercially (Ambion 8540G21). Samples were then homogenized as described above. The homogenates were then transferred to a new tube. 50 µL of 2M Na Acetate pH 4.5 (Fischer Scientific 50-843-077) were added to the lysate and briefly vortexed. Samples were again placed on ice for 10 minutes. Next, 500µL of Acid Phenol:Chloroform (Ambion 10095904) was added to the lysate and the samples were thoroughly vortexed for 15s. The tubes were then centrifuged at 20000g for 20 min at room temperature. From the resulting separation of phases, the aqueous phase on top (approx. 400µL) was transferred to a new tube. 1.5µL of glycogen (Sigma G1767) was added to these tubes followed by 1mL of 100% Ethanol. Samples were briefly vortexed and placed at -20°C overnight.

Submitted for Review

The following day, precipitated RNA was pelleted by centrifugation and washed at least 3 times with 70% Ethanol to eliminate any residual contamination. Tubes were then spin dried in vacuum and RNA was resuspended in 20µL of RNA resuspension buffer (EDTA 0.1mM, pH 8.0). RNA was then stored at -80°C till RT-PCR.

mirVana miRNA isolation kit (Ambion Life Technologies AM1560):

Total RNA (including miRNA) was extracted using the column kit according to manufacturer's instructions with no modifications.

RNA quality, integrity and assay:

RNA quantity was assayed using UV spectrophotometry on Nanodrop One (Thermo Scientific). Optical density absorption ratios A260/A280 & A260/A230 of the samples were measured along with the respective yields. RNA integrity was also assessed using Agilent Bioanalyzer.

RTqPCR:

500ng of Total RNA was reverse transcribed with Random Primers (Promega C1181) and MMLV Reverse Transcriptase (Sigma M1302) according to prescribed protocols. Quantitative Real time PCR (qPCR) was performed using Absolute SYBR ROX 2X qPCR mix (Thermo AB1162B) as a fluorescent detection dye. All reactions were carried out in a final volume of 7µl in 384 well plates with 300 nM gene specific primers, around 3.5ng of cDNA (at 100% RT efficiency) and 1X SYBR Master Mix in each well. Each reaction was performed in triplicates. All qPCR experiments were performed on BioRad CFX384 with a No-Template-Control (NTC) to check for primer dimers and a No-RT-Control (NRT) to check for any genomic DNA contamination.

Primer design:

All primers used in the study were designed using the Primer 3 plus software (https://primer3plus.com/cgi-bin/dev/primer3plus.cgi). Splice variants and the protein coding sequence of the genes were identified using the Ensembl database (www.ensembl.org). Constitutively expressed exons among all splice variants were then identified using the ExonMine database (https://imm.medicina.ulisboa.pt/group/exonmine/ack.html) (Mollet et al., 2010) Primer sequences that generated amplicons spanning two constitutively expressed exons were then designed using the Primer 3 plus software. Detailed information on Primer sequences and amplification efficiencies are described in a previous study (Sundaram et al., 2019).

Statistical analysis and Data Visualization :

qPCR readouts were analyzed in Precision Melt Analysis Software v1.2. The amplicons were subjected to Melt Curve analysis and were verified for a single dissociation peak at a Melting Temperature (T_m) > 75°C as expected from the primer constructs. Cq values were determined by regression and the Cq data was exported to Microsoft Excel for further calculations. Each biological sample had 3 technical replicates thereby generating 3 individual Cq values. The arithmetic mean of the triplicates was taken to be the Cq representing the biological sample. The

Submitted for Review

standard deviation (SD) of the triplicates was also calculated and samples that exhibited SD>0.20 were considered inconsistent. In such cases, one outlier Cq was removed to have at least duplicate Cq values for each biological sample and an SD<0.20. Relative expression of genes was quantified using the $2^{-\Delta\Delta Ct}$ method (Livak and Schmittgen, 2001; Schmittgen and Livak, 2008). The Trizol group was used as the experimental calibrator and data was visualized using Graph Pad Prism v7.0.

Transmission Electron Microscopy (TEM) :

Adult mice were deeply anesthetized by intraperitoneal injection of 40 mg/kg ketamine and 30 mg/kg xylazine and then intracardially perfused with 4% paraformaldehyde, 2.5% glutaraldehyde in 0.1M phosphate buffer, pH 7.4. Tissues were dissected and immersed in the same fixative solution at 4°C overnight, washed in phosphate buffer, post fixed in 2% osmium tetroxide, dehydrated in graded ethanol series and embedded in epoxy resin. For electron microscopy, ultrathin sections (50–90 nm) were cut on an ultramicrotome (8800 Ultrotome III; LKB Bromma) and collected on 300-mesh nickel grids. Staining was performed on drops of 4% aqueous uranyl acetate, followed by Reynolds's lead. Ultrastructural analyses were performed in a JEOL jem-1011 electron microscope and digitalized with Digital Micrograph software.

Submitted for Review

Results

RNA yield and Purity:

We first extracted RNA from Post-natal day 7 (P7) mice using the three different methods(Trizol, mirVana and Acid Phenol Chloroform – abbreviated as APC). The yield and purity of the samples were measured by UV Spectrophotometry on Nanodrop One and the results are detailed in **Figure 2.**

In terms of total RNA yield, Trizol extraction renders 190.3 ± 7 ng/µL (mean ± SD) and mirVana fares a little poorer at 179.3 ± 37.9 ng/µL (**Figure 2A**). The best yield, however, is obtained using the APC method which renders 349.9 ± 18 ng/µL (**Figure 2A**). In terms of consistency, we find that the Trizol method fares the best as it exhibits the least variance among all the three. We would also like to note that ample care was taken to standardize tissue harvesting and no palpable differences exist in the amount of tissue dissected from mice. Hence, the variations observed in the yield can be safely attributed to the intrinsic efficacy of these methods and it is not due to any experimental errors.

We further observed that all the three methods are efficient in removing protein contamination from the extracted RNA. They exhibited A260/A280 ratios between 1.7 to 2.0 (**Figure 2B**). The best results were however achieved from the mirVana method which showed the highest A260/A280 ratio.

With respect to guanidine contamination, APC method fares the best with the highest A260/A230 ratio of 2.12 ± 0.15 (mean ± SD) **(Figure 2C)**. Trizol method is the second best at 1.69 ± 0.3. The highest variation and significantly lower purity is observed in the mirVana method which stands at 1 ± 0.45 **(Figure 2C)**. We next assessed RNA integrity of the all the samples extracted using the three methods using Agilent Bioanalyzer and the results are summarized in the table below (**Table 1**).

Trizol samples exhibit RIN values from 8.5 to 9.2. MirVana RIN values range from 9.4 to 10 and APC RIN values range from 8.9 to 10 (**Table 1**). These results suggest that the integrity of the mirVana and the APC samples are relatively better than the Trizol samples. However, all the three methods show RIN values above 8 suggesting that all these samples exhibit adequate RNA integrity for downstream applications such as RTqPCR and RNA-seq.

Validation by RTqPCR:

We next sought to compare each method using RTqPCR by amplifying the expression of two commonly used reference genes *Actb* and *Tbp*. Based on the results from UV spectrophotometry, we reasoned that if equal quantity of RNA (500ng) is reverse transcribed, we should obtain similar Cq values for these genes across all the three methods. However, much to our surprise, we observed significant differences in Cq values (and therefore mRNA quantities) for both *Actb* and *Tbp* across the three methods (**Figure 3A, Figure 3B, Supplementary Table S1**).

Submitted for Review

In Trizol samples, *Actb* was detected from 16.6 ± 0.27 cycles (mean ± SD) and *Tbp* was detected at 24.87 ± 0.3 cycles. In the mirVana samples, *Actb* was detected from 17.35 ± 0.36 cycles and *Tbp* was detected from 25.83 ± 0.38 cycles. Similarly, in APC samples, *Actb* was detected from 17.76 ± 0.27 cycles and *Tbp* was detected from 26.27 ± 0.26 cycles (**Supplementary Table S1**).

These differences in Cq values indeed could not result from the differences in the purity or the integrity of these samples. This is because APC samples which exhibit the highest purity (**Figure 2B, 2C and Table 1**), shows significantly higher Cq values when compared to the Trizol group which exhibits relatively lower purity. Moreover, although these differences in Cq values look negligible at first glance, the true extent of this variation is revealed when the data is represented as fold changes with the Trizol group used as the experimental calibrator (**Figure 3A, Figure 3B**). We see that *Actb* expression in the mirVana group is reduced by one-thirds and that of the APC group is reduced by half (**Figure 3A**). A similar and almost congruent reduction in *Tbp* expression is also observed in mirVana and APC groups (**Figure 3B**).

To explain such drastic differences, we cautiously analyzed our raw data to root out any experimental errors during RTqPCR. Upon inspection, we observed that RNA concentrations determined by Nanodrop and Bioanalyzer do not concur especially in the mirVana and the APC groups (**Figure 3C and Supplementary Table S2**). In general, RNA concentrations assessed by Bioanalyzer are lower than that of Nanodrop, but the difference is more pronounced in the mirVana and the APC samples. In the Trizol group, Nanodrop concentrations are estimated to be 1.2 ± 0.1 (mean ± SD) folds higher than Bioanalyzer values whereas in the mirVana and the APC, the fold increase is 3.3 ± 0.4 and 4.7 ± 1.1 folds respectively (**Supplementary Table 2**).

As we performed RTqPCR based on Nanodrop concentrations, we wanted to ascertain if the differences in RNA quantity used for reverse transcription could potentially cause the Cq value changes in qPCR among the three groups. Therefore, we recalculated the total amount of RNA that was used in reverse transcription based on the Bioanalyzer concentrations (**Supplementary Table S3**). We then plotted these RNA quantities as fold-differences with respect to the Trizol group (experimental control) **(Figure 3D)**. This is was done in order to compare the revised fold-differences in RNA quantities used for RTqPCR with the qPCR fold changes observed in *Actb* and *Tbp* among the three groups.

The revised RNA quantities expressed as fold-differences seemed to concur with the fold changes observed in qPCR (**Figure 3A, 3B and 3D**). Consequently, to validate our observation, we performed a correlation analysis (Spearman's correlation) between the qPCR fold-changes and the revised RNA fold-differences across all samples and methods. The results of this analysis are detailed in the correlation matrix below (**Table 2**).

We observe that the *Actb* and *Tbp* expression positively correlates with the revised RNA quantity fold-differences across all methods (r = 0.82 and r = 0.80 respectively). As expected, we also observe an almost perfect correlation between *Actb* and *Tbp* (r = 0.98) qPCR results across the three methods.

Submitted for Review

These results, taken together, show that Nanodrop drastically overestimates the concentration of RNA in mirVana and APC samples. Furthermore, qPCR results demonstrate that the bioanalyzer concentration values are more reliable than Nanodrop and care must be employed while constructing RTqPCR experiments especially if RNA is extracted by the mirVana kit or the APC method.

Reliability of the Trizol Method:

Although RNA quantification by Nanodrop is not reliable when compared to the bioanalyzer, the Trizol method offers an advantage on two fronts. Firstly, the RNA yield from Trizol extraction is the highest when compared to the other two methods as indicated by the Bioanalyzer results (**Figure 3C**). Secondly, the consistency of the yield is also conserved irrespective of the method employed for RNA quantification.

In the Trizol samples, the intragroup variation in RNA yield assessed through Nanodrop is 3.7% (co-efficient of variation) and that of Bioanalyzer is marginally higher at 8.5% (**Supplementary Table S2**). This pales in comparison to mirVana samples whose intragroup variation is 21% in Nanodrop and 27% in Bioanalyzer. Although the differences in yield variation between Nanodrop and Bioanalyzer are quite similar in the mirVana group, a variation of more than 20% in the yield is rather high. As for the APC samples, this difference in yield variation is more flagrant as they exhibit an intragroup variation of 5.2% in Nanodrop but a staggering 24.4% in Bioanalyzer. These results taken together suggest that the Trizol method produces the highest and the most consistent yields. Additionally, the differences in yield variation is the least between Nanodrop and Bioanalyzer in the Trizol group.

Subsequently, we assayed the RNA yield from the Trizol method from sciatic nerves harvested from mice at P0, P7, P21 and 8 weeks **(Figure 3E)** without pooling nerves from different mice. On an average, at P0 we obtain 629.2ng (N=5, 14.3% variation), at P7 we obtain 3805.3 ng (N=5, 3.7% variation), at P21 we obtain 3501.5ng (N=5, 6.6% variation), at 8 weeks we obtain 3000.7 ng (N=4, 6.8% variation). Our data thus demonstrates that the extraction of total RNA using Trizol renders sufficient yields in neonates as well as in adult mice.

Submitted for Review

Discussion:

The primary objective of this study was to set up an RNA extraction protocol for mouse sciatic nerves that can render consistent and abundant yields irrespective of the tissue size. We have shown that the use of the conventional Trizol protocol caters to this objective. However, the protocol needs to be adapted to the sciatic nerve which is a tissue that is enriched in lipids and collagens. We have also observed that the use of this protocol as per the manufacturer's instructions does not guarantee consistent yields across all ages.

A step by step approach of our modified version is described in Figure 4B. During the optimization of this protocol, we encountered several difficulties in isolating the aqueous phase without retrieving contaminants from the interphase that is enriched with lipids. This problem often occurs in adult nerves (aged 8 weeks and above) where the interphase forms a white opaque deposit on the walls of the tube thus blinding the observer's view on the separation of the aqueous phase above (containing RNA) and the organic phase below (enriched in DNA and proteins). This issue, however, did not arise in young or neonatal mice. The plausible reason can be attributed to the fact that younger mice (aged between P0 and P21) do not possess completely formed myelin sheaths which account for the majority of the lipid content in the sciatic nerve (Jessen and Mirsky, 2005; Salzer, 2015).

To circumnavigate this issue, we performed a preliminary centrifugation step after tissue homogenization and before the addition of chloroform. This brings the lipid layer to the top of the homogenate. The homogenate is then carefully pipetted out from the bottom and transferred to a new tube before continuing with the protocol. This troubleshooting method is often practiced while extracting RNA from the adipose tissue which is also highly enriched in lipids (Cirera, 2013).

One of the crucial steps of RNA extraction from the sciatic nerve is tissue disruption and homogenization. We initially used the RETSCH MM300 homogenizer with 5mm stainless steel beads and we observed that the tissues were not completely disrupted even after 3 cycles at 20Hz. We then switched to the Fisherbrand™ Bead Mill 24 Homogenizer with 2.8mm ceramic beads and we could substantially increase tissue disruption and homogenization. Moreover, incubation of the nerves in Trizol for 10 minutes on ice prior to homogenization improved tissue disruption. In adult or aged mice, sciatic nerves can also be cut into smaller pieces using microdissection Vannas scissors immediately after placing them in tubes containing Trizol. This step ensures complete homogenization and prevents left-over tissue aggregates after lysis.

During RNA precipitation, we replaced isopropanol with ethanol for two reasons. As the precipitation process occurs overnight at -20°C in the presence of glycogen, the use of ethanol would reduce the co-precipitation of salts and also enhance the precipitation of smaller RNA species such as microRNA (Farrell, 2010). This would ensure that our protocol also caters to researchers who would like to study miRNA expression and regulation in peripheral nerves.

Submitted for Review

A noteworthy limitation of the proposed method is that the maximum yield that is obtained is around 3µg of RNA even from adult mice. Although the tissue mass increases rather significantly as mice age, it has no bearing on the total yield after P7 **(Figure 3E**). This is due to the fact that the tissue becomes more fibrous and lipid rich with age due to the deposition of collagen and an increase in the myelin sheath thickness. Fibrous tissues pose a major hurdle in RNA extraction as they hinder tissue disruption at the cellular level (Peeters et al., 2016; Reimann et al., 2019). However, despite this drawback, the amount of RNA extracted is largely sufficient for downstream applications.

Another observation that requires explanation is the discrepancies that we observed in the quantification of RNA between Nanodrop and Bioanalyzer in the mirVana and APC samples (**Figure 3C**). We believe that the overestimation by Nanodrop is due to UV absorbance of an unknown molecule at 260nm that eventually skews the results. This issue is possibly due to the co-precipitation of free nucleotides (dNTPs) along with RNA molecules in the mirVana and the APC methods. The absorbance of these free dNTPs is picked up by the nanodrop at 260nm and hence it overestimates the actual amount of RNA present. Our reasoning is also supported by the fact that APC samples show the highest concentration values in Nanodrop (Figure 2A) as they are subjected to overnight precipitation as opposed to the mirVana samples where precipitation is performed at the bench for a few minutes and the RNA is retrieved by silica based spin columns. This explains why the overestimation due to the presence of dNTPs is moderate in mirVana samples but very high in APC samples (**Figure 3C**). It should be noted that both these methods employ similar lysis buffers followed by Acid Phenol Chloroform to separate and retrieve the aqueous phase. In Trizol however, we think that the amount of dNTPs that are co-precipitated with RNA are significantly lower and hence the Nanodrop and Bioanalyzer estimates differ only by a small margin (**Figure 3C**). Besides, Bioanalyzer does not quantify RNA based on spectrophotometry but the quantification is achieved through fluorescence. In a conventional Bioanalyzer setup, RNA molecules are electrophoretically passed through microchannels that are filled with fluorescent RNA intercalants. The fluorescence is then measured for large RNA molecules that bind to the intercalants thus resulting in specific fluorescence peaks for specific RNA populations at specific locations along the microchannel after electrophoresis. The instrument then computes an integrity score (RIN) based on the fluorescence profile of the separated RNA populations. It also computes the total RNA concentration based on the overall fluorescence. Therefore, free dNTPs that are present in the sample either do not bind to these intercalants or they emit feeble amounts of fluorescence that fall below the detection threshold of the Bioanalyzer. Thus, the methodological difference in assaying RNA quantities coupled with the presence of dNTPs in the mirVana and APC samples could possibly explain the differences observed in RNA quantification between Nanodrop and Bioanalyzer.

Additionally, we also looked at the kind of acetate salts used for RNA precipitation in all the three methods since the kind of salt used for nucleic acid precipitation can influence the co-precipitation of free dNTPs (Farrell, 2010). All three methods use Sodium Acetate in an acidic pH (around 4.0) which increases the chances of co-precipitating free nucleotides (Farrell, 2010).

Submitted for Review

However, should our dNTP hypothesis be true, it is intriguing as to why the Trizol method co-precipitates lesser dNTPs than the other two methods. Thus, further investigation is required to confirm the provenance of this variation in RNA quantification between Nanodrop and Bioanalyzer.

Nevertheless, despite the minor drawbacks in terms of the total yield and discrepancies in RNA quantification between methods, Trizol extraction proves to be reliable in terms of total RNA yield and consistency in neonatal as well as adult mouse sciatic nerves.

Submitted for Review

Figures and Figure Legends:

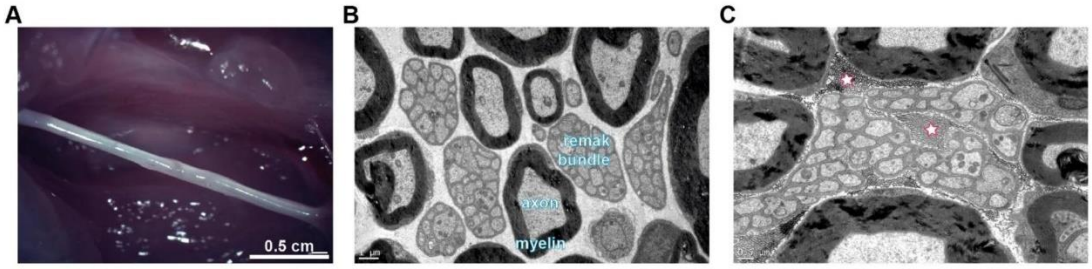


Figure 1 : Cellular composition of the sciatic nerve.

(A)The macroscopic view of an adult 8-week-old nerve during dissection. The nerve appears as an opaque fibrous tissue that is situated between the muscles of the hindlimbs. The nerve is first separated from surrounding tissue and is dissected distally at the level of the gastrocnemius muscle. The second incision is made proximally near the spinal cord where the sciatic emerges near the lumbar vertebrae L4 and L5 in mice (Rigaud et al., 2008). Scale bar = 0.5cm

(B) An electron micrograph of a sciatic nerve transverse section (8 weeks old). The cellular anatomy of the nerve reveals two distinct types Schwann cells enwrapping axons. The myelin sheath and the axonal body are depicted for a given axon/schwann cell unit. Smaller axons are ensheathed in a cellular matrix and packed into distinct structures called as Remak Bundles. These small axonal bundles are wrapped by non-myelinating Schwann cells. Scale bar = 1um

(C) A magnified image of the Extra Cellular Matrix (ECM) around Schwann cells. Small circular structures are dispersed in the ECM around schwann cells. These are collagen deposits (depicted by an asterisk) synthesized by other glial cells in the endoneurial space. The fibres are concentrated in specific locations and extend longitudinally along the nerve. Scale bar = 0.5um

Submitted for Review

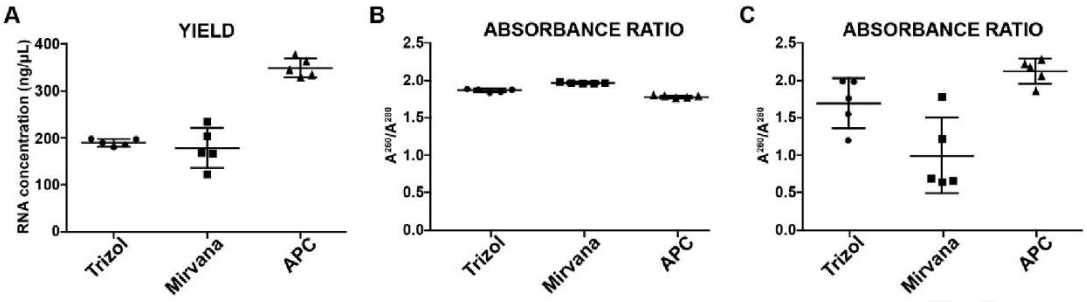


Figure 2 : RNA yield and purity of P7 sciatic nerves measured using Nanodrop One.

(A) Concentration of RNA (ng/uL) across the three different protocols of RNA extraction using Trizol, mirVana kit and the conventional Acid Phenol Chlorofom (APC). RNA was extracted from P7 nerves and was resuspended in a final volume of 20uL.

(B) Optical Density (OD) absorbance ratio A260/A280. Nucleic Acids absorb UV radiation at a wavelength of 260nm and proteins absorb at 280nm. This ratio is computed to assess the amount of RNA with respect to the amount of proteins that hinder downstream applications such as RTqPCR. A260/A280 ratios above 1.8 are exhibited samples are enriched in nucleic acids.

(C) Optical Density (OD) absorbance ratio A260/A230.Chemical contaminants such as Guanidine salts and phenol absorb UV radiation at 230nm. This ratio is computed to assess the amount of RNA with respect to the amount of chemical contaminants. A260/A230 ratios above 1.8 are exhibited by samples that contain relatively sparing amounts of chemical contaminants from the extraction process.

Submitted for Review

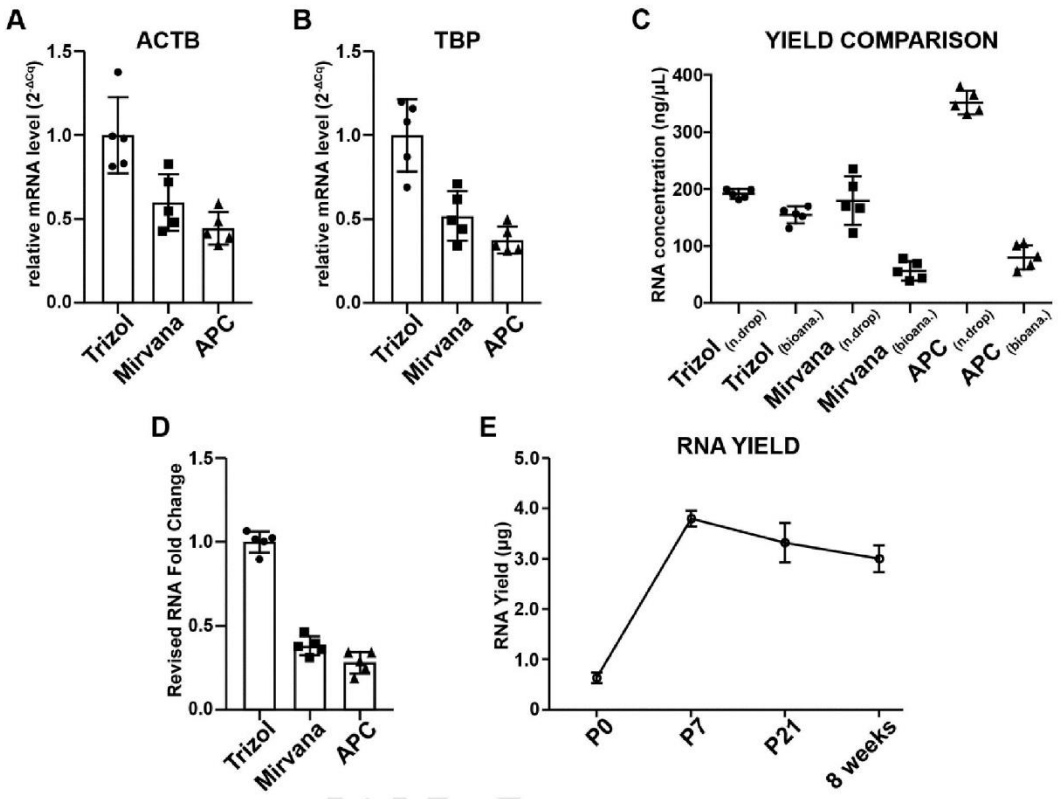


Figure 3 : Validation of RNA extraction by RTqPCR.

RNA extracted from the three methods were subjected to RTqPCR to check for the expression of *Actb* and *Tbp*.

(A) Relative expression of *Actb* across the three different protocols. Cq values were linearized and expressed as fold changes ($2^{-\Delta Cq}$) with respect to the Trizol group that is used as the experimental calibrator. Data is represented as histograms with the mean and error bars that signify the Standard Deviation.

(B) Relative expression of *Tbp* across the three different protocols. Cq values were linearized and expressed as fold changes ($2^{-\Delta Cq}$) with respect to the Trizol group that is used as the experimental calibrator. Data is represented as histograms with the mean and error bars that signify the Standard Deviation.

(C) A comparative analysis of RNA quantification between Nanodrop and Bioanalyzer across the three different methods. Bioanalyzer RNA concentrations are always lower than the nanodrop assessments. The difference is more pronounced in the mirVana group and the APC group. Data is represented with the mean and the error bars denoting the standard deviation.

Submitted

(D) Revised RNA quantities used for RTqPCR. Based on the Bioanalyzer values, the amount of RNA used for RTqPCR was recalculated. The revised RNA amounts are expressed as fold differences with respect to the Trizol group that is used as the experimental calibrator. Data is represented as histograms with the mean and error bars that signify the Standard Deviation.

(E) RNA yield of the Trizol method across different developmental timepoints from Post Natal Day 0 (P0) to 8 weeks.

Submitted for Review

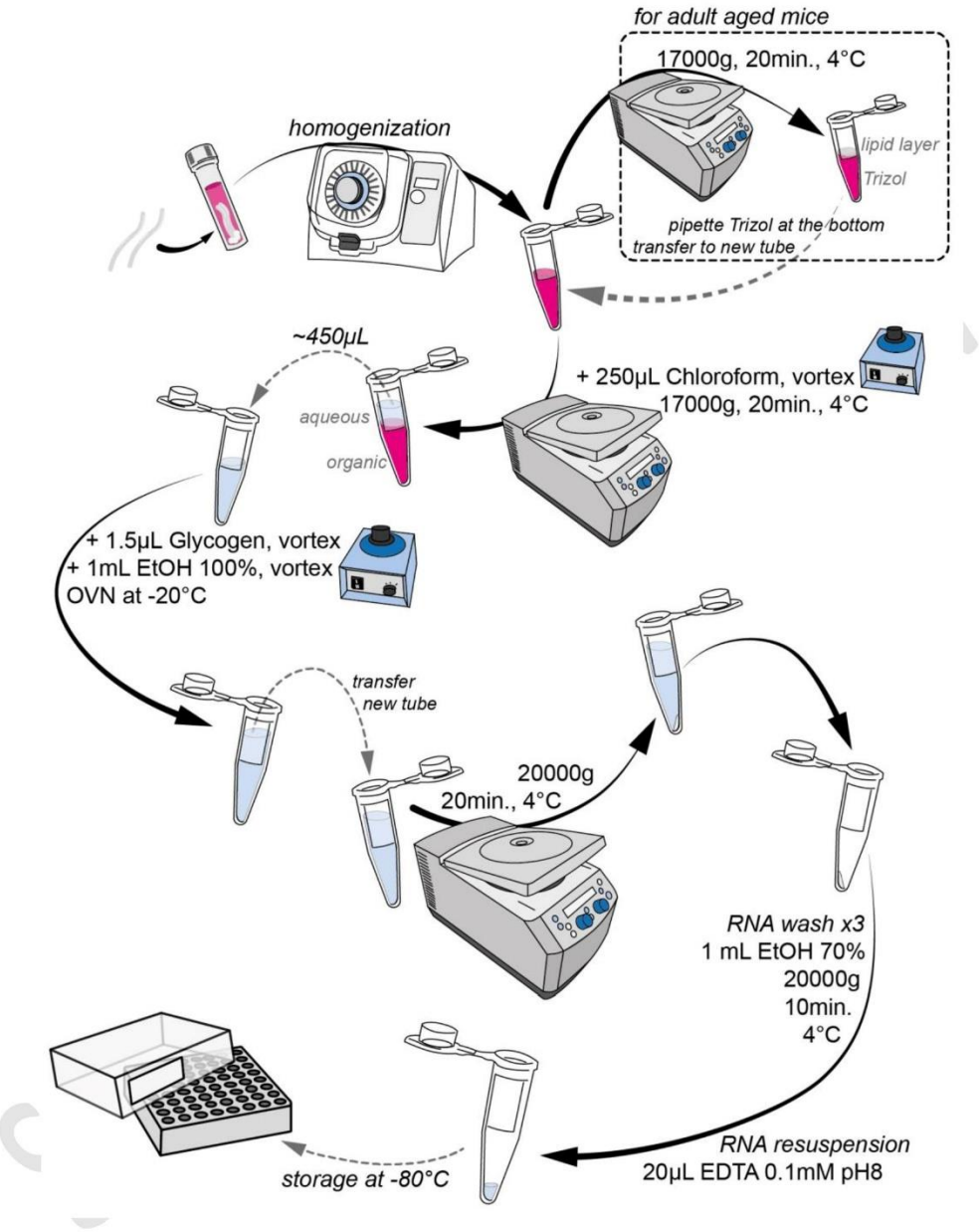


Figure 4: A step-by-step depiction of the Trizol protocol with modifications

Detailed description of the different steps of RNA extraction from Sciatic Nerves using Trizol. Tissues are harvested from mice and immediately placed in 1mL of Trizol solution in Fisherband Tubes. They are then incubated for 10 minutes on ice. Next, samples are homogenized in a bead mill homogenizer. Tissue homogenates are then transferred to a new eppendorf tube (1.5mL). For adult and aged mice, a

preliminary centrifugation step is performed with the lysates to bring the lipid layer to the top. Trizol is then pipetted out from the bottom carefully and transferred to a new tube. 250µL of Chloroform is added to the lysate and the tubes are vortexed for 15sec – 30sec. Samples are then placed at room temperature for 3 minutes followed by centrifugation at 17000g for 20 minutes at 4°C. The organic phase separates from the aqueous phase post centrifugation. The aqueous phase which contains the RNA is then carefully transferred to a new tube. 1.5µL of glycogen is added to each sample and the tubes are briefly vortexed. This is followed by the addition of 1mL 100% Ethanol and the tubes are again vortexed briefly. The samples are then placed at -20°C overnight to facilitate RNA precipitation. The following day, the contents of the tube are transferred to a new one followed by centrifugation at 20000g for 20 min at 4°C. The supernatant is decanted, and the pellet is washed with 70% Ethanol at least thrice before being dried in a speed-vac. Dry RNA is then resuspended in20µL of RNA resuspension buffer (0.1mM EDTA, pH 8) and stored at -80°C till RTqPCR.

Submitted for Review

Tables and Table Legends:

Table 1

Sample	***RIN***
Trizol_1	***9***
Trizol_2	***8.8***
Trizol_3	***8.4***
Trizol_4	***8.5***
Trizol_5	***9.2***
Mirvana_1	***9.4***
Mirvana_2	***9.8***
Mirvana_3	***10***
Mirvana_4	***9.9***
Mirvana_5	***9.9***
APC_1	***8.9***
APC_2	***10***
APC_3	***10***
APC_4	***9.7***
APC_5	***9.6***

Table 1: Assessment of RNA integrity using Agilent Bioanalyzer. 5µL of each sample was placed on RNA-Nanochips. RNA was then electrophoretically separated into different rRNA populations. The fluorescence of each rRNA population is measured by the instrument and based on the fluorescence profile and the intactness of the rRNA populations, the instrument computes an RNA Integrity Number (RIN) for each sample. RIN scores above 8 signify that the sample can be further used for sequencing or RTqPCR. Samples with no RNA degradation present with a perfect RIN score of 10.

Submitted for Review

Table 2

Spearman's r Matrix	*Actb* *Fold changes*	*Tbp* *Fold Changes*	RNA fold difference (Revised)
Actb Fold changes	n/a	0.98	0.82
Tbp Fold changes	0.98	n/a	0.80
RNA fold difference (Revised)	0.82	0.80	n/a

P-Value Matrix	*Actb* *Fold changes*	*Tbp* *Fold Changes*	RNA fold difference (Revised)
Actb Fold changes	n/a	3.88E-09	3.54E-04
Tbp Fold changes	3.88E-09	n/a	6.46E-04
RNA fold difference (Revised)	3.54E-04	6.46E-04	n/a

Table 2: Spearman's correlation matrix to compare qPCR results with the revised RNA quantities (based on Bioanalyzer estimates) used for RTqPCR. The actual amount of RNA used for RTqPCR was recalculated using the Bioanlyzer values and expressed as fold differences with respect to the Trizol group. These fold differences were correlated to the qPCR fold changes of *Actb* and *Tbp* using Spearman's correlation. The correlation matrix of *Spearman's r* values along with the corresponding P values for each comparison is detailed in the table. R values closer to 1 indicate strong positive correlation between the datasets. P values lesser than 0.05 are considered statistically significant. The correlation of the datasets with themselves are denoted by 'n/a' and are omitted from analysis.

Submitted for Review

References

Chen, P., Cescon, M., and Bonaldo, P. (2015). The Role of Collagens in Peripheral Nerve Myelination and Function. *Mol. Neurobiol.* 52, 216–225. doi:10.1007/s12035-014-8862-y.

Chomczynski, P., and Sacchi, N. (1987). Single-step method of RNA isolation by acid guanidinium thiocyanate-phenol-chloroform extraction. *Anal. Biochem.* 162, 156–159. doi:10.1016/0003-2697(87)90021-2.

Cirera, S. (2013). Highly efficient method for isolation of total RNA from adipose tissue. *BMC Res. Notes* 6, 472. doi:10.1186/1756-0500-6-472.

Farrell, R. E. (2010). *RNA Methodologies: Laboratory Guide for Isolation and Characterization*. doi:10.1016/B978-0-12-374727-3.00025-5.

Groppe, J. C., and Morse, D. E. (1993). Isolation of Full-Length RNA Templates for Reverse Transcription from Tissues Rich in RNase and Proteoglycans. *Anal. Biochem.* 210, 337–343. doi:10.1006/abio.1993.1205.

Jessen, K. R., and Mirsky, R. (2005). The origin and development of glial cells in peripheral nerves. *Nat Rev Neurosci* 6, 671–682. doi:nrn1746 [pii]\n10.1038/nrn1746.

Lan, T., Yao, B., Shen, Y., and Wang, X. (2013). Isolation of high-quality total RNA from lipid-rich seeds. *Anal. Biochem.* 438, 11–13. doi:10.1016/J.AB.2013.03.012.

Livak, K. J., and Schmittgen, T. D. (2001). Analysis of relative gene expression data using real-time quantitative PCR and the 2^-ΔΔCT Method. *Methods* 25, 402–408. doi:10.1006/meth.2001.1262.

Mollet, I. G., Ben-Dov, C., Felício-Silva, D., Grosso, A. R., Eleutério, P., Alves, R., et al. (2010). Unconstrained mining of transcript data reveals increased alternative splicing complexity in the human transcriptome. *Nucleic Acids Res.* 38, 4740–4754. doi:10.1093/nar/gkq197.

Monk, K. R., Feltri, M. L., and Taveggia, C. (2015). New insights on schwann cell development. *Glia* 63, 1376–1393. doi:10.1002/glia.22852.

Morell, P., and Quarles, R. H. (1999). Characteristic Composition of Myelin. Available at: https://www.ncbi.nlm.nih.gov/books/NBK28221/ [Accessed November 30, 2017].

Peeters, M., Huang, C. L., Vonk, L. A., Lu, Z. F., Bank, R. A., Helder, M. N., et al. (2016). Optimisation of high-quality total ribonucleic acid isolation from cartilaginous tissues for real-time polymerase chain reaction analysis. *Bone Jt. Res.* 5, 560–568. doi:10.1302/2046-3758.511.BJR-2016-0033.R3.

Phay, M., Kim, H. H., and Yoo, S. (2015). Dynamic Change and Target Prediction of Axon-Specific MicroRNAs in Regenerating Sciatic Nerve. *PLoS One* 10, e0137461. doi:10.1371/journal.pone.0137461.

Reimann, E., Abram, K., Kõks, S., Kingo, K., and Fazeli, A. (2019). Identification of an optimal method for extracting RNA from human skin biopsy, using domestic pig as a model system. *Sci. Rep.* 9, 1–10. doi:10.1038/s41598-019-56579-5.

Rigaud, M., Gemes, G., Barabas, M.-E., Chernoff, D. I., Abram, S. E., Stucky, C. L., et al. (2008).

Submitted for Review

Species and strain differences in rodent sciatic nerve anatomy: Implications for studies of neuropathic pain. *Pain* 136, 188–201. doi:10.1016/j.pain.2008.01.016.

Salzer, J. L. (2015). Schwann cell myelination. *Cold Spring Harb. Perspect. Biol.* 7, 1–26. doi:10.1101/cshperspect.a020529.

Schmittgen, T. D., and Livak, K. J. (2008). Analyzing real-time PCR data by the comparative C(T) method. *Nat. Protoc.* 3, 1101–8.

Schrader, C., Schielke, A., Ellerbroek, L., and Johne, R. (2012). PCR inhibitors - occurrence, properties and removal. *J. Appl. Microbiol.* 113, 1014–1026. doi:10.1111/j.1365-2672.2012.05384.x.

Shellswell, G. B., Restall, D. J., Duance, V. C., and Bailey, A. J. (1979). Identification and differential distribution of collagen types in the central and peripheral nervous systems. *FEBS Lett.* 106, 305–308. doi:10.1016/0014-5793(79)80520-7.

Sundaram, V. K., Sampathkumar, N. K., Massaad, C., and Grenier, J. (2019). Optimal use of statistical methods to validate reference gene stability in longitudinal studies. *PLoS One* 14, e0219440. doi:10.1371/journal.pone.0219440.

Wang, L., and Stegemann, J. P. (2010). Extraction of high quality RNA from polysaccharide matrices using cetyltrimethylammonium bromide. *Biomaterials* 31, 1612–8. doi:10.1016/j.biomaterials.2009.11.024.

Woodhoo, A., and Sommer, L. (2008). Development of the Schwann cell lineage: From the neural crest to the myelinated nerve. *Glia* 56, 1481–1490. doi:10.1002/glia.20723.

Wu, D., and Murashov, A. K. (2013). MicroRNA-431 regulates axon regeneration in mature sensory neurons by targeting the Wnt antagonist Kremen1. *Front. Mol. Neurosci.* 6, 35. doi:10.3389/fnmol.2013.00035.

Yu, B., Zhou, S., Wang, Y., Qian, T., Ding, G., Ding, F., et al. (2012). Mir-221 and mir-222 promote Schwann cell proliferation and migration by targeting LASS2 after sciatic nerve injury. *J. Cell Sci.* 125, 2675–2683. doi:10.1242/jcs.098996.

Submitted for Review

CHAPTER III: RESULTS

ARTICLE:

ICOS-ICOSL Interaction Is Necessary For The Maintenance of Self Tolerance In The Peripheral Nervous System

Authors: Rasha Barakat, Assaad Eid, Charbel Massaad, Christian Boitard

Corresponding Author: Christian Boitard

Key Words:

Abreviations: T1D: Type 1 Diabetes; PNS: Peripheral Nervous System; ICOS: Inducible T-cell Costimulator; ICOSL: Inducible T-cell Costimulator Ligand; NOD: Non-Obese Diabetic; CIDP: Chronic Inflammatory Demyelinating Polyradiculopathy

ABSTRACT

The knockout of ICOS/ICOSL results in the deviation of the autoimmune system from the pancreas towards the PNS in a NOD background. NOD ICOS$^{-/-}$ and NOD ICOSL$^{-/-}$ mice develop a severe autoimmune neuropathy characterized by behavioral, electrophysiological, and histological deficits. The NOD ICOS$^{-/-}$ and NOD ICOSL$^{-/-}$ mice have motor and sensory deficits characterized by poor motor coordination, reduced grip strength, altered perception of heat, and pathological CMAP responses. The ultrastructure of the nerve is also affected; there are demyelinated areas, defected myelinated axons, and defected Remak bundles in the NOD KO mice. The phenotype appears earlier in the NOD ICOS$^{-/-}$ (26 weeks) than in the NOD ICOSL$^{-/-}$ (35 weeks). Peripheral nerve lesions also develop earlier brachial nerves than in sciatic nerves. By contrast, neither C57BL/6J ICOS$^{-/-}$ or NOD.*scid* ICOSL$^{-/-}$ mice developed a peripheral neuropathy. The characterization of the nerve infiltrates in NOD ICOS$^{-/-}$ and NOD ICOSL$^{-/-}$ mice revealed the presence of CD4^{+} and CD8^{+} T-cells as well as macrophages. Our data shows that ICOS is not expressed in the PNS. However ICOSL mRNA is detected in the nerve and particularly in Schwann cells. Our model shows that an autoimmune-prone genetic background is required for the development of the peripheral neuropathy, as well as the importance of the ICOS-ICOSL interactions in the maintenance of self-tolerance to peripheral nerves in NOD mice. Taken together, our results provide a robust animal model for immune-mediated neuropathies and in particular CIDP.

INTRODUCTION

Type 1 diabetes (T1D) is an autoimmune disorder where the β-cells of the pancreas are destroyed by autoreactive T-cells. Even though the initiation mechanism of the auto-immune response to β-cells remains elusive in the spontaneous development of diabetes, and likely multifactorial, the T-cells require an activation via costimulatory signals. They consist of an interaction between CD28 expressed by T-cells and B7 isoforms on antigen-presenting cells. The classical animal model used for the study of T1D is the non-obese diabetic (NOD) mouse due to its autoimmune-prone background. Defective expression of molecules from the CD28-B7 superfamily prevents the development of autoimmunity to pancreatic islet β-cells, and in the case of B7.2, ICOS, or ICOSL, leads to the deviation of autoimmunity from β-cells to peripheral nerves (Prevot et al., 2010; Salomon et al., 2001). We previously reported that NOD ICOS$^{-/-}$ and NOD ICOSL$^{-/-}$ mice fail to develop diabetes but instead develop a spontaneous autoimmune neuropathy exclusively present in the peripheral nervous system. The pathology was shown to be mediated by CD4^{+} T-cells as the blocking of CIITA hinders the development of neuritis while the blocking of β2-microglobulin has no effect on the development of the peripheral nerve disease (Briet et al., 2017). Moreover, the neuropathy is transferred into NOD*scid* recipients upon injection of CD4^{+} T cells, but not with CD8^{+} T cells, obtained from NOD ICOSL$^{-/-}$ spleens. The peripheral neuropathy seen in ICOS$^{-/-}$ or ICOSL$^{-/-}$ mice shows striking similarities with the human Chronic Inflammatory Demyelinating Polyneuropathy (CIDP) seen in patients suffering from a chronic or a relapse-remitting course of neuropathy with motor and sensory deficits (B. C. Kieseier et al., 2018). Histological findings show myelin lesions with onion bulb formation, and an infiltration by T-cells (Lehmann et al., 2019; Mathey et al., 2015). Even though the evaluation of neuropathy in NOD ICOS$^{-/-}$ and NOD ICOSL$^{-/-}$ mice was evaluated through a scoring system, no thorough behavioral assessment was done. Moreover, studies have mainly focused on the immunological characterization of the spontaneous autoimmune neuropathy without emphasizing the neurological aspect.

To better understand the immune mediated neuritis in NOD ICOS$^{-/-}$ and NOD ICOSL$^{-/-}$ mice, we performed an array of behavioral and electrophysiological tests to assess fine motor coordination, muscular strength, and nerve function. Histological data was performed to evaluate the myelin defects, the nerve lesions. This study also shows the implication of ICOS/ICOSL in the nerve across different time points.

Material and Methods

Mice

NOD, NOD ICOS$^{-/-}$, NOD ICOSL$^{-/-}$, NOD.*scid* WT, NOD.*scid* ICOSL$^{-/-}$, C57BL/6J WT and C57BL/6J ICOS$^{-/-}$ female mice were bred and housed in our facilities under specific pathogen-free conditions. NOD ICOS$^{-/-}$ and NOD ICOSL$^{-/-}$ were generated as described (Prevot et al., 2010). The C57BL/6J ICOS$^{-/-}$ were purchased from the Jackson Laboratory. Animal studies were approved by institutional review (Authorization APAFIS # 2018062917427646).

Behavioral and Functional Tests

Neuropathy was assessed using different behavioral tests. The locotronic (Intelli-bio, France) was used to evaluate fine motor coordination. The animals had to cross three time a horizontal ladder with a rest period of 30 min between each passage. Infrared sensors placed below the ladder were able to detect any foot faults. The results included the average time to cross the ladder and the average number of foot slips. Grip strength (Bioseb) was measured for the front paws and all four limbs. Each mouse was subjected to 3 successive attempts separated by a 30-minute rest period between the "front paw pull" and the "all paw pull". The mice were placed on a hot plate (Bioseb) at 52°C for the assessment of hyeperalgesia. The paw retrieval latency was measured for each animal with a cutoff value at 30 s.

For the CMAP measurement (Dantec® Keypoint® Focus EMG / NCS / EP System Natus), mice were anesthesized by an intra-peritoneal injection of 100 mg/kg of Ketamine and 10 mg/kg of Xylazine. Stimulation was done at the level of the sciatic notch and the recording electrode was placed in the tibialis. The latency and the maximum amplitude (base to peak) were measured.

All the tests and data analysis were made blind to the experimenter.

Histological Analysis

To evaluate demyelination and nerve inflammation, nerves were fixed in TEM fixation buffer (4% formaldehyde, 2.5% glutaraldehyde, and 0.1M phosphate buffer, pH 7.4) then embedded in epoxy resin or 4% formaldehyde then embedded in paraffin. The tissues in resin were processed at previously described (Hichor et al., 2018). A myelinated and unmyelinated axon density analysis was performed where the number of myelinated and unmyelinated axons were counted per μm^2. Defected myelinated and unmyelinated axons were also assessed. The structures were considered defected based on certain criteria. Myelinated axons were considered defected if the following anomalies were present: axon fragmentation, enlarged mitochondria, uncompact myelin. Remak bundles were considered defected if the following anomalies were found: hypertrophied axons, absence of cytoplasm, enlarged mitochondria, large vacuoles inside the axons. Paraffin sections were stained with Hematoxylin and Eosin. For IHC-P, unstained

parrafin sections were stained with Rabbit anti-CD3 (Abcam 5690, 1/50), Rat anti-CD4 Biotin (Clone: 4SM95, eBioscience 14976682, 1/50), Rat anti-CD8 Biotin (Clone: 4SM15, eBioscience 14080882, 1/50). The following secondary antibodies were used: SAV anti-Rat HRP (Genemed 10-0010, 1/400) and Goat anti-Rabbit HRP (Abcam ab97200, 1/200) For IF, the following antibodies were used: Chicken anti-MPZ (PZO Aves, 1/500), Rabbit anti-NFH (AB5539 Merck, 1/1000), and Rat anti-F4/80 (eBioscience 14-4801-82, 1/1000) using an immunofluorescence technique. Nuclei were labelled using Hoechst 33342 (5µg/mL). The secondary antibodies used were Donkey anti-Chicken Cy3 (703-005-155 Jackson, 1/1000), Donkey anti-Rabbit A488 (711-545-152 Jackson, 1/1000), and Donkey anti-Rat (A647 705-605-147 Jackson, 1/100).

Flow cytometry

Sciatic and brachial nerves were dissected from NOD WT (n=11), NOD ICOS KO (n=7), and NOD ICOSL KO (n=5) mice at 35 weeks. The nerves were digested in collagenase IV (1.6 mg/mL). Infiltrating cells were collected using a Percoll gradient and cultured overnight without IL-2. Surface staining was performed using the following antibodies: TCR, CD45, CD4 (RM4-5), CD8 (53-6.7), B220 (RA3-6B2) from BD Bioscience. Isotype control mAbs were included. The living cells were gated on a density plot with the side scatter versus the forward scatter. Flow cytometry was performed with a BD LSR-Fortessa (Becton Dickinson) and the data were analyzed with the FlowJo 9.2 software (Tree Star Inc.).

DRG Schwann cell coculture and primary Schwann cells cultures

A total of 40 DRGs were harvested from each embryo as described (Venkat Krishnan Sundaram, Barakat, Massaad, & Grenier, 2020). DRGs were then trypsinized (0.25% Trypsin in HBSS1X) for 30min at 37°C. Trypsinization was stopped using L-15 media containing 10% Horse Serum (Gibco). DRGs were then spun down at 1500 rpm for 5min. The supernatant was removed, and the tissues were resuspended in DRG plating medium (refer to Media Compositions). The tissues were then triturated 10-20 times using flamed Pasteur pipettes until a homogenous cell suspension was obtained. Dissociated DRGs were then plated on 12 well plates for each time point –DIV1 (Days In Vitro 1), DIV3, DIV5, DIV7. 40 DRGs from each embryo were plated into 8 wells at approximately 5 dissociated DRGs per well. 2 wells were assigned to each time point. The cells were first plated with DRG plating medium for 16h. The following day the medium was replaced by N2/NGF serum free medium to promote neurite growth and Schwann cell proliferation.

Primary Schwann cell cultures were established from dissociated DRG cultures based on existing protocols with slight modifications (Venkat Krishnan Sundaram et al., 2020). Briefly, neurite-Schwann cell 10 networks from 1-week old, dissociated cultures were mechanically lifted from the culture plates using a 11 fine 27G1/2 needle. They were then digested using Trypsin-Collagenase (0.25% Trypsin & 0.1% Collagenase 12 Type I in HBSS1X). Enzymatic digestion was quenched using Immunopanning media. The digested cells were briefly triturated 5 – 10

times using Pasteur pipettes and were 14 pelleted using centrifugation. Cells were then resuspended in immunopanning media and incubated for 15 15 min at 37°C to promote the turnover expression of cell surface markers for efficient immunopanning. Contaminating fibroblasts were removed by immunopanning based on existing protocols (Lutz 2014).

RT-qPCR Experiments

Nerves dissected from mice or cells were extracted with 1mL of TRIzol reagent (Ambion Life Technologies 15596018) as previously described (V. K. Sundaram, Sampathkumar, Massaad, & Grenier, 2019). 500 ng of high quality Total RNA was reversed transcribed with Random Primers (Promega C1181) and MMLV Reverse Transcriptase (Sigma M1302) according to prescribed protocols. Quantitative Real Time PCR (qPCR) was done using Absolute SYBR ROX 2X qPCR mix (Thermo AB1162B) as a fluorescent detection dye. All reactions were carried out in a final volume of 7µl in 384 well plates with 300 nM gene specific primers, 3.5 ng of cDNA (at 100% RT efficiency), and 1X SYBR Master Mix in each well. Each reaction was performed in triplicates. All qPCR experiments were performed on BioRad CFX384. The sequences of the primers used are listed in the following publications (Venkat Krishnan Sundaram et al., 2020; V. K. Sundaram, Sampathkumar, et al., 2019).

Statistical analysis

Results are expressed as mean ± standard deviation (SD). Statistical significance was assessed by one-way ANOVA (ANOVA), followed by Dunn's post hoc when more than two variables were analyzed. Two group comparisons were performed by Student's t-test followed by a Mann-Whitney. Statistical significance was determined as a probability (P value) of less than 0.05. All statistical analysis was performed with Prism 6 software (GraphPad Software).

RESULTS

Description of the animal model on a NOD background

A panel of behavioral tests was performed on these animals to assess fine motor coordination (locotronic), neuromuscular strength (grip strength), and hyperalgesia (hot plate test). We looked at different timepoints ranging from 12 weeks to 52 weeks in order to determine at which timepoint the clinical signs appear. At 26 weeks the NOD ICOS$^{-/-}$ animals showed deficits in fine motor coordination which were exacerbated at 35 weeks, whereas the NOD ICOSL$^{-/-}$ show deficits at 35 weeks accompanied by a progressive deterioration with time. The NOD ICOS$^{-/-}$ took a longer time to cross the locotronic and had more foot slips compared to the NOD WT starting 26 weeks. This can be seen in the NOD ICOSL$^{-/-}$ at 52 weeks (Fig 1.A). We also observed a significant reduction in grip strength in the NOD ICOS$^{-/-}$ mice at 20 weeks and in the NOD ICOSL$^{-/-}$ at 35 weeks compared to their control littermates (Fig 1.B). Prior to the aforementioned timepoints, no difference was observed between the three groups in neither the behavioral nor histological changes (Supplementary 1). Thermal hyperalgesia was also observed in NOD ICOS KO mice at 30 weeks. These animals showed an increased latency in paw withdrawal on a hot plate compared to their control and ICOSL$^{-/-}$ littermates (Fig 1.C). Electrophysiological studies were performed on these animals at 35 weeks. CMAP was recorded in the tibialis. The NOD ICOS$^{-/-}$ showed a significant reduction in amplitude and a delay in latency compared to the controls. Similarly, the experiment yielded the same trend with the NOD ICOSL $^{-/-}$ compared to the NOD WT but without any statistical significance (Fig 1.D). Our results showed that the knock out of ICOS or ICOSL in a NOD background had an effect on fine motor coordination, grip strength, pain perception, and CMAP response with an earlier phenotype in NOD ICOS$^{-/-}$ mice than NOD ICOSL$^{-/-}$. Since NOD ICOS$^{-/-}$ animals show clinical symptoms ahead, they were preferentially used in the rest of the experiments.

Histological analysis of myelin in the NOD animals at 35 weeks

We looked at the ultrastructure of the nerves and at the state of myelin using immunofluorescence (IF) and electron microscopy. First, we looked at MPZ expression in both brachial and sciatic nerves. Our data showed that we have less myelin content in the KO mice at 35 weeks, specifically in the brachial nerve compared to sciatic (Fig 2.A, 2.C). Next, we performed qPCR experiments to assess mRNA expression of two myelin genes expressed in myelinating Schwann cells; PMP22 and MPZ (Fig 2.B, 2.D). Our data showed no statistical difference in PMP22 expression between NOD WT, NOD ICOS$^{-/-}$, and NOD ICOSL$^{-/-}$. However, MPZ translational levels were drastically reduced in KO mice nerve; in the brachial nerve of the NOD ICOS$^{-/-}$ ($P<0.01$) and in the sciatic nerve of the NOD ICOSL$^{-/-}$ ($P<0.01$) as compared to the NOD WT. Myelin state was also assessed by looking at electron microscopy sections. The results corroborated the IF data; the brachial nerves were more impacted than the sciatic nerves with a larger demyelinated area (Fig 2.E, 2.J). However, focal demyelination was still observed in the sciatic nerve of the NOD ICOS$^{-/-}$ animals. Scar tissue was seen in the

infiltrated nerves along with degenerating axons. We measured the thickness of the myelin sheath by calculating the g-ratio. In both brachial and sciatic nerves, no difference was observed in the g-ratio between the NOD WT, the NOD ICOS$^{-/-}$, and the NOD ICOSL$^{-/-}$ (Fig 2.F, 2.G, 2.K, 2.L). We looked at the overall density and the defected axon density in myelinated and unmyelinated axons. We observe in the NOD ICOS$^{-/-}$ and NOD ICOSL$^{-/-}$ animals a significant reduction in both myelinated and unmyelinated axon density in the brachial nerves but no difference in the defected structures between the KO mice and the WT (Fig 2.H, 2.I). As for the sciatic nerves, there no statistical difference in the myelinated and unmyelinated axon density between the KO animals and their controls however there is an increased of defected structures (Fig 2.M, 2.N). Taken together, our data shows defects in myelin and in nerves of NOD ICOS$^{-/-}$ and NOD ICOSL$^{-/-}$ mice at 35 weeks.

Description of the control strains: C57BL/6J and NOD.SCID

The development of autoimmune neuropathy in ICOS$^{-/-}$ and ICOSL$^{-/-}$ NOD mice raised the issue of the role of the NOD genetic background in disease development. To address this issue, we studied C57BL/6J ICOS$^{-/-}$ and NOD.*scid* ICOSL$^{-/-}$mice and performed the same behavioral analysis as in ICOS$^{-/-}$ and ICOSL$^{-/-}$ NOD mice. Locotronic and grip strength data showed no difference between KO and WT mice at 52 weeks of age (Fig 2.A, 2.B). When measuring CMAP, a similar motor response was obtained upon stimulation with no significant delay in latency (Fig 2.C). Furthermore, electron microscopy analysis shows no difference histological defects in C57BL/6J ICOS$^{-/-}$ mice in comparison to their WT littermates. H&E staining of nerve sections did not show any infiltrate neither in the nerves of the ICOS KO animals nor in the WT animals (Fig 2.I). NOD SCID animals were also used to evaluate whether the absence of ICOSL expression had deleterious consequences on nerve development or maintenance in the absence of an adaptive immune system and could have impacted peripheral nerve-immune interactions in ICOS$^{-/-}$ and ICOSL$^{-/-}$ NOD mice. Again, our data showed no difference between 1-year-old NOD SCID WT and NOD.*scid* ICOSL$^{-/-}$ animals in the locotronic or the grip strength test (Fig 2.J, 2.K). Electron microscopy images did not reveal any lesions in the nerve in the NOD.*scid* ICOSL$^{-/-}$ compared to the NOD.*scid* WT; there is no reduction in myelinated axon and Remak bundle density nor an increase in defected myelinated axon and defected Remak bundle densities (Fig 2.L, 2.O, 2.P). As for the g-ratio, the measurements made did not reflect any change in myelin thickness between the two groups (Fig 2.M, 2.N). All in all, the knock out of ICOS or ICOSL in C57BL/6J or NOD.*scid* background respectively did not generate a visible phenotype. Behavioral deficits were not observed in genetic backgrounds that do not have a reactive autoimmune system.

Presence of an infiltration in the nerves of the NOD ICOS KO and NOD ICOSL KO mice.

Next, we studied the infiltration in the peripheral nervous system. Flow cytometry was performed on lysates of sciatic and brachial nerves taken from NOD WT, NOD ICOS$^{-/-}$, and NOD ICOSL$^{-/-}$ mice at 35 weeks (Fig 4.A). The nerves of the animals contained TCR+ cells but a higher number of events was seen in the KO groups compared to the WT. Moreover, ICOS$^{-/-}$ and ICOSL$^{-/-}$ NOD nerves were infiltrated with CD4^{+} and CD8+ T-cells. At 35 weeks the NOD ICOS KO showed a strong endoneurial infiltrate with a positive IP staining of CD3, CD4, and CD8 confirming the phenotype of the infiltrate (Fig 4.B). IF staining of F4/80 showed the presence of macrophage in the nerve of the KO animals. Electron microscopy images corroborated the presence of macrophages previously shown by IF (Fig 4.C). Altogether, our data showed a striking infiltration of peripheral nerves by T lymphocytes and macrophages in NOD ICOS$^{-/-}$.

Expression of ICOS and ICOSL during myelination and development

Our next step focused on detecting whether ICOS or ICOSL were expressed in nerves of NOD WT mice between P0 and P21 as well as in primary fibroblasts, primary Schwann cells, DRG co-cultures, and in nerves undergoing myelination in the C57 background. We evaluated the transcriptional levels ICOS/ICOSL during myelination. We isolated sciatic nerves from NOD WT and C57BL/6J WT pups at the beginning of myelination (P0), during myelination (P7 and P14), and at the end of myelination (P23). As expected, ICOS mRNA was not detected by qPCR. However, a stable ICOSL mRNA expression was detected during myelination (Fig 5.A, 5.B). We quantified the levels of ICOS and ICOSL by qPCR in primary cultures of fibroblasts and primary Schwann cells isolated from C57 WT mice. Again, no ICOS mRNA was detected in both cell types. By contrast, ICOSL mRNA was detected in the primary Schwann cells at both the proliferation and differentiation stages with a non-significant reduction in differentiating Schwann cells (Fig 5.C). DRGs were isolated from C57 WT embryos at E13.5 and were placed in culture. qPCR experiments were done at 4 different timepoints; DIV1, DIV3, DIV5, and DIV7. Even though we did not detect any ICOS mRNA expression, we were able to detect ICOSL mRNA in all the timepoints. ICOSL mRNA levels increase between DIV1 and DIV5 and then stabilizes (Fig 5.D). Our data shows that ICOSL is expressed in the PNS by the Schwann cells but ICOS is not detected.

DISCUSSION – CONCLUSION

Upon knocking out ICOS or ICOSL in a NOD background, the autoimmunity shifts from the pancreas towards the peripheral nervous system. Neuropathy, characterized by sensory and motor deficits, develops in both NOD ICOS$^{-/-}$ and NOD ICOSL -/- mice at a different incidence rate. The phenotype appears earlier in the NOD ICOS -/- with the first clinical signs showing between 20-26 weeks compared to the NOD ICOSL -/- where the first signs appears between 30-35 weeks. Even though there is a heterogeneity in the neuropathy onset intra- and inter- KO animals, eventually all -/- mice develop neuropathy as was shown in 1-year-old NOD ICOSL -/- animals that served as a positive control (the NOD ICOS -/- do not survive until 1 year). The NOD ICOS -/- model is preferentially used in some experiments because the neuropathy appears earlier. When the KO models were created there was a bigger fragment of non-NOD origin in the NOD ICOS -/- mouse compared to the NOD ICOSL -/- mouse. However, the non-NOD origin fragments in both KO mice do not overlap with any Insulin Dependent Diabetes (Idd) loci or Quantitative Trait Loci (QTL) linked to neuropathy (Bour-Jordan et al., 2013; Briet et al., 2017; Jiang et al., 2009). Taken together, these data show that the NOD ICOS -/- and NOD ICOSL -/- do not have any genetic differences that might have an impact on the phenotype. Furthermore, our lab has shown that the disease is mediated by CD4+ T-cells since NOD ICOSL -/- CIITA -/- mice do not develop a neuropathy but the NOD ICOSL -/- B2M -/- do. This result shows the crucial role of T-cells in the appearance of neuropathy hence the choice of focusing on the NOD ICOS -/- model.

In addition to behavioral and electrophysiological deficits, myelin injury is present. The extent of nerve injury in IF processed sections is more pronounced in the brachial nerve compared to sciatic nerve in 35 weeks old NOD ICOS -/- and NOD ICOSL -/- mice. As for the mRNA expression of PMP22 and MPZ, we can observe differences between the NOD WT and the KO animals. There is an important inter-group variation in the PMP22 mRNA levels amongst the KO groups. An upregulation or downregulation in myelin genes or protein is detrimental for proper nerve functioning. Interestingly, transcriptional expression of MPZ crashes in NOD ICOS -/- and NOD ICOSL -/- in both sciatic and brachial nerves. It has been previously reported in the literature that the NOD B7.2 -/- has antigens against MPZ (Kim, Jung, Jensen, Dukala, & Soliven, 2008; Louvet et al., 2009) however none were detected in our model. While looking at the g-ratio data of the NOD mice at 35 weeks, there is no observed statistical differences between the WT and KO mice even though the KO animals suffer from neuropathy. In the more damaged brachial nerve, the lack of statistical difference is due to a sampling bias; the measured axons for the g-ratio are the residual axons which are less than 150 axons per animal due to the extensive demyelination. The calculation of myelinated axon and Remak bundle density helps in illustrating this point; there is a significant reduction in the NOD ICOS -/- group and a non-significant reduction in the NOD ICOSL -/- animals. Since the residual axon density was low, we are not able to observe any difference in defected myelinated axons and

Remak bundles in the KO mice compared to the NOD WT. In the sciatic nerve, sampling bias also explains that fact there is no difference in the g-ratio. The nerves are less damaged, and axonal loss is not as prominent as in the brachial nerve. The intra-group variation in the KO animals is greater than the NOD WT because of the heterogeneous nature of autoimmune diseases. For example, within the same pancreas of a diabetic mouse some islets are not infiltrated whereas others are completely destroyed. Similarly to diabetes, the lesions in autoimmune neuropathies are focal in nature (B. C. Kieseier et al., 2018); you may have within the same nerve a fascicle that is more damaged than the others, as well demyelinated areas and "normal" areas within a single fascicle. The axons used for the g-ratio calculation were essentially taken from areas that were not demyelinated because the demyelinated areas would have very little quantifiable axons. Even though there was not a statistically significant difference in myelinated axons or Remak bundle density we can see a significant increase in defected myelinated axons and defected Remak bundle density.

Behavioral, electrophysiological, and histological data from C57 ICOS -/- and NOD SCID ICOSL -/- mice at 1 year do not show any behavioral deficits or infiltration within the nerves. The C57 mice have a fully functional immune system whereas the NOD SCID do not have any T-cells or B-cells. In either case, the animals are not able to develop a spontaneous autoimmune neuropathy. This result was also shown in the C57 B7.2 -/- mice that do not develop any autoimmune neuropathy compared to their NOD B7.2 littermates (Salomon et al., 2001). This shows the importance of having a reactive autoimmune background for the development of neuropathy. The NOD background can therefore be described as having an immune system resembling a gun with either a hair trigger or a missing safety lock. The occurrence of autoimmunity in this animal model would be a result of an enhancement of immunogenic stimuli or a decreased self tolerance. Autoimmunity in the NOD background is explained by a population of T-cells escaping double negative selection in the thymus, recognizing self-antigens, destroying the β-cells of pancreas, and leading to diabetes (Carrasco-Marin, Shimizu, Kanagawa, & Unanue, 1996). However, the reason for the deviation from the pancreas towards the PNS remains unknown. The ICOS-ICOSL interaction in the nerve is needed for self-tolerance but this costimulatrory pathway in the pancreas is required for the development of diabetes. A possible reason for this deviation is epitope spreading; which is the development of an immune response to epitopes that are different from, and that do not cross react with the pathology-causing epitope (Powell & Black, 2001). In pre-diabetic NOD mice, the peri-islets Schwann cells (pSC) surrounding the β-cells of pancreas are injured and there are autoreactive T-cells against pSCs (Winer et al., 2003). Epitope spreading from the β-cells to the pSCs could occur in the context of diabetes and the following could be extrapolated to the Schwann cells present in the nerves. Although the pSCs share the same embryonic origin as the nerve Schwann cells, there are differences between these two subtypes; pSCs are part of the autonomic nervous system and they express GFAP which is present in the Remak bundles (Tsui, Winer, Jakowsky, & Dosch, 2003). Interestingly, pSCs express MPZ which is not typically found in non myelinating Schwann cells (Georgiou & Charlton, 1999).

We have observed a CD4+ and CD8+ T-cell infiltrate in the nerves of the NOD ICOS -/- and the NOD ICOSL -/- mice. However, it is still not known if the immune response is triggered from inside the nerve or if the circulating T-cells become activated outside the nerve and infiltrate it. By looking at our flow cytometry data, we can observe a population of CD4+ and CD8+ T-cells in the NOD WT nerves. This result shows the presence of T-cells in the nerves of NOD animals regardless of the presence or absence of neuropathy. It has been shown that there is an imbalance between Tregs and Effector T-cells (Teff) in the nerve and the spleen of NOD ICOS -/- and NOD ICOSL -/- mice as well as other models of spontaneous autoimmune neuropathy (Meyer zu Hörste et al., 2014; Prevot et al., 2010). This reduction in Tregs, which have immunosuppressive properties and are responsible for the downregulation of induction and proliferation of Teff, could have an impact on the inflammatory status of the nerve. Moreover, the Schwann cells can act as professional APCs by presenting MHCII molecules under pro-inflammatory conditions (Hartlehnert et al., 2017; Meyer zu Horste et al., 2008; zu Hörste et al., 2010). In our KO model, the reduction in Tregs could have played a role in creating a pro-inflammatory milieu thus making the Schwann cells express MHCII molecules. The Schwann cells would then be recognized by resident macrophages of the nerve and the immune response would be initiated (Klein & Martini, 2016; Rudolf Martini et al., 2008).

We have also looked at which cells in the PNS could express ICOS or ICOSL in the PNS RT-qPCR. No ICOS was detected, however ICOSL was expressed in the nerve. A definite candidate that expresses ICOSL is the Schwann cell as it is detected in the primary Schwann cultures at the proliferation and differentiation stages. RT-qPCR performed on DRG Schwann cell co-cultures and on post-natal nerves undergoing myelination show an expression of ICOSL. Nevertheless, there are other cell populations present in the nerve that could potentially express ICOSL such as endoneurial fibroblasts, and resident macrophages.

The NOD ICOS -/- and NOD ICOSL -/- mice are a robust animal model for the study of immune mediated neuropathies. Their phenotype shares a strong resemblance to the CIDP form of autoimmune neuropathy; our model suffers from a chronic non-relapsing-remitting course of the disease with similar electrophysiological and histopathological findings (Lehmann et al., 2019; Mathey et al., 2015). The KO mice have a reduced CMAP with an increased latency, T-cell infiltration in the nerve, and suffer from demyelinated nerves. Both CIDP patients and NOD ICOS -/- and NOD ICOSL -/- mice develop neuropathy in period that correspond to their middle age. There is a difference in the sex ratio; CIDP patients are males with a 3:2 ratio compared to the NOD mouse where the females develop the autoimmune neuropathy. One major difference is the absence of autoantibodies in the serum of NOD WT, NOD WT diabetic, NOD ICOS -/- pre-neuropathic, and NOD ICOS -/- neuropathic (not shown). There is no reaction against myelin proteins, nodal and paranodal proteins (NF-155, NF-186, CNTN, CASPR1), IgG, nor IgM which can be found in CIDP patients (Delmont et al., 2017; Querol et al., 2017). Interestingly, MPZ has been reported as an autoantigen in the NOD B7.2 -/- mouse model of spontaneous autoimmune neuropathy (Kim et al., 2008). Nonetheless, the lack of autoantibodies in the serum does not

discredit the model. As a matter of fact, discrepancies exists in detected antibodies between the NOD model and human T1D. Antibodies against insulin are found in the NOD mouse and rarely in adult human patient (Yu et al., 2000). The opposite is also valid where several autoantibodies solely detected T1D patients such as GAD65 and zinc transporter 8 (Han, Donelan, Wang, Reeves, & Yang, 2013; Roep & Peakman, 2012). A RNA Seq experiment was also performed on sciatic nerves extracted from pre-diabetic NOD WT and pre-neuropathic NOD ICOS -/- mice. The aim of this experiment is to detect any changes in mRNA before the onset of the disease and to verify if the fold changes observed in certain genes are linked to a form of neuropathy seen in humans (ongoing work). In human T1D there are several alleles of predisposition to the disease; HLA-DR3, HLA-DR4, HLA-DQ2, HLA-DQ8 (Baisch et al., 1990; van Belle, Coppieters, & von Herrath, 2011). In patients with immune mediated neuropathies, these alleles have not been reported. However, there is a strong evidence factor for DRB*15 in CIDP patients with anti-NF155 antibodies (Martinez-Martinez et al., 2017).

In conclusion, the abrogation of ICOS or ICOSL in a NOD background results in the development a severe autoimmune neuropathy instead of T1D. This neuropathy is characterized by behavioral and electrophysiological deficits as well as a nerve lesions and myelin defects. However, these deficits were not present in C57BL/6J ICOS -/- or NOD SCID ICOSL -/- proving the importance of having a reactive autoimmune background. The NOD ICOS -/- and NOD ICOSL -/- mice have CD4+ and CD8+ T-cells, and macrophages infiltrating their PNS. Even though our data shows that the Schwann cell expresses ICOSL we still do not have conclusive evidence that the Schwann cell is the APC in our animal model. Our model simply shows the necessity of the ICOS-ICOSL interaction in the maintenance of self tolerance in the nerves of NOD animals. Taken all together, our results provide a robust animal model for immune-mediated neuropathies and in particular CIDP. This model will help in elucidating the mechanisms underlying Schwann cell injury as well as designing a potential immunotheraphy for the treatment of autoimmune neuropathies.

Fig 1: Description of the animal model on a NOD background

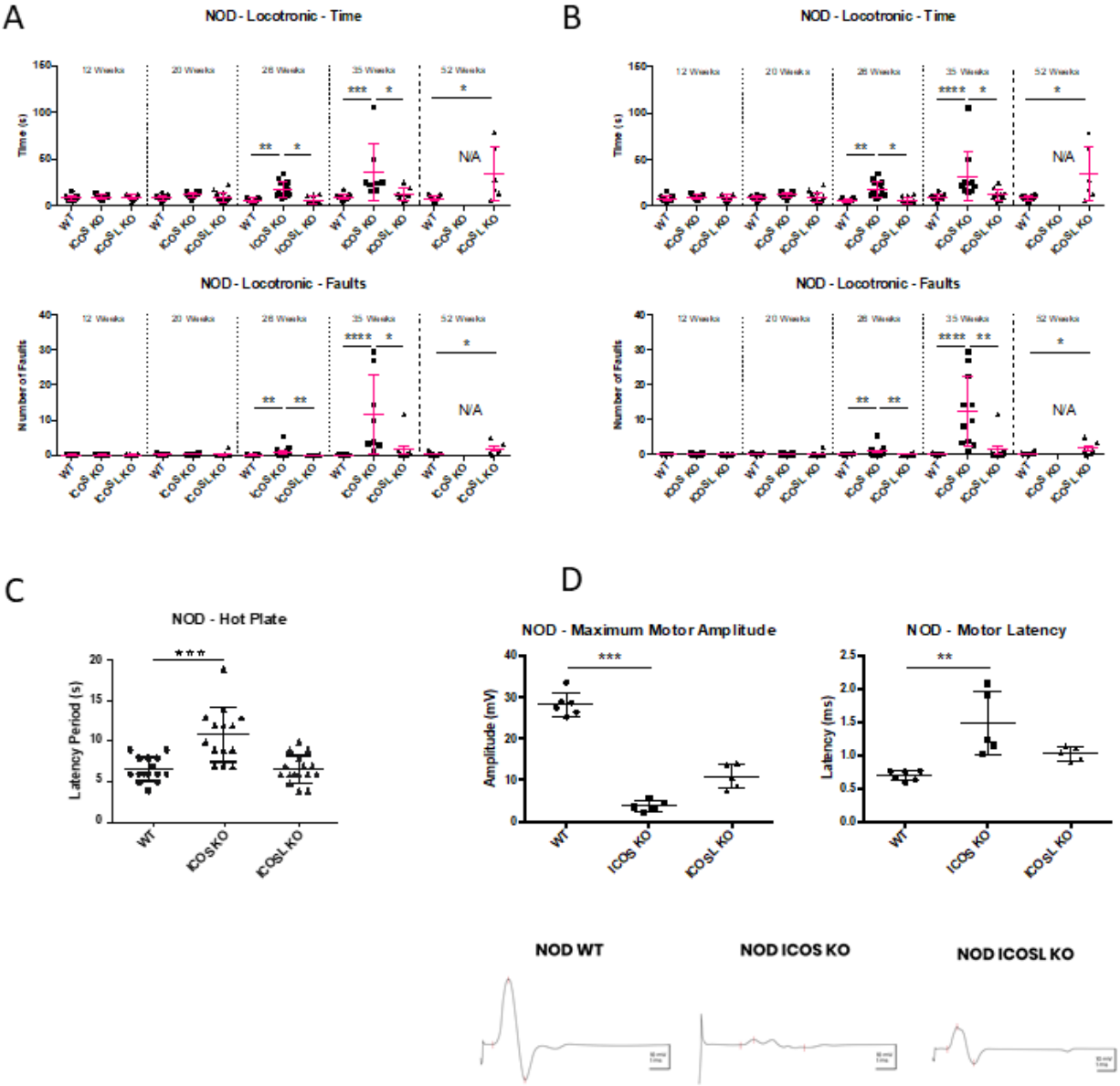
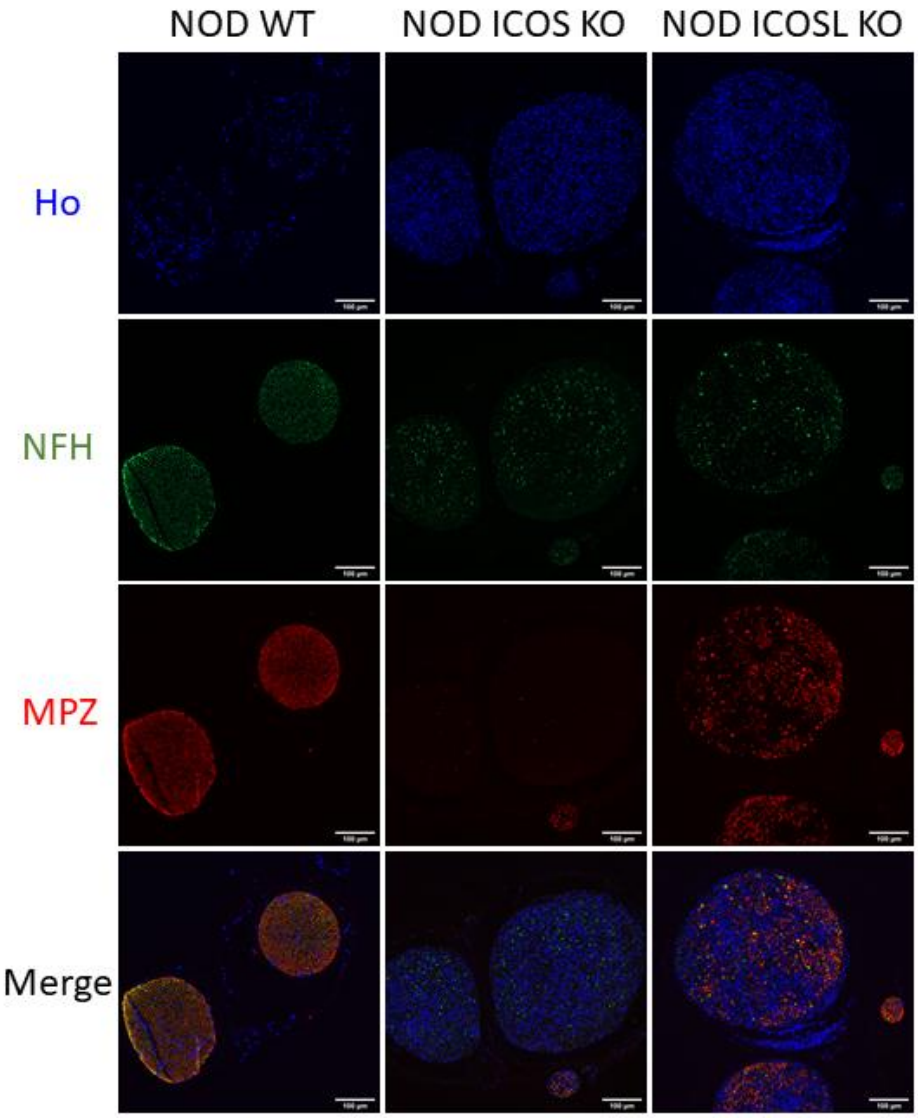


Figure 1: Description of the animal model on a NOD background

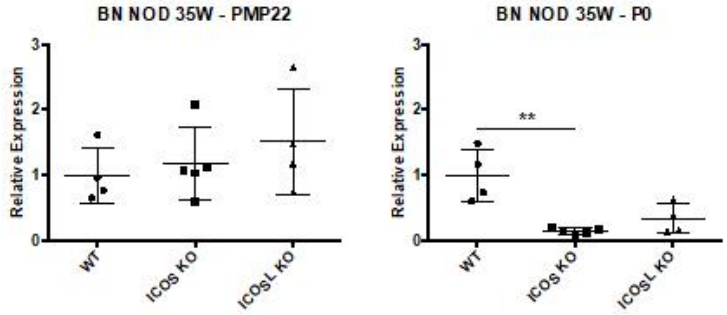
(A) The locotronic and (B) grip strength test were performed of NOD WT, NOD ICOS KO, and NOD ICOSL KO mice at 12, 20, 26, and 35 weeks with at least n=11 per group. The time taken to cross the locotronic and the number of faults was measured as well as the front paw and all four paw grip strength. The same tests were performed on NOD WT and NOD ICOSL KO animals at 52 weeks with at least n=5 per group. (C) The hot plate test was done on all three groups at 35 weeks with at least n=14. (D) CMAP was measured in the tibialis of NOD WT (n=6), NOD ICOS KO (n=5), and NOD ICOSL KO (n=5) at 35 weeks. Each bar represents the mean +/- SD of values obtained. A one-way ANOVA was performed followed by Dunn's Post Hoc analysis to compare all three groups. For the NOD WT and NOD ICOSL KO comparison at 52 weeks a Mann Whitney was done. The α value threshold was set at 5% with the following P-values: * $P<0.05$, ** $P<0.01$, ***$P<0.001$, ****$P<0.0001$. Horizontal lines spanning the two groups compared are present where there is a statistical difference. The lack of asterisk indicates that there is no statistical difference.

Fig 2: Histological analysis of myelin in the NOD animals at 35 weeks

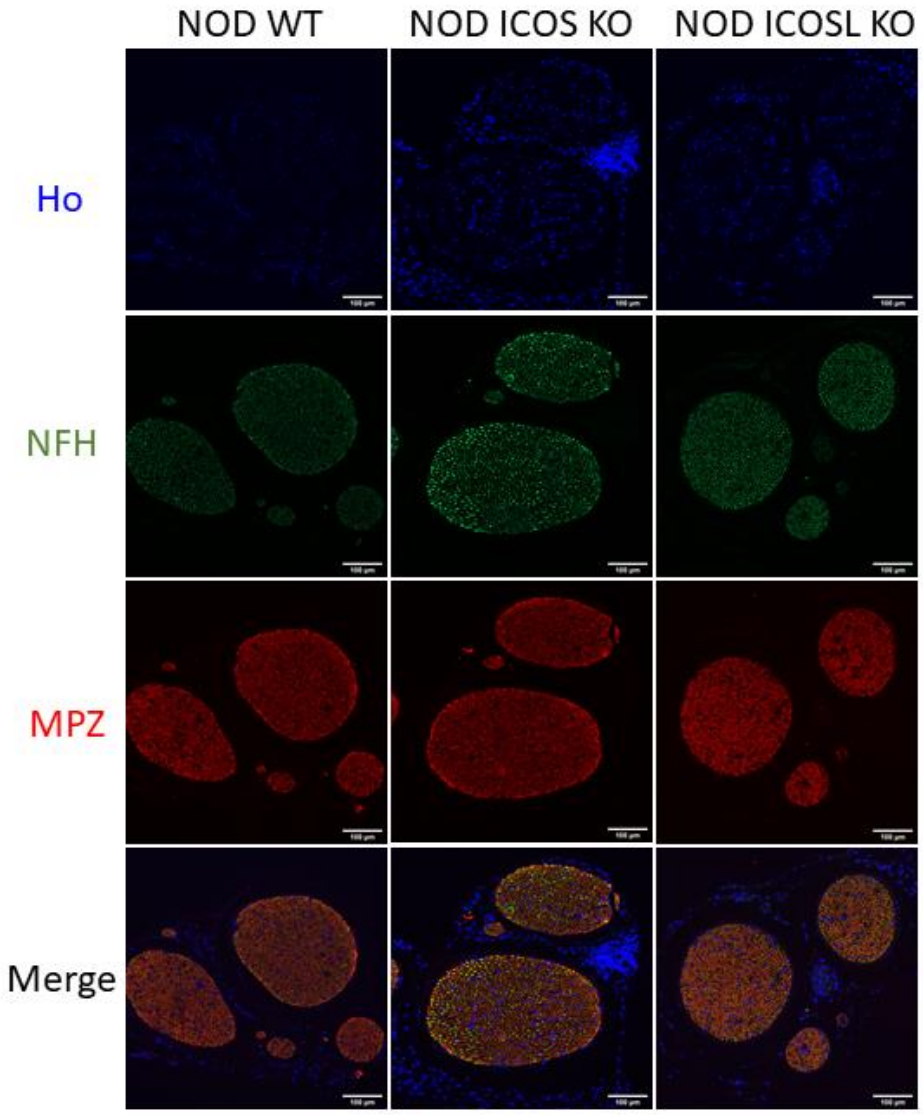
A



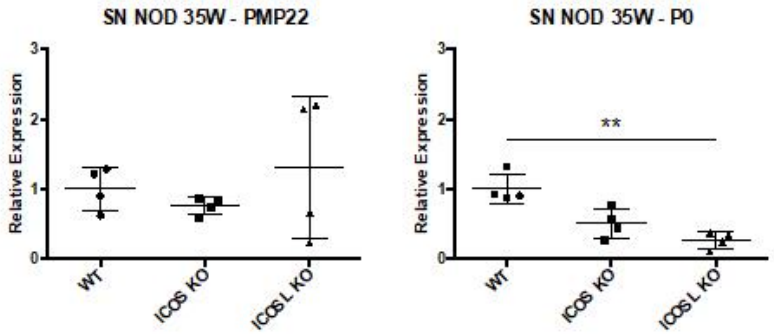
B



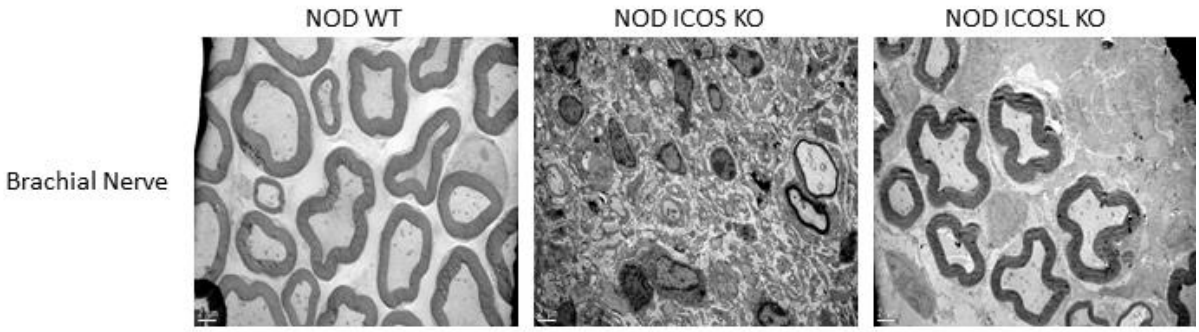
C


NOD WT
NOD ICOS KO
NOD ICOSL KO
Ho
NFH
MPZ
Merge

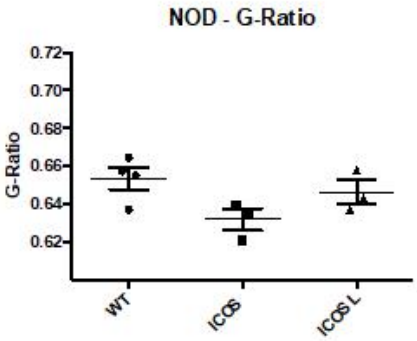
D


SN NOD 35W - PMP22
Relative Expression
WT
ICOS KO
ICOSL KO
SN NOD 35W - P0
**
Relative Expression
WT
ICOS KO
ICOSL KO

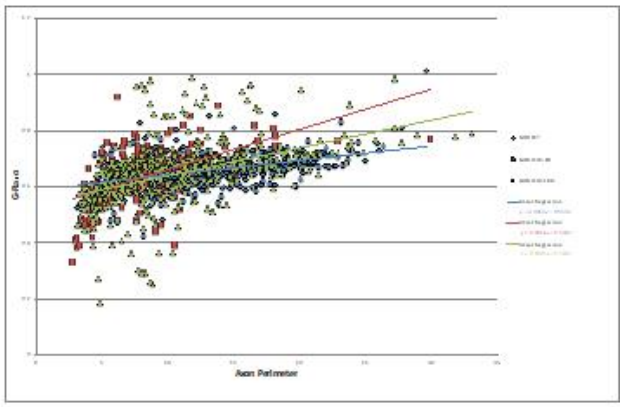
E


NOD WT
NOD ICOS KO
NOD ICOSL KO
Brachial Nerve

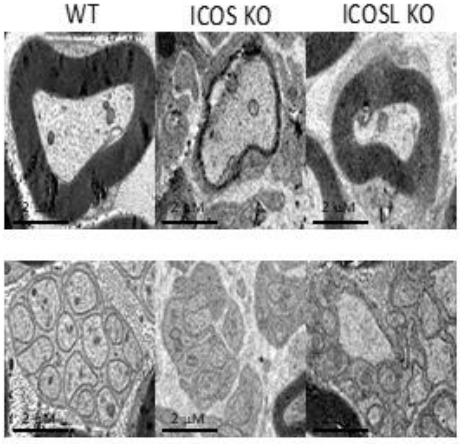
F


NOD - G-Ratio
G-Ratio
0.72
0.70
0.68
0.66
0.64
0.62
WT
ICOS
ICOS L

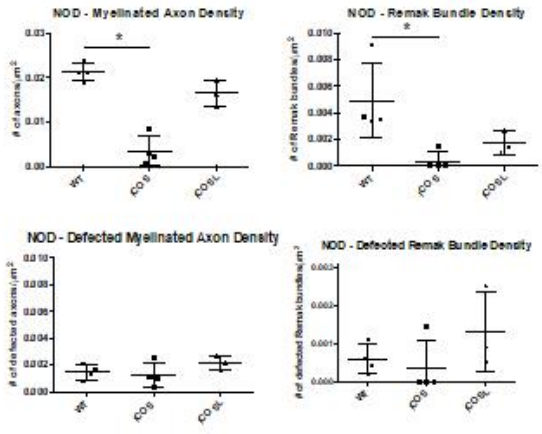
G


G-Ratio
Axon Perimeter

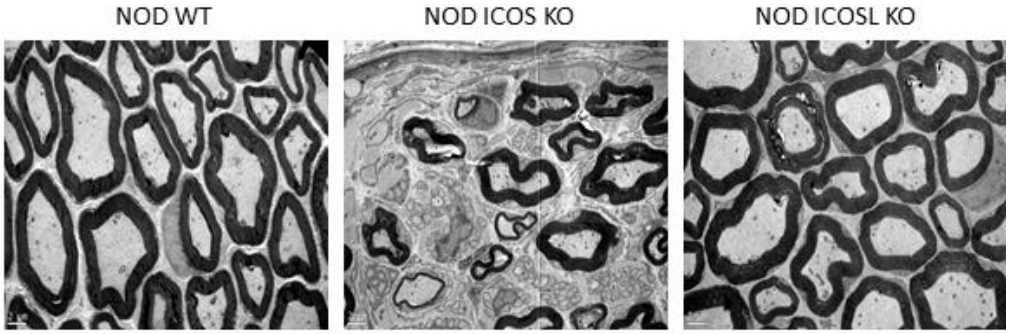
H


WT
ICOS KO
ICOSL KO
2 µM

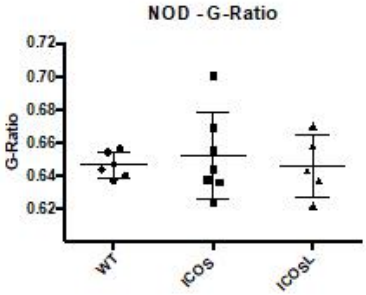
I


NOD - Myelinated Axon Density
NOD - Remak Bundle Density
NOD - Defected Myelinated Axon Density
NOD - Defected Remak Bundle Density
WT
ICOS
ICOSL

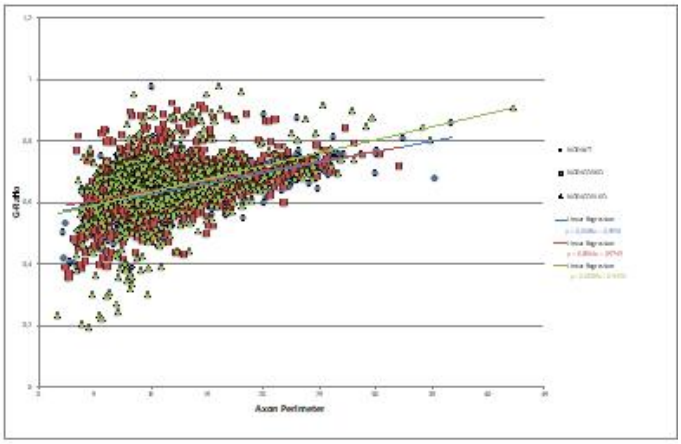
J


NOD WT
NOD ICOS KO
NOD ICOSL KO
Sciatic Nerve

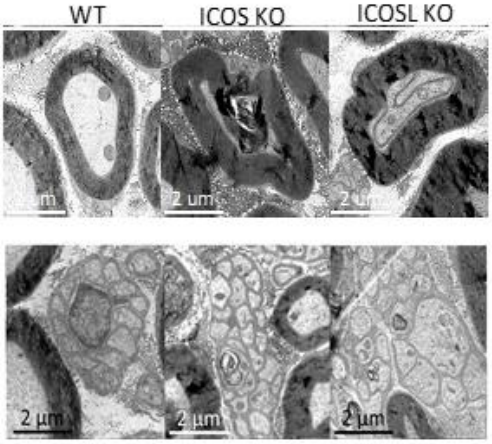
K


NOD - G-Ratio
G-Ratio
0.72
0.70
0.68
0.66
0.64
0.62
WT
ICOS
ICOSL

L


G-Ratio
Axon Perimeter

M


WT
ICOS KO
ICOSL KO
2 um
2 µm

N

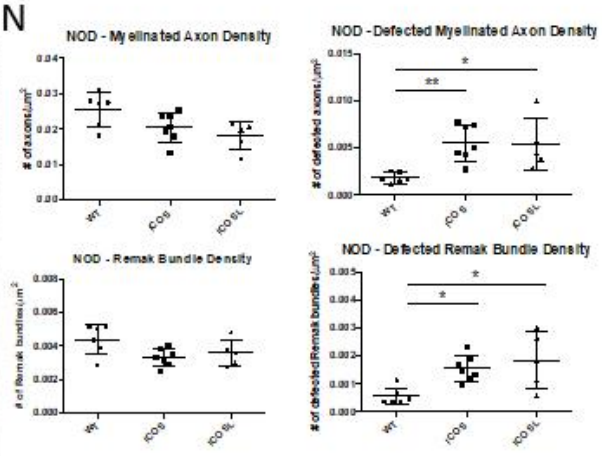
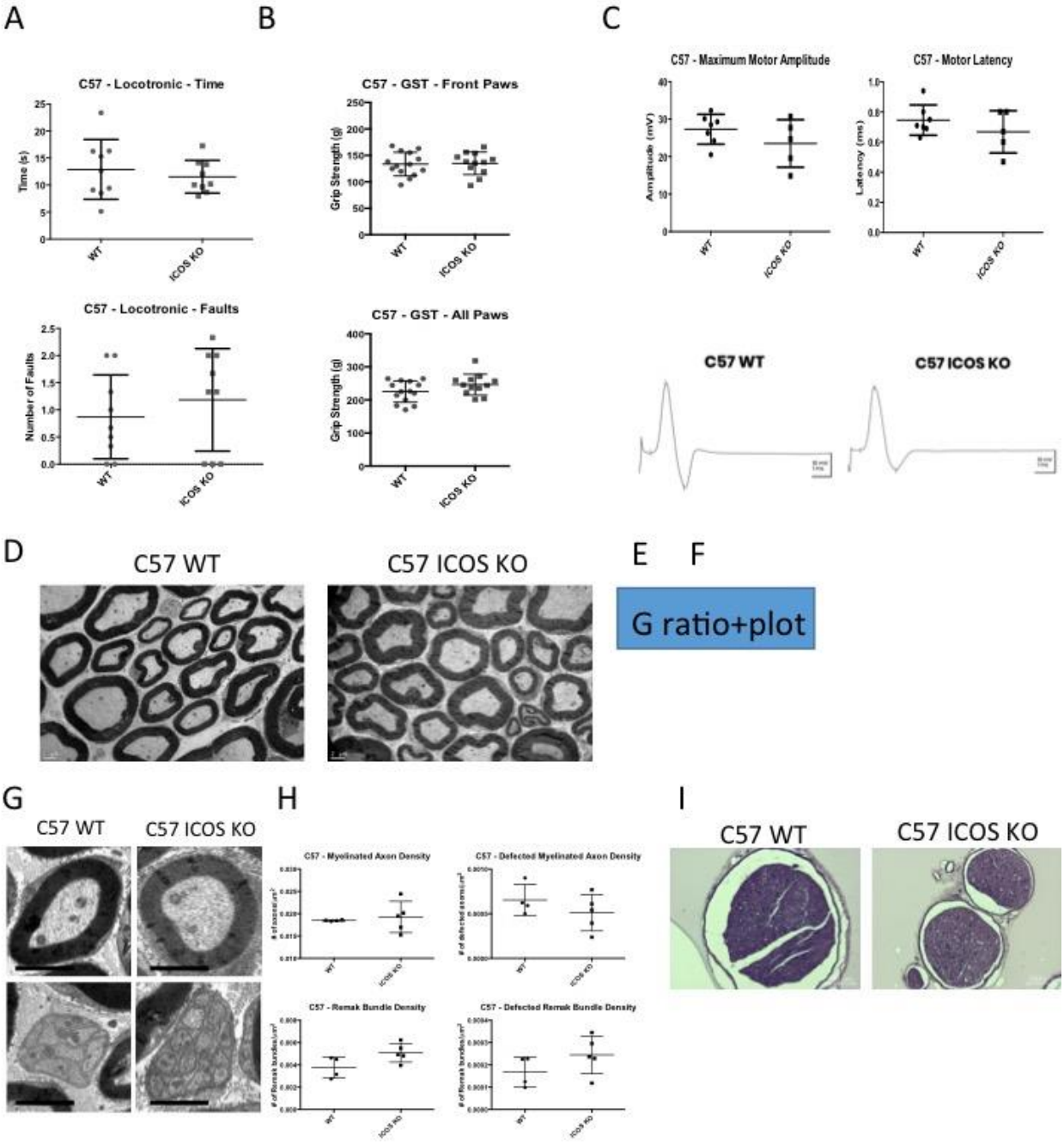

NOD - Myelinated Axon Density
NOD - Defected Myelinated Axon Density
NOD - Remak Bundle Density
NOD - Defected Remak Bundle Density
WT
ICOS
ICOSL

Figure 2: Histological analysis of myelin in the NOD animals at 35 weeks

Representative immunofluorescence image of cross section (A) brachial nerves and (C) sciatic nerves from 35 weeks old NOD WT, NOD ICOS KO, and NOD ICOSL KO stained with MPZ (Schwann cell myelin), NFH (axon), Ho (Hoechst for nuclei). (B) Expression profiles of PMP22, and MPZ in brachial nerves of NOD WT (n=4), NOD ICOS KO (n=5), NOD ICOSL KO (n=4) are represented relative to the NOD WT which was used as the experimental calibrator. GAPDH/HSP60 was used for normalization. (D) Expression profiles of PMP22, and MPZ in sciatic nerves of NOD WT (n=4), NOD ICOS KO (n=4), NOD ICOSL KO (n=4) are represented relative to the NOD WT which was used as the experimental calibrator. RPS26/HSP60 was used for normalization. (E) Brachial nerve and (J) sciatic nerve electron microscopy images from 35 weeks old NOD WT, NOD ICOS KO, and NOD ICOSL KO. Scale is set at 2 μM. The G-ratio was calculated to evaluated myelin thickness in the (F) brachial nerve (NOD WT n=4, NOD ICOS KO n=3, and NOD ICOSL KO n=3) and (K) sciatic nerve (NOD WT n=6, NOD ICOS KO n=7, and NOD ICOSL KO n=5). (G) The brachial nerve G-ratio and (L) sciatic nerve G-ratio were plotted as function of the brachial and sciatic axon perimeter respectively. The linear regression curve for each group is displayed on the graphs. Representative (H) brachial and (M) sciatic myelinated axons and Remak bundles electron microscopy images. Scale bar=2 μM. (I) Brachial and (N) sciatic myelinated axon density, defected myelinated axon density, Remak bundle density, and defected Remak bundle density were calculated in all three groups. Results are represented by the mean +- SD. A one-way ANOVA with a Dunn's pot hoc test was used to study statistical differences between the 3 groups in the sciatic and in the brachial nerve. $P<0.05$: *, $P<0.01$: **.

Fig 3: Description of the controls strains: C57BL/6J and NOD SCID



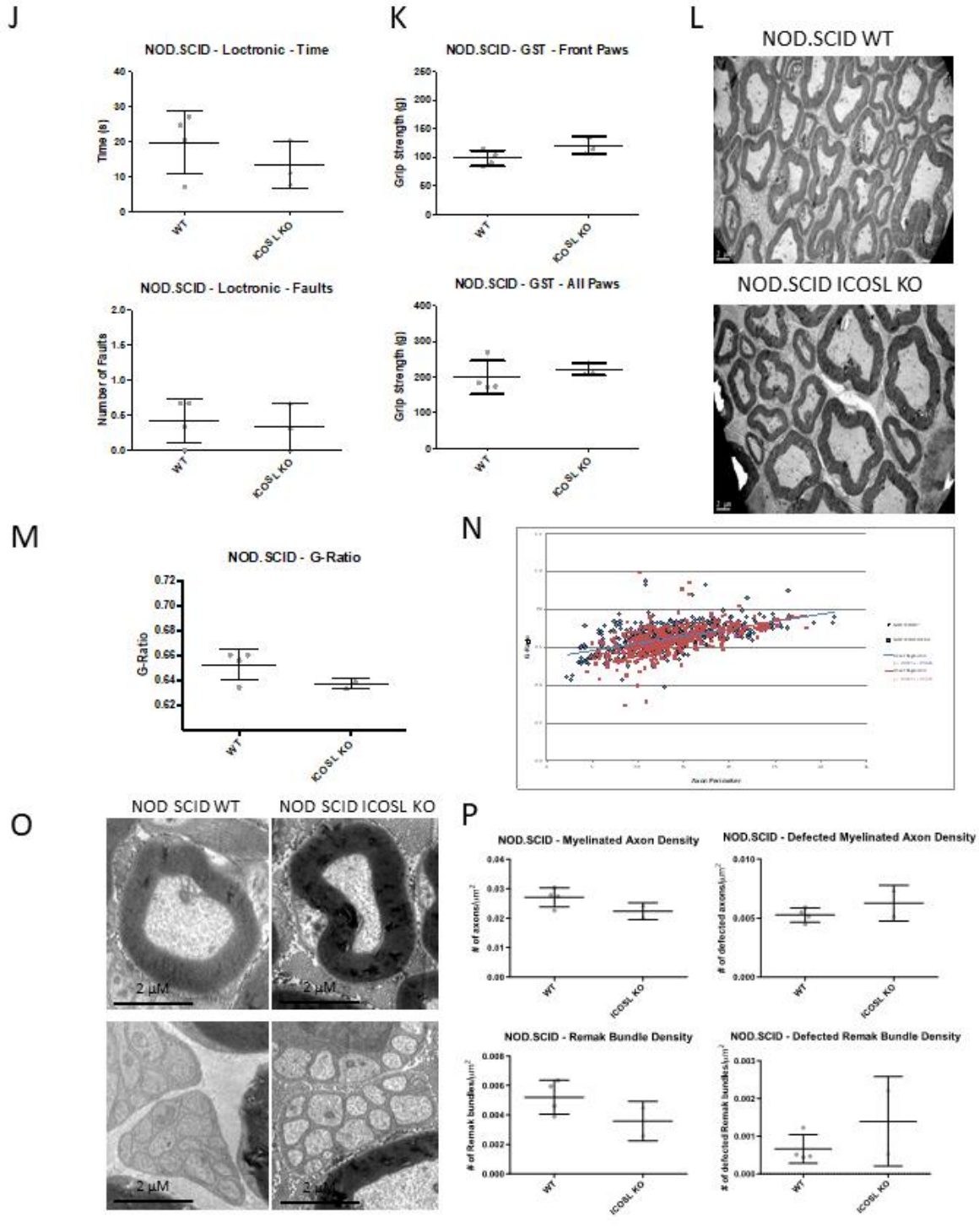
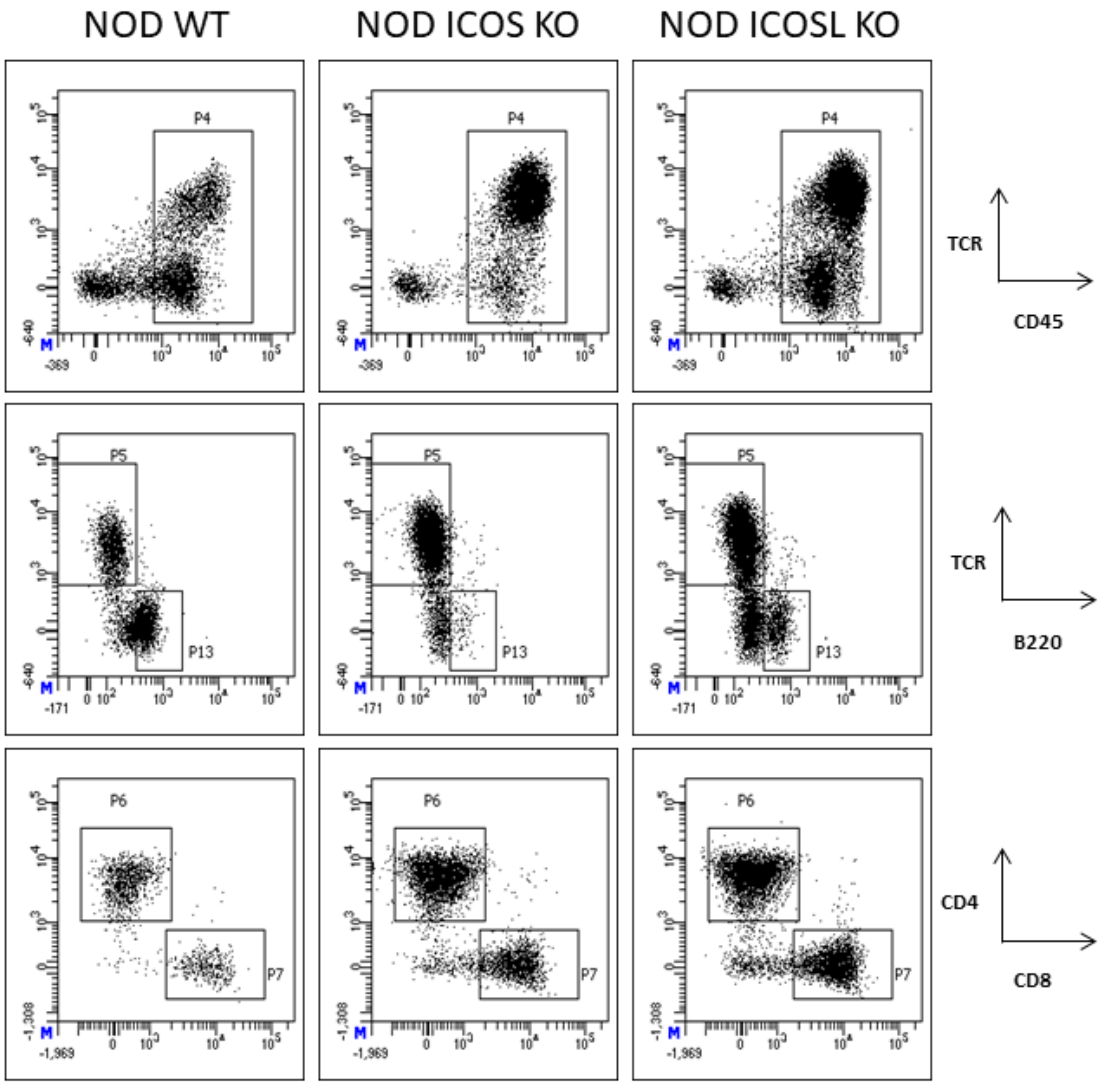

J
NOD.SCID - Loctronic - Time
Time (s)
WT
ICOSL KO
NOD.SCID - Loctronic - Faults
Number of Faults
K
NOD.SCID - GST - Front Paws
Grip Strength (g)
NOD.SCID - GST - All Paws
L
NOD.SCID WT
NOD.SCID ICOSL KO
M
NOD. SCID - G-Ratio
G-Ratio
N
O
NOD SCID WT
NOD SCID ICOSL KO
2 µM
P
NOD.SCID - Myelinated Axon Density
# of axons/µm²
NOD.SCID - Defected Myelinated Axon Density
# of defected axons/µm²
NOD.SCID - Remak Bundle Density
# of Remak bundles/µm²
NOD.SCID - Defected Remak Bundle Density
# of defected Remak bundles/µm²

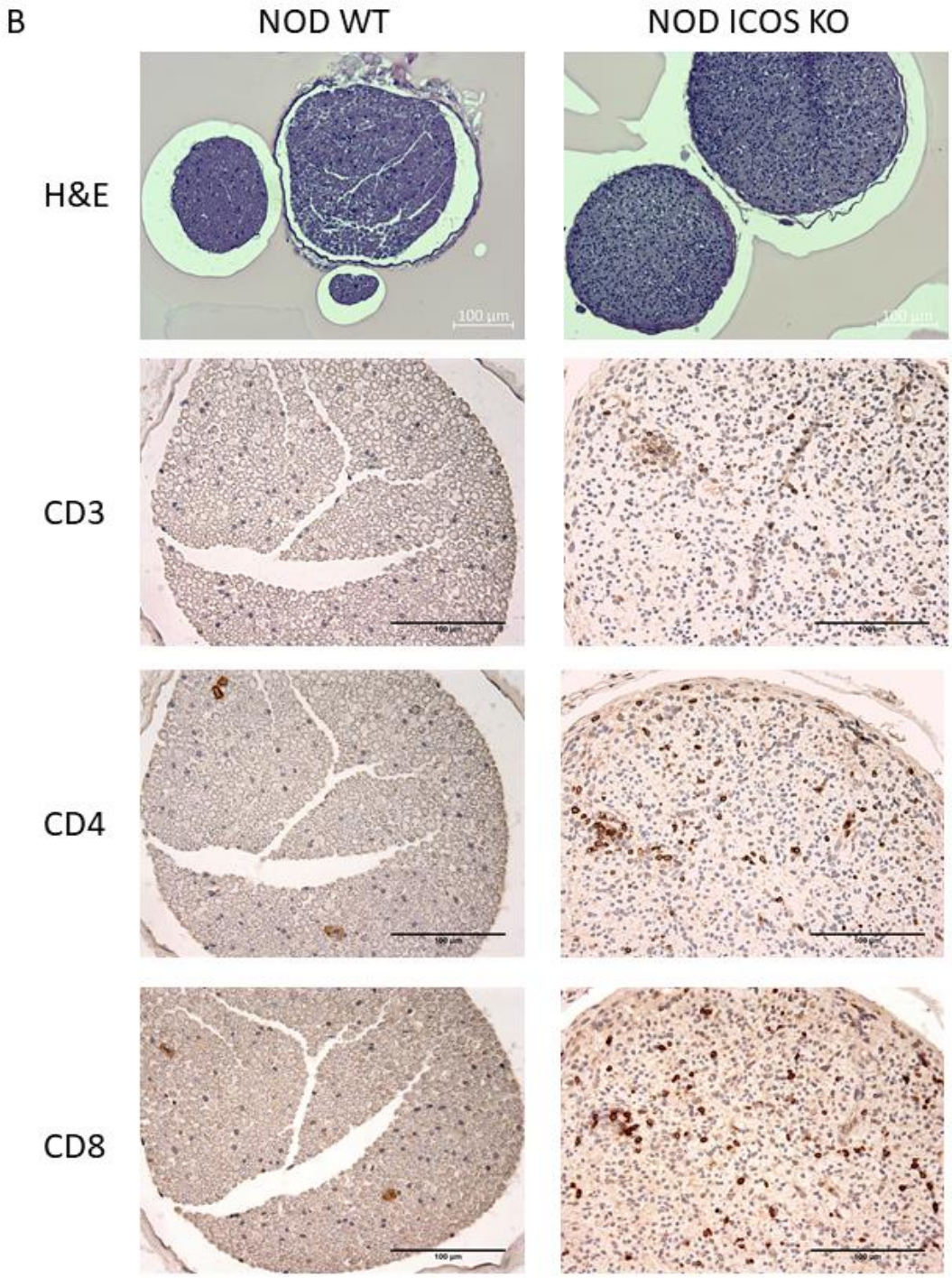
Figure 3: Description of the control strains: C57BL/6J and NOD.SCID

(A) Fine motor coordination and (B) muscular strength were evaluated in C57 WT and C57 ICOS KO with at least n=9 per group. (C) CMAP was measured in the tibialis of both groups with the maximum motor amplitude and motor latency represented. (D) Sciatic nerve electron microscopy images from 52 weeks old C57 WT and C57 ICOS KO. Scale is set at 2 µM. (E F) G-Ratio and plot pending. (G) Representative myelinated axons and Remak bundles electron microscopy images. Scale bar=2 µM. (H) Myelinated axon density, defected myelinated axon density, Remak bundle density, and defected Remak bundle density were calculated in both groups. (I) Representative images of nerve cross sections stained with H&E show the absence of infiltration in the nerve. Scale bar=100 µM. (J) The locotronic test and (K) the grip strength test were performed on NOD.SCID WT (n=4) and NOD.SCID ICOSL KO (n=3). (L) Electron microscopy images of ultra-thin nerve sections provide a general overview of the myelin state. Scale bar=2 µM. (M) The myelin thickness of the axons was estimated by G-ratio (NOD.SCID WT (n=4) and NOD.SCID ICOSL KO (n=2)). (N) G-ratio vs. axon perimeter was plotted to show myelinated axon size distribution along with the linear regression curve for each group. (O) Representative myelinated axons and Remak bundles electron microscopy images. Scale bar=2 µM. (P) Myelinated axon density, defected myelinated axon density, Remak bundle density, and defected Remak bundle density were calculated in both groups. Results are represented by the mean +- SD. Statistical significance was assessed by a Mann-Whitney test.

Fig 4: Presence of an infiltration in the nerves of the NOD ICOS KO and NOD ICOSL KO mice

A




B
NOD WT
NOD ICOS KO
H&E
CD3
CD4
CD8
100 µm

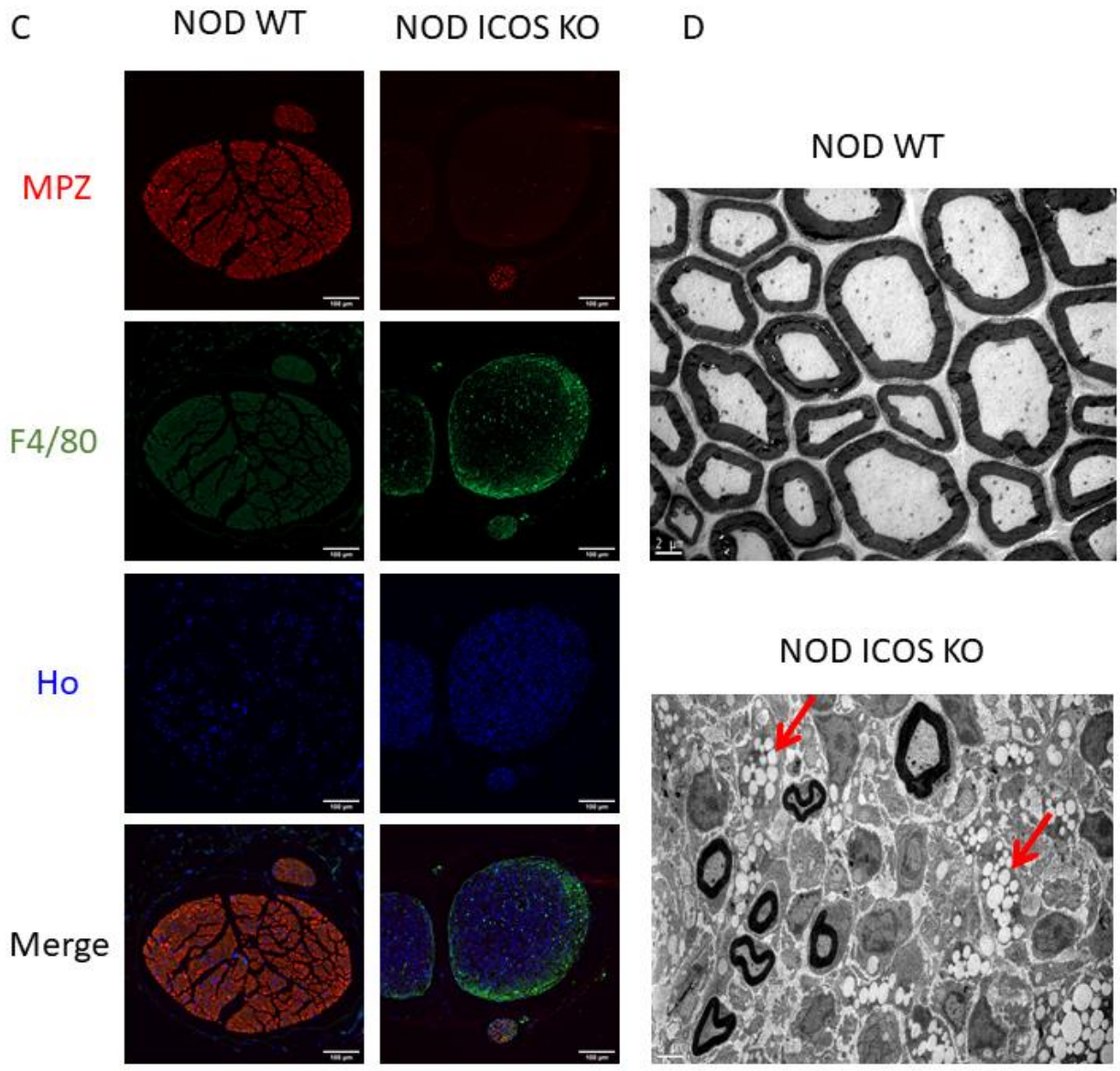

C
NOD WT
NOD ICOS KO
D
MPZ
F4/80
Ho
Merge
NOD WT
NOD ICOS KO

Figure 4: Presence of an infiltration in the nerves of the NOD ICOS KO and NOD ICOSL KO mice.

(A) Dot plots showing the presence of TCR+, CD4+, and CD8+ positive cells in the nerves of NOD WT (n=11), NOD ICOS KO (n=7), and NOD ICOSL KO (n=5) at 35 weeks. (B) Representative cross sections of NOD WT and NOD ICOS KO nerves showing the presence of infiltration by H&E stain and immunoperoxidase stain for CD3, CD4, CD8. (C) F4/80 (macrophages) and MPZ immunofluorescence stain of nerve cross section showing the presence of macrophages and electron microscopy ultra-thin images with a macrophage infiltration (red arrows). Nuclei were stained with Hoechst. Scale bar is set at 100 μM.

Fig 5: Expression of ICOS/ICOSL during myelination and development

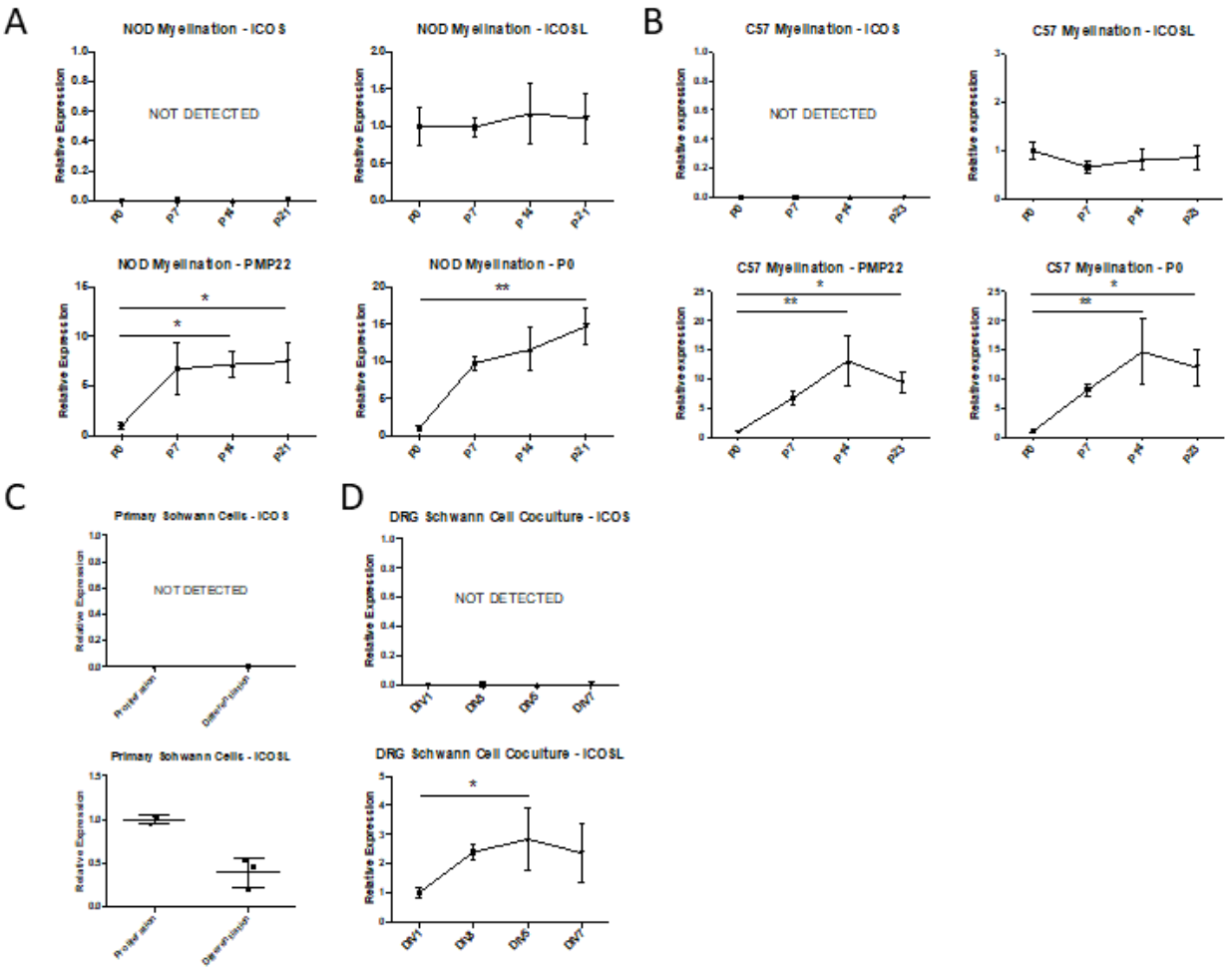
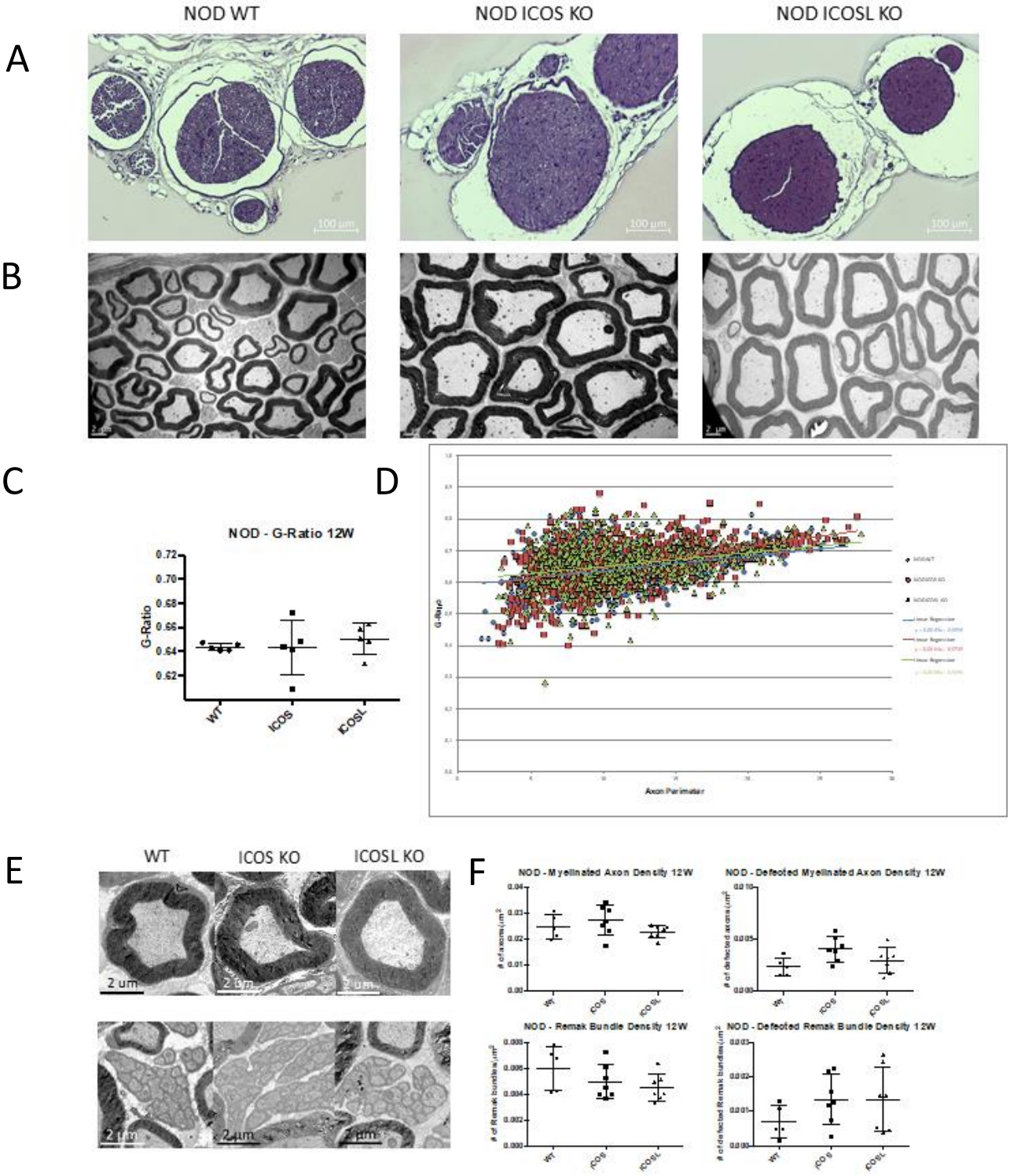


Figure 5: Expression of ICOS and ICOSL during myelination and development

(A) Expression profiles of ICOS, ICOSL, PMP22, and MPZ at P0 (n=5), P7 (n=4), P14 (n=4), and P21 (n=4) from NOD WT mice are represented relative to P0 which was used as the experimental calibrator. ACTB/HSP60 was used for normalization. (B) Expression profiles of ICOS, ICOSL, PMP22, and MPZ at P0 (n=5), P7 (n=5), P14 (n=4), and P21 (n=6) from C57 WT mice are represented relative to P0 which was used as the experimental calibrator. ACTB/RPL13A was used for normalization. (C) Expression profiles of ICOS and ICOSL were studied in proliferating (n=3) and differentiating (n=3) primary Schwann cells. Results were represented as a comparison to the proliferation group. MRLP10/SDHA was used for normalization. (D) Expression profiles of ICOS, ICOSL, PMP22, and MPZ at DIV1 (n=5), DIV3 (n=5), DIV5 (n=4), and DIV7 (n=5) from C57 WT embryos at E13.5 are represented relative to DIV1 which was used as the experimental calibrator. PPIA/TBP was used for normalization. Results are represented by the mean +- SD. Statistical significance was assessed by a one-way ANOVA follow by a Dunn's post hoc test when comparing three groups or a Mann-Whitney test when comparing two groups with * $P<0.05$, ** $P<0.01$.

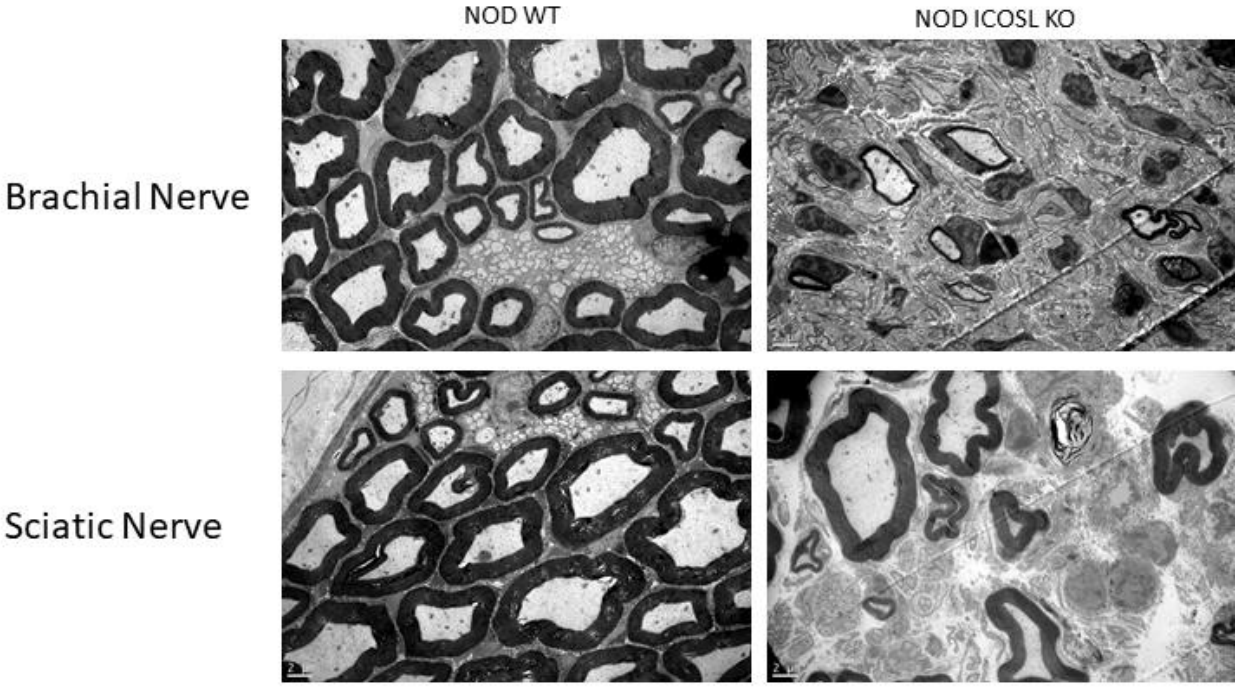
Supplementary 1: Histological analysis of myelin in the NOD animals at 12 weeks



Supplementary 1: Histological analysis of myelin in the NOD animals at 12 weeks

(A) Representative cross sections of NOD WT, NOD ICOS KO, and NOD ICOSL KO nerves stained with H&E. (B) Sciatic nerve electron microscopy images from 12 weeks old NOD WT, NOD ICOS KO, and NOD ICOSL KO. Scale is set at 2 μM. The G-ratio was calculated to evaluated myelin thickness in the (C) sciatic nerve (NOD WT n=5, NOD ICOS KO n=5, and NOD ICOSL KO n=5). (D) The G-ratio was plotted as function of sciatic axon perimeter. The linear regression curve for each group is displayed on the graphs. (E) Representative sciatic myelinated axons and Remak bundles electron microscopy images. Scale bar=2 μM. (F) Sciatic myelinated axon density, defected myelinated axon density, Remak bundle density, and defected Remak bundle density were calculated in all three groups. Results are represented by the mean +- SD.

Supplementary 2: Electron microscopy of NOD WT and NOD ICOSL KO at 1 year



Supplementary 2: Electron microscopy of NOD WT and NOD ICOSL KO at 1 year

Brachial nerve and sciatic nerve electron microscopy images from 1-year-old NOD WT and NOD ICOSL KO. Scale is set at 2 μM.

REFERENCES

Baisch, J. M., Weeks, T., Giles, R., Hoover, M., Stastny, P., & Capra, J. D. (1990). Analysis of HLA-DQ Genotypes and Susceptibility in Insulin-Dependent Diabetes Mellitus. *New England Journal of Medicine, 322*(26), 1836-1841. doi:10.1056/nejm199006283222602

Bour-Jordan, H., Thompson, H. L., Giampaolo, J. R., Davini, D., Rosenthal, W., & Bluestone, J. A. (2013). Distinct genetic control of autoimmune neuropathy and diabetes in the non-obese diabetic background. *J Autoimmun, 45*, 58-67. doi:10.1016/j.jaut.2013.06.005

Briet, C., Bourdenet, G., Rogner, U. C., Becourt, C., Tardivel, I., Drouot, L., . . . Boitard, C. (2017). The Spontaneous Autoimmune Neuromyopathy in ICOSL(-/-) NOD Mice Is CD4(+) T-Cell and Interferon-γ Dependent. *Front Immunol, 8*, 287. doi:10.3389/fimmu.2017.00287

Carrasco-Marin, E., Shimizu, J., Kanagawa, O., & Unanue, E. R. (1996). The class II MHC I-Ag7 molecules from non-obese diabetic mice are poor peptide binders. *J Immunol, 156*(2), 450-458.

Delmont, E., Manso, C., Querol, L., Cortese, A., Berardinelli, A., Lozza, A., . . . Devaux, J. J. (2017). Autoantibodies to nodal isoforms of neurofascin in chronic inflammatory demyelinating polyneuropathy. *Brain, 140*(7), 1851-1858. doi:10.1093/brain/awx124

Georgiou, J., & Charlton, M. P. (1999). Non-myelin-forming perisynaptic schwann cells express protein zero and myelin-associated glycoprotein. *Glia, 27*(2), 101-109. doi:10.1002/(sici)1098-1136(199908)27:2<101::aid-glia1>3.0.co;2-h

Han, S., Donelan, W., Wang, H., Reeves, W., & Yang, L.-J. (2013). Novel autoantigens in type 1 diabetes. *Am J Transl Res, 5*(4), 379-392.

Hartlehnert, M., Derksen, A., Hagenacker, T., Kindermann, D., Schäfers, M., Pawlak, M., . . . Meyer Zu Horste, G. (2017). Schwann cells promote post-traumatic nerve inflammation and neuropathic pain through MHC class II. *Sci Rep, 7*(1), 12518. doi:10.1038/s41598-017-12744-2

Hichor, M., Sundaram, V. K., Eid, S. A., Abdel-Rassoul, R., Petit, P. X., Borderie, D., . . . Massaad, C. (2018). Liver X Receptor exerts a protective effect against the oxidative stress in the peripheral nerve. *Sci Rep, 8*(1), 2524. doi:10.1038/s41598-018-20980-3

Jiang, F., Yoshida, T., Nakaki, F., Terawaki, S., Chikuma, S., Kato, Y., . . . Okazaki, T. (2009). Identification of QTLs that modify peripheral neuropathy in NOD.H2b-Pdcd1-/- mice. *Int Immunol, 21*(5), 499-509. doi:10.1093/intimm/dxp020

Kieseier, B. C., Mathey, E. K., Sommer, C., & Hartung, H.-P. (2018). Immune-mediated neuropathies. *Nature Reviews Disease Primers, 4*(1), 1-23.

Kim, H. J., Jung, C. G., Jensen, M. A., Dukala, D., & Soliven, B. (2008). Targeting of myelin protein zero in a spontaneous autoimmune polyneuropathy. *J Immunol, 181*(12), 8753-8760. doi:10.4049/jimmunol.181.12.8753

Klein, D., & Martini, R. (2016). Myelin and macrophages in the PNS: An intimate relationship in trauma and disease. *Brain Res, 1641*(Pt A), 130-138. doi:10.1016/j.brainres.2015.11.033

Lehmann, H. C., Burke, D., & Kuwabara, S. (2019). Chronic inflammatory demyelinating polyneuropathy: update on diagnosis, immunopathogenesis and treatment. *J Neurol Neurosurg Psychiatry, 90*(9), 981-987. doi:10.1136/jnnp-2019-320314

Louvet, C., Kabre, B. G., Davini, D. W., Martinier, N., Su, M. A., DeVoss, J. J., . . . Bluestone, J. A. (2009). A novel myelin P0-specific T cell receptor transgenic mouse develops a fulminant autoimmune peripheral neuropathy. *J Exp Med, 206*(3), 507-514. doi:10.1084/jem.20082113

Martinez-Martinez, L., Lleixà, M. C., Boera-Carnicero, G., Cortese, A., Devaux, J., Siles, A., . . . Querol, L. (2017). Anti-NF155 chronic inflammatory demyelinating polyradiculoneuropathy strongly associates to HLA-DRB15. *J Neuroinflammation, 14*(1), 224. doi:10.1186/s12974-017-0996-1

Martini, R., Fischer, S., López-Vales, R., & David, S. (2008). Interactions between Schwann cells and macrophages in injury and inherited demyelinating disease. *Glia, 56*(14), 1566-1577. doi:10.1002/glia.20766

Mathey, E. K., Park, S. B., Hughes, R. A., Pollard, J. D., Armati, P. J., Barnett, M. H., . . . Lin, C. S. (2015). Chronic inflammatory demyelinating polyradiculoneuropathy: from pathology to phenotype. *J Neurol Neurosurg Psychiatry, 86*(9), 973-985. doi:10.1136/jnnp-2014-309697

Meyer zu Hörste, G., Cordes, S., Mausberg, A. K., Zozulya, A. L., Wessig, C., Sparwasser, T., . . . Kieseier, B. C. (2014). FoxP3+ regulatory T cells determine disease severity in rodent models of inflammatory neuropathies. *PLoS One, 9*(10), e108756. doi:10.1371/journal.pone.0108756

Meyer zu Horste, G., Hu, W., Hartung, H. P., Lehmann, H. C., & Kieseier, B. C. (2008). The immunocompetence of Schwann cells. *Muscle Nerve, 37*(1), 3-13. doi:10.1002/mus.20893

Powell, A. M., & Black, M. M. (2001). Epitope spreading: protection from pathogens, but propagation of autoimmunity? *Clinical and Experimental Dermatology, 26*(5), 427-433. doi:10.1046/j.1365-2230.2001.00852.x

Prevot, N., Briet, C., Lassmann, H., Tardivel, I., Roy, E., Morin, J., . . . Boitard, C. (2010). Abrogation of ICOS/ICOS ligand costimulation in NOD mice results in autoimmune deviation toward the neuromuscular system. *Eur J Immunol, 40*(8), 2267-2276. doi:10.1002/eji.201040416

Querol, L., Devaux, J., Rojas-Garcia, R., & Illa, I. (2017). Autoantibodies in chronic inflammatory neuropathies: diagnostic and therapeutic implications. *Nat Rev Neurol, 13*(9), 533-547. doi:10.1038/nrneurol.2017.84

Roep, B. O., & Peakman, M. (2012). Antigen targets of type 1 diabetes autoimmunity. *Cold Spring Harb Perspect Med, 2*(4), a007781. doi:10.1101/cshperspect.a007781

Salomon, B., Rhee, L., Bour-Jordan, H., Hsin, H., Montag, A., Soliven, B., . . . Bluestone, J. A. (2001). Development of spontaneous autoimmune peripheral polyneuropathy in B7-2-deficient NOD mice. *J Exp Med, 194*(5), 677-684. doi:10.1084/jem.194.5.677

Sundaram, V. K., Barakat, R., Massaad, C., & Grenier, J. (2020). Retracing Schwann cell developmental transitions in embryonic dissociated DRG cultures. *bioRxiv*, 2020.2007.2031.231258. doi:10.1101/2020.07.31.231258

Sundaram, V. K., Sampathkumar, N. K., Massaad, C., & Grenier, J. (2019). Optimal use of statistical methods to validate reference gene stability in longitudinal studies. *PLoS One, 14*(7), e0219440. doi:10.1371/journal.pone.0219440

Tsui, H., Winer, S., Jakowsky, G., & Dosch, H. M. (2003). Neuronal elements in the pathogenesis of type 1 diabetes. *Rev Endocr Metab Disord, 4*(3), 301-310. doi:10.1023/a:1025374531151

van Belle, T. L., Coppieters, K. T., & von Herrath, M. G. (2011). Type 1 diabetes: etiology, immunology, and therapeutic strategies. *Physiol Rev, 91*(1), 79-118. doi:10.1152/physrev.00003.2010

Winer, S., Tsui, H., Lau, A., Song, A., Li, X., Cheung, R. K., . . . Dosch, H. M. (2003). Autoimmune islet destruction in spontaneous type 1 diabetes is not beta-cell exclusive. *Nat Med, 9*(2), 198-205. doi:10.1038/nm818

Yu, L., Robles, D. T., Abiru, N., Kaur, P., Rewers, M., Kelemen, K., & Eisenbarth, G. S. (2000). Early expression of antiinsulin autoantibodies of humans and the NOD mouse: Evidence for early determination of subsequent diabetes. *Proceedings of the National Academy of Sciences, 97*(4), 1701-1706. doi:10.1073/pnas.040556697

zu Hörste, G. M., Heidenreich, H., Mausberg, A. K., Lehmann, H. C., ten Asbroek, A. L., Saavedra, J. T., . . . Kieseier, B. C. (2010). Mouse Schwann cells activate MHC class I and II restricted T-cell responses, but require external peptide processing for MHC class II presentation. *Neurobiology of disease, 37*(2), 483-490.

CHAPTER IV: DISCUSSION

1. Phenotype differences between NOD ICOS-/- and NOD ICOSL-/-

In the used animal model, neuropathy develops in both NOD ICOS-/- and NOD ICOSL-/- mice but at a different incidence rate. The phenotype appears earlier in the NOD ICOS-/- with the first clinical signs showing between 20-26 weeks compared to the NOD ICOSL-/- where the first signs appears between 30-35 weeks. Even though there is a heterogeneity in the neuropathy onset intra- and inter- KO animals, eventually all KO mice develop neuropathy as was shown in 1-year-old NOD ICOSL-/- animals that served as a positive control (the NOD ICOS-/- do not survive until 1 year). The NOD ICOS-/- model is preferentially used in some experiments because the neuropathy appears earlier.

When the KO models were created there was a bigger fragment of non-NOD origin in the NOD ICOS-/- mouse compared to the NOD ICOSL-/- mouse. However, the non-NOD origin fragments in both KO mice do not overlap with any Insulin Dependent Diabetes (Idd) loci or Quantitative Trait Loci (QTL) linked to neuropathy (Bour-Jordan et al., 2013; Briet et al., 2017; Jiang et al., 2009). Taken altogether, these data show that the NOD ICOS-/- and NOD ICOSL-/- do not have any genetic differences that might have an impact on the phenotype.

Furthermore, our lab has shown that the disease is mediated by CD4+ T-cells since NOD ICOSL-/- CIITA-/- mice do not develop a neuropathy but the NOD ICOSL-/- B2M-/- do. This result shows the crucial role of T-cells in the appearance of neuropathy hence the choice of focusing on the NOD ICOS-/- model.

2. Histological differences between NOD ICOS-/- and NOD ICOSL-/-

We can observe that the extent of nerve injury is more pronounced in the brachial nerve compared to sciatic nerve in IF processed sections of 35 weeks old NOD ICOS-/- and NOD ICOSL-/- mice. As for the mRNA expression of PMP22 and MPZ, we can observe differences between the NOD WT and the KO animals. There is an important inter-group variation in the PMP22 mRNA levels amongst the KO groups. An upregulation or downregulation in myelin genes or protein is detrimental for proper nerve functioning. Interestingly, transcriptional expression of MPZ crashes in NOD ICOS-/- and NOD ICOSL-/- in both sciatic and brachial nerves. It has been previously reported in the literature that the NOD B7.2-/- has antigens against MPZ (Kim et al., 2008; Louvet et al., 2009) however none were detected in our model.

While looking at the g-ratio data of the NOD mice at 35 weeks, there is no observed statistical differences between the WT and KO mice even though the KO animals suffer from neuropathy. In the more damaged brachial nerve, the lack of statistical difference is due to a sampling bias; the measured axons for the g-ratio are the residual axons which were less than 150 axons per animal due to the extensive demyelination. The calculation of myelinated axon and Remak bundle density helps in illustrating this point; there is a significant reduction in the NOD ICOS-/- group and a non-significant reduction in the NOD ICOSL-/- animals. Since the residual axon density was low, we are not able to observe any difference in defected myelinated axons and Remak bundles in the KO mice compared to the NOD WT. A structure was deemed to be defected based on certain criteria. Myelinated axons were considered defected if the following anomalies were present: axon fragmentation, enlarged mitochondria, uncompact myelin. As for Remak bundles, they would be labeled as defected if the following anomalies were found:

hypertrophied axons, absence of cytoplasm, enlarged mitochondria, large vacuoles inside the axons.

In the sciatic nerve, sampling bias also explains that fact there is no difference in the g-ratio. The nerves are less damaged, and axonal loss is not as prominent as in the brachial nerve. The intra-group variation in the KO animals is greater than the NOD WT because of the heterogeneous nature of autoimmune diseases. For example, within the same pancreas of a diabetic mouse some islets are not infiltrated whereas others are completely destroyed. Similarly to diabetes, the lesions in autoimmune neuropathies are focal in nature (B. C. Kieseier et al., 2018); you may have within the same nerve a fascicle that is more damaged than the others, as well demyelinated areas and "normal" areas within a single fascicle. The axons used for the g-ratio calculation were essentially taken from areas that were not demyelinated because the demyelinated areas would have very little quantifiable axons. Even though there was not a statistically significant difference in myelinated axons or Remak bundle density we can see a significant increase in defected myelinated axons and defected Remak bundle density.

Data from 1-year-old NOD ICOSL-/- animals confirm that both brachial and sciatic nerves are damaged, showing that the neuropathy is progressive.

The use of an inside visium spatial technology, a technique used to perform single-cell sequencing on cross-sections, would help us in finding out which genes are dysregulated in the injured areas. This comparison approach between demyelinated and myelinated areas within the same nerve would shed some light on why an area is affected and the other is not.

3. Absence of neuropathy in the C57 and NOD SCID backgrounds

Behavioral, electrophysiological, and histological data from C57 ICOS KO and NOD SCID ICOSL KO mice at 1 year do not show any behavioral deficits or infiltration within the nerves. The C57 mice have a fully functional immune system whereas the NOD SCID do not have any T-cells or B-cells. In either case, the animals are not able to develop a spontaneous autoimmune neuropathy. This result was also shown in the C57 B7.2-/- mice that do not develop any autoimmune neuropathy compared to their NOD B7.2 littermates (Salomon et al., 2001). This shows the importance of having a reactive autoimmune background for the development of neuropathy. The NOD background can therefore be described as having an immune system resembling a gun with either a hair trigger or a missing safety lock. The occurrence of autoimmunity in this animal model would be a result of an enhancement of immunogenic stimuli or a decreased self tolerance.

Autoimmunity in the NOD background is explained by a population of T-cells escaping double negative selection in the thymus, recognizing self-antigens, destroying the β-cells of pancreas, and leading to diabetes (Carrasco-Marin et al., 1996). However, the reason for the deviation from the pancreas towards the PNS remains unknown. The ICOS-ICOSL interaction in the nerve is needed for self-tolerance but this costimulatrory pathway in the pancreas is required for the development of diabetes.

A possible reason for this deviation is epitope spreading; which is the development of an immune response to epitopes that are different from, and that do not cross react with the pathology-causing epitope (Powell & Black, 2001). Epitope spreading has been described in the NOD mouse model where the immunoreactivity spreads from glutamic acid decarboxylase (GAD) 65, the potential trigger of the immune response, to other antigengens such as insulin,

carboxypetidase H, and heat shock protein 65. In pre-diabetic NOD mice, the peri-islets Schwann cells (pSC) surrounding the β-cells of pancreas are injured and there are autoreactive T-cells against pSCs (Winer et al., 2003). Epitope spreading from the β-cells to the pSCs could occur in the context of diabetes and the following could be extrapolated to the Schwann cells present in the nerves. Although the pSCs share the same embryonic origin as the nerve Schwann cells, there are differences between these two subtypes; pSCs are part of the autonomic nervous system and they express GFAP which is present in the Remak bundles (Tsui et al., 2003). Interestingly, pSCs express MPZ which is not typically found in non myelinating Schwann cells (Georgiou & Charlton, 1999).

4. Infiltration of the nerve

We have observed a CD4+ and CD8+ T-cell infiltrate in the nerves of the NOD ICOS-/- and the NOD ICOSL-/- mice. However, it is still not known if the immune response is triggered from inside the nerve or if the circulating T-cells become activated outside the nerve and infiltrate it. By looking at our flow cytometry data, we can observe a population of CD4+ and CD8+ T-cells in the NOD WT nerves. This result shows the presence of T-cells in the nerves of NOD animals regardless of the presence or absence of neuropathy.

It has been shown that there is an imbalance between Tregs and Effector T-cells (Teff) in the nerve and the spleen of NOD ICOS-/- and NOD ICOSL-/- mice as well as other animal models of spontaneous autoimmune neuropathy (Meyer zu Hörste et al., 2014; Prevot et al., 2010). This reduction in Tregs, which have immunosuppressive properties and are responsible for the downregulation of induction and proliferation of Teff, could have an impact on the inflammatory

status of the nerve. Moreover, the Schwann cells can act as professional APCs by presenting MHCII molecules under pro-inflammatory conditions (Hartlehnert et al., 2017; zu Hörste et al., 2010). In our KO model, the reduction in Tregs could have played a role in creating a pro-inflammatory milieu thus making the Schwann cells express MHCII molecules. The Schwann cells would then be recognized by resident macrophages of the nerve and the immune response would be initiated (Klein & Martini, 2016; Rudolf Martini et al., 2008).

5. Variation of ICOS and ICOSL expression in the nerve throughout different timepoints

We have also looked at which cells could express ICOS or ICOSL in the PNS by RT-qPCR. We were not able to detect any ICOS, however ICOSL was expressed in the nerve. A definite candidate that expresses ICOSL is the Schwann cell as it is detected in the primary Schwann cultures at the proliferation and differentiation stages. RT-qPCR performed on DRG Schwann cell co-cultures and on post-natal nerves undergoing myelination show an expression of ICOSL. Nevertheless, there are other cell populations present in the nerve that could potentially express ICOSL such as endoneurial fibroblasts, and resident macrophages. A FISH experiment is being conducted to identify which cells could express ICOSL.

6. Similarities between the animal model and the human disease

The NOD ICOS-/- and NOD ICOSL-/- mice are a robust animal model for the study of immune mediated neuropathies. Their phenotype shares a strong resemblance to the CIDP form of autoimmune neuropathy; our model suffers from a chronic non-relapsing-remitting course of

the disease with similar electrophysiological and histopathological findings (Lehmann et al., 2019; Mathey et al., 2015). The KO mice have a reduced CMAP with an increased latency, T-cell infiltration in the nerve, and suffer from demyelinated nerves. Both CIDP patients and NOD ICOS-/- and NOD ICOSL-/- mice develop neuropathy in period that correspond to their middle age. There is a difference in the sex ratio; CIDP patients are males with a 3:2 ratio compared to the NOD mouse where the females develop the autoimmune neuropathy.

One major difference is the absence of autoantibodies in the serum of NOD WT, NOD WT diabetic, NOD ICOS-/- pre-neuropathic, and NOD ICOS-/- neuropathic (work in collaboration with Dr Jerome Devaux, Institut de Neurosciences de Montpellier). There was no reaction against myelin proteins, nodal and paranodal proteins (NF-155, NF-186, CNTN, CASPR1), IgG, nor IgM which can be present in CIDP patients (Delmont et al., 2017; Querol et al., 2017). Interestingly, MPZ has been reported as an autoantigen in the NOD B7.2 KO mouse model of spontaneous autoimmune neuropathy (Kim et al., 2008). Nonetheless, the lack of autoantibodies in the serum does not discredit the model. As a matter of fact, discrepancies exists in detected antibodies between the NOD model and human T1D. Antibodies against insulin are found in the NOD mouse and rarely in adult human patient (Yu et al., 2000). The opposite is also valid where several autoantibodies solely detected T1D patients such as GAD65 and zinc transporter 8 (Han et al., 2013; Roep & Peakman, 2012). An RNA Seq experiment was also performed on sciatic nerves extracted from pre-diabetic NOD WT and pre-neuropathic NOD ICOS-/- mice. The aim of this experiment is to detect any changes in mRNA before the onset of the disease and to verify if the fold changes observed in certain genes are linked to a form of neuropathy seen in humans (ongoing work).

In human T1D there are several alleles of predisposition to the disease; HLA-DR3, HLA-DR4, HLA-DQ2, HLA-DQ8 (Baisch et al., 1990; van Belle et al., 2011). In patients with immune mediated neuropathies, these alleles have not been reported. However, there is a strong evidence factor for DRB*15 in CIDP patients with anti-NF155 antibodies (Martinez-Martinez et al., 2017).

CHAPTER V: PERSPERCTIVES AND CONCLUSION

1. Could a "leaky" BNB trigger the neuropathy?

The NOD strain is not immune to the development of certain pathologies as was mentioned in the introduction. The permeability of the BNB could be compromised in our animal model especially in the KO mice. This would facilitate the entry of autoreactive T-cells which will in turn secrete chemokines and cytokines that will activate the resident macrophages.

Suggested experiment: Injection of presympromatic NOD WT, NOD ICOS-/-, and NOD ICOSL-/- mice at 12 weeks with Evans blue stain to check for BNB permeability.

2. What role does ICOS-ICOSL play in remyelination?

In our animal model, the interaction of ICOS-ICOSL seems to be necessary for the protection of the PNS from an autoimmune neuropathy. If the KO model is challenged by a nerve injury prior to the onset of neuropathy, would the animal be able to remyelinate properly in the absence of the ICOS-ICOSL interaction?

Suggested experiment: Perform a mechanical injury, nerve crush, and a chemical injury, Polyinosinic:polycytidylic acid (poly I:C or PIC) injections, on pre-neuropathic NOD ICOS-/- and NOD ICOSL-/-. The output analysis would be behavioral assessment, histology, and RT-qPCR to check for metabolic pathways that are altered during nerve injury. The nerve crush experiment would allow us to study Wallerian degeneration as well as remyelination. PIC injections would stimulate Toll-like receptor 3 (TLR3) which is expressed in Schwann cells. In a

humanized mouse model expressing HLA-DQ8 and human insulin, the mice developed T1D upon PIC injections (Luce et al., 2018).

It would also be of a great value to perform the same experiment on NOD ICOSL$^{f/f}$::PlpERT2Cre to study the impact of ICOSL abrogation before and after the onset of injury. The rationale behind this experiment is similar to the Experimental Autoimmune Encephalitis (EAE) mouse model that receives antibodies before or after the induction of the disease. The blocking of co-stimulatory or inhibitory molecules before or after inducing EAE has different outcomes. The administration antibodies against CIITA and ICOS during the induction phase increases the severity of the disease whereas blocking ICOS, CIITA, B7.1, and B7.2 post immunization leads to a protection of EAE (Racke et al., 1995; Rottman et al., 2001).

3. What other animal models could be generated to study autoimmune neuropathy?

Different HLA alleles have been linked to the development of autoimmune diseases. The creation of a humanized mouse model with a predisposition allele for CIDP would help the scientific community in designing a potential immunotherapy as well as the identification of a possible biomarker.

Suggested experiment: create a humanized NOD mouse expressing DRB*15 to study the combination of a reactive autoimmune background with an HLA allele associated NF155+ CIDP.

4. Conclusion

In conclusion, the abrogation of ICOS or ICOSL in a NOD background results in the deviation of autoimmunity from the pancreas towards the PNS. The KO animals develop a severe autoimmune neuropathy instead of T1D. This neuropathy is characterized by behavioral and electrophysiological deficits as well as a nerve lesions and myelin defects. However, these deficits were not present in C57BL/6J ICOS KO or NOD SCID ICOSL KO proving the importance of having a reactive autoimmune background. The NOD ICOS-/- and NOD ICOSL-/- mice have CD4+ and CD8+ T-cells, and macrophages infiltrating their PNS. Even though our data shows that the Schwann cell expresses ICOSL we still do not have conclusive evidence that the Schwann cell is the APC in our animal model. Our ongoing RNA Seq experiment, where we compare pre-diabetic NOD WT and pre-neuropathic NOD ICOS-/- mice, will also shed some light on the changes occurring prior to the onset of neuropathy. Our model simply shows the necessity of the ICOS-ICOSL interaction in the maintenance of self-tolerance in the nerves of NOD animals. Taken all together, our results provide a robust animal model for immune-mediated neuropathies and in particular CIDP. This model will help in elucidating the mechanisms underlying Schwann cell injury as well as designing a potential immunotheraphy for the treatment of autoimmune neuropathies.

REFERENCES

Abbas, N., Zou, L. P., Pelidou, S. H., Winblad, B., & Zhu, J. (2000). Protective effect of Rolipram in experimental autoimmune neuritis: protection is associated with down-regulation of IFN-gamma and inflammatory chemokines as well as up-regulation of IL-4 in peripheral nervous system. *Autoimmunity, 32*(2), 93-99. doi:10.3109/08916930008994078

Abromson-Leeman, S., Bronson, R., & Dorf, M. E. (1995). Experimental autoimmune peripheral neuritis induced in BALB/c mice by myelin basic protein-specific T cell clones. *J Exp Med, 182*(2), 587-592. doi:10.1084/jem.182.2.587

Acha-Orbea, H., & McDevitt, H. O. (1987). The first external domain of the nonobese diabetic mouse class II I-A beta chain is unique. *Proc Natl Acad Sci U S A, 84*(8), 2435-2439. doi:10.1073/pnas.84.8.2435

Aggarwal, B. B., Gupta, S. C., & Kim, J. H. (2012). Historical perspectives on tumor necrosis factor and its superfamily: 25 years later, a golden journey. *Blood, 119*(3), 651-665. doi:10.1182/blood-2011-04-325225

Anderson, M. S., & Bluestone, J. A. (2005). The NOD mouse: a model of immune dysregulation. *Annu Rev Immunol, 23*, 447-485. doi:10.1146/annurev.immunol.23.021704.115643

Archelos, J. J., Previtali, S. C., & Hartung, H.-P. (1999). The role of integrins in immune-mediated diseases of the nervous system. *Trends in neurosciences, 22*(1), 30-38.

Arthur-Farraj, P. J., Latouche, M., Wilton, D. K., Quintes, S., Chabrol, E., Banerjee, A., . . . Jessen, K. R. (2012). c-Jun reprograms Schwann cells of injured nerves to generate a repair cell essential for regeneration. *Neuron, 75*(4), 633-647. doi:10.1016/j.neuron.2012.06.021

Azhary, H., Farooq, M. U., Bhanushali, M., Majid, A., & Kassab, M. Y. (2010). Peripheral neuropathy: differential diagnosis and management. *American family physician, 81*(7), 887-892.

Azuma, M. (2019). Co-signal Molecules in T-Cell Activation : Historical Overview and Perspective. *Adv Exp Med Biol, 1189*, 3-23. doi:10.1007/978-981-32-9717-3_1

Bae, C.-J., & Saint-Jeannet, J.-P. (2014). Induction and specification of neural crest cells: Extracellular signals and transcriptional switches *Neural crest cells* (pp. 27-49): Elsevier.

Bae, J. S., Yuki, N., Kuwabara, S., Kim, J. K., Vucic, S., Lin, C. S., & Kiernan, M. C. (2014). Guillain-Barre syndrome in Asia. *J Neurol Neurosurg Psychiatry, 85*(8), 907-913. doi:10.1136/jnnp-2013-306212

Baisch, J. M., Weeks, T., Giles, R., Hoover, M., Stastny, P., & Capra, J. D. (1990). Analysis of HLA-DQ Genotypes and Susceptibility in Insulin-Dependent Diabetes Mellitus. *New England Journal of Medicine, 322*(26), 1836-1841. doi:10.1056/nejm199006283222602

Beirowski, B., Adalbert, R., Wagner, D., Grumme, D. S., Addicks, K., Ribchester, R. R., & Coleman, M. P. (2005). The progressive nature of Wallerian degeneration in wild-type and slow Wallerian degeneration (WldS) nerves. *BMC Neurosci, 6*, 6. doi:10.1186/1471-2202-6-6

Blum, S., Reddel, S., Spies, J., & McCombe, P. (2013). Clinical features of patients with Guillain-Barré syndrome at seven hospitals on the East Coast of Australia. *Journal of the peripheral nervous system, 18*(4), 316-320.

Bouche, P., Moulonguet, A., Younes-Chennoufi, A. B., Adams, D., Baumann, N., Meininger, V., . . . Said, G. (1995). Multifocal motor neuropathy with conduction block: a study of 24 patients. *J Neurol Neurosurg Psychiatry, 59*(1), 38-44. doi:10.1136/jnnp.59.1.38

Bour-Jordan, H., Thompson, H. L., Giampaolo, J. R., Davini, D., Rosenthal, W., & Bluestone, J. A. (2013). Distinct genetic control of autoimmune neuropathy and diabetes in the non-obese diabetic background. *J Autoimmun, 45*, 58-67. doi:10.1016/j.jaut.2013.06.005

Bourde, O., Kiefer, R., Toyka, K. V., & Hartung, H. P. (1996). Quantification of interleukin-6 mRNA in wallerian degeneration by competitive reverse transcription polymerase chain reaction. *J Neuroimmunol, 69*(1-2), 135-140. doi:10.1016/0165-5728(96)00087-2

Bretscher, P., & Cohn, M. (1970). A theory of self-nonself discrimination. *Science, 169*(3950), 1042-1049. doi:10.1126/science.169.3950.1042

Briet, C., Bourdenet, G., Rogner, U. C., Becourt, C., Tardivel, I., Drouot, L., . . . Boitard, C. (2017). The Spontaneous Autoimmune Neuromyopathy in ICOSL(-/-) NOD Mice Is CD4(+) T-Cell and Interferon-γ Dependent. *Front Immunol, 8*, 287. doi:10.3389/fimmu.2017.00287

Brisebois, M., Zehntner, S. P., Estrada, J., Owens, T., & Fournier, S. (2006). A pathogenic role for CD8+ T cells in a spontaneous model of demyelinating disease. *J Immunol, 177*(4), 2403-2411. doi:10.4049/jimmunol.177.4.2403

Calida, D. M., Kremlev, S. G., Fujioka, T., Hilliard, B., Ventura, E., Constantinescu, C. S., . . . Rostami, A. (2000). Experimental allergic neuritis in the SJL/J mouse: induction of severe and reproducible disease with bovine peripheral nerve myelin and pertussis toxin with or without interleukin-12. *J Neuroimmunol, 107*(1), 1-7. doi:10.1016/s0165-5728(00)00249-6

Cao-Lormeau, V.-M., Blake, A., Mons, S., Lastère, S., Roche, C., Vanhomwegen, J., . . . Larre, P. (2016). Guillain-Barré Syndrome outbreak associated with Zika virus infection in French Polynesia: a case-control study. *The Lancet, 387*(10027), 1531-1539.

Carrasco-Marin, E., Shimizu, J., Kanagawa, O., & Unanue, E. R. (1996). The class II MHC I-Ag7 molecules from non-obese diabetic mice are poor peptide binders. *J Immunol, 156*(2), 450-458.

Cats, E. A., Jacobs, B. C., Yuki, N., Tio-Gillen, A. P., Piepers, S., Franssen, H., . . . van der Pol, W. L. (2010). Multifocal motor neuropathy: association of anti-GM1 IgM antibodies with clinical features. *Neurology, 75*(22), 1961-1967. doi:10.1212/WNL.0b013e3181ff94c2

Cats, E. A., van der Pol, W. L., Piepers, S., Franssen, H., Jacobs, B. C., van den Berg-Vos, R. M., . . . van den Berg, L. H. (2010). Correlates of outcome and response to IVIg in 88 patients with multifocal motor neuropathy. *Neurology, 75*(9), 818-825. doi:10.1212/WNL.0b013e3181f0738e

Chang, K.-H., Lyu, R.-K., Lin, W.-T., Huang, Y.-T., Lin, H.-S., & Chang, S.-H. (2019). Gulllain-Barre Syndrome after trivalent influenza vaccination in adults. *Frontiers in neurology, 10*, 768.

Chaudhry, V., & Cornblath, D. R. (1992). Wallerian degeneration in human nerves: serial electrophysiological studies. *Muscle Nerve, 15*(6), 687-693. doi:10.1002/mus.880150610

Chen, Y., Zhang, J., Chu, X., Xu, Y., & Ma, F. (2019). Vaccines and the risk of Guillain-Barré syndrome. *European Journal of Epidemiology*, 1-8.

Chen, Z. L., Yu, W. M., & Strickland, S. (2007). Peripheral regeneration. *Annu Rev Neurosci, 30*, 209-233. doi:10.1146/annurev.neuro.30.051606.094337

Chernoff, G. F. (1981). Shiverer: an autosomal recessive mutant mouse with myelin deficiency. *J Hered, 72*(2), 128. doi:10.1093/oxfordjournals.jhered.a109442

Chiba, A., Kusunoki, S., Obata, H., Machinami, R., & Kanazawa, I. (1993). Serum anti-GQ1b IgG antibody is associated with ophthalmoplegia in Miller Fisher syndrome and Guillain-Barre syndrome: clinical and immunohistochemical studies. *Neurology, 43*(10), 1911-1917. doi:10.1212/wnl.43.10.1911

Dace, D. S., Khan, A. A., Stark, J. L., Kelly, J., Cross, A. H., & Apte, R. S. (2009). Interleukin-10 overexpression promotes Fas-ligand-dependent chronic macrophage-mediated demyelinating polyneuropathy. *PLoS One, 4*(9), e7121. doi:10.1371/journal.pone.0007121

de Seze, J., Kremer, L., do Rego, C. A., Taleb, O., Lam, D., Beiano, W., . . . Brun, S. (2016). Chronic inflammatory demyelinating polyradiculoneuropathy: A new animal model for new therapeutic targets. *Revue neurologique, 172*(12), 767-769.

Delmont, E., Manso, C., Querol, L., Cortese, A., Berardinelli, A., Lozza, A., . . . Devaux, J. J. (2017). Autoantibodies to nodal isoforms of neurofascin in chronic inflammatory demyelinating polyneuropathy. *Brain, 140*(7), 1851-1858. doi:10.1093/brain/awx124

Deretzi, G., Zou, L. P., Pelidou, S. H., Nennesmo, I., Levi, M., Wahren, B., . . . Zhu, J. (1999). Nasal administration of recombinant rat IL-4 ameliorates ongoing experimental autoimmune neuritis and inhibits demyelination. *J Autoimmun, 12*(2), 81-89. doi:10.1006/jaut.1998.0259

Dimachkie, M. M., Barohn, R. J., & Katz, J. (2013). Multifocal motor neuropathy, multifocal acquired demyelinating sensory and motor neuropathy, and other chronic acquired demyelinating polyneuropathy variants. *Neurol Clin, 31*(2), 533-555. doi:10.1016/j.ncl.2013.01.001

Doneddu, P. E., Cocito, D., Manganelli, F., Fazio, R., Briani, C., Filosto, M., . . . Nobile-Orazio, E. (2019). Atypical CIDP: diagnostic criteria, progression and treatment response. Data from the Italian CIDP Database. *J Neurol Neurosurg Psychiatry, 90*(2), 125-132. doi:10.1136/jnnp-2018-318714

Dong, C., & Nurieva, R. I. (2003). Regulation of immune and autoimmune responses by ICOS. *J Autoimmun, 21*(3), 255-260. doi:10.1016/s0896-8411(03)00119-7

Doppler, K., Appeltshauser, L., Villmann, C., Martin, C., Peles, E., Krämer, H. H., . . . Sommer, C. (2016). Auto-antibodies to contactin-associated protein 1 (Caspr) in two patients with painful inflammatory neuropathy. *Brain, 139*(10), 2617-2630.

Drenthen, J., Maathuis, E. M., Visser, G. H., van Doorn, P. A., Blok, J. H., & Jacobs, B. C. (2013). Limb motor nerve dysfunction in Miller Fisher syndrome. *J Peripher Nerv Syst, 18*(1), 25-29. doi:10.1111/jns5.12003

EFNS, J. T. F. o. t., & PNS, t. (2010). European Federation of Neurological Societies/Peripheral Nerve Society Guideline on management of chronic inflammatory demyelinating polyradiculoneuropathy: Report of a joint task force of the European Federation of Neurological Societies and the Peripheral Nerve Society – First Revision. *Journal of the peripheral nervous system, 15*(1), 1-9. doi:10.1111/j.1529-8027.2010.00245.x

Elliott, J. F., Liu, J., Yuan, Z. N., Bautista-Lopez, N., Wallbank, S. L., Suzuki, K., . . . Kavanagh, K. M. (2003). Autoimmune cardiomyopathy and heart block develop spontaneously in HLA-DQ8 transgenic IAbeta knockout NOD mice. *Proc Natl Acad Sci U S A, 100*(23), 13447-13452. doi:10.1073/pnas.2235552100

Eylar, E. H., Toro-Goyco, E., Kessler, M. J., & Szymanska, I. (1982). Induction of allergic neuritis in rhesus monkeys. *J Neuroimmunol, 3*(2), 91-98. doi:10.1016/0165-5728(82)90043-1

Freeman, G. J., Long, A. J., Iwai, Y., Bourque, K., Chernova, T., Nishimura, H., . . . Honjo, T. (2000). Engagement of the PD-1 immunoinhibitory receptor by a novel B7 family member leads to negative regulation of lymphocyte activation. *J Exp Med, 192*(7), 1027-1034. doi:10.1084/jem.192.7.1027

Gabriel, C. M., Hughes, R. A., Moore, S. E., Smith, K. J., & Walsh, F. S. (1998). Induction of experimental autoimmune neuritis with peripheral myelin protein-22. *Brain, 121 (Pt 10)*, 1895-1902. doi:10.1093/brain/121.10.1895

Garbay, B., Heape, A. M., Sargueil, F., & Cassagne, C. (2000). Myelin synthesis in the peripheral nervous system. *Prog Neurobiol, 61*(3), 267-304. doi:10.1016/s0301-0082(99)00049-0

Gaudet, A. D., Popovich, P. G., & Ramer, M. S. (2011). Wallerian degeneration: gaining perspective on inflammatory events after peripheral nerve injury. *Journal of Neuroinflammation, 8*(1), 110. doi:10.1186/1742-2094-8-110

Georgiou, J., & Charlton, M. P. (1999). Non-myelin-forming perisynaptic schwann cells express protein zero and myelin-associated glycoprotein. *Glia, 27*(2), 101-109. doi:10.1002/(sici)1098-1136(199908)27:2<101::aid-glia1>3.0.co;2-h

Giese, K. P., Martini, R., Lemke, G., Soriano, P., & Schachner, M. (1992). Mouse P0 gene disruption leads to hypomyelination, abnormal expression of recognition molecules, and degeneration of myelin and axons. *Cell, 71*(4), 565-576. doi:10.1016/0092-8674(92)90591-y

Gilbert, S. F. (2008). Developmental Biology 9th Edition.

Gilliatt, R. W., & Hjorth, R. J. (1972). Nerve conduction during Wallerian degeneration in the baloon. *J Neurol Neurosurg Psychiatry, 35*(3), 335-341. doi:10.1136/jnnp.35.3.335

Ginhoux, F., & Jung, S. (2014). Monocytes and macrophages: developmental pathways and tissue homeostasis. *Nature Reviews Immunology, 14*(6), 392-404. doi:10.1038/nri3671

Godschalk, P. C., Kuijf, M. L., Li, J., St Michael, F., Ang, C. W., Jacobs, B. C., . . . Gilbert, M. (2007). Structural characterization of Campylobacter jejuni lipooligosaccharide outer cores associated with Guillain-Barre and Miller Fisher syndromes. *Infect Immun, 75*(3), 1245-1254. doi:10.1128/iai.00872-06

Gomez-Sanchez, J. A., Carty, L., Iruarrizaga-Lejarreta, M., Palomo-Irigoyen, M., Varela-Rey, M., Griffith, M., . . . Jessen, K. R. (2015). Schwann cell autophagy, myelinophagy, initiates myelin clearance from injured nerves. *Journal of Cell Biology, 210*(1), 153-168. doi:10.1083/jcb.201503019

Gould, D. J. (2019). *BRS Neuroanatomy*: Lippincott Williams & Wilkins.

Greenwald, R. J., Freeman, G. J., & Sharpe, A. H. (2005). The B7 family revisited. *Annu Rev Immunol, 23*, 515-548. doi:10.1146/annurev.immunol.23.021704.115611

Griffin, J. W., George, R., & Ho, T. (1993). Macrophage Systems in Peripheral Nerves. A Review. *Journal of Neuropathology & Experimental Neurology, 52*(6), 553-560. doi:10.1097/00005072-199311000-00001

Griffin, J. W., Li, C. Y., Macko, C., Ho, T. W., Hsieh, S. T., Xue, P., . . . Asbury, A. K. (1996). Early nodal changes in the acute motor axonal neuropathy pattern of the Guillain-Barre syndrome. *J Neurocytol, 25*(1), 33-51. doi:10.1007/bf02284784

Hafer-Macko, C., Hsieh, S. T., Li, C. Y., Ho, T. W., Sheikh, K., Cornblath, D. R., . . . Griffin, J. W. (1996). Acute motor axonal neuropathy: an antibody-mediated attack on axolemma. *Ann Neurol, 40*(4), 635-644. doi:10.1002/ana.410400414

Halstead, S. K., O'Hanlon, G. M., Humphreys, P. D., Morrison, D. B., Morgan, B. P., Todd, A. J., . . . Willison, H. J. (2004). Anti-disialoside antibodies kill perisynaptic Schwann cells and damage motor nerve terminals via membrane attack complex in a murine model of neuropathy. *Brain, 127*(Pt 9), 2109-2123. doi:10.1093/brain/awh231

Han, S., Donelan, W., Wang, H., Reeves, W., & Yang, L.-J. (2013). Novel autoantigens in type 1 diabetes. *Am J Transl Res, 5*(4), 379-392.

Hartlehnert, M., Derksen, A., Hagenacker, T., Kindermann, D., Schäfers, M., Pawlak, M., . . . Meyer Zu Horste, G. (2017). Schwann cells promote post-traumatic nerve inflammation and neuropathic pain through MHC class II. *Sci Rep, 7*(1), 12518. doi:10.1038/s41598-017-12744-2

Hartung, H. P., Reiners, K., Schmidt, B., Stoll, G., & Toyka, K. V. (1991). Serum interleukin-2 concentrations in Guillain-Barré syndrome and chronic idiopathic demyelinating polyradiculoneuropathy: Comparison with other neurological diseases of presumed immunopathogenesis. *Annals of Neurology: Official Journal of the American Neurological Association and the Child Neurology Society, 30*(1), 48-53.

Hattori, M., Buse, J. B., Jackson, R. A., Glimcher, L., Dorf, M. E., Minami, M., . . . et al. (1986). The NOD mouse: recessive diabetogenic gene in the major histocompatibility complex. *Science, 231*(4739), 733-735. doi:10.1126/science.3003909

Hauck, L. J., White, C., Feasby, T. E., Zochodne, D. W., Svenson, L. W., & Hill, M. D. (2008). Incidence of Guillain–Barré syndrome in Alberta, Canada: an administrative data study. *Journal of Neurology, Neurosurgery & Psychiatry, 79*(3), 318-320.

Hays, A. P., Latov, N., Takatsu, M., & Sherman, W. H. (1987). Experimental demyelination of nerve induced by serum of patients with neuropathy and an anti-MAG IgM M-protein. *Neurology, 37*(2), 242-256. doi:10.1212/wnl.37.2.242

Hayward, S. L., Bautista-Lopez, N., Suzuki, K., Atrazhev, A., Dickie, P., & Elliott, J. F. (2006). CD4 T cells play major effector role and CD8 T cells initiating role in spontaneous autoimmune myocarditis of HLA-DQ8 transgenic IAb knockout nonobese diabetic mice. *J Immunol, 176*(12), 7715-7725. doi:10.4049/jimmunol.176.12.7715

Herman, A. E., Freeman, G. J., Mathis, D., & Benoist, C. (2004). CD4+CD25+ T regulatory cells dependent on ICOS promote regulation of effector cells in the prediabetic lesion. *J Exp Med, 199*(11), 1479-1489. doi:10.1084/jem.20040179

Hichor, M., Sundaram, V. K., Eid, S. A., Abdel-Rassoul, R., Petit, P. X., Borderie, D., . . . Massaad, C. (2018). Liver X Receptor exerts a protective effect against the oxidative stress in the peripheral nerve. *Sci Rep, 8*(1), 2524. doi:10.1038/s41598-018-20980-3

Ho, T. W., Mishu, B., Li, C. Y., Gao, C. Y., Cornblath, D. R., Griffin, J. W., . . . McKhann, G. M. (1995). Guillain-Barre syndrome in northern China. Relationship to Campylobacter jejuni infection and anti-glycolipid antibodies. *Brain, 118 (Pt 3)*, 597-605. doi:10.1093/brain/118.3.597

Hoffman, P. M., Powers, J. M., Weise, M. J., & Brostoff, S. W. (1980). Experimental allergic neuritis. I. Rat strain differences in the response to bovine myelin antigens. *Brain Res, 195*(2), 355-362. doi:10.1016/0006-8993(80)90071-2

Hu, Y., Nakagawa, Y., Purushotham, K. R., & Humphreys-Beher, M. G. (1992). Functional changes in salivary glands of autoimmune disease-prone NOD mice. *Am J Physiol, 263*(4 Pt 1), E607-614. doi:10.1152/ajpendo.1992.263.4.E607

Hudspeth, A. J., Jessell, T. M., Kandel, E. R., Schwartz, J. H., & Siegelbaum, S. A. (2013). *Principles of neural science*: McGraw-Hill, Health Professions Division.

Hughes, R. A., & Cornblath, D. R. (2005). Guillain-barre syndrome. *The Lancet, 366*(9497), 1653-1666.

Hughes, R. A., Swan, A. V., & van Doorn, P. A. (2011). Cochrane Review: Intravenous immunoglobulin for Guillain-Barré syndrome. *Evidence-Based Child Health: A Cochrane Review Journal, 6*(4), 1176-1231. doi:10.1002/ebch.810

Jacob, C. (2015). Transcriptional control of neural crest specification into peripheral glia. *Glia, 63*(11), 1883-1896. doi:10.1002/glia.22816

Jacobs, B., Rothbarth, P., Van der Meché, F., Herbrink, P., Schmitz, P., De Klerk, M., & Van Doorn, P. (1998). The spectrum of antecedent infections in Guillain-Barré syndrome: a case-control study. *Neurology, 51*(4), 1110-1115.

Jenkins, M. K., & Schwartz, R. H. (1987). Antigen presentation by chemically modified splenocytes induces antigen-specific T cell unresponsiveness in vitro and in vivo. *J Exp Med, 165*(2), 302-319. doi:10.1084/jem.165.2.302

Jessen, K. R., & Mirsky, R. (2005). The origin and development of glial cells in peripheral nerves. *Nat Rev Neurosci, 6*(9), 671-682. doi:10.1038/nrn1746

Jessen, K. R., & Mirsky, R. (2008). Negative regulation of myelination: relevance for development, injury, and demyelinating disease. *Glia, 56*(14), 1552-1565. doi:10.1002/glia.20761

Jiang, F., Yoshida, T., Nakaki, F., Terawaki, S., Chikuma, S., Kato, Y., . . . Okazaki, T. (2009). Identification of QTLs that modify peripheral neuropathy in NOD.H2b-Pdcd1-/- mice. *Int Immunol, 21*(5), 499-509. doi:10.1093/intimm/dxp020

Jindal, G., Parmar, V. R., & Gupta, V. K. (2009). Isolated ptosis as acute ophthalmoplegia without ataxia, positive for anti-GQ1b immunoglobulin G. *Pediatr Neurol, 41*(6), 451-452. doi:10.1016/j.pediatrneurol.2009.07.008

Jung, S., Gaupp, S., Korn, T., Köllner, G., Hartung, H. P., & Toyka, K. V. (2004). Biphasic form of experimental autoimmune neuritis in dark Agouti rats and its oral therapy by antigen-specific tolerization. *J Neurosci Res, 75*(4), 524-535. doi:10.1002/jnr.10879

Kaji, R., Oka, N., Tsuji, T., Mezaki, T., Nishio, T., Akiguchi, I., & Kimura, J. (1993). Pathological findings at the site of conduction block in multifocal motor neuropathy. *Ann Neurol, 33*(2), 152-158. doi:10.1002/ana.410330204

Katz, J. S., Saperstein, D. S., Gronseth, G., Amato, A. A., & Barohn, R. J. (2000). Distal acquired demyelinating symmetric neuropathy. *Neurology, 54*(3), 615-615. doi:10.1212/wnl.54.3.615

Kieseier, B., Clements, J., Pischel, H., Wells, G., Miller, K., Gearing, A., & Hartung, H. P. (1998). Matrix metalloproteinases MMP-9 and MMP-7 are expressed in experimental autoimmune neuritis and the Guillain-Barre syndrome. *Annals of neurology, 43*(4), 427-434.

Kieseier, B. C., Kiefer, R., Gold, R., Hemmer, B., Willison, H. J., & Hartung, H. P. (2004). Advances in understanding and treatment of immune-mediated disorders of the peripheral nervous system. *Muscle & Nerve: Official Journal of the American Association of Electrodiagnostic Medicine, 30*(2), 131-156.

Kieseier, B. C., Mathey, E. K., Sommer, C., & Hartung, H.-P. (2018). Immune-mediated neuropathies. *Nature Reviews Disease Primers, 4*(1), 1-23.

Kikutani, H., & Makino, S. (1992). The murine autoimmune diabetes model: NOD and related strains. *Adv Immunol, 51*, 285-322. doi:10.1016/s0065-2776(08)60490-3

Kim, H. J., Jung, C. G., Jensen, M. A., Dukala, D., & Soliven, B. (2008). Targeting of myelin protein zero in a spontaneous autoimmune polyneuropathy. *J Immunol, 181*(12), 8753-8760. doi:10.4049/jimmunol.181.12.8753

Klein, D., & Martini, R. (2016). Myelin and macrophages in the PNS: An intimate relationship in trauma and disease. *Brain Res, 1641*(Pt A), 130-138. doi:10.1016/j.brainres.2015.11.033

KUSUMI, M., NAKASHIMA, K., NAKAYAMA, H., & TAKAHASHI, K. (1995). Epidemiology of inflammatory neurological and inflammatory neuromuscular diseases in Tottori Prefecture, Japan. *Psychiatry and Clinical Neurosciences, 49*(3), 169-174. doi:10.1111/j.1440-1819.1995.tb02223.x

Kusunoki, S., Kaida, K., & Ueda, M. (2008). Antibodies against gangliosides and ganglioside complexes in Guillain-Barre syndrome: new aspects of research. *Biochim Biophys Acta, 1780*(3), 441-444. doi:10.1016/j.bbagen.2007.10.001

Kusunoki, S., Shimizu, J., Chiba, A., Ugawa, Y., Hitoshi, S., & Kanazawa, I. (1996). Experimental sensory neuropathy induced by sensitization with ganglioside GD1b. *Ann Neurol, 39*(4), 424-431. doi:10.1002/ana.410390404

Kuwabara, S., & Yuki, N. (2013). Axonal Guillain-Barré syndrome: concepts and controversies. *Lancet Neurol, 12*(12), 1180-1188. doi:10.1016/s1474-4422(13)70215-1

Kwa, M., Van Schaik, I., Brand, A., Baas, F., & Vermeulen, M. (2001). Investigation of serum response to PMP22, connexin 32 and P0 in inflammatory neuropathies. *Journal of neuroimmunology, 116*(2), 220-225.

Larue, S., Bombelli, F., Viala, K., Neil, J., Maisonobe, T., Bouche, P., . . . Léger, J. M. (2011). Non-anti-MAG DADS neuropathy as a variant of CIDP: clinical, electrophysiological, laboratory features and response to treatment in 10 cases. *European Journal of Neurology, 18*(6), 899-905. doi:10.1111/j.1468-1331.2010.03312.x

Lassmann, H., Fierz, W., Neuchrist, C., & Meyermann, R. (1991). Chronic relapsing experimental allergic neuritis induced by repeated transfer of P2-protein reactive T cell lines. *Brain, 114 (Pt 1B)*, 429-442. doi:10.1093/brain/114.1.429

Laughlin, R. S., Dyck, P. J., Melton, L. J., Leibson, C., Ransom, J., & Dyck, P. J. B. (2009). Incidence and prevalence of CIDP and the association of diabetes mellitus. *Neurology, 73*(1), 39-45. doi:10.1212/WNL.0b013e3181aaea47

Le Douarin, N. M., & Dupin, E. (2014). The neural crest, a fourth germ layer of the vertebrate embryo: significance in chordate evolution *Neural crest cells* (pp. 3-26): Elsevier.
LeBlanc, A. C., & Poduslo, J. F. (1990). Axonal modulation of myelin gene expression in the peripheral nerve. *J Neurosci Res, 26*(3), 317-326. doi:10.1002/jnr.490260308
Lefter, S., Hardiman, O., & Ryan, A. M. (2017). A population-based epidemiologic study of adult neuromuscular disease in the Republic of Ireland. *Neurology, 88*(3), 304-313. doi:10.1212/wnl.0000000000003504
Léger, J. M., Guimarães-Costa, R., & Muntean, C. (2016). Immunotherapy in Peripheral Neuropathies. *Neurotherapeutics, 13*(1), 96-107. doi:10.1007/s13311-015-0401-7
Lehmann, H. C., Burke, D., & Kuwabara, S. (2019). Chronic inflammatory demyelinating polyneuropathy: update on diagnosis, immunopathogenesis and treatment. *J Neurol Neurosurg Psychiatry, 90*(9), 981-987. doi:10.1136/jnnp-2019-320314
Lewis, R. A., Sumner, A. J., Brown, M. J., & Asbury, A. K. (1982). Multifocal demyelinating neuropathy with persistent conduction block. *Neurology, 32*(9), 958-964. doi:10.1212/wnl.32.9.958
Lindqvist, A. K., Nakken, B., Sundler, M., Kjellén, P., Jonsson, R., Holmdahl, R., & Skarstein, K. (2005). Influence on spontaneous tissue inflammation by the major histocompatibility complex region in the nonobese diabetic mouse. *Scand J Immunol, 61*(2), 119-127. doi:10.1111/j.0300-9475.2005.01550.x
Linsley, P. S., Greene, J. L., Brady, W., Bajorath, J., Ledbetter, J. A., & Peach, R. (1994). Human B7-1 (CD80) and B7-2 (CD86) bind with similar avidities but distinct kinetics to CD28 and CTLA-4 receptors. *Immunity, 1*(9), 793-801. doi:10.1016/s1074-7613(94)80021-9
Liu, G., Jiang, R., & Jin, Y. (2014). Sciatic nerve injury repair: a visualized analysis of research fronts and development trends. *Neural Regen Res, 9*(18), 1716-1722. doi:10.4103/1673-5374.141810
Liu, J. X., Willison, H. J., & Pedrosa-Domellof, F. (2009). Immunolocalization of GQ1b and related gangliosides in human extraocular neuromuscular junctions and muscle spindles. *Invest Ophthalmol Vis Sci, 50*(7), 3226-3232. doi:10.1167/iovs.08-3333
Locksley, R. M., Killeen, N., & Lenardo, M. J. (2001). The TNF and TNF receptor superfamilies: integrating mammalian biology. *Cell, 104*(4), 487-501. doi:10.1016/s0092-8674(01)00237-9
Louvet, C., Kabre, B. G., Davini, D. W., Martinier, N., Su, M. A., DeVoss, J. J., . . . Bluestone, J. A. (2009). A novel myelin P0-specific T cell receptor transgenic mouse develops a fulminant autoimmune peripheral neuropathy. *J Exp Med, 206*(3), 507-514. doi:10.1084/jem.20082113
Luce, S., Guinoiseau, S., Gadault, A., Letourneur, F., Blondeau, B., Nitschke, P., . . . Boitard, C. (2018). Humanized Mouse Model to Study Type 1 Diabetes. *Diabetes, 67*(9), 1816-1829. doi:10.2337/db18-0202
Lupski, J. R., & Garcia, C. A. (1992). Molecular genetics and neuropathology of Charcot-Marie-Tooth disease type 1A. *Brain Pathol, 2*(4), 337-349. doi:10.1111/j.1750-3639.1992.tb00710.x
Mahdi-Rogers, M., & Hughes, R. A. C. (2014). Epidemiology of chronic inflammatory neuropathies in southeast England. *European Journal of Neurology, 21*(1), 28-33. doi:10.1111/ene.12190
Makino, S., Kunimoto, K., Muraoka, Y., Mizushima, Y., Katagiri, K., & Tochino, Y. (1980). Breeding of a non-obese, diabetic strain of mice. *Jikken Dobutsu, 29*(1), 1-13. doi:10.1538/expanim1978.29.1_1
Makowska, A., Pritchard, J., Sanvito, L., Gregson, N., Peakman, M., Hayday, A., & Hughes, R. (2008). Immune responses to myelin proteins in Guillain–Barré syndrome. *Journal of Neurology, Neurosurgery & Psychiatry, 79*(6), 664-671.
Many, M. C., Maniratunga, S., & Denef, J. F. (1996). The non-obese diabetic (NOD) mouse: an animal model for autoimmune thyroiditis. *Exp Clin Endocrinol Diabetes, 104 Suppl 3*, 17-20. doi:10.1055/s-0029-1211673

Markus, A., Patel, T. D., & Snider, W. D. (2002). Neurotrophic factors and axonal growth. *Curr Opin Neurobiol, 12*(5), 523-531. doi:10.1016/s0959-4388(02)00372-0

Martinez-Martinez, L., Lleixà, M. C., Boera-Carnicero, G., Cortese, A., Devaux, J., Siles, A., . . . Querol, L. (2017). Anti-NF155 chronic inflammatory demyelinating polyradiculoneuropathy strongly associates to HLA-DRB15. *J Neuroinflammation, 14*(1), 224. doi:10.1186/s12974-017-0996-1

Martini, R., Fischer, S., López-Vales, R., & David, S. (2008). Interactions between Schwann cells and macrophages in injury and inherited demyelinating disease. *Glia, 56*(14), 1566-1577. doi:10.1002/glia.20766

Martini, R., Zielasek, J., Toyka, K. V., Giese, K. P., & Schachner, M. (1995). Protein zero (P0)-deficient mice show myelin degeneration in peripheral nerves characteristic of inherited human neuropathies. *Nat Genet, 11*(3), 281-286. doi:10.1038/ng1195-281

Mathey, E. K., Park, S. B., Hughes, R. A., Pollard, J. D., Armati, P. J., Barnett, M. H., . . . Lin, C. S. (2015). Chronic inflammatory demyelinating polyradiculoneuropathy: from pathology to phenotype. *J Neurol Neurosurg Psychiatry, 86*(9), 973-985. doi:10.1136/jnnp-2014-309697

Mäurer, M., & Gold, R. (2002). Animal models of immune-mediated neuropathies. *Curr Opin Neurol, 15*(5), 617-622. doi:10.1097/00019052-200210000-00013

McCombe, P. A., Harness, J., & Pender, M. P. (1999). Effects of cyclosporin A treatment on clinical course and inflammatory cell apoptosis in experimental autoimmune encephalomyelitis induced in Lewis rats by inoculation with myelin basic protein. *J Neuroimmunol, 97*(1-2), 60-69. doi:10.1016/s0165-5728(99)00047-8

Mellor, A. L., & Munn, D. H. (2004). IDO expression by dendritic cells: tolerance and tryptophan catabolism. *Nat Rev Immunol, 4*(10), 762-774. doi:10.1038/nri1457

Meyer zu Hörste, G., Cordes, S., Mausberg, A. K., Zozulya, A. L., Wessig, C., Sparwasser, T., . . . Kieseier, B. C. (2014). FoxP3+ regulatory T cells determine disease severity in rodent models of inflammatory neuropathies. *PLoS One, 9*(10), e108756. doi:10.1371/journal.pone.0108756

Meyer zu Hörste, G., Hartung, H. P., & Kieseier, B. C. (2007). From bench to bedside--experimental rationale for immune-specific therapies in the inflamed peripheral nerve. *Nat Clin Pract Neurol, 3*(4), 198-211. doi:10.1038/ncpneuro0452

Meyer zu Horste, G., Hu, W., Hartung, H. P., Lehmann, H. C., & Kieseier, B. C. (2008). The immunocompetence of Schwann cells. *Muscle Nerve, 37*(1), 3-13. doi:10.1002/mus.20893

Meyer zu Horste, G., Mausberg, A. K., Cordes, S., El-Haddad, H., Partke, H. J., Leussink, V. I., . . . Kieseier, B. C. (2014). Thymic epithelium determines a spontaneous chronic neuritis in Icam1(tm1Jcgr)NOD mice. *J Immunol, 193*(6), 2678-2690. doi:10.4049/jimmunol.1400367

Miledi, R., & Slater, C. R. (1970). On the degeneration of rat neuromuscular junctions after nerve section. *J Physiol, 207*(2), 507-528. doi:10.1113/jphysiol.1970.sp009076

Miletic, H., Utermöhlen, O., Wedekind, C., Hermann, M., Stenzel, W., Lassmann, H., . . . Deckert, M. (2005). P0(106-125) is a neuritogenic epitope of the peripheral myelin protein P0 and induces autoimmune neuritis in C57BL/6 mice. *J Neuropathol Exp Neurol, 64*(1), 66-73. doi:10.1093/jnen/64.1.66

Misawa, S., Kuwabara, S., Mori, M., Kawaguchi, N., Yoshiyama, Y., & Hattori, T. (2001). Serum levels of tumor necrosis factor–α in chronic inflammatory demyelinating polyneuropathy. *Neurology, 56*(5), 666-669.

Mitsui, Y., Kusunoki, S., Arimura, K., Kaji, R., Kanda, T., Kuwabara, S., . . . Takada, K. (2015). A multicentre prospective study of Guillain-Barre syndrome in Japan: a focus on the incidence of subtypes. *J Neurol Neurosurg Psychiatry, 86*(1), 110-114. doi:10.1136/jnnp-2013-306509

Mittrücker, H. W., Kursar, M., Köhler, A., Yanagihara, D., Yoshinaga, S. K., & Kaufmann, S. H. (2002). Inducible costimulator protein controls the protective T cell response against Listeria monocytogenes. *J Immunol, 169*(10), 5813-5817. doi:10.4049/jimmunol.169.10.5813

Miyahira, Y., Akiba, H., Ogawa, S. H., Ishi, T., Watanabe, S., Kobayashi, S., . . . Watanabe, N. (2003). Involvement of ICOS-B7RP-1 costimulatory pathway in the regulation of immune responses to Leishmania major and Nippostrongylus brasiliensis infections. *Immunol Lett, 89*(2-3), 193-199. doi:10.1016/s0165-2478(03)00137-8

Miyaji, K., Sawai, S., Devaux, J., Yuki, N., Mori, M., & Kuwabara, S. (2014). Moesin is a possible target molecule for cytomegalovirus-related Guillain-Barré syndromeAuthor ResponseAuthor Response. *Neurology, 83*(24), 2314-2315.

Miyamoto, K., Oka, N., Kawasaki, T., Satoi, H., Matsuo, A., & Akiguchi, I. (1999). The action mechanism of cyclooxygenase-2 inhibitor for treatment of experimental allergic neuritis. *Muscle Nerve, 22*(12), 1704-1709. doi:10.1002/(sici)1097-4598(199912)22:12<1704::aid-mus13>3.0.co;2-a

Miyashiro, A., Matsui, N., Shimatani, Y., Nodera, H., Izumi, Y., Kuwabara, S., . . . Kaji, R. (2014). Are multifocal motor neuropathy patients underdiagnosed? An epidemiological survey in Japan. *Muscle Nerve, 49*(3), 357-361. doi:10.1002/mus.23930

Mizisin, A. P., & Weerasuriya, A. (2011). Homeostatic regulation of the endoneurial microenvironment during development, aging and in response to trauma, disease and toxic insult. *Acta Neuropathol, 121*(3), 291-312. doi:10.1007/s00401-010-0783-x

Monk, K. R., Feltri, M. L., & Taveggia, C. (2015). New insights on Schwann cell development. *Glia, 63*(8), 1376-1393. doi:10.1002/glia.22852

Mori, M., & Kuwabara, S. (2011). Fisher syndrome. *Curr Treat Options Neurol, 13*(1), 71-78. doi:10.1007/s11940-010-0103-8

Mori, M., Kuwabara, S., Fukutake, T., & Hattori, T. (2007). Intravenous immunoglobulin therapy for Miller Fisher syndrome. *Neurology, 68*(14), 1144-1146. doi:10.1212/01.wnl.0000258673.31824.61

Nachamkin, I., Barbosa, P. A., Ung, H., Lobato, C., Rivera, A. G., Rodriguez, P., . . . Perez, J. C. (2007). Patterns of Guillain-Barre syndrome in children: results from a Mexican population. *Neurology, 69*(17), 1665-1671.

Nanji, S. A., Hancock, W. W., Anderson, C. C., Adams, A. B., Luo, B., Schur, C. D., . . . Shapiro, A. M. (2004). Multiple combination therapies involving blockade of ICOS/B7RP-1 costimulation facilitate long-term islet allograft survival. *Am J Transplant, 4*(4), 526-536. doi:10.1111/j.1600-6143.2004.00384.x

Nobile-Orazio, E. (2001). Multifocal motor neuropathy. *J Neuroimmunol, 115*(1-2), 4-18. doi:10.1016/s0165-5728(01)00266-1

Nurieva, R. I. (2005). Regulation of immune and autoimmune responses by ICOS-B7h interaction. *Clin Immunol, 115*(1), 19-25. doi:10.1016/j.clim.2005.02.010

Overell, J. R., Hsieh, S. T., Odaka, M., Yuki, N., & Willison, H. J. (2007). Treatment for Fisher syndrome, Bickerstaff's brainstem encephalitis and related disorders. *Cochrane Database Syst Rev*(1), Cd004761. doi:10.1002/14651858.CD004761.pub2

Ozkaynak, E., Gao, W., Shemmeri, N., Wang, C., Gutierrez-Ramos, J. C., Amaral, J., . . . Hancock, W. W. (2001). Importance of ICOS-B7RP-1 costimulation in acute and chronic allograft rejection. *Nat Immunol, 2*(7), 591-596. doi:10.1038/89731

Pardoll, D. M. (2012). The blockade of immune checkpoints in cancer immunotherapy. *Nat Rev Cancer, 12*(4), 252-264. doi:10.1038/nrc3239

Parry, R. V., Rumbley, C. A., Vandenberghe, L. H., June, C. H., & Riley, J. L. (2003). CD28 and inducible costimulatory protein Src homology 2 binding domains show distinct regulation of phosphatidylinositol 3-kinase, Bcl-xL, and IL-2 expression in primary human CD4 T lymphocytes. *J Immunol, 171*(1), 166-174. doi:10.4049/jimmunol.171.1.166

Patton, K. T., & Thibodeau, G. A. (2018). *Anthony's Textbook of Anatomy & Physiology-E-Book*: Elsevier Health Sciences.

Pearson, J. A., Wong, F. S., & Wen, L. (2016). The importance of the Non Obese Diabetic (NOD) mouse model in autoimmune diabetes. *J Autoimmun, 66*, 76-88. doi:10.1016/j.jaut.2015.08.019

Pestronk, A., & Choksi, R. (1997). Multifocal motor neuropathy. Serum IgM anti-GM1 ganglioside antibodies in most patients detected using covalent linkage of GM1 to ELISA plates. *Neurology, 49*(5), 1289-1292. doi:10.1212/wnl.49.5.1289

Powell, A. M., & Black, M. M. (2001). Epitope spreading: protection from pathogens, but propagation of autoimmunity? *Clinical and Experimental Dermatology, 26*(5), 427-433. doi:10.1046/j.1365-2230.2001.00852.x

Prevot, N., Briet, C., Lassmann, H., Tardivel, I., Roy, E., Morin, J., . . . Boitard, C. (2010). Abrogation of ICOS/ICOS ligand costimulation in NOD mice results in autoimmune deviation toward the neuromuscular system. *Eur J Immunol, 40*(8), 2267-2276. doi:10.1002/eji.201040416

Quarles, R. H. (2007). Myelin-associated glycoprotein (MAG): past, present and beyond. *J Neurochem, 100*(6), 1431-1448. doi:10.1111/j.1471-4159.2006.04319.x

Querol, L., Devaux, J., Rojas-Garcia, R., & Illa, I. (2017). Autoantibodies in chronic inflammatory neuropathies: diagnostic and therapeutic implications. *Nat Rev Neurol, 13*(9), 533-547. doi:10.1038/nrneurol.2017.84

Racke, M. K., Scott, D. E., Quigley, L., Gray, G. S., Abe, R., June, C. H., & Perrin, P. J. (1995). Distinct roles for B7-1 (CD-80) and B7-2 (CD-86) in the initiation of experimental allergic encephalomyelitis. *J Clin Invest, 96*(5), 2195-2203. doi:10.1172/jci118274

Rasband, M. N. (2016). Glial Contributions to Neural Function and Disease. *Mol Cell Proteomics, 15*(2), 355-361. doi:10.1074/mcp.R115.053744

Readhead, C., Popko, B., Takahashi, N., Shine, H. D., Saavedra, R. A., Sidman, R. L., & Hood, L. (1987). Expression of a myelin basic protein gene in transgenic shiverer mice: correction of the dysmyelinating phenotype. *Cell, 48*(4), 703-712. doi:10.1016/0092-8674(87)90248-0

Richter, G., & Burdach, S. (2004). ICOS: a new costimulatory ligand/receptor pair and its role in T-cell activion. *Onkologie, 27*(1), 91-95. doi:10.1159/000075612

Rigaud, M., Gemes, G., Barabas, M. E., Chernoff, D. I., Abram, S. E., Stucky, C. L., & Hogan, Q. H. (2008). Species and strain differences in rodent sciatic nerve anatomy: implications for studies of neuropathic pain. *Pain, 136*(1-2), 188-201. doi:10.1016/j.pain.2008.01.016

Riley, J. L., Blair, P. J., Musser, J. T., Abe, R., Tezuka, K., Tsuji, T., & June, C. H. (2001). ICOS costimulation requires IL-2 and can be prevented by CTLA-4 engagement. *J Immunol, 166*(8), 4943-4948. doi:10.4049/jimmunol.166.8.4943

Rinaldi, S., Brennan, K. M., Kalna, G., Walgaard, C., Van Doorn, P., Jacobs, B. C., . . . Willison, H. J. (2013). Antibodies to heteromeric glycolipid complexes in Guillain-Barré syndrome. *PLoS One, 8*(12).

Roep, B. O., & Peakman, M. (2012). Antigen targets of type 1 diabetes autoimmunity. *Cold Spring Harb Perspect Med, 2*(4), a007781. doi:10.1101/cshperspect.a007781

Ross, H., Kaye, G., & Pawlina, W. (2003). Histology, a text and atlas 4th edition: Lippincott Williams & Wilkins Philedelphia.

Rottman, J. B., Smith, T., Tonra, J. R., Ganley, K., Bloom, T., Silva, R., . . . Coyle, A. J. (2001). The costimulatory molecule ICOS plays an important role in the immunopathogenesis of EAE. *Nat Immunol, 2*(7), 605-611. doi:10.1038/89750

Rudant, J., Dupont, A., Mikaeloff, Y., Bolgert, F., Coste, J., & Weill, A. (2018). Surgery and risk of Guillain-Barré syndrome: A French nationwide epidemiologic study. *Neurology, 91*(13), e1220-e1227.

Rutitzky, L. I., Ozkaynak, E., Rottman, J. B., & Stadecker, M. J. (2003). Disruption of the ICOS-B7RP-1 costimulatory pathway leads to enhanced hepatic immunopathology and increased gamma interferon production by CD4 T cells in murine schistosomiasis. *Infect Immun, 71*(7), 4040-4044. doi:10.1128/iai.71.7.4040-4044.2003

Salomon, B., Rhee, L., Bour-Jordan, H., Hsin, H., Montag, A., Soliven, B., . . . Bluestone, J. A. (2001). Development of spontaneous autoimmune peripheral polyneuropathy in B7-2-deficient NOD mice. *J Exp Med, 194*(5), 677-684. doi:10.1084/jem.194.5.677

Salzer, J. L. (2015). Schwann cell myelination. *Cold Spring Harb Perspect Biol, 7*(8), a020529. doi:10.1101/cshperspect.a020529

Saperstein, D. S., Amato, A. A., Wolfe, G. I., Katz, J. S., Nations, S. P., Jackson, C. E., . . . Barohn, R. J. (1999). Multifocal acquired demyelinating sensory and motor neuropathy: the Lewis-Sumner syndrome. *Muscle Nerve, 22*(5), 560-566. doi:10.1002/(sici)1097-4598(199905)22:5<560::aid-mus2>3.0.co;2-q

Saperstein, D. S., Katz, J. S., Amato, A. A., & Barohn, R. J. (2001). Clinical spectrum of chronic acquired demyelinating polyneuropathies. *Muscle Nerve, 24*(3), 311-324. doi:10.1002/1097-4598(200103)24:3<311::aid-mus1001>3.0.co;2-a

Sawai, S., Satoh, M., Mori, M., Misawa, S., Sogawa, K., Kazami, T., . . . Ishige, T. (2014). Moesin is a possible target molecule for cytomegalovirus-related Guillain-Barré syndrome. *Neurology, 83*(2), 113-117.

Schafflick, D., Kieseier, B. C., Wiendl, H., & Meyer Zu Horste, G. (2017). Novel pathomechanisms in inflammatory neuropathies. *J Neuroinflammation, 14*(1), 232. doi:10.1186/s12974-017-1001-8

Schwartz, R. H. (1992). Costimulation of T lymphocytes: the role of CD28, CTLA-4, and B7/BB1 in interleukin-2 production and immunotherapy. *Cell, 71*(7), 1065-1068. doi:10.1016/s0092-8674(05)80055-8

Sejvar, J. J., Baughman, A. L., Wise, M., & Morgan, O. W. (2011). Population incidence of Guillain-Barré syndrome: a systematic review and meta-analysis. *Neuroepidemiology, 36*(2), 123-133.

Setoguchi, R., Hori, S., Takahashi, T., & Sakaguchi, S. (2005). Homeostatic maintenance of natural Foxp3(+) CD25(+) CD4(+) regulatory T cells by interleukin (IL)-2 and induction of autoimmune disease by IL-2 neutralization. *J Exp Med, 201*(5), 723-735. doi:10.1084/jem.20041982

Shahrizaila, N., Kokubun, N., Sawai, S., Umapathi, T., Chan, Y.-C., Kuwabara, S., . . . Yuki, N. (2014). Antibodies to single glycolipids and glycolipid complexes in Guillain-Barré syndrome subtypes. *Neurology, 83*(2), 118-124.

Shang, P., Zhu, M., Wang, Y., Zheng, X., Wu, X., Zhu, J., . . . Zhang, H. L. (2020). Axonal variants of Guillain-Barre syndrome: an update. *J Neurol*. doi:10.1007/s00415-020-09742-2

Shin, I. S. J., Baer, A. N., Kwon, H. J., Papadopoulos, E. J., & Siegel, J. N. (2006). Guillain-Barré and Miller Fisher syndromes occurring with tumor necrosis factor α antagonist therapy. *Arthritis & Rheumatism: Official Journal of the American College of Rheumatology, 54*(5), 1429-1434.

Silveira, P. A., & Baxter, A. G. (2001). The NOD mouse as a model of SLE. *Autoimmunity, 34*(1), 53-64. doi:10.3109/08916930108994126

Slattery, R. M., Kjer-Nielsen, L., Allison, J., Charlton, B., Mandel, T. E., & Miller, J. F. (1990). Prevention of diabetes in non-obese diabetic I-Ak transgenic mice. *Nature, 345*(6277), 724-726. doi:10.1038/345724a0

Smith-Slatas, C., & Barbarese, E. (2000). Myelin basic protein gene dosage effects in the PNS. *Mol Cell Neurosci, 15*(4), 343-354. doi:10.1006/mcne.1999.0829

Snyder, D. H., Stone, S. H., & Raine, C. S. (1977). Attempts to induce chronic experimental allergic neuritis in strain 13 and Hartley guinea pigs. *J Neuropathol Exp Neurol, 36*(3), 488-498. doi:10.1097/00005072-197705000-00007

Solinas, C., Gu-Trantien, C., & Willard-Gallo, K. (2020). The rationale behind targeting the ICOS-ICOS ligand costimulatory pathway in cancer immunotherapy. *ESMO Open, 5*(1). doi:10.1136/esmoopen-2019-000544

Spiryda, L. B. (1998). Myelin protein zero and membrane adhesion. *J Neurosci Res, 54*(2), 137-146. doi:10.1002/(sici)1097-4547(19981015)54:2<137::aid-jnr2>3.0.co;2-f

St Charles, J. L., Bell, J. A., Gadsden, B. J., Malik, A., Cooke, H., Van de Grift, L. K., . . . Mansfield, L. S. (2017). Guillain Barré Syndrome is induced in Non-Obese Diabetic (NOD) mice following Campylobacter jejuni infection and is exacerbated by antibiotics. *J Autoimmun, 77*, 11-38. doi:10.1016/j.jaut.2016.09.003

Steiner, I., Argov, Z., Cahan, C., & Abramsky, O. (1985). Guillain-Barré syndrome after epidural anesthesia: Direct nerve root damage may trigger disease. *Neurology, 35*(10), 1473-1473.

Stirling, D. P., & Stys, P. K. (2010). Mechanisms of axonal injury: internodal nanocomplexes and calcium deregulation. *Trends Mol Med, 16*(4), 160-170. doi:10.1016/j.molmed.2010.02.002

Stoll, G., Griffin, J., Li, C. Y., & Trapp, B. (1989). Wallerian degeneration in the peripheral nervous system: participation of both Schwann cells and macrophages in myelin degradation. *J Neurocytol, 18*(5), 671-683.

Stoll, G., & Muller, H. W. (1999). Nerve injury, axonal degeneration and neural regeneration: basic insights. *Brain Pathol, 9*(2), 313-325. doi:10.1111/j.1750-3639.1999.tb00229.x

Stoll, G., Schwendemann, G., Heininger, K., Köhne, W., Hartung, H. P., Seitz, R., & Toyka, K. V. (1986). Relation of clinical, serological, morphological, and electrophysiological findings in galactocerebroside-induced experimental allergic neuritis. *J Neurol Neurosurg Psychiatry, 49*(3), 258-264. doi:10.1136/jnnp.49.3.258

Sundaram, V. K., Barakat, R., Massaad, C., & Grenier, J. (2020). Retracing Schwann cell developmental transitions in embryonic dissociated DRG cultures. *bioRxiv*, 2020.2007.2031.231258. doi:10.1101/2020.07.31.231258

Sundaram, V. K., Massaad, C., & Grenier, J. (2019). Liver X Receptors and Their Implications in the Physiology and Pathology of the Peripheral Nervous System. *Int J Mol Sci, 20*(17). doi:10.3390/ijms20174192

Sundaram, V. K., Sampathkumar, N. K., Massaad, C., & Grenier, J. (2019). Optimal use of statistical methods to validate reference gene stability in longitudinal studies. *PLoS One, 14*(7), e0219440. doi:10.1371/journal.pone.0219440

Susuki, K., Rasband, M. N., Tohyama, K., Koibuchi, K., Okamoto, S., Funakoshi, K., . . . Yuki, N. (2007). Anti-GM1 antibodies cause complement-mediated disruption of sodium channel clusters in peripheral motor nerve fibers. *J Neurosci, 27*(15), 3956-3967. doi:10.1523/jneurosci.4401-06.2007

Swallow, M. M., Wallin, J. J., & Sha, W. C. (1999). B7h, a novel costimulatory homolog of B7.1 and B7.2, is induced by TNFalpha. *Immunity, 11*(4), 423-432. doi:10.1016/s1074-7613(00)80117-x

Syndrome, F. C. G. o. P. E. i. G. B. (1997). Appropriate number of plasma exchanges in Guillain-Barré syndrome. *Annals of neurology, 41*(3), 298-306.

Taylor, W. A., & Hughes, R. A. (1985). Experimental allergic neuritis induced in SJL mice by bovine P2. *J Neuroimmunol, 8*(2-3), 153-157. doi:10.1016/s0165-5728(85)80055-2

Touma, E., Kato, S., Fukui, K., & Koike, T. (2007). Calpain-mediated cleavage of collapsin response mediator protein(CRMP)-2 during neurite degeneration in mice. *Eur J Neurosci, 26*(12), 3368-3381. doi:10.1111/j.1460-9568.2007.05943.x

Tsui, H., Winer, S., Jakowsky, G., & Dosch, H. M. (2003). Neuronal elements in the pathogenesis of type 1 diabetes. *Rev Endocr Metab Disord, 4*(3), 301-310. doi:10.1023/a:1025374531151

Uncini, A., & Kuwabara, S. (2015). Nodopathies of the peripheral nerve: an emerging concept. *J Neurol Neurosurg Psychiatry, 86*(11), 1186-1195. doi:10.1136/jnnp-2014-310097

Uncini, A., & Vallat, J. M. (2018). Autoimmune nodo-paranodopathies of peripheral nerve: the concept is gaining ground. *J Neurol Neurosurg Psychiatry, 89*(6), 627-635. doi:10.1136/jnnp-2017-317192

van Belle, T. L., Coppieters, K. T., & von Herrath, M. G. (2011). Type 1 diabetes: etiology, immunology, and therapeutic strategies. *Physiol Rev, 91*(1), 79-118. doi:10.1152/physrev.00003.2010

Van Den Berg, B., Walgaard, C., Drenthen, J., Fokke, C., Jacobs, B. C., & Van Doorn, P. A. (2014). Guillain–Barré syndrome: pathogenesis, diagnosis, treatment and prognosis. *Nature Reviews Neurology, 10*(8), 469.

Van den Berg, L. H., Kerkhoff, H., Oey, P. L., Franssen, H., Mollee, I., Vermeulen, M., . . . Wokke, J. H. (1995). Treatment of multifocal motor neuropathy with high dose intravenous immunoglobulins: a double blind, placebo controlled study. *J Neurol Neurosurg Psychiatry, 59*(3), 248-252. doi:10.1136/jnnp.59.3.248

van Schaik, I. N., Bossuyt, P. M., Brand, A., & Vermeulen, M. (1995). Diagnostic value of GM1 antibodies in motor neuron disorders and neuropathies: a meta-analysis. *Neurology, 45*(8), 1570-1577. doi:10.1212/wnl.45.8.1570

Vlam, L., van der Pol, W. L., Cats, E. A., Straver, D. C., Piepers, S., Franssen, H., & van den Berg, L. H. (2011). Multifocal motor neuropathy: diagnosis, pathogenesis and treatment strategies. *Nat Rev Neurol, 8*(1), 48-58. doi:10.1038/nrneurol.2011.175

Wakerley, B. R., Uncini, A., & Yuki, N. (2014). Guillain-Barre and Miller Fisher syndromes--new diagnostic classification. *Nat Rev Neurol, 10*(9), 537-544. doi:10.1038/nrneurol.2014.138

Waksman, B. H., & Adams, R. D. (1955). Allergic neuritis: an experimental disease of rabbits induced by the injection of peripheral nervous tissue and adjuvants. *J Exp Med, 102*(2), 213-236. doi:10.1084/jem.102.2.213

Watanabe, N., Gavrieli, M., Sedy, J. R., Yang, J., Fallarino, F., Loftin, S. K., . . . Murphy, K. M. (2003). BTLA is a lymphocyte inhibitory receptor with similarities to CTLA-4 and PD-1. *Nat Immunol, 4*(7), 670-679. doi:10.1038/ni944

Watts, T. H. (2005). TNF/TNFR family members in costimulation of T cell responses. *Annu Rev Immunol, 23*, 23-68. doi:10.1146/annurev.immunol.23.021704.115839

Weerasuriya, A., & Mizisin, A. P. (2011). The blood-nerve barrier: structure and functional significance. *Methods Mol Biol, 686*, 149-173. doi:10.1007/978-1-60761-938-3_6

Weerth, S., Berger, T., Lassmann, H., & Linington, C. (1999). Encephalitogenic and neuritogenic T cell responses to the myelin-associated glycoprotein (MAG) in the Lewis rat. *J Neuroimmunol, 95*(1-2), 157-164. doi:10.1016/s0165-5728(99)00004-1

Wicker, L. S., Miller, B. J., & Mullen, Y. (1986). Transfer of autoimmune diabetes mellitus with splenocytes from nonobese diabetic (NOD) mice. *Diabetes, 35*(8), 855-860. doi:10.2337/diab.35.8.855

Willison, H. J., Jacobs, B. C., & Van Doorn, P. A. (2016). Guillain-barre syndrome. *The Lancet, 388*(10045), 717-727.

Winer, S., Tsui, H., Lau, A., Song, A., Li, X., Cheung, R. K., . . . Dosch, H. M. (2003). Autoimmune islet destruction in spontaneous type 1 diabetes is not beta-cell exclusive. *Nat Med, 9*(2), 198-205. doi:10.1038/nm818

Yang, M., Peyret, C., Shi, X. Q., Siron, N., Jang, J. H., Wu, S., . . . Zhang, J. (2015). Evidence from Human and Animal Studies: Pathological Roles of CD8(+) T Cells in Autoimmune Peripheral Neuropathies. *Front Immunol, 6*, 532. doi:10.3389/fimmu.2015.00532

Yi, K. H., & Chen, L. (2009). Fine tuning the immune response through B7-H3 and B7-H4. *Immunol Rev, 229*(1), 145-151. doi:10.1111/j.1600-065X.2009.00768.x

Yoshida, T., Jiang, F., Honjo, T., & Okazaki, T. (2008). PD-1 deficiency reveals various tissue-specific autoimmunity by H-2b and dose-dependent requirement of H-2g7 for diabetes in NOD mice. *Proc Natl Acad Sci U S A, 105*(9), 3533-3538. doi:10.1073/pnas.0710951105

Yoshinaga, S. K., Whoriskey, J. S., Khare, S. D., Sarmiento, U., Guo, J., Horan, T., . . . Senaldi, G. (1999). T-cell co-stimulation through B7RP-1 and ICOS. *Nature, 402*(6763), 827-832. doi:10.1038/45582

Yu, L., Robles, D. T., Abiru, N., Kaur, P., Rewers, M., Kelemen, K., & Eisenbarth, G. S. (2000). Early expression of antiinsulin autoantibodies of humans and the NOD mouse: Evidence for early

determination of subsequent diabetes. *Proceedings of the National Academy of Sciences, 97*(4), 1701-1706. doi:10.1073/pnas.040556697

Yuki, N., Koga, M., & Hirata, K. (1998). Isolated internal ophthalmoplegia associated with immunoglobulin G anti-GQ1b antibody. *Neurology, 51*(5), 1515-1516. doi:10.1212/wnl.51.5.1515-b

Yuki, N., Odaka, M., & Hirata, K. (2001). Acute ophthalmoparesis (without ataxia) associated with anti-GQ1b IgG antibody: clinical features. *Ophthalmology, 108*(1), 196-200. doi:10.1016/s0161-6420(00)00420-6

Yuki, N., Yamada, M., Koga, M., Odaka, M., Susuki, K., Tagawa, Y., . . . Hirata, K. (2001). Animal model of axonal Guillain-Barré syndrome induced by sensitization with GM1 ganglioside. *Ann Neurol, 49*(6), 712-720.

Zautner, A. E., Johann, C., Strubel, A., Busse, C., Tareen, A. M., Masanta, W. O., . . . Gross, U. (2014). Seroprevalence of campylobacteriosis and relevant post-infectious sequelae. *Eur J Clin Microbiol Infect Dis, 33*(6), 1019-1027. doi:10.1007/s10096-013-2040-4

Zehntner, S. P., Brisebois, M., Tran, E., Owens, T., & Fournier, S. (2003). Constitutive expression of a costimulatory ligand on antigen-presenting cells in the nervous system drives demyelinating disease. *Faseb j, 17*(13), 1910-1912. doi:10.1096/fj.03-0199fje

Zeng, X. L., Nagavalli, A., Smith, C. J., Howard, J. F., & Su, M. A. (2013). Divergent effects of T cell costimulation and inflammatory cytokine production on autoimmune peripheral neuropathy provoked by Aire deficiency. *J Immunol, 190*(8), 3895-3904. doi:10.4049/jimmunol.1203001

Zhai, Q., Wang, J., Kim, A., Liu, Q., Watts, R., Hoopfer, E., . . . He, Z. (2003). Involvement of the ubiquitin-proteasome system in the early stages of wallerian degeneration. *Neuron, 39*(2), 217-225. doi:10.1016/s0896-6273(03)00429-x

Zhu, J., Zou, L., Zhu, S., Mix, E., Shi, F., Wang, H., . . . Ljunggren, H. (2001). Cytotoxic T lymphocyte-associated antigen 4 (CTLA-4) blockade enhances incidence and severity of experimental autoimmune neuritis in resistant mice. *J Neuroimmunol, 115*(1-2), 111-117. doi:10.1016/s0165-5728(01)00255-7

Zou, L. P., Ljunggren, H. G., Levi, M., Nennesmo, I., Wahren, B., Mix, E., . . . Zhu, J. (2000). P0 protein peptide 180-199 together with pertussis toxin induces experimental autoimmune neuritis in resistant C57BL/6 mice. *J Neurosci Res, 62*(5), 717-721. doi:10.1002/1097-4547(20001201)62:5<717::aid-jnr11>3.0.co;2-p

zu Hörste, G. M., Heidenreich, H., Mausberg, A. K., Lehmann, H. C., ten Asbroek, A. L., Saavedra, J. T., . . . Kieseier, B. C. (2010). Mouse Schwann cells activate MHC class I and II restricted T-cell responses, but require external peptide processing for MHC class II presentation. *Neurobiology of disease, 37*(2), 483-490.